2005

DETERMINING PHYSICAL CONDITIONS IN STAR FORMING REGIONS

Nicholas Paul Abel
University of Kentucky, npabel2@uky.edu

ABSTRACT FOR DISSERTATION

Nicholas Paul Abel

The Graduate School

University of Kentucky

2005

DETERMINING PHYSICAL CONDITIONS IN STAR FORMING REGIONS

ABSTRACT OF DISSERTATION

A dissertation submitted in partial fulfillment of the
requirements for the degree of Doctor of Philosophy in the
College of Arts and Sciences
at the University of Kentucky

By
Nicholas Paul Abel

Lexington, Kentucky

Director: Dr. Gary Ferland, Professor of

Lexington, Kentucky

2005

ABSTRACT OF DISSERTATION

DETERMINING PHYSICAL CONDITIONS IN STAR FORMING REGIONS

This dissertation is a study of the physical conditions in star-forming regions, and combines observational data and theoretical calculations.

We studied the physical conditions of Orion's Veil, which is an absorbing screen that lies along the line of sight to the Orion H II region. We computed photoionization models of the Veil. We combined calculations with UV, radio, and optical spectra that resolve the Veil into two velocity components. We derive many physical parameters for each component seen in 21 cm absorption. We find the magnetic field energy dominates turbulent and thermal energies in one component while the other component is close to equipartition between turbulent and magnetic energies. We observe H_2 absorption for highly excited levels. We find that the low ratio of H_2/H^0 in the Veil is due to the high UV flux incident upon the Veil. We detect blueshifted S^{+2} and P^{+2} ions which must arise from ionized gas between the neutral portions of the Veil and the Trapezium and shields the Veil from ionizing radiation. We determine the ionized and neutral layers of the Veil will collide in less than 85,000 years.

The second part of this dissertation involved self-consistently calculating the thermal and chemical structure of an H II region and photodissociation region (PDR) that are in pressure equilibrium. This differs from previous work, which used separate calculations for each gas phase. Our calculations span a wide range of initial conditions. We describe improvements made to the spectral synthesis code Cloudy which made these calculations possible. These include the addition of a molecular network with ~1000 reactions involving 68 molecules and improved treatment of the grain physics. Archival data are used to derive important physical characteristics of observed H II regions and PDRs. These include stellar temperatures, electron densities, ionization parameters, UV flux, and PDR density. The contribution of the H II region to PDR emission line

diagnostics is also calculated. Finally, these calculations are used to derive emission line ratios than can tell us the equation of state in star-forming regions.

KEYWORDS: star-formation, molecular formation, infrared astronomy, magnetic fields, interstellar medium

Nicholas Paul Abel

September 22, 2005

DETERMINING PHYSICAL CONDITIONS IN STAR FORMING REGIONS

By

Nicholas Paul Abel

Gary J. Ferland
Director of Dissertation

Thomas T. Troland
Director of Graduate Studies

September 22, 2005

RULES FOR THE USE OF DISSERTATIONS

Unpublished dissertations submitted for the Doctor's degree and deposited in the University of Kentucky Library are as a rule open for inspection, but are to be used only with due regard to the rights of the authors. Bibliographical references may be noted, but quotations or summaries of parts may be published only with the permission of the author, and with the usual scholarly acknowledgments.

Extensive copying or publication of the dissertation in whole or in part also requires the consent of the Dean of the Graduate School of the University of Kentucky.

A library that borrows this dissertation for use by its patrons is expected to secure the signature of each user.

Name	Date

DISSERTATION

Nicholas Paul Abel

The Graduate School

University of Kentucky

2005

DETERMINING PHYSICAL CONDITIONS IN STAR FORMING REGIONS

DISSERTATION

A dissertation submitted in partial fulfillment of the
requirements for the degree of Doctor of Philosophy in the
College of Arts and Sciences
at the University of Kentucky

By
Nicholas Paul Abel

Lexington, Kentucky

Director: Dr. Gary Ferland, Professor of

Lexington, Kentucky

2005

ACKNOWLEDGEMENTS

To thank the people who have influenced this work would be a dissertation unto itself. However, I would be remiss (and probably in the doghouse!!) if I did not start with the support and love of my beautiful wife Kristal. Even though you know little about astrophysics, you make me a better scientist and person. I would also like to thank my parents and siblings, especially my mom, whose constant supply of star-trek inspired questions always keeps me on my toes.

I would also like to thank the many teachers and advisors who have made this work possible. In particular, I would like to thank Gary Ferland for taking me on as a graduate student 3 plus years ago, and then being patient with me as I tried to understand basic astrophysics. I would also like to thank Tom Troland for his time, humor, and insightful explanation of astrophysical phenomena. At Miami of Ohio, Stephen Alexander gave me my first opportunity to study astrophysics, I would like to thank him for his friendship and never-ending supply of Uranus jokes. Other teachers I would like to thank include Helen Nugent, Dan Callon, Nick Steph, Glenn Julian, and Michael Eides.

I would like to thank the many peers whose friendship made this academic pursuit very enjoyable. In particular, I would like to thank the following: Ricky Lindsey, Dan Rector, John Batty, all my teammates at Franklin College, Karen Kosiba, Andy Neely, George Litsas, Rob Compton, Joey & Amelia Carpenter, Chris Fuse, Vjeko, Slobo, Chris Jones (go 'Cats!!!) and all my friends at Miami of Ohio, Elizabeth Mayo, Emily Flynn, Joel Handley, Matt Sirocky, Matt Lykins, Humeshkar Nemala, Terri Yun, Ryan Porter, Robert Bauman, Nilmani Mathur, Anuj Sarma, Geetashree, and last but certainly not least, Gargi Shaw.

I cannot help but thank one final group. It is well known that I am a football junkie. Therefore, I would like to thank the University of Kentucky football program for their continuing lack of success. I fear that, if they had put together a winning team, my studies may have suffered catastrophically. Their lack of success allowed me more time to study, which also allowed for a timely completion of this dissertation.

Table of Contents

List of Tables

List of Figures

Chapter 1: Introduction

1.1 Historical perspective

Since the beginning; whenever, however, and whatever one believes about the beginning, humanity has wondered about the lights in the night sky. What are they? How do they move? How far away are they? Such questions are not asked only by astrophysicists, but are asked by people from all ages and backgrounds.

The answers to our questions about the lights in the night sky have evolved over history. The ancients thought of the lights we now call stars as fixed to a giant "celestial sphere", with the earth at the center (Figure 1.1). The stars on these spheres were there for all creation, never changing. Observations of the celestial sphere, however, showed that stars did evolve over time. Tycho Brahe observed a supernova, a star explosion, in 1572 (and earlier, in 1054, a supernova created what is now the Crab Nebula). Later, Johannas Kepler observed a supernova in 1604. These observations led to the conclusion that the celestial sphere can undergo change. Additionally, some stars in the night sky appeared to wonder across the celestial sphere. These were called planets (from the Greek for "wanderer"). The ancients believed the planets orbited around the earth in perfect circles. Observations showed, however, that this "geocentric" model did not accurately predict the position of the planets over time. To account for this, Ptolemy introduced the concept of an epicycle, which is a small circular orbit that a planet moves on in addition to the primary orbit of the planet around the earth (Figure 1.2). However, in 1543, another theory of the motions of the planets was postulated by Nicholas Copernicus. Copernicus proposed that the Sun was at the center of the universe, and the earth and planets orbited around the Sun. This "heliocentric" model was studied by Kepler, who used the observations of Brahe to show that the orbit of the planets in the heliocentric model was not a

circle, but an ellipse. Galileo found in 1610, with the development of the telescope, that there are moons orbiting Jupiter. These observations showed that not all objects orbit around the earth. Finally, Isaac Newton combined his theory of gravity with observation to show that the sun is at the center of the solar system, and the earth is nothing more than a planet moving around the sun in an elliptical orbit.

With the fundamental foundation of an earth-centered universe and the celestial sphere proven incorrect, new questions about our universe began to be asked. No one thought to ask "how far are stars from the earth?" before, it was understood that they were all on the celestial sphere and therefore the same distance away from earth. No one thought to ask "How are stars formed?" as until the 16th century everyone thought stars were placed on the perfect celestial sphere by the creator, with stars being neither created or destroyed. No one really thought about what stars were made of, either, as it seemed like a question that was impossible to answer.

The answers to questions about the properties of stars again came with technological advances in the telescope and an old surveyors' technique for determining distances. In 1837, William Bessel measured a parallax of a star. Parallax is the angular shift in position of a star against a much further background due to observing a star at two positions in the earth's orbit (usually 6 months apart). Parallax is easily seen by holding a pencil a few inches from one's face, looking at the pencil with only the right eye open, then switching back and forth between your right and left eye. The apparent shift in position is due to parallax, and can be related to distance (Figure 1.3). To measure the parallax of a star, better telescopes were needed than the ones used by Galileo, and these telescopes only became available in the 19th century. Now, space missions such as Hipparchos can routinely measure the parallax of thousands of stars, and techniques also exist to estimate the distance to galaxies. What is found is a universe where the nearest stars are a few parsecs away (where 1 parsec equals

17.64 trillion miles and is the distance an object would be if the observed parallax equaled one arc second), and galaxies are many kilo- or mega-parsecs away from earth.

The advent of spectroscopic analysis and quantum mechanics in the 19th and 20th centuries allowed us to answer the question "What are stars made of?" Spectroscopy is used across many disciplines. A common phrase that summarizes the importance of spectroscopy is "a picture is worth a thousand words, but a spectrum is worth a thousand pictures". Absorption or emission lines can tell us about chemical composition, velocity, temperature, magnetic field, and many other physical quantities. However, without quantum mechanics, the spectrum would not carry nearly as much information. Quantum mechanics allows us to say precisely what element or molecule is producing the emission or absorption line, along with the wavelength and transition probability of the line. From the analysis of spectral lines, astrophysicists have found that, by number, 90% of the observable matter in the universe is hydrogen, ~10% is helium, and ~0.01% is locked up in other elements.

We also believe that we have a general ideal about how stars and planets form. The current theory of star formation is that massive clouds collapse due to gravity. The force of gravity is balanced by thermal, turbulent, and magnetic pressure. If the gravitational force is great enough, then eventually a region of the cloud becomes so dense that hydrogen fusion occurs. When this happens, a star is born. The star will sometimes have leftover material still orbiting it, which is called a protoplanetary disk (Figure 1.4). Through collisions and gravitational influences, the protoplanetary disk accretes into a small number of larger particles called planetesimals. Planetesimals are the building blocks of planets, and through further collisions planetesimals are converted into a few objects orbiting around the parent star. At this stage, a solar system is formed.

A very surprising result about the giant clouds from which stars and planets are born is that almost all the elements are in the form of molecules. This was first realized in the 1940's with detections of CH and CN. Future observations in the UV, radio, millimeter, and infrared made it clear that molecular clouds are the environments from which stars are formed. We now know that the most abundant molecules in molecular clouds are H_2 and CO, and that over 100 molecules have been observed in space.

A molecular cloud is a complex environment. Stars forming in molecular clouds emit large amounts of radiation, altering the environment through the photodissociation of molecules and the photoionization of atoms. Additionally, the environment is dynamic, with the gas and dust (small (~0.1 μm) solid particles made up predominately of carbonaceous and silicate-rich material) moving in response to magnetic, turbulent, thermal, and gravitational forces.

With the advent of the computer age, the complexities of star formation can be studied by combining observational data with theoretical calculations that include all the relevant physical processes that occur in star-forming regions. How are molecules created and destroyed? How are atoms ionized and made neutral again (recombine)? What is the role of the magnetic field? What heats and cools the molecular cloud? How is the radiation transported through a molecular cloud? What is the role of dust? What role does dynamics play? All of these mechanisms, and many others, must be simultaneously and self-consistently solved in any calculation of the physical conditions in star-forming environments.

1.2 Topics of Dissertation

This dissertation is a study of the physical conditions in regions of active star-formation. In Chapter 2 & 3, the physical conditions in a region known as Orion's Veil are derived from UV, radio, and optical spectra combined with theoretical calculations. In Chapter 4, self-consistent calculations of ionized,

atomic, and molecular gas are presented, and the relevance of the calculations to the study of star-forming regions are discussed. In Chapter 5, spectral diagnostics are presented that can determine the role of magnetic fields in star formation. Chapter 6 gives a series of conclusions drawn from this work.

1.3 A Quick Note on Terminology

The terminology used in astrophysics may be confusing to someone not in the field. For instance, astrophysics uses two different notations for identifying an absorption/emission line and the atom that is producing the spectral feature. If one wants to refer to a spectral feature produced by an element in a particular stage, a roman numeral is used to indicate the stage of ionization, with I being the neutral, II the first ion, III the second ion, etc. If instead one wants to refer to the element producing the spectral feature, then a subscript (+) is used, with a coefficient in front of the plus to indicate the stage of ionization. In this notation, 0 indicates the neutral, + the first ion, 2+ the second ion, etc. Therefore, H I refers to the spectral feature, and H^0 the atom producing the spectral feature. Another piece of terminology unique to astrophysics is the dex. Because astrophysicists deal with numbers ranging from the extremely small ($< 10^{-10}$) to the extremely large ($>10^{50}$), often times researchers will report the logarithm of a particular quantity. The dex is a convenient way to report the logarithm, and is just the exponent of the measurement. If a measurement of a physical quantity yields a value of 10^{45}, then this could be reported as Log[X] = 45, or as 45 dex, where the dex makes it understood that we are referring to a logarithmic scale.

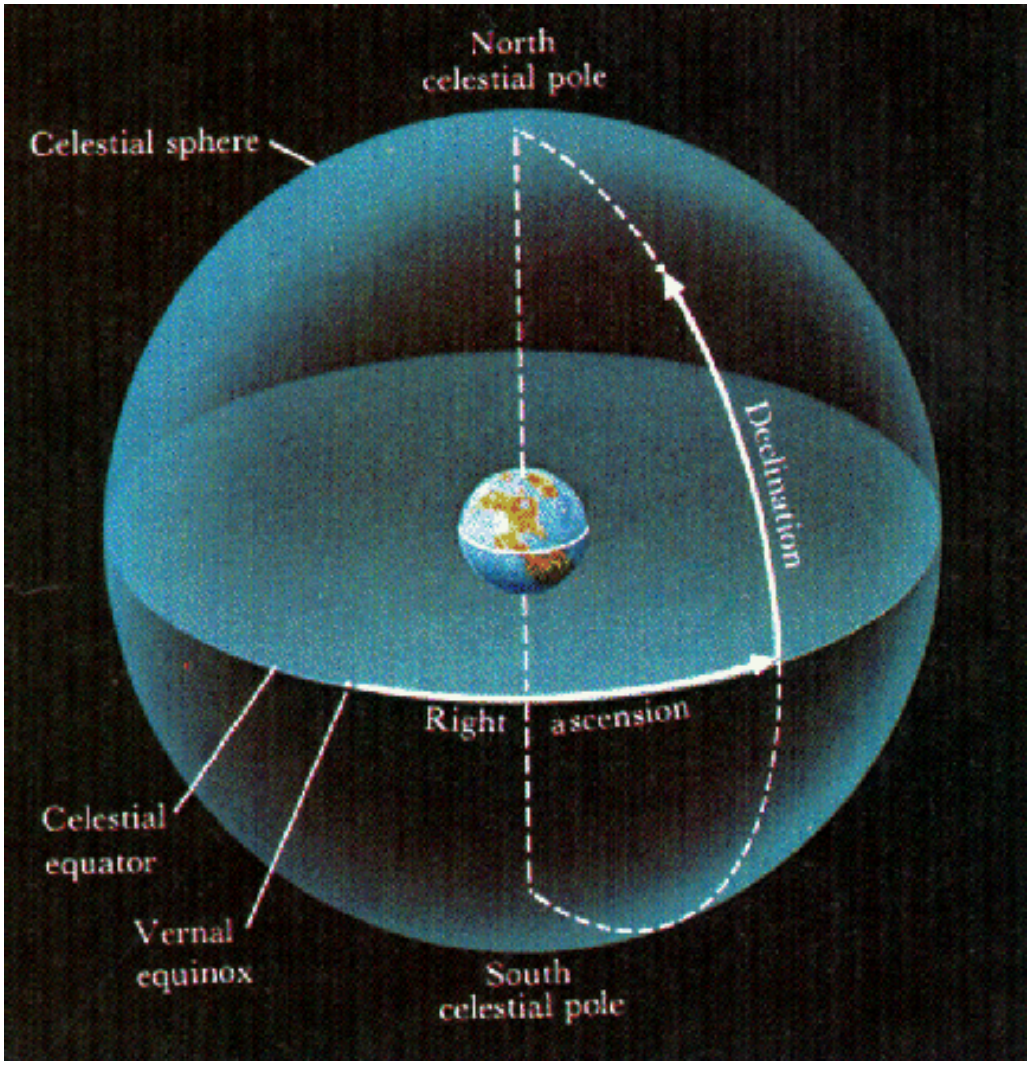

Figure 1.1 The celestial sphere. The ancients believed that all stars were fixed to the inside of the celestial sphere, therefore all stars were the same distance away from earth, which was placed at the center of the celestial sphere.

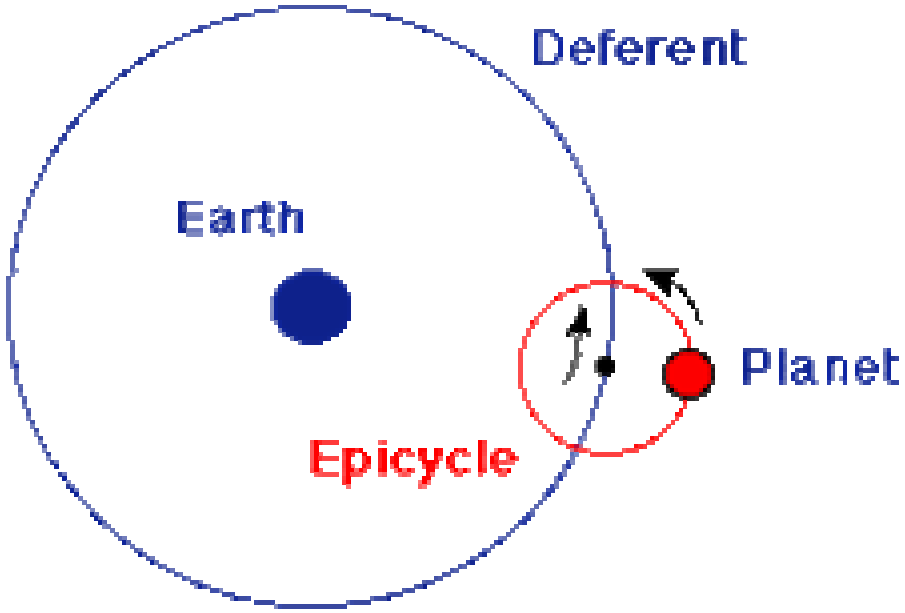

Figure 1.2 The geometry of an epicycle. In the geocentric model of the solar system, planets must always travel in the same direction. However, astronomers in the ancient world noticed that Mars, Jupiter, and Saturn would, for short periods of time, reverse direction. The concept of an epicycle was therefore proposed by Ptolemy around 100 AD, which allowed for both a geocentric model and retrograde motion. In a heliocentric model of the solar system, retrograde motion is a natural consequence of orbital motion.

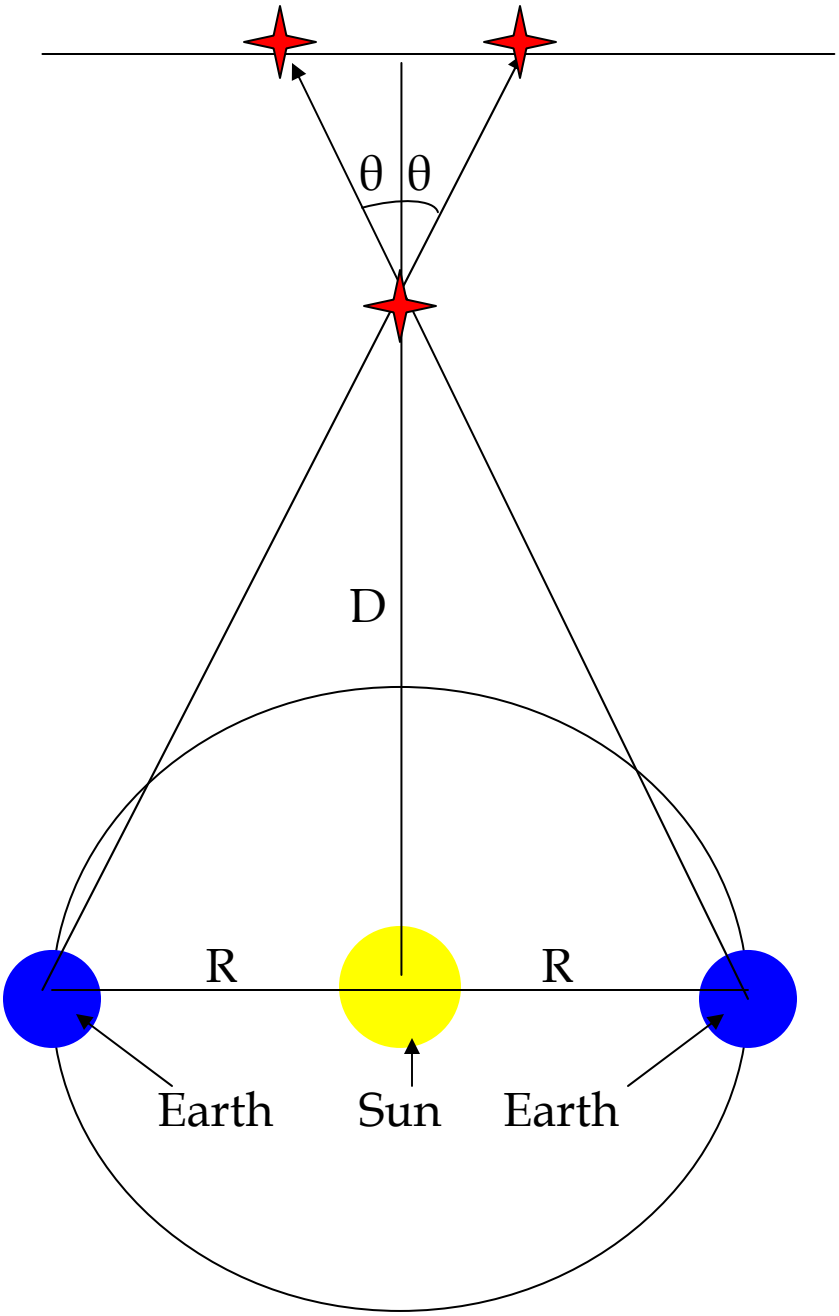

Figure 1.3 The concept of parallax. As the earth orbits around the sun, a nearby star will appear to shift in position relative to background stars due to our different viewing angle. Observations of a star's position spaced six months apart (2θ), combined with knowledge of the earth's distance from the sun (R), then gives the distance of the star from earth (D).

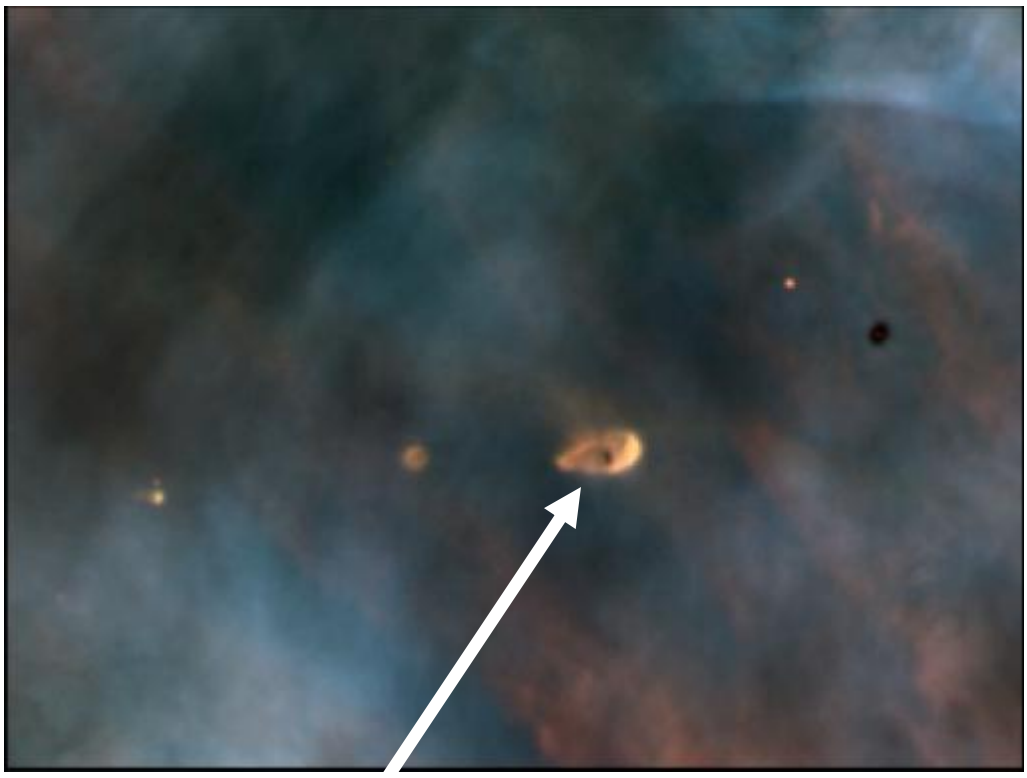

Figure 1.4 A protoplanetary disk in the Orion Nebula (O'Dell 2001). The material surrounding the star is leftover from the formation of the star. It is believed that the gas and dust that surrounds the star will eventually, through collisions and gravitational interactions, form a planetary system.

Chapter 2: Physical Conditions in Orion's Veil

2.1 Introduction

The Orion Complex is one of the best-studied regions of active star formation. These studies include a wide variety of observations of the magnetic field on many angular scales (e.g. van der Werf et al. 1993, Heiles 1997). Star formation is controlled by a complex and dynamic interplay between gravitational, thermal, and magnetic forces. Magnetic effects, in particular, can be complex. Yet they must be considered if we are to achieve a comprehensive understanding of the star formation process.

The Orion region consists of ionized (H^+), atomic (H^0), and molecular gas. The H II region is mainly the illuminated face of the background molecular cloud, Orion Molecular Cloud 1 (OMC1; see the comprehensive review by O'Dell 2001). It is heated and ionized by the light of the Trapezium cluster, with the single O6 V star θ^1 Ori C (Walborn & Panek, 1984) providing most of the energy. The "Veil" is the layer of largely atomic gas that lies between the Trapezium and us. Reddening within the H II region itself is small (O'Dell 2002). Also, optical obscuration toward the nebula correlates well with H^0 column density in the Veil (O'Dell & Yusef-Zadeh 2000). Therefore, nearly all obscuration toward the H II region occurs within the Veil. Moreover, studies of stellar extinction as a function of distance establish that the Veil is associated with the Orion complex (Goudis, 1982).

A wealth of observational data reveals physical properties of the Veil. In particular, the Veil is one of the few interstellar regions where we have accurate *maps* of the line of sight component of the local magnetic field (Troland et al. 1989). These magnetic field maps are derived from Zeeman splitting of the H I 21 cm line, seen in absorption against the H II region continuum emission. Other

physical properties of the Veil such as density, temperature, and level of ionization, can be determined by combining optical and UV absorption line measurements with photoionization calculations. Altogether, these data present a unique opportunity to test modern theories of the physical state of the interstellar medium in star-forming regions.

Section 2.2 summarizes what is known about the physical state of gas in Orion's Veil. Section 2.3 confronts these observations with simulations of the expected thermal and ionization equilibrium. In Section 2.4 we discuss the significance of the model results to magnetic energy equipartition in the Veil, and in Section 2.5 we summarize our conclusions.

2.2 Observed properties of the Veil

2.2.1 Column densities and extinction

Observations of absorption lines reveal the column densities of a number of atomic and molecular species in the Veil. Shuping & Snow (1997; henceforth referred to as SS97) derive the atomic hydrogen column density, $N(H^0)$, from IUE observations of the Lyα line. Their value of $N(H^0) = (4 \pm 1) \times 10^{21}$ cm^{-2} is a factor of ~4 larger than the previous OAO-2 and Copernicus measurements (Savage & Jenkins 1972; Savage et al. 1977). Column densities of other species were also measured by SS97. Among the most important for this study are excited states of C^0, O^0, and Si^+. Since the populations of more than one excited state have been measured for each, they can be used as density indicators. The atomic and singly ionized column densities of C, Mg, and S were also measured, and this information constrains the ionization state of the Veil. We assume that the physical properties of the gas within the Veil are driven by the radiation emitted by the nearby Trapezium stars.

Reddening and extinction to the Trapezium stars and over the entire H II region have been measured by a number of authors (Bohlin & Savage 1981; Cardelli, Clayton, & Mathis 1989; O'Dell & Yusef-Zadeh 2000). The color excess E(B-V) = 0.32 mag, and the extinction is A_V = 1.6 mag. Therefore the ratio of total to selective extinction R = 5.0, significantly larger than the average value of 3.1 in the diffuse ISM. The high value of R suggests that the reddening is caused by grains with a larger than normal size distribution. The measured visual extinction and the SS97 value for $N(H^0)$ yield a ratio, $A_V/N(H^0)$, of $(4 \pm 1) \times 10^{-22}$ mag cm^2. This value is slightly lower than the average ratio in the diffuse interstellar medium (5.3×10^{-22} mag cm^2), and it is also consistent with larger than normal grains. If any ionized hydrogen is present in the Veil, the ratio of visual extinction to total hydrogen column density will be even smaller.

The line of sight to the Trapezium has a surprisingly low fraction of molecular gas. Copernicus observations established that $N(H_2) < 3.5 \times 10^{17}$ cm^{-2} (Savage et al. 1977). This value implies $N(H_2)/N(H^0) \lesssim 10^{-4}$ (other regions within the Orion complex are molecular, of course). However, observed correlations between $N(H_2)/N(H^0)$ and A_V (Savage et al. 1977) suggest that the Veil should be predominantly molecular. This anomaly has long been thought to arise from the Veil's abnormal grain properties (SS97), although a high UV flux has also been suggested (Savage et al. 1977). Larger grains are less effective at producing H_2 since the grain surface area per unit grain mass is smaller. Also, large grains are less effective in shielding H_2 from photodissociation by the Lyman-Werner bands because of the smaller projected area per unit mass. The observed $N(H^0)$ and the absence of H_2 in the Veil (toward the Trapezium stars) will be important constraints on the model calculations presented in Section 2.3.

2.2.2 H I 21 cm velocity components

Van de Werf & Goss (1989) reported at least three separate velocity components in the 21cm H I absorption lines seen against the background H II region. More recent observations of these same 21 cm lines are presented in Figure 2.1 and were taken by Troland et al. (2005; in preparation). This line profile reveals two relatively narrow components toward the Trapezium and possibly a broader underlying component. For the purposes of this analysis, we fitted the Troland et al. H I optical depth profile with just two Gaussian components. Inclusion of the underlying broad component does not alter the analysis below in any significant way. Of the two components in the fit, the "narrow" component has (V_{LSR}, ΔV_{FWHM}) = 5.3 and 2.0 km s^{-1}, the "wide" component has (V_{LSR}, ΔV_{FWHM}) = 1.3 and 3.8 km s^{-1}. (Add 18.1 km s^{-1} to convert LSR to heliocentric velocities.) If the line widths result from thermal broadening alone, kinetic temperatures are 87 and 315 K in the narrow and wide components, respectively. However, 21 cm H I lines are almost always broader than thermal, indicating the presence of supersonic motions (Heiles & Troland, 2003). Therefore, actual kinetic temperatures may be significantly less.

2.2.3 Optical velocity components

For reference, a schematic geometry of the central regions of Orion, based on O'Dell (1993), is shown in Figure 2.2.

Line profiles can be used to reveal kinematics of the various regions. The SS97 UV data had insufficient spectral resolution to resolve lines into individual components. However, the much higher resolution optical study performed by O'Dell et al. (1993) detected many components in the Ca II absorption line toward the Trapezium stars (θ^1 Ori A, B, C, and D) and toward θ^2 Ori. The Ca II profiles for Ori A-D have an absorption component in the same velocity range as the H I 21 cm absorption. (Ca II and 21 cm H I lines are shown in Figure 2.1.) Yet the Ca II profile has other components not seen in 21 cm H I absorption.

The lack of a strong correlation between Ca II and 21 cm H I absorption profiles may have a simple explanation. The Ca^+ column densities measured by O'Dell et al. (1993) show little variation, ranging from 10.7 to 12.9×10^{11} cm^{-2}. For a gas phase Ca/H abundance of 2×10^{-8} (Baldwin et al. 1991, hereafter BFM), the associated H^0 column density is 6×10^{19} cm^{-2}. This value is less than 2% of $N(H^0)$ measured by SS97. Therefore, Ca^+ is a trace constituent within the Veil. Photoionization calculations presented later confirm this conclusion. We believe H^0 samples most of the matter in the Veil, so we will focus on this species in our calculations.

2.2.4 Physical location, size, and geometry

Statistical arguments suggest that the Veil is ~0.6 pc away from θ^1 Ori C. This estimate is based on the 3-D distribution of stars in the Orion Nebula Cluster given by Hillenbrand & Hartmann (1998) and upon observations of the fraction of proplyds that are protected by the Veil from photoionization and seen in silhouette (Bally et al. 2000). The uncertainty of this value is hard to estimate.

Another constraint on the Veil location comes from the fact that the Veil emission in Hβ is not prominent compared with the Hβ surface brightness of the background H II region (5×10^{-12} erg s^{-1} cm^{-2} $arcsec^{-2}$, BFM 1991). This constraint requires the Veil to be much further away from the Trapezium stars than the main photoionized region (~0.25 parsecs, Figure 2.2). Since the Veil's position is poorly constrained by these arguments, we will treat it as a free parameter.

The geometric properties of the Veil and its density are partly constrained by observational data. The Veil subtends at least 10 arc minutes in the plane of the sky since it covers both M42 and M43 (van der Werf & Goss 1989). This dimension amounts to 1.5 pc at 500 pc. The thickness L can be deduced from the SS97 H^0 column density if the atomic hydrogen density $n(H^0)$ is also known since $L \sim 4x10^{21}/n(H^0)$ cm. If the Veil extends no more than ~1.5 pc in the plane of the sky, then this relation sets a lower limit to the density, $n(H^0) > 10^2$ cm^{-3}, since the

Veil is probably not cigar-shaped pointed in our direction. There is no real physical upper limit to the density. If $n(H^0) \geq 10^3$ cm^{-3}, then the Veil is a sheet viewed face on. Such sheet-like structures are commonly seen in the diffuse ISM (Heiles & Troland 2003).

2.2.5 Harmonic mean temperature of H^0

The 21 cm H I and Lyα data establish the harmonic mean temperature of the Veil. (See Section 2.3.3) The 21 cm absorption measures $N(H^0)/T_{spin}$ because of the correction for stimulated emission (Spitzer 1978; equation 3-37). From the 21 cm data of van der Werf and Goss (1989), $N(H^0)/T_{spin} = 4.3 \times 10^{19}$ cm^{-2} K^{-1} toward the Trapezium stars (integrated across the full line). This value, and the measured $N(H^0)$ from SS97, imply a harmonic mean spin temperature of 70-120K (corresponding to the lower and upper limits to $N(H^0)$ derived by SS97). However, the narrow H I component must have T < 87 K, the temperature equivalent of its full width.

Harmonic mean H^0 temperatures, estimated from Lyα and 21 cm data are only accurate if both data sample the same absorbing gas. This assumption need not be correct since the Lyα and 21 cm data sample very different projected areas through the Veil (sub-arcsec for the UV vs ~15 arcsec for the radio). However, maps of optical extinction suggest it is fairly smooth across the Veil (O'Dell & Yusef-Zadeh 2000), so the Lyα and 21 cm data likely sample comparable regions.

2.2.6 Magnetic properties

Using the Zeeman effect in the 21 cm absorption lines, Troland et al. (1989, 2004) measure line-of-sight magnetic field strengths B_{los} independently in the narrow and wide H I velocity components. Across much of the Veil, they find comparable values for the two components, typically -50 μG, where the minus sign indicates a field pointed toward the observer. Along the line of sight to the Trapezium, $B_{los} = -45 \pm 5$ and -54 ± 4 μG for the narrow and wide components, respectively. For a statistical ensemble of randomly-directed fields of the same

strength, the average total field strength is $2B_{los}$. Therefore, toward the Trapezium stars, we take the total field strength to be ~100 μG in the Veil.

Field strengths this high are almost exclusively associated with regions of massive star formation where $n > 10^3$-10^4 cm^{-3} (Crutcher et al. 1999). They are never seen in diffuse, absorbing H I gas of the cold neutral medium (CNM) studied by Heiles & Troland (2003). Nor are they commonly found in molecular clouds associated with low and intermediate mass star formation (Crutcher et al. 1993, Troland et al. 1996). High field strengths in the Veil almost certainly reflect the history of this layer, a history associated with a large, self-gravitating region of massive star formation rather than with more typical diffuse ISM.

Equipartition between the (non-thermal) kinetic energy in MHD waves and the energy in the magnetic field is thought to arise commonly in the ISM (Zweibel & McKee 1995). Also, such equipartition is consistent with observations of regions where magnetic field strengths have been measured (Myers & Goodman 1988; Crutcher 1999). If equipartition exists between magnetic field energy and the energy of non-thermal motions in the gas, then we can express the gas density in terms of the field strength B and the contribution to the line width from non-thermal motions Δv_{NT}. Equating the magnetic field energy with the energy of non-thermal motions,

$$B^2/8\pi = \frac{1}{2}\rho\Delta v_{NT}^2 \ , \tag{2.1}$$

we find upon appropriate units conversion

$$n_{eq} = \left[\frac{2.5B}{\Delta v_{NT}}\right]^2 \ [\text{cm}^{-3}]. \tag{2.2}$$

Here n_{eq} is the equipartition *proton* density $[n(\text{H}^0) + 2n(\text{H}_2)]$, B is in μG, and Δv_{NT} is the FWHM line width attributable to non-thermal motions in the gas

(km s^{-1}). If $n/n_{eq} > 1$, non-thermal kinetic energy dominates. If $n/n_{eq} < 1$, magnetic energy dominates, and the field lines should be relatively uniform.

2.3 Photoionization calculations

2.3.1 The density – distance grid

Our goal is to deduce the density of the Veil and its distance from the Trapezium stars by comparing photoionization models of this layer with observations. We used the development version of the spectral synthesis code Cloudy, last described by Ferland et al. (1999). Bottorff et al. (1998) and Armour et al. (1999) provide further details about this code.

Our Veil models incorporate several important improvements in Cloudy. We use the improved grain physics described by van Hoof et al. (2001) which explicitly solves for the grain temperature and charge as a function of grain size. We divide the grain size distribution into ten size bins, and include grains that are composed of graphite and silicates. Our size distribution is designed to reproduce the flat UV extinction curve observed by Cardelli et al. (1989) towards Orion. We will see below (Section 3.4 and Table 1) that the best-fit models predict about 5% of the hydrogen along the line of sight to the Trapezium is ionized and so is not seen in H^+ absorption line studies. This result, combined with the neutral column density measurements of SS97, leads to $A_V/N(H_{tot}) \approx 4\times10^{-22}$ mag cm^2, a ratio which is ~75% of that seen in the general ISM. We scaled our grain abundance to match this ratio.

We have implemented a complete model of the H_2 molecule into Cloudy. Energies and radiative transition probabilities for the 301 ro-vibrational levels within the ground electronic state $1s\ ^1\Sigma_g$ (denoted as X) are taken from Stancil (2002, private communication) and Wolnievicz et al. (1998). We have included the ro-vibrational levels within the lowest 6 electronic excited states that are

coupled to the ground electronic state by permitted electronic transitions. Energies and radiative transition probabilities for excited electronic states are from Abgrall, Roueff, & Drira (2000). These electronic excited states are important because they determine the Solomon process, which destroys H_2 through the absorption of Lyman-Werner band photons from the ground electronic state followed by decays into the X continuum. These photo-excitations are also an indirect source of population of excited ro-vibration levels within X which decay to produce infrared emission lines with the selection rule $\delta J = 0, \pm 2$. We have taken photoionization cross sections for transitions into the continuum of the Lyman and Werner bands from Allison & Dalgarno (1969). Effects of cosmic rays and the x-ray continuum are included as well. H_2 can be formed either on dust grains in a cold dusty environment or from H^- in a hot dust-free environment. The state specific (v and J resolved) formation rates of H_2 on grain surfaces and via H^- route have been taken from Cazaux & Tielens (2002); Takahashi, Junko, & Uehara (2001); and Launay, Dourneuf, & Zeippen (1991). Line overlap and self-shielding are also considered. In addition, our calculations are designed to reproduce the observationally determined H_2 formation rate on grains in the diffuse ISM, determined by Jura (1974) to be $\sim 3x10^{-17}$ cm^{-3} s^{-1}.

Other important input parameters to the models include gas-phase abundances and the adopted stellar ionizing continuum. We use gas-phase abundances observed in the Orion Nebula (Rubin et al. 1991; Osterbrock et al 1992, Baldwin et al. 1991). A few of the abundances by number are He/H = 0.095, C/H = $3.0x10^{-4}$, N/H = $7.0\ x10^{-5}$, O/H=$4.0\ x10^{-4}$, Ne/H=$6.0x10^{-5}$ and Ar/H =$3.0\ x10^{-6}$. However, all of the lightest thirty elements are included in our models. The stellar ionizing continuum is the modified Kurucz LTE atmosphere described by Rubin et al. (1991), which was modified to reproduce high-ionization lines seen in the H II region. We set the total number of ionizing photons emitting by θ^1 Ori C equal to $10^{49.34}$ s^{-1}, a typical value for an O6 star

(Osterbrock, 1989). The radiation field falls off as the inverse square of the separation from the star, so the star-Veil separation becomes a model parameter. Finally, the ionization and thermal effects of background galactic cosmic rays are included using the ionization rate quoted by McKee (1999).

We computed a large grid of models in which two parameters were varied. These parameters are the Veil's total hydrogen density, denoted by $n_H = n\left(H^+\right) + n\left(H^0\right) + 2n\left(H_2\right)$, and the distance between the side of the Veil facing the Trapezium and the Trapezium itself, which is designated by *D*. For simplicity we assume a single constant-density layer. This is a reasonable assumption since the predicted gas temperatures depend upon the shielding of the layer from the radiation field, not on the details of how this shielding occurs. All calculated models have the total atomic hydrogen column density measured by SS97, $\log[N(H^0)] = 21.6$. From our results we were able to identify ranges of densities and distances that reproduce the observed features of the Veil. A more thorough description of our results is described next.

2.3.2 Column densities, ionization structure, and depletion

SS97 derived column densities of many species in the Veil in addition to H^0. These results, along with the upper limit to the H_2 column density, allow us to constrain the level of ionization, density, and to some extent the distance of the Veil from the Trapezium cluster. Our primary focus here is on column densities for species with more than one stage of ionization. These include atomic and singly ionized C, Mg, and S. Column density ratios of different ion states of the same element determine the level of ionization in a way that does not depend on the abundance. These data determine the ionization parameter, the ratio of the flux of ionizing photons to the density. SS97 derived column densities of many more elements (such as Fe, Zn, and P), but they were detected in only one stage of ionization. Therefore, these column densities do not constrain the model since we could easily reproduce them by simply scaling the abundances. The column

densities of excited state O^0, C^0, and Si^+ have also been measured. The ratio of column densities of excited to ground state determines the density if the density is less than the critical density of the species. If the density is known, then the measured ionization parameter can be used to determine the distance from the continuum source. The measured column densities are summarized in Table .

Model grids for species with more than one observed ionization or excitation state are shown in Figures 2.3 {A, B, and C} and 2.4 {A, B, C, D, and E}, respectively. Figure 2.3 shows our predicted ratios of Mg^0/Mg^+, S^0/S^+, and C^0/C^+. There is a large range of parameters that match the observations. All regions that produce $N(Mg^0)/N(Mg^+) < 10^{-3}$ are also consistent with the observed ratios $N(S^0)/N(S^+)$ and $N(C^0)/N(C^+)$. The parameter space with large distances and densities predict these species to be mostly atomic, and is therefore excluded. Figure 2.4 shows the predicted ratios of excited to ground state column densities for the five species measured by SS97. As expected, these ratios are very sensitive to the hydrogen density. Our calculation reproduce the N(CI*)/ N(CI) and N(CI**)/ N(CI) ratios to within a factor of two for densities $>10^3$ cm^{-3}. Observational uncertainties were not stated for these column densities. The N(OI*)/ N(OI) and N(OI**)/ N(O I) column density ratios are a better constraint in the models since, like Mg, 1σ error bars are given. The 1σ ranges are given in Table . The N(OI*)/ N(OI) ratio suggests $n \sim 10^{3\pm0.4}$ cm^{-3}, while the N(OI**)/ N(OI) suggests a density closer to $10^{3.7\pm0.5}$ cm^{-3}. The N(SiII*)/ N(SiII) ratio gives $n = 10^{4.5\pm0.5}$. A density of $n \sim 10^3$ cm^{-3} matches the observed column densities within 3σ.

Both the H_2 formation and destruction physics are included in a self-consistent manner. We show in the Appendix that the predicted H_2 column density is very sensitive to the method used in calculating the Solomon process. We also show in the Appendix the sensitivity of predicted H_2 column densities to the grain size distribution. We find that the lack of H_2 in the Veil is due to the efficiency of the Trapezium stars in destroying H_2, and to the sensitivity of molecular hydrogen

formation to the grain size distribution. The continuum radiation responsible for the Solomon process is mainly the high-energy range of the Balmer continuum, between 11.2 and 13.6 eV. The right side of Figure 2.5 gives G_o, the average interstellar flux between 6 and 13.6 eV as defined in Tielens & Hollenbach (1985), for the range of distances we consider. Its large value ($G_o > 10^3$) leads to most of our calculated H_2 column densities being well under the Copernicus limit of $N(H_2) < 3.5x10^{17}$ cm^{-2}. Generally, only in regions of parameter space of higher density further away from the ionizing star ($D \sim 10^{19.0}$ cm) does G_o become small enough for a large amount of H_2 to form.

Figure 2.6 can be used to derive a constraint to the distance D if the density n_H is known. Section 3.4 shows that the range of densities that best reproduce observations is $\sim 10^3 < n_H < 10^4$ cm^{-3}. Since the H_2 column density must be less than the upper limit derived by Copernicus, $N(H_2) < 3.5x10^{17}$ cm^{-2}, our models constrain D to be less than 3 parsecs.

2.3.3 The spin temperature and surface brightness

The temperature measured by the 21 cm/Lyα ratio is an $N(H^0)$ -weighted harmonic mean temperature, given by the relationship

$$\frac{1}{< T_{spin} >} = \frac{\int \frac{n}{T_{spin}} dr}{N(H^0)}. \qquad (2.3)$$

Predicted values are shown in Figure 2.6. Like the excited state column densities, the spin temperature is sensitive to the density. For our calculations, the primary heating and cooling mechanisms are grain photoionization and collisional excitation of heavy element fine structure lines respectively. The two most efficient coolants were the [C II] 158μm and the [O I] 63μm lines. For lower densities both [C II] and [O I] contribute to the cooling. However, for densities larger than the [C II] 158μm critical density of ~3x10^3 cm^{-3}, cooling becomes less efficient, and the heating rate increases with a power of density greater than the

cooling rate. This explains the increase in temperature seen in Figure 2.6 for densities greater than 10^3 cm^{-3}. For the 1 σ range of spin temperature set by the observed 21 cm/Lyα limit, $70 < T_{spin} < 110$ K, our predictions agree with observations for densities between $10^{3.5}$-$10^{4.5}$ cm^{-3}. The 3 σ range for the spin temperature, 50-200 K, allows densities greater than ~10^2 cm^{-3}.

Although the Veil is known to be deficient in small grains (Section 2.2), we considered the possible effects of PAHs in the model calculations. Very small grains, or large molecules like PAHs, are known to be very efficient at heating gas. As a check on their effects, we ran one set of models with PAHs present at an abundance of $n(PAH) / n(H) = 3 \times 10^{-7}$. As expected, the PAHs raised our predicted temperatures by factors between 1.5 and 2 over those shown in Figure 2.6. The effect of higher temperatures can only be accommodated at lower densities. That is, the models predict slightly lower densities with the inclusion of PAHs. Therefore, conclusions in Section 2.4 based upon relatively low Veil densities are not endangered by the effects of PAHs in the models.

Figure 2.7 shows the predicted Hβ surface brightness emitted by the ionized face of the Veil. The contours are very nearly parallel, depending mainly on the distance, since the surface brightness in a recombination line is determined by the flux of ionizing photons striking the gas. Furthermore, the ionizing flux (hence, the Hβ surface brightness) is an inverse square function of the star-cloud distance. If we assure that the surface brightness in the Veil is no more than half of that observed in the main ionization front, then a lower limit for the distance from the Veil to θ^1 Ori C is $D \sim 10^{18.0}$ cm (~0.33pc).

A firmer lower limit on D can be derived through the use of [N II] 6583Å emission, which must be occurring at the surface of the Veil that faces θ^1 Ori C. The difficulty is distinguishing Veil emission from radiation from the main body of the nebula. An upper limit on the [N II] 6583Å Veil emission can be placed by assuming the Veil accounts for the red shoulder of the main nebular emission

line. In this case the surface brightness of the Veil is 1.5×10^{-13} ergs $cm^{-2}\, s^{-1}$ arcsec^{-2} (or about -12.8 on a logarithmic scale), after correction for extinction (O'Dell & Yusef-Zadeh 2000). However, this is a generous upper limit since it is likely that much of the red shoulder is caused by red-shifted nebular light that is scattered by dust in the dense PDR that lies beyond the main ionization front of the nebula (O'Dell 2001).

Figure 2.8 shows the predicted [N II] surface brightness as a function of density and distance. All combinations of density and distance in Figure 2.8 with [N II] greater than -12.8 (corresponding to contours below the -12.8 contour in Figure 2.8) are excluded by observation. For densities less than 10^4 cm^{-3}, this constraint places a lower limit on the distance of ~$10^{18.5}$ cm (~1 parsecs). Our best models (Section 3.4) calculate n_H to be between 10^3 and 10^4 cm^{-3}. Therefore, this upper limit upon D applies. The limit $D > 1$ pc is about two times larger than the value deduced on statistical grounds (Section 2.4). Since our calculations best match observations for densities between 10^3 and 10^4 cm^{-3}, we are only concerned with the part of Figure 2.8 that constrains the distance to around 1 parsecs. As discussed below, our models with $D > 10^{18.5}$ cm also yield the best agreement with the rest of the observational data.

In Figure 2.9 we present contours of H^+ column density as a function of D and n_H. For high density and large D, the amount of H^+ starts to drop off. For high density, the amount of H^+ starts to drop off due to a lower ionization parameter, defined as the dimensionless ratio of hydrogen ionizing flux to density. This behavior also affects the [N II] surface brightness at high density and large D (Figure 2.8). Since nitrogen has a higher ionization potential than hydrogen, nitrogen will only be ionized in regions where hydrogen is also ionized. This leads to less N^+ in these regimes and therefore a lower surface brightness for the 6583 Å line.

2.3.4 A "best model" for the Veil and its consequences

In this section we will define a "best model" that most accurately reproduces the observational features in the Veil. Based on our calculations for the excited state abundance ratios and spin temperatures discussed in Section 3.2 & 3.3, a density between 10^3-10^4 cm^{-3} would reproduce all the observational data to within 3 σ. The distance of the Veil, ~$10^{18.5}$ to $10^{19.0}$ cm (1 to 3 parsecs), is set by the observed upper limits on both the surface brightness of [N II] 6583Å and the column density of H_2. These are the broad limits to any successful model of the Veil.

We derived a "best" model using the optimization methods that are part of Cloudy, starting with density and distance near the center of the allowed range but allowed to vary. The observables that we optimized include column densities of CI, CII, MgI, MgII, SI, SII, SiII, OI, SiII*, OI*, OI**, CI*, CI**, H_2, and the temperature T_{spin}. We used as confidence intervals the 1 σ error estimates given by SS97. When these are not given a percent error of 20% was assumed. Where upper limits were given (as in the case of C^+, S^0, and H_2) all that was required in the calculation was that the predicted column densities be less than these upper limits. We then calculated a χ^2 based on the formula:

$$\chi^2 = \left(\frac{F_{obs} - F_{pred}}{\sigma \times min\left(F_{obs}, F_{pred}\right)} \right)^2 \qquad (2.4)$$

where F_{obs} is the observed mean value, F_{pred} is the predicted value generated by Cloudy, and σ is the error in the observed value.

Tables 2.1 & 2.2 along with Figure 2.10 {a, b, and c} summarize our calculation that had the lowest χ^2 and therefore represents our "best model" of the physical conditions in the Veil. The distance is $10^{18.8 \pm 0.1}$cm (~2 parsecs) and hydrogen

density is n_H = ~$10^{3.1\pm0.2}$ cm^{-3}, where the ranges correspond to densities and distances that yield a χ^2 that are within a factor of two of the lowest value. The general conclusions drawn from our "best model" are representative of all models in this general range of the parametric diagrams.

Our optimal calculations predict column densities in unobserved stages of ionization. The majority of calcium in the Veil is in the form of Ca^{++} (see Table 2.2 & Figure 2.10b). Doubly ionized calcium has a closed shell and hence is undetectable in UV or optical radiation. Optical studies must work with Ca^{+} which is a trace stage of ionization. It is for this reason that we take the 21 cm H I absorption line as the principal tracer of atomic gas (Section 2.3). We also predict that about 5% of the hydrogen in the Veil is ionized.

Formalized optimization aside, how certain can we be that Veil densities are as low as n_H ~10^3 cm^{-3} (best model) and not $n_H \geq 10^4$ cm^{-3} as required for magnetic equipartition in the narrow HI component (Section 2.4)? The best determined line ratios (therefore, the best diagnostics for determining density) are O I*/O I, O I**/O I, Si II*/Si II, and Mg^0/Mg+ (Section 2.3). Line ratios involving C and S either have undetermined observational errors or else errors too high to be useful (see Table 2.1). For our optimized density (n_H = ~$10^{3.1\pm0.2}$ cm^{-3}), the predicted O I*/O I ratio is within 1 σ of observation. If $n_H \geq 10^4$ cm^{-3}, then the predicted ratio is only within 3 σ of observation. Likewise, the predicted ratio Mg^0/Mg^+ at the optimized density lies within 1 σ of observation, while the predicted density for $n_H \geq 10^4$ cm^{-3} falls only within 3 σ of observation. However, our models do not predict the Si II*/Si II ratio very well at either n_H = ~10^3 or 10^4 cm^{-3}. For both densities, the predicted ratio barely falls within 3 σ of observation. Also, the predicted ratio O I**/O I lies within 2 σ of observation at either value for n_H. In general, our calculations show that densities >10^4 cm^{-3} combined with distances greater than 1 parsec (the minimum distance allowed by the [N II] surface brightness measurement), will predict the Veil to be both less ionized and more

molecular than suggested by observation. However, the best case for n_H = ~10^3 cm^{-3} as opposed to 10^4 cm^{-3} comes from the ratios O I*/O I and Mg^0/Mg^+ mentioned above.

Future observations of the line of sight towards θ^1 Ori C done at higher spectral resolution could further increase our knowledge of the physical conditions in the Veil. Observations in the UV, done at higher resolution than possible by IUE, would allow for the determination of the physical properties in each of the Veil's components seen in H I 21 cm absorption. In a manner similar to what we have done in this work, excited state column densities along with column densities of elements seen in more than one ionization state could be calculated for each component in the Veil. This information could then be used to derive the density, temperature, and level of ionization for each component in the Veil. Additionally, observations of H_2 performed with greater sensitivity than the Copernicus mission could yield a more precise value for the column density of H_2 in the Veil.

2.4 Implications for the magnetic field in the Veil

2.4.1 Magnetic vs. non-thermal energies in the Veil

Knowledge of the magnetic field strength, gas density, and non-thermal line width in the Veil allows us to estimate the energetic importance of the magnetic field. The ratio of energy in non-thermal motions to energy in the field equals n_H/n_{eq}, the ratio of the actual gas density to the equilibrium density (Section 2.2, densities are proton densities, i.e. densities for H^0). Values of n are inferred from our models where, for the Veil, $n_H \approx n(H^0)$. In these models, higher n is associated with higher T_s over a wide range of Veil distance d (Figure 2.6). A lower limit to n_{eq} comes from equation 2.2 assuming $\Delta v_{NT} = \Delta v_{obs}$, that is, the observed line width Δv_{obs}, has no thermal broadening. For non-zero temperature, $\Delta v_{NT} < \Delta v_{obs}$, and n_{eq} is higher. Therefore, the question of magnetic

energy dominance is addressed by estimating the ratio n_H / n_{eq} as a function of T_s over the allowable T_s range for the Veil. To do so, we make use of the model-determined T_s - n_H relationship of Figure 2.6.

2.4.2 The narrow H I component

We now consider the ratio n_H / n_{eq} for the narrow H I component. The upper limit to T_s is 87 K, set by Δv_{obs}. Although the harmonic mean temperature of the Veil is 70-120 K (Section 2.2.5), the 21 cm and Lyα data set no lower limit upon T_s for the narrow component alone. We have estimated the ratio n_H / n_{eq} over the range $0 < T_s < 87$ K. To do so, we used $\Delta v_{obs} = 2$ km s^{-1}, $B = 100$ μG (Section 2.2.6), implying $n_{eq} \geq 1.6 \times 10^4$ cm^{-3}. We also used the n_H - T_s relationship in Figure 2.6 over the range $D = 10^{18.8 \pm 0.1}$ cm of our best models (Section 2.2). At all values of T_s, the ratio $n_H / n_{eq} < 0.025$, that is, magnetic energy is greater than the energy of non-thermal motions by at least a factor of 40. Even at the minimum possible $B = B_{los} \approx 50$ μG (Section 2.2), the magnetic energy dominates by an order of magnitude. Note that for $T_s < 87$ K, Figure 2.6 allows for higher densities ($n_H > 10^4$ cm^{-2}) at larger values of D ($> 10^{19}$ cm). However, this range of parameter space is excluded by the observed upper limit upon $N(H_2)$ as shown in Figure 2.5. That is, a high density Veil located far from θ^1 C Ori would become largely molecular, contrary to observations. The conclusion seems quite certain that magnetic fields dominate non-thermal motions in the narrow H I component.

It is possible that the field lies nearly along the line-of-sight with transverse MHD wave motions nearly in the plane of the sky. In such a case, the measured (line-of-sight) line width of the narrow component yields an underestimate of the actual non-thermal motions, hence, an underestimate of n_H / n_{eq}. We regard such an effect as very unlikely. A very high degree of alignment and MHD wave coherence would be necessary to reduce significantly the gas motions along the line-of-sight compared to those in the plane of the sky.

Such a pronounced dominance of magnetic field energy is unknown anywhere else in the interstellar medium. It is unexpected theoretically and unprecedented observationally (Section 2.2). Dominance by the magnetic field implies that the field should be rather uniform owing to tension in the magnetic field lines (e.g. Chandrasekhar & Fermi 1953). In fact, the magnetic field map across the Veil reveals a rather uniform distribution of B_{los} except in the northeast where B_{los} increases substantially in the direction of the dark bay of obscuring material (Troland et al., 2004; in preparation). Magnetic dominance and a uniform field might arise if there is little input of mechanical energy to the gas or if the mechanical energy has damped out. Perhaps this is the case in the narrow component. Van der Werf & Goss (1989) identified this component with quiescent gas undisturbed by the H II region. However, Watson, Wiebe and Crutcher (2001) analyzed the statistics of variation of magnetic fields in the Troland et al. data set. They concluded that field variations across the Veil were consistent with magnetic equipartition. Such a conclusion seems difficult to reconcile with the present results for the narrow component.

Turbulent line broadening is not necessarily related to MHD waves. For example, O'Dell, Peimbert & Peimbert (2003) argue that the anomalous broadening of 10 to 20 km/s, observed in optical emission lines from the H II region, is not an MHD effect. Conceivably, H^0 gas in the Veil may also exhibit non-magnetic turbulent broadening. However, the Veil is known to have a significant magnetic field. Therefore, non-thermal motions in the Veil will inevitably be coupled to the field unless magnetic flux freezing is extremely inefficient. Therefore, our assumption that line broadening in the Veil is magnetic seems inescapable.

2.4.3 The wide H I component

A similar assertion of magnetic dominance cannot be made for the wide H I component (Δv_{obs} = 3.8 km s^{-1}). For this component $n_{eq} \geq 4 \times 10^3$ cm^{-3} (equation 2.2 with B = 100 μG and $\Delta v_{NT} = \Delta v_{obs}$). This limit upon the equipartition density is comparable to the best fit model density of $10^{3.1}$ cm^{-3}, so $n_H / n_{eq} \approx 1$. In short, parameters for the wide H I component are consistent with magnetic equilibrium in this layer of the Veil so they are consistent with the analysis of Watson et al. (2001).

Table 2.1

Best Fit Parameters for the Veil

Parameter	Model[1]	Observed 1 σ range[1]	Reference
n_H (cm^{-3})	$10^{3.1}$	-	
T_{spin} (K)	68	70-120	2, 3
Distance to θ[1] Ori C (pc)	1.91	~1.0	4
$S(H\beta)$ (erg s^{-1}cm^{-2} arcsec^{-2})	$4.3x10^{-14}$	$< 5x10^{-12}$	4
$S[NII]$ λ6583	$7.3x10^{-14}$	$< 1.49x10^{-13}$	5
$N(CI^{*})/N(CI)$	-0.3	~ -0.1	2
$N(CI^{**})/N(CI)$	-0.6	~ -0.2	2
$N(OI^{*})/N(OI)$	-3.0	-3.5 ± 0.7	2
$N(OI^{**})/N(OI)$	-4.2	-3.4 ± 0.7	2
$N(SiII^{*})/N(SiII)$	-2.2	-1.4 ± 0.4	2
$N(C^0)/N(C^+)$	-4.0	> -4.35	2
$N(Mg^0)/N(Mg^+)$	-3.0	-3.4 ± 0.5	2
$N(S^0)/N(S^+)$	-4.5	~ -4.2 ± 1.0	2
$N(H_2)$ (cm^{-2})	$1.6x10^{15}$	$< 3.5x10^{17}$	6
$N(H^+)$ (cm^{-2})	$1.2x10^{20}$	unknown	

1 Ratios are in logarithmic units

2 Shuping & Snow, 1997

3 van der Werf & Goss, 1989

4 Baldwin et al. 1991

5 O'Dell & Yusef-Zadeh 2000

6 Savage et al. 1977

Table 2.2

Log of Column Densities for Best-fitting Model

	Stage of Ionization			
	I	II	III	IV
H	21.6	20.1		
He	20.6	18.8		
Li	7.8	11.3		
Be		1.6		
B	7.5	11.6	8.8	7.0
C	14.1	18.1	15.9	11.0
N	17.4	15.8	15.3	10.5
O	18.2	16.6	15.7	
F	1.6			
Ne	17.4	15.9	14.3	
Na	12.8	15.1	10.3	
Mg	13.1	16.1	14.4	
Al	10.4	14.9	12.8	11.4
Si	11.4	16.2	14.4	12.
P	10.5	14.8	13.0	10.8
S	12.1	16.6	14.9	12.2
Cl	10.4	14.6	12.7	9.4
Ar	16.1	14.3	14.3	10.9
K	11.3	13.6	11.5	7.3
Ca	8.7	11.8	13.9	7.5
Sc		0.2	1.6	
Ti	8.5	12.3	11.8	9.8
V	8.3	11.6	10.0	8.8
Cr	9.5	13.6	12.0	10.6
Mn	11.4	14.0	12.4	10.8
Fe	12.4	16.1	14.4	13.6
Co		1.6		
Ni	11.5	14.6	12.9	11.3
Cu	9.1	12.8	11.2	9.3
Zn	11.0	13.9	12.0	10.0

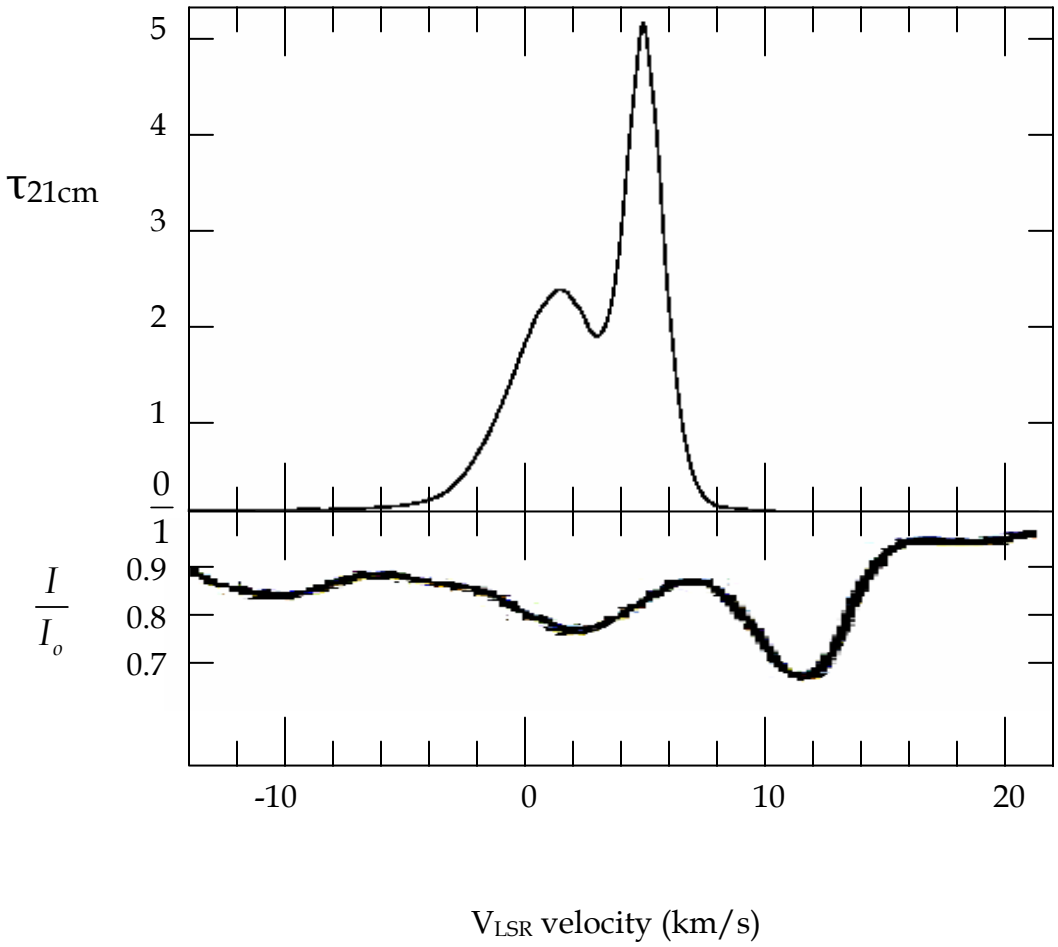

Figure 2.1 H I 21 cm (upper) and Ca II (lower) profiles observed along the line of sight to central regions of Orion. The 21 cm profile has optical depth on the y-axis, while the Ca II profile is in units relative to the continuum. Note that there does not seem to be a strong correlation between the two profiles, implying that Ca^{+} is not associated with the bulk of the material in the Veil.

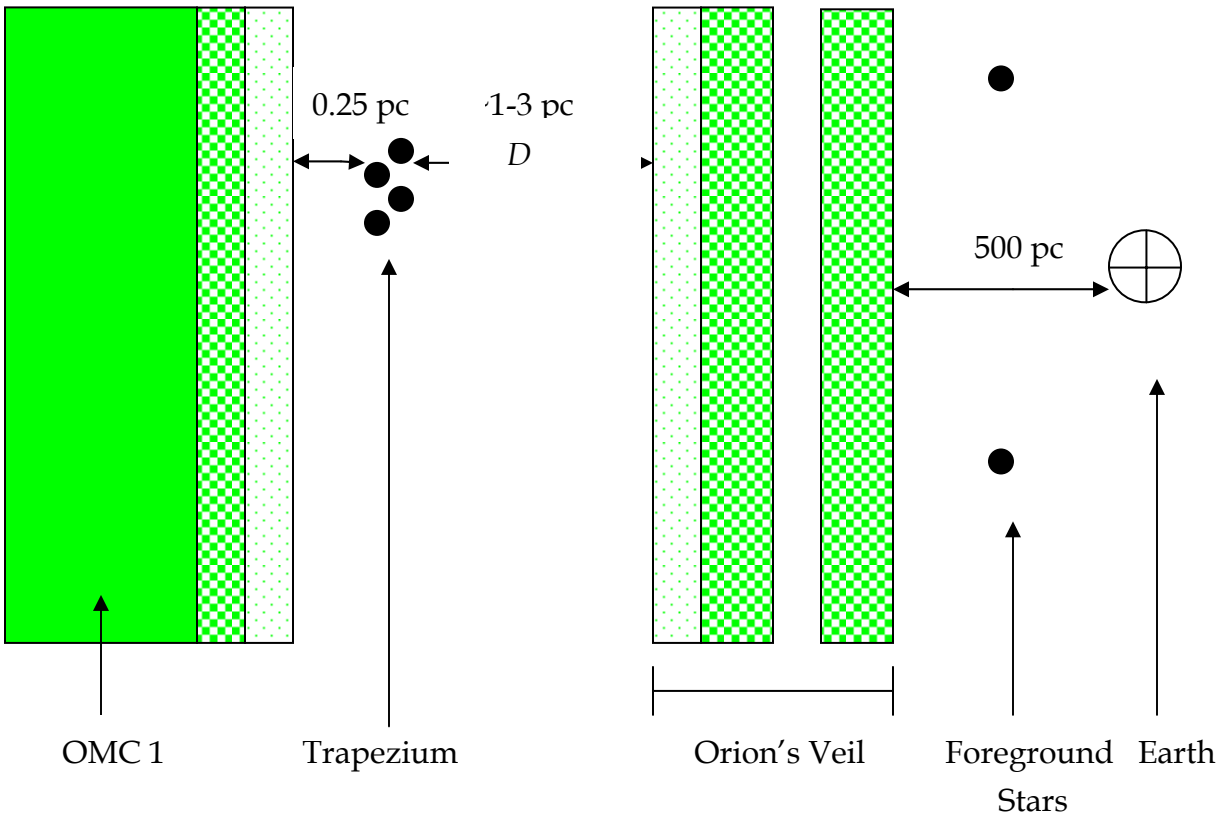

Figure 2.2 The geometry of the central regions of the Orion Nebula and the Veil. For this figure, solid regions correspond to H_2, checkered regions to H^0, and dotted regions to H^+. Starting with the side of the Veil facing the Trapezium, we have a small H^+ zone followed by a PDR. Because of the strong UV flux coming from the Trapezium cluster, H_2 never readily forms but instead we have a thick region of atomic hydrogen. The segmented regions in the Veil represent the multiple components seen in the 21 cm optical depth profile in Figure 1. The distance *D* represents the distance from the side of the Veil facing the Trapezium to the Trapezium itself, and is the same distance used in all subsequent contour plots.

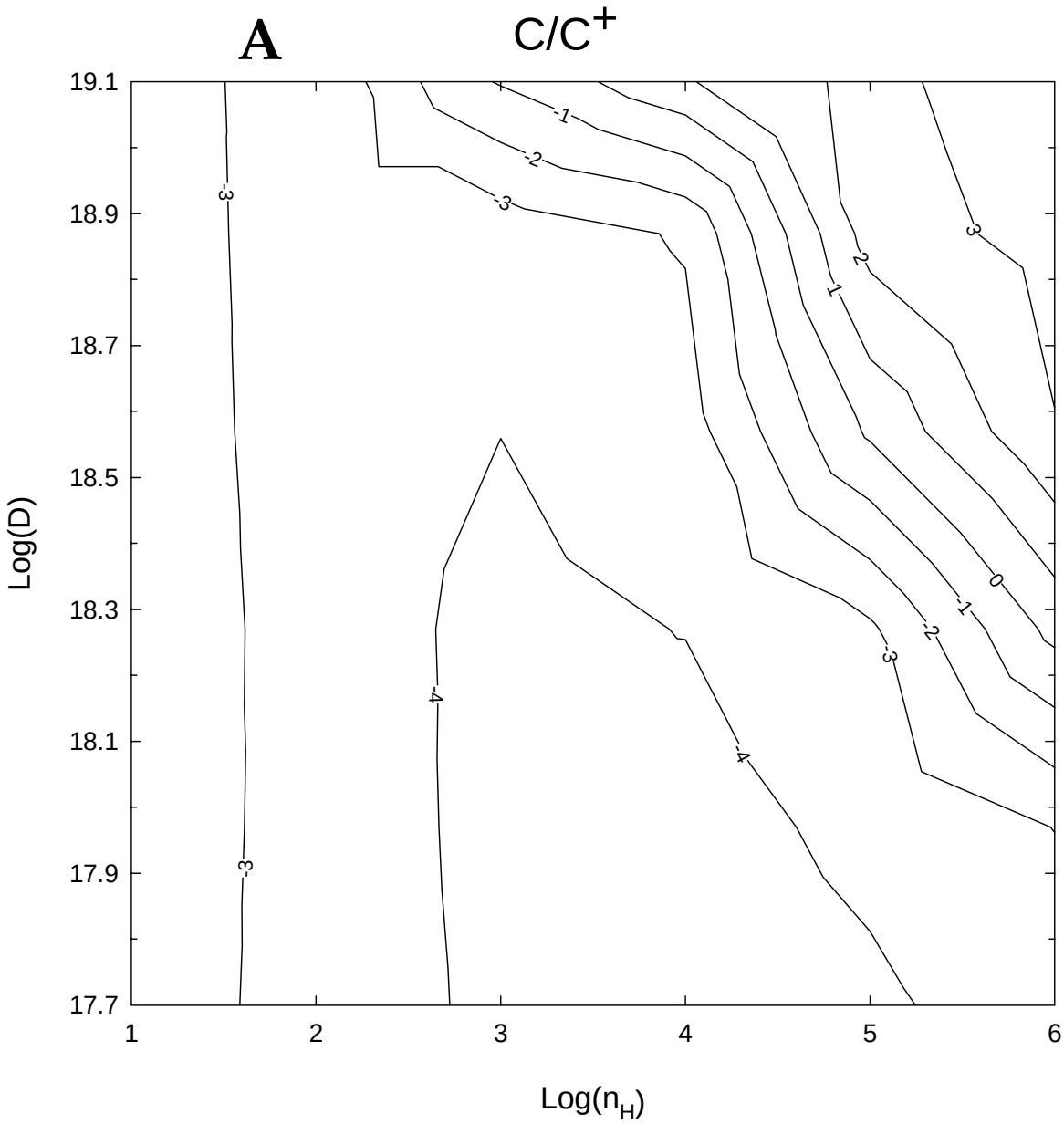
A
C/C+
19.1
18.9
18.7
18.5
18.3
18.1
17.9
17.7
Log(D)
1
2
3
4
5
6
Log(nH)
-3
-1
-2
-3
3
2
1
0
-1
-2
-3
-4
-4
-3

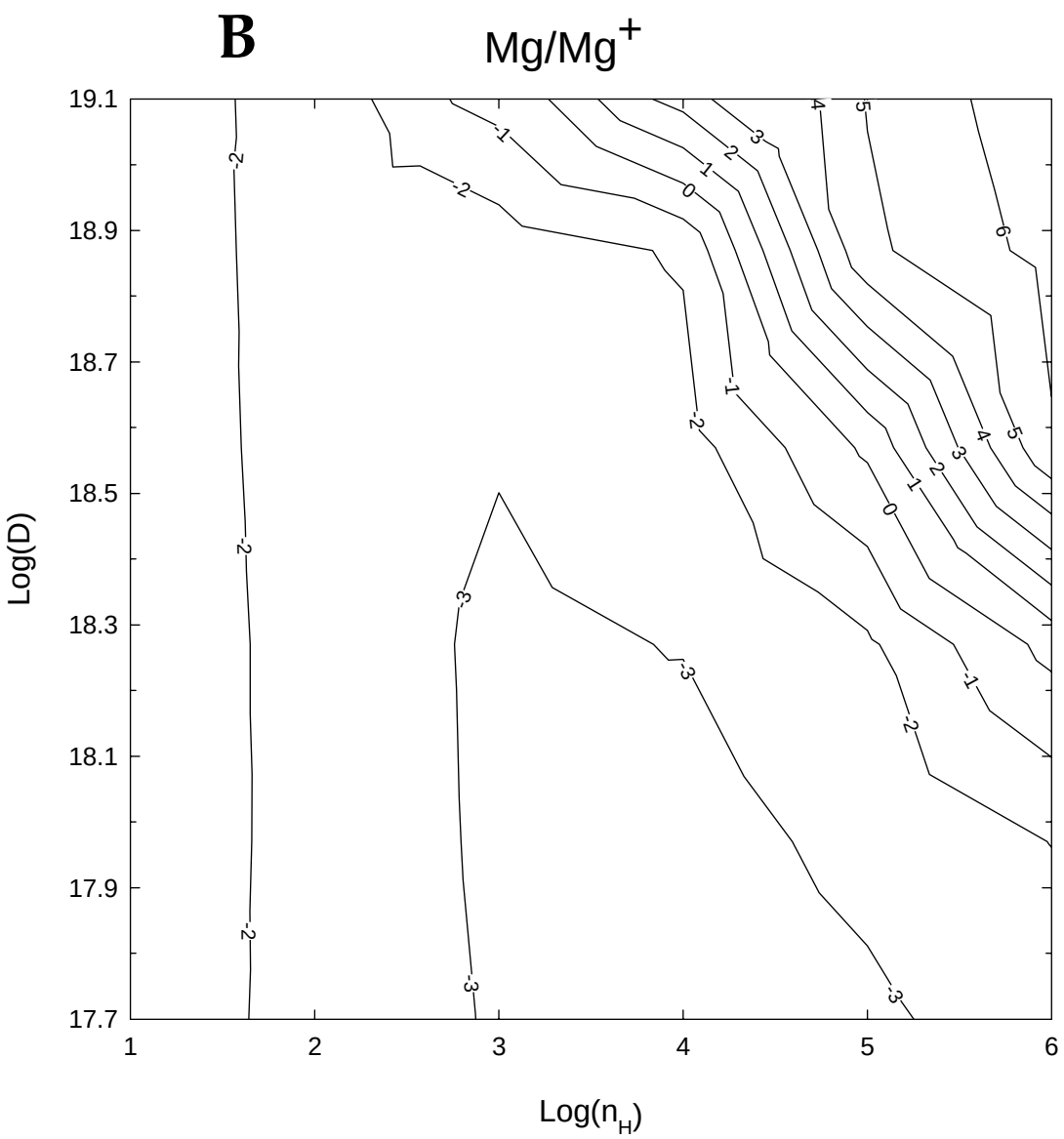
B
Mg/Mg+
19.1
18.9
18.7
18.5
18.3
18.1
17.9
17.7
Log(D)
1
2
3
4
5
6
Log(nH)

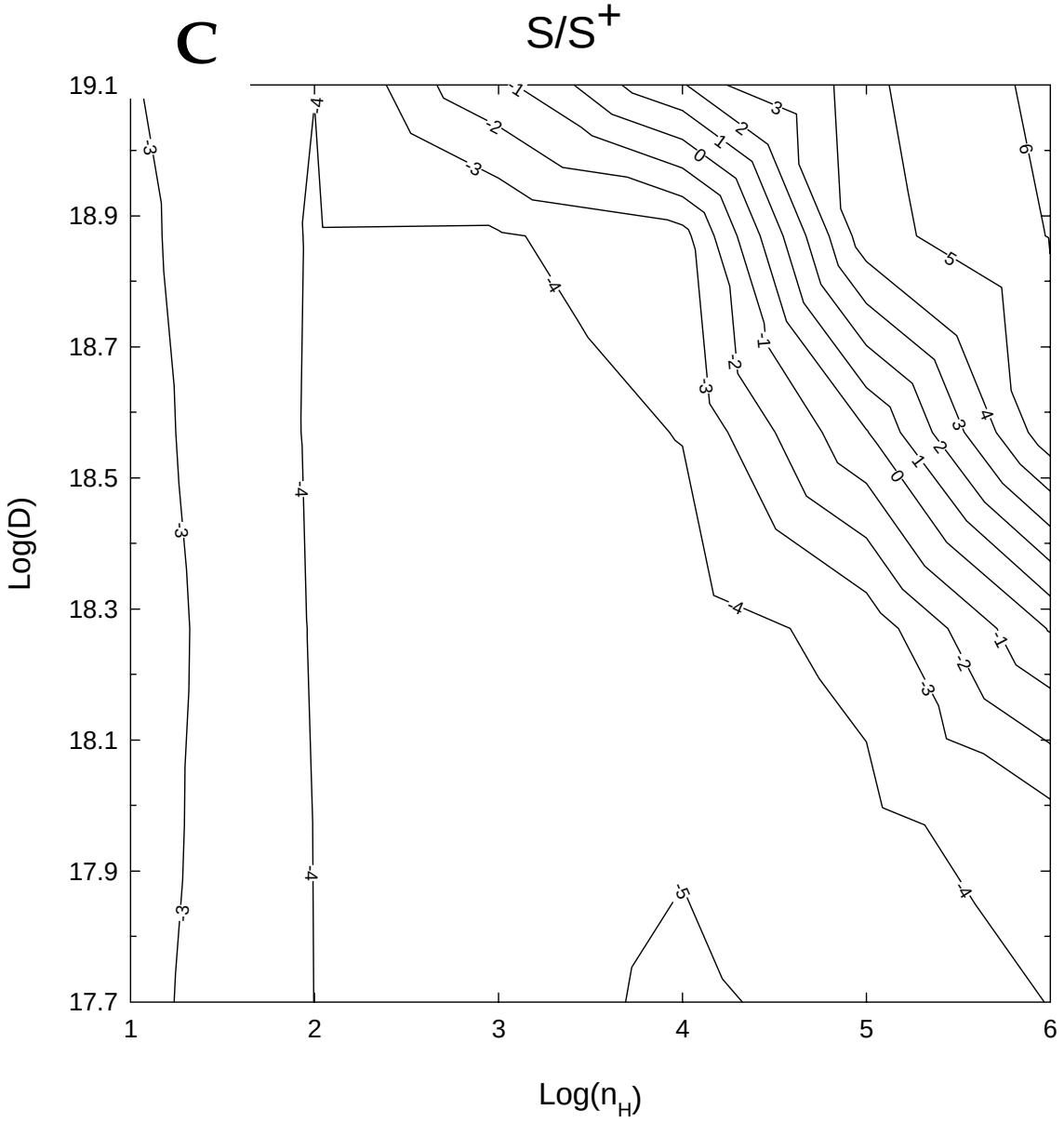

Figure 2.3 The log of the ratio of atomic to ionized C (A), Mg (B), and S (C), which correspond to the column densities measured in more than one stage of ionization by SS97. The observed 1 σ ratios of C (>-4.35), Mg (-3.4 ± 0.5), and S (-4.2 ± 1.0) agree with most of our calculations. In this and all subsequent contour plots the parameter $n_H = n\left(H^+\right) + n\left(H^0\right) + 2n\left(H_2\right)$ (cm^{-3}), the total hydrogen density in all forms.

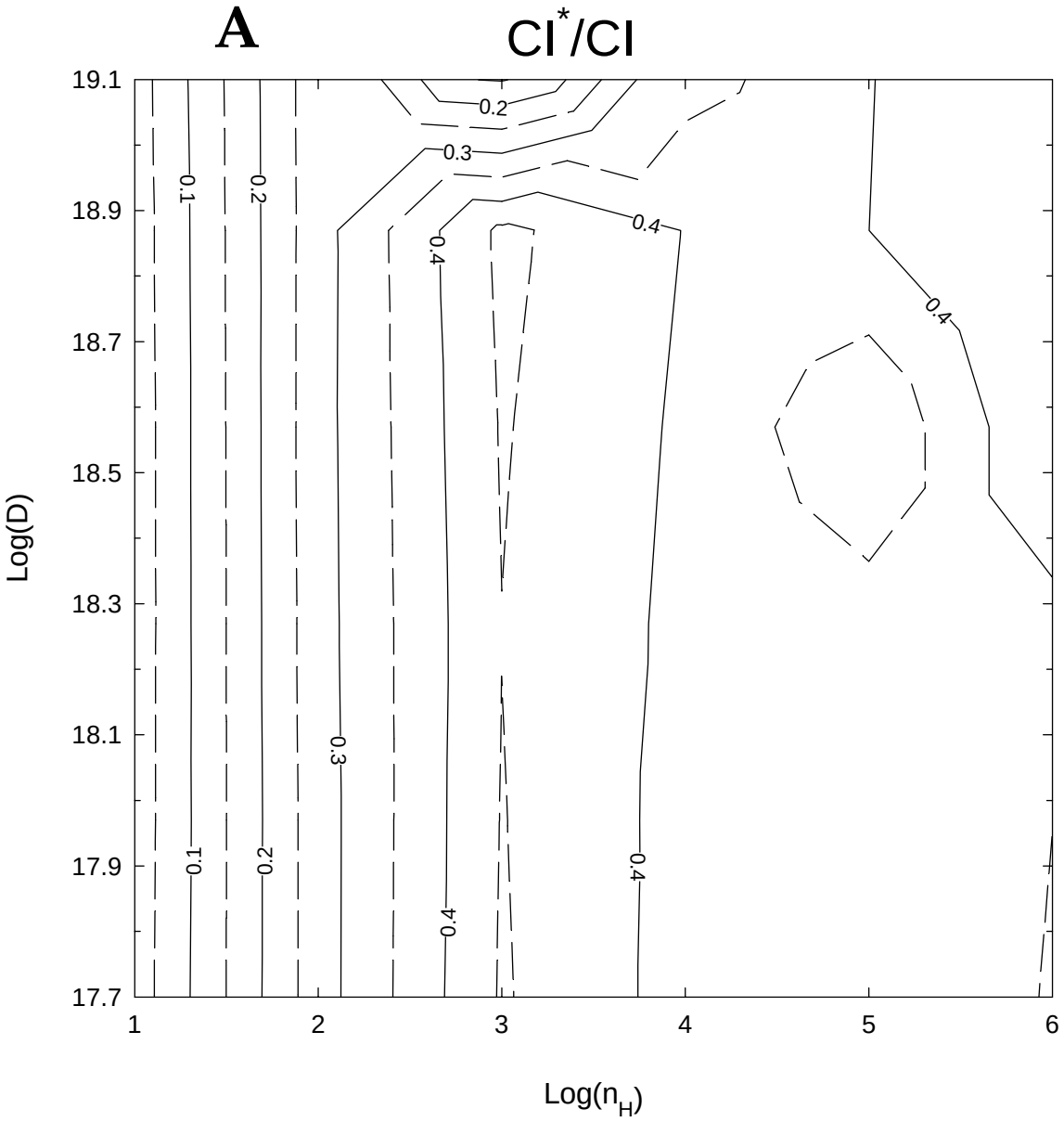
A
CI*/CI
19.1
18.9
18.7
18.5
18.3
18.1
17.9
17.7
Log(D)
1
2
3
4
5
6
Log(n_H)
0.1
0.2
0.3
0.4

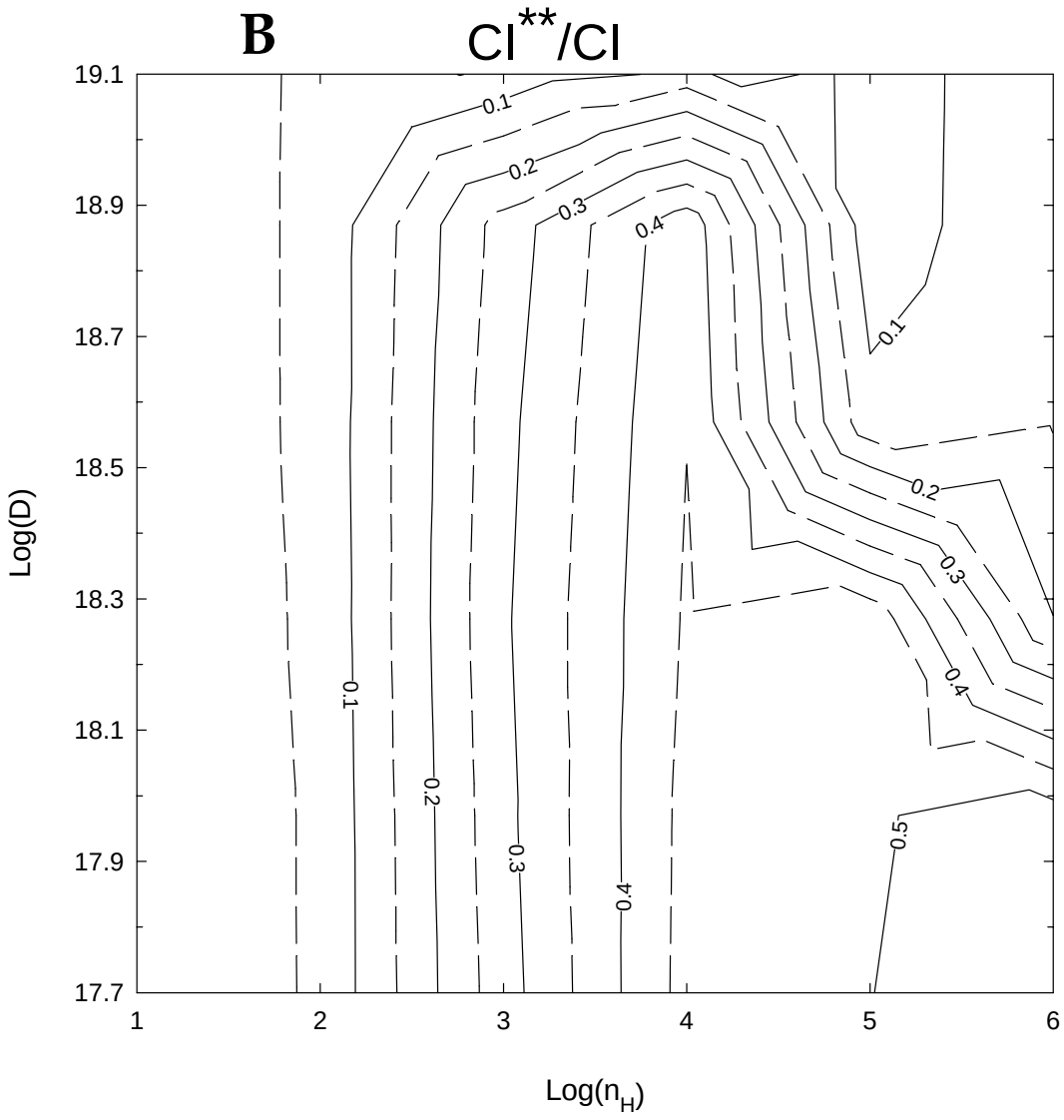
B
CI**/CI
19.1
18.9
18.7
18.5
18.3
18.1
17.9
17.7
Log(D)
1
2
3
4
5
6
Log(n_H)
0.1
0.2
0.3
0.4
0.5

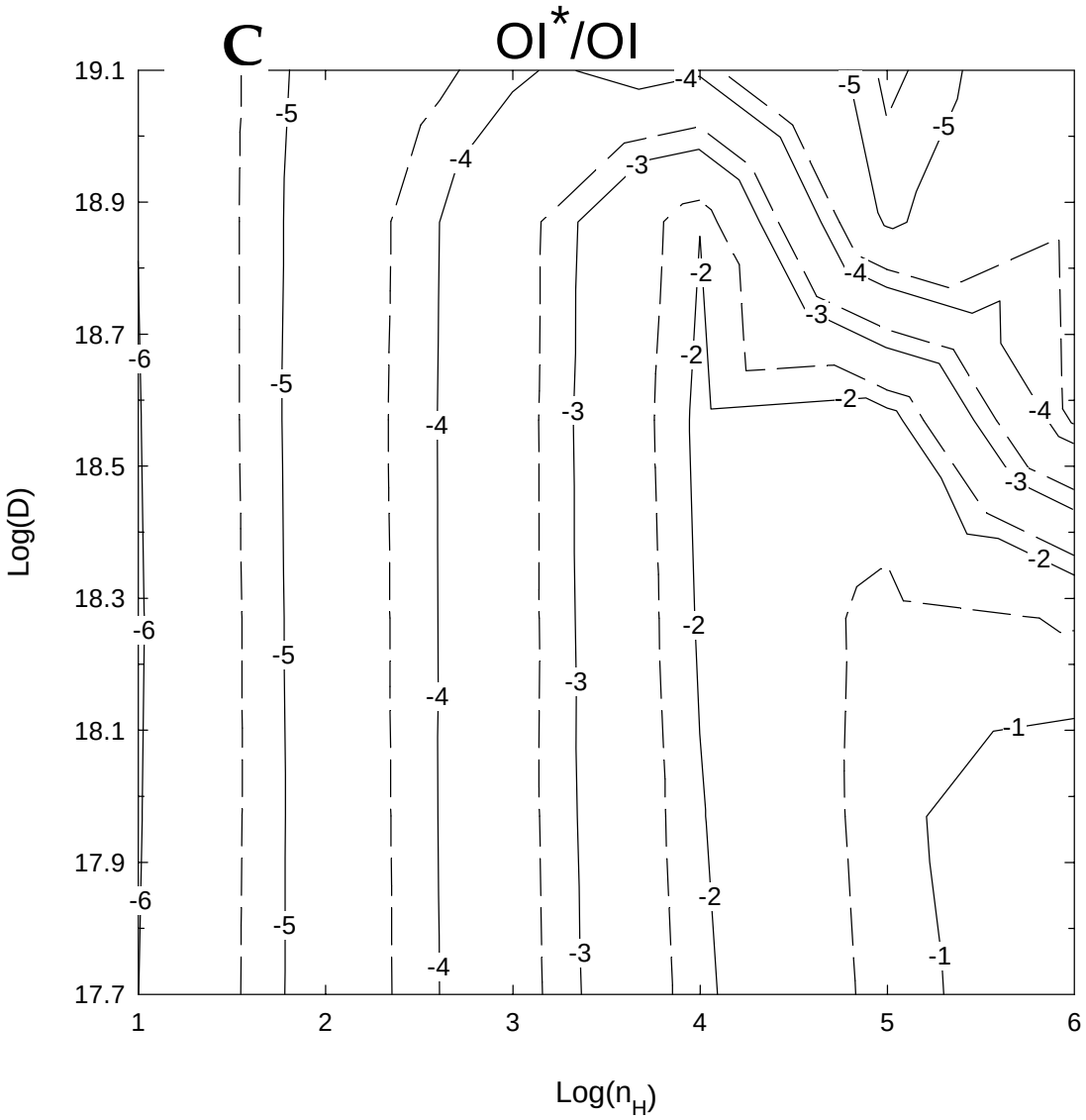
C
OI*/OI
19.1
18.9
18.7
18.5
18.3
18.1
17.9
17.7
Log(D)
1
2
3
4
5
6
Log(n_H)

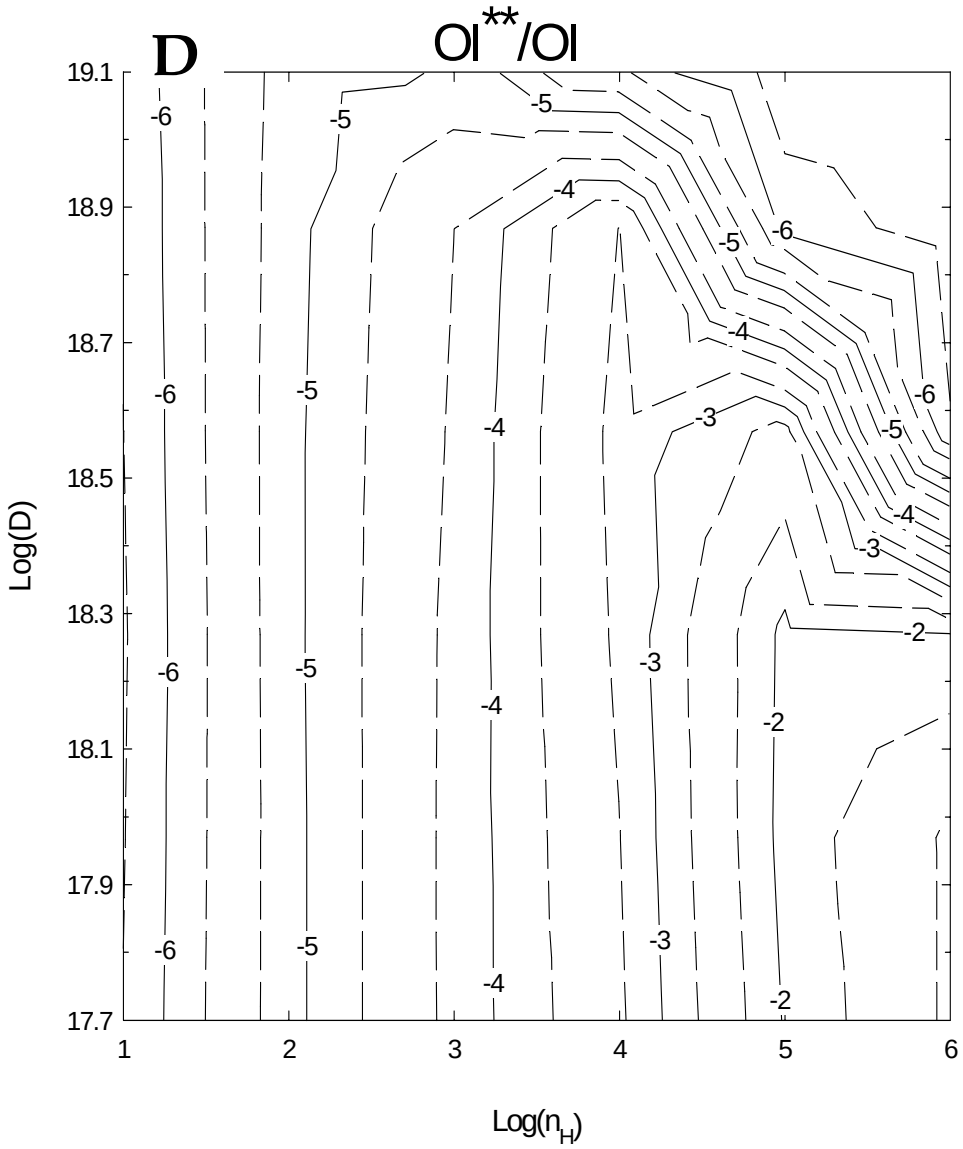
D
OI**/OI
19.1
18.9
18.7
18.5
18.3
18.1
17.9
17.7
Log(D)
1
2
3
4
5
6
Log(n_H)
-6
-5
-4
-3
-2

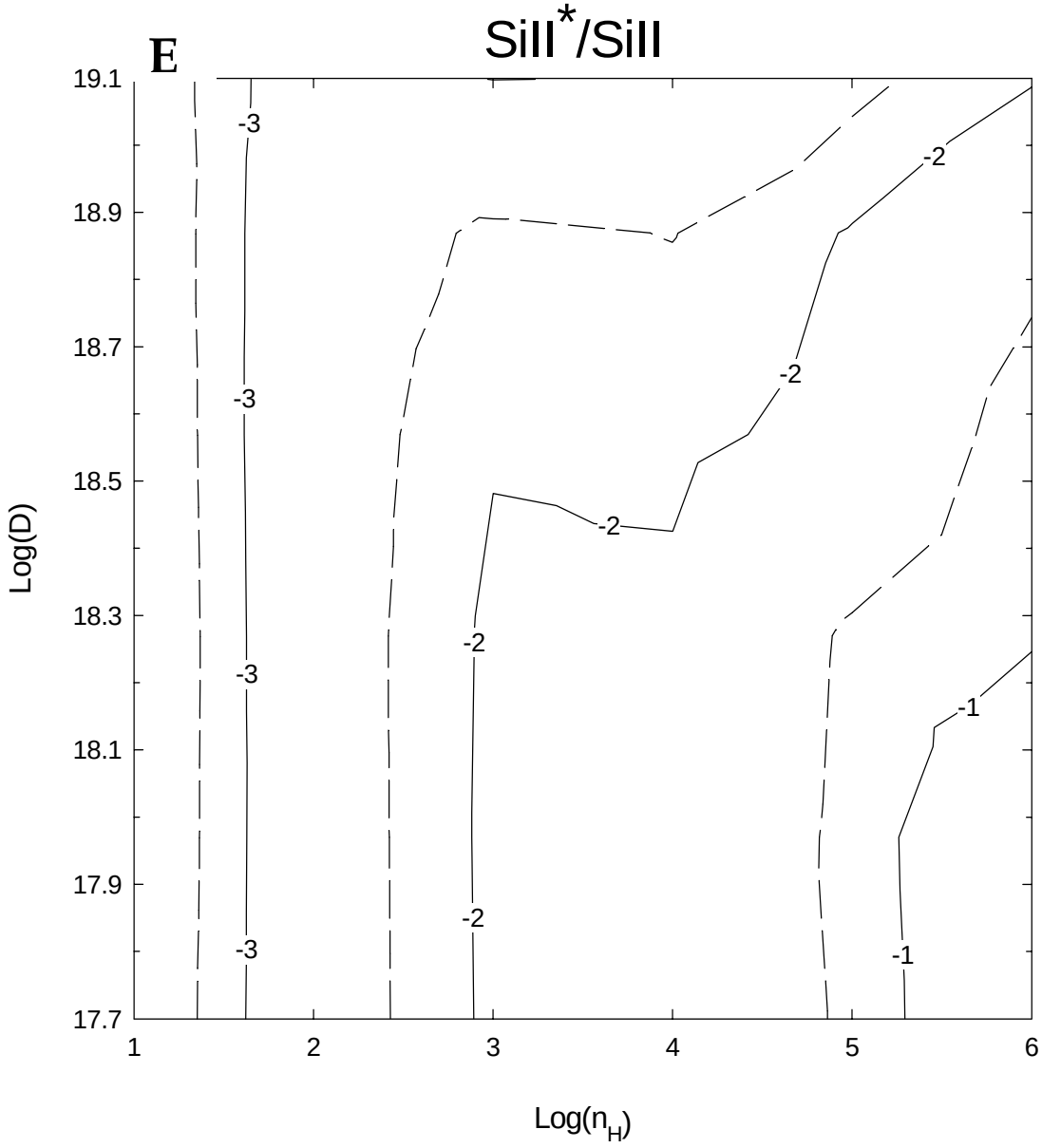

Figure 2.4 Ratio of excited to ground state column densities of carbon (A & B), oxygen (C & D), and Si^+ (E). The observed values, with 1σ ranges when available, are: $N(CI^*)/N(CI)$ ~ (-0.1), $N(CI^{**})/N(CI)$ ~ (-0.2), $N(OI^*)/N(OI)$ (-3.5 ± 0.7), $N(OI^{**})/N(OI)$ (-3.4 ± 0.7), and $N(SiII^*)/N(SiII)$ (-1.4 ± 0.4) The parallel contours show their usefulness as density indicators.

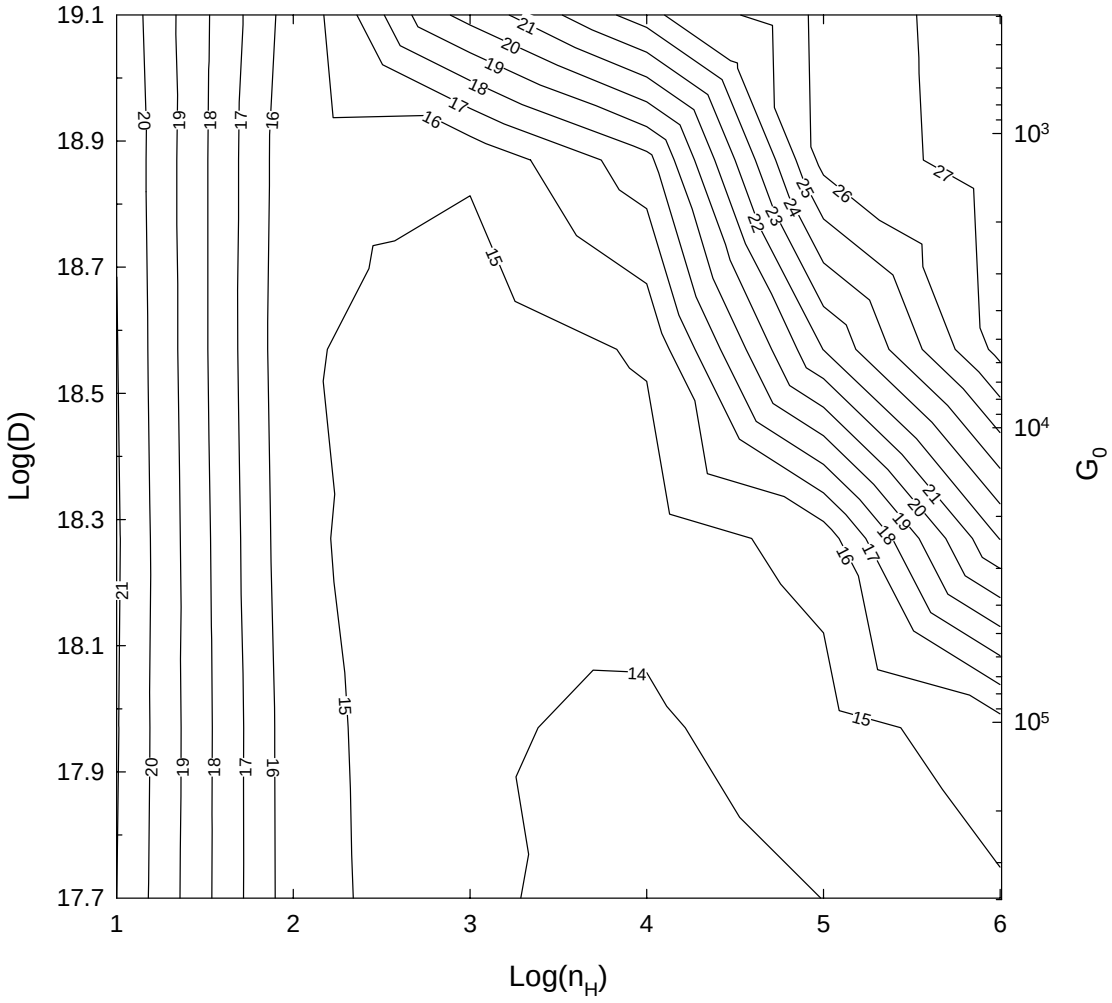

Figure 2.5 The log of the predicted H_2 column density (cm^{-2})is shown. Copernicus observations set an upper limit of $N(H_2) < 3.5 \times 10^{17}$ cm^{-2} ($Log[H_2] < 17.55$). In addition to distance, on the right the scale is in units of the average UV radiation field (Tielens and Hollenbach 1985). For the range of densities that our calculations predict for the Veil (10^3-10^4 cm^{-3}), our calculations predict an H_2 column density less than the Copernicus upper limit for distances less than ~$10^{19.0}$ cm. For very low densities, the large thickness of the H^+ region causes the value of G_0 to decrease because of geometrical dilution. By the time the hydrogen becomes atomic at these low densities, G_0 has decreased to one Habing for all distances. This is why the contours are vertical at low density.

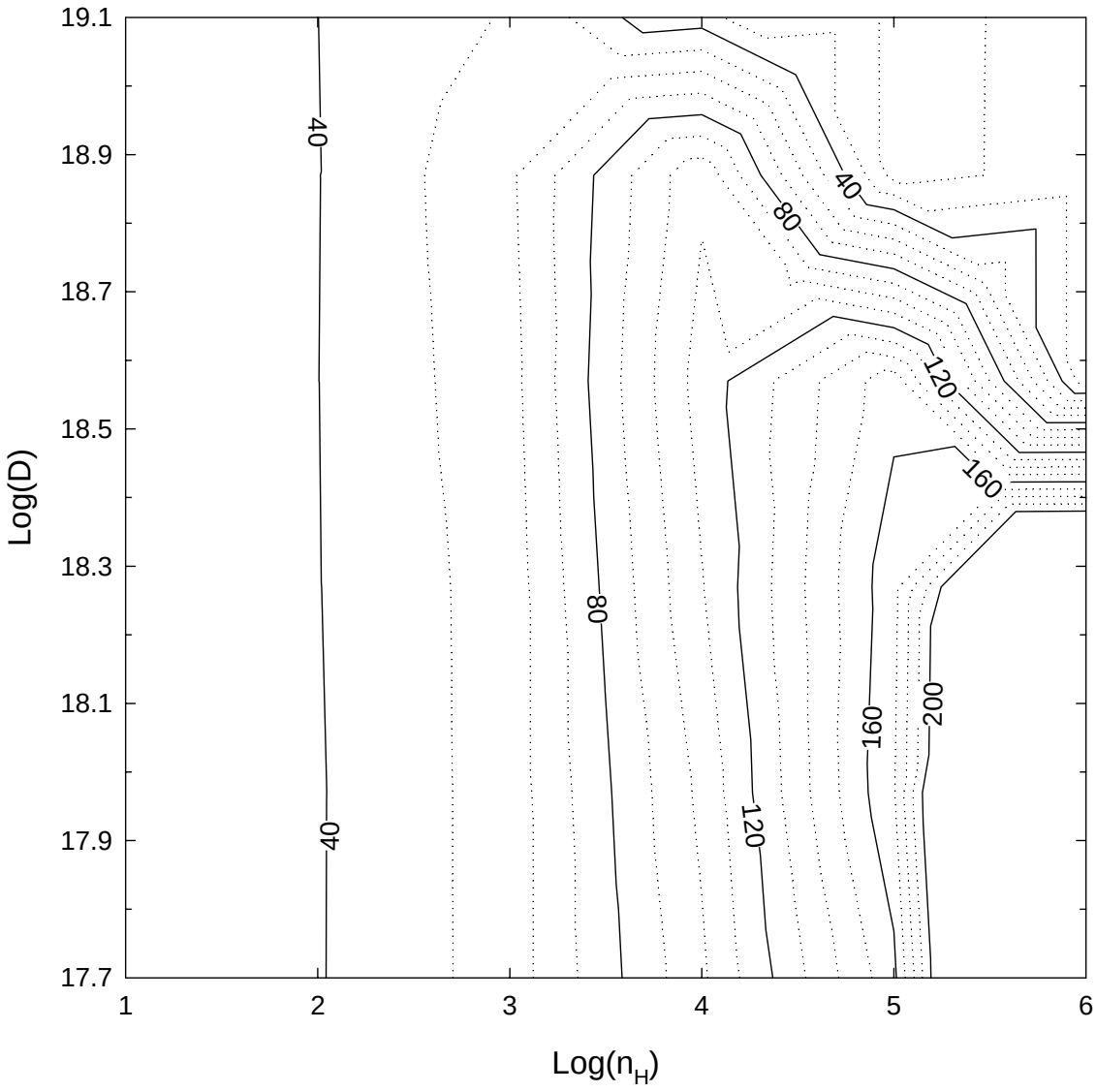

Figure 2.6 The predicted H I spin temperature (K). For densities less than the critical density of [C II] 158μ ($3x10^3$ cm^{-3}), the temperature remains relatively constant. However, for densities greater than this [C II] is no longer an efficient coolant and the heating rate increases with a power of density greater than the cooling. The upper left corner corresponds to calculations that have a large abundance of molecules.

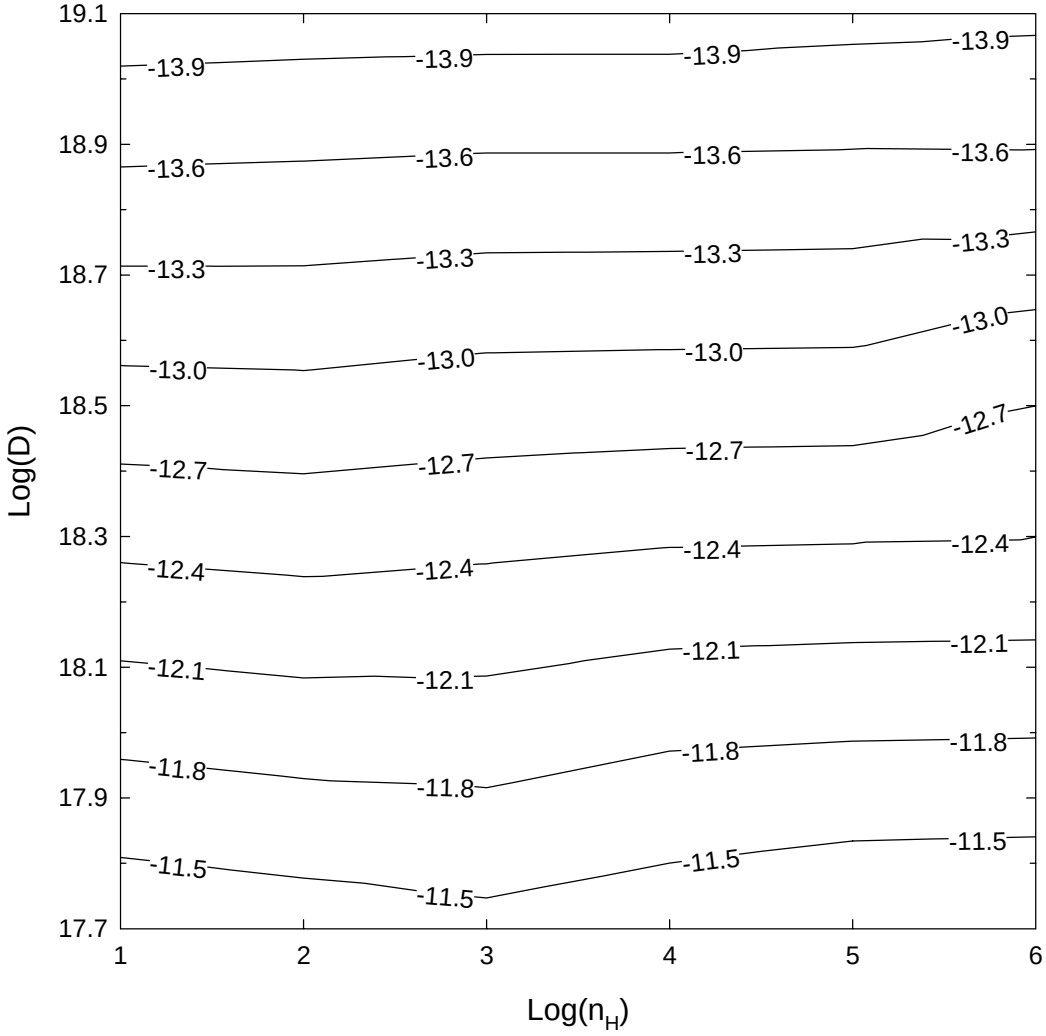

Figure 2.7 The log of the predicted Hβ surface brightness (ergs cm^{-2} s^{-1} $arcsec^{-2}$). The parallel horizontal contours are expected, given the inverse square relationship of surface brightness with distance. The actual surface brightness must be substantially smaller than the total observed surface brightness of $5x10^{-12}$ (*Log[Hβ]* **=** -11.3), which mainly comes from the main ionization front.

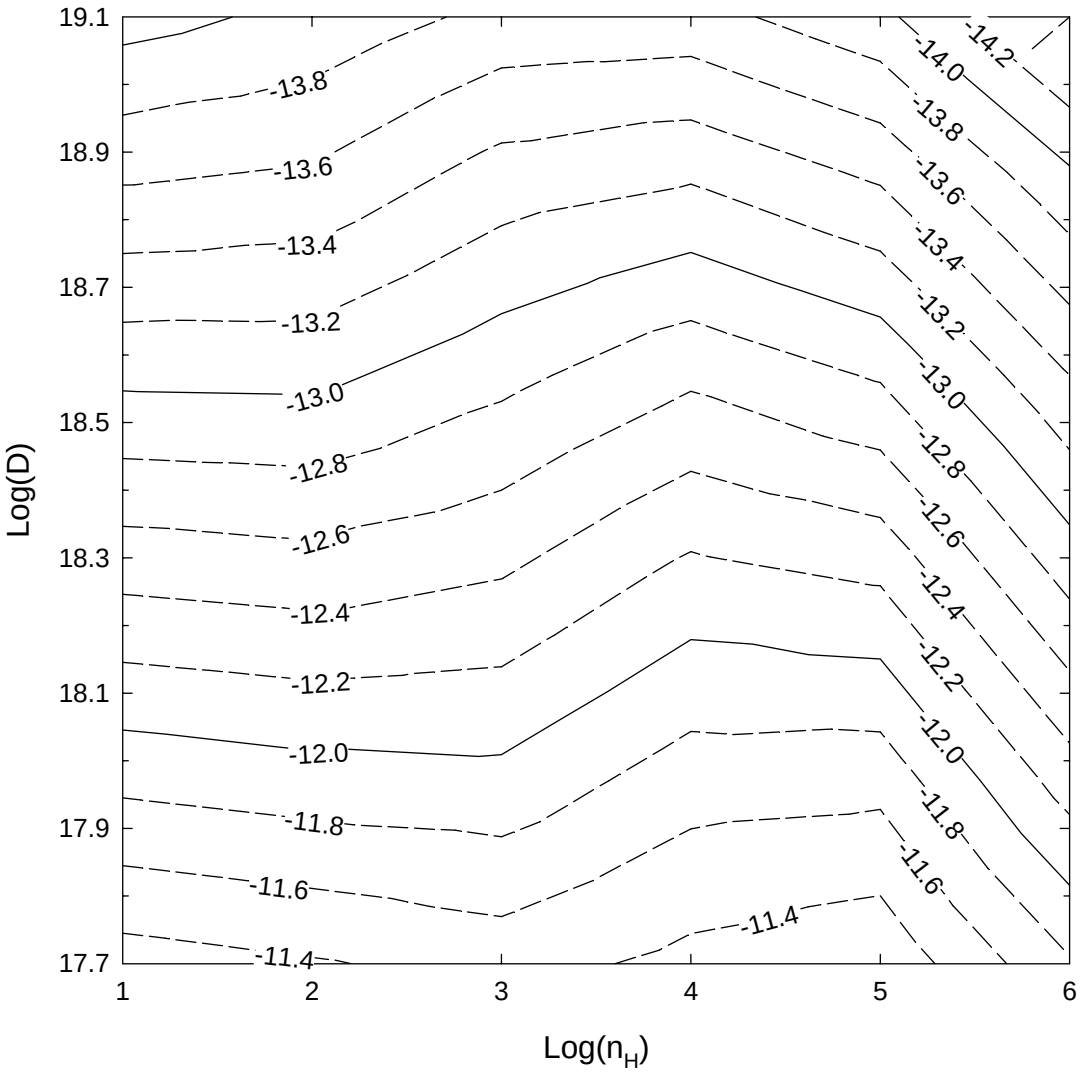

Figure 2.8 The predicted [N II] surface brightness (ergs cm^{-2} s^{-1} $arcsec^{-2}$). Based on calculations by O'Dell, Peimbert, & Peimbert (2003), the upper limit to the Veil surface brightness is found to be $1.49x10^{-13}$ ergs s^{-1} cm^{-2} $arcsec^{-2}$ (-12.8). For the range of densities that our calculations predict are most likely for the Veil (10^3-10^4 cm^{-3}), this corresponds to a lower limit to the distance of ~$10^{18.5}$ cm.

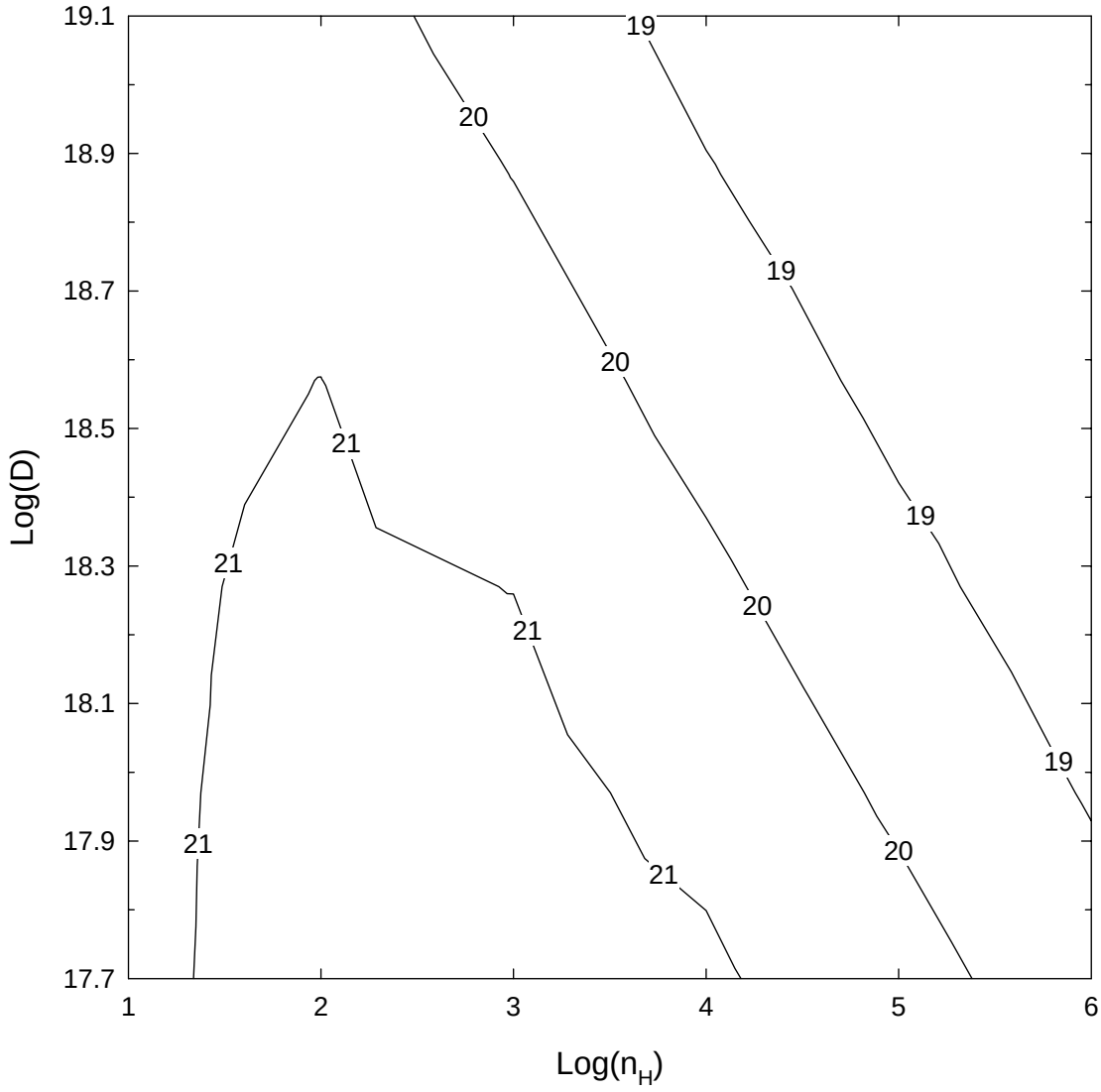

Figure 2.9 The log of the predicted H^+ column density (cm^{-2}). This is sensitive to the ionization parameter, which is the dimensionless ratio of flux to density. As expected, larger distances from the ionizing source (and hence smaller flux) and larger densities combine to lower the ionization parameter and hence the H^+ column density. For our "best model", about 5% of the total hydrogen is in the form of H^+.

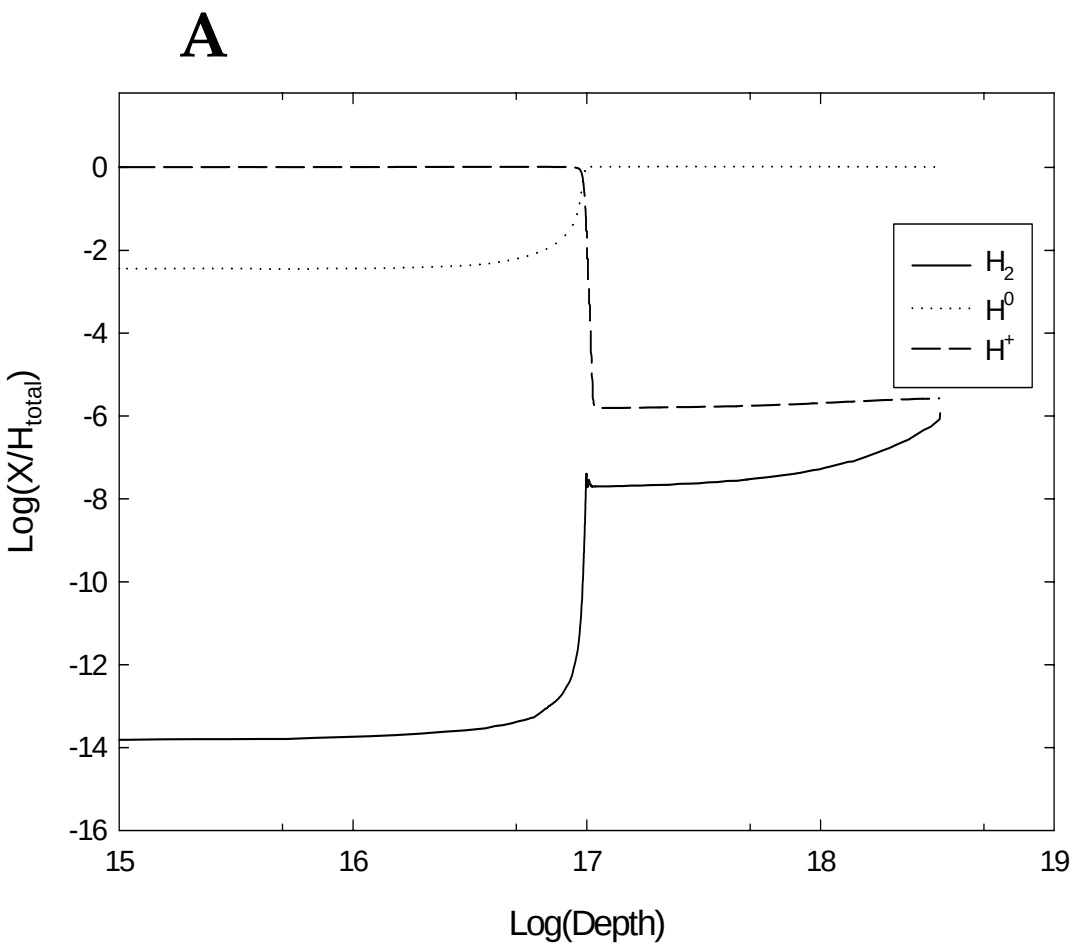
A
0
-2
-4
-6
-8
-10
-12
-14
-16
15
16
17
18
19
Log(X/H_total)
Log(Depth)
H2
H0
H+

B

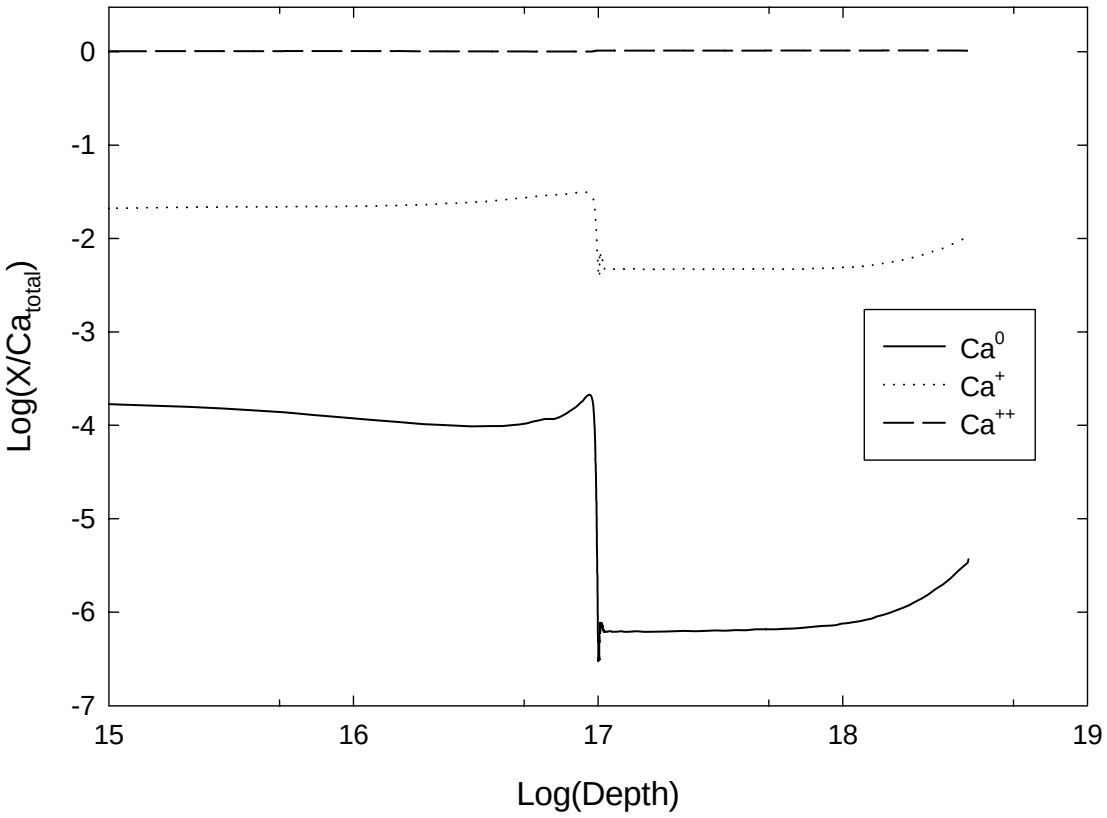

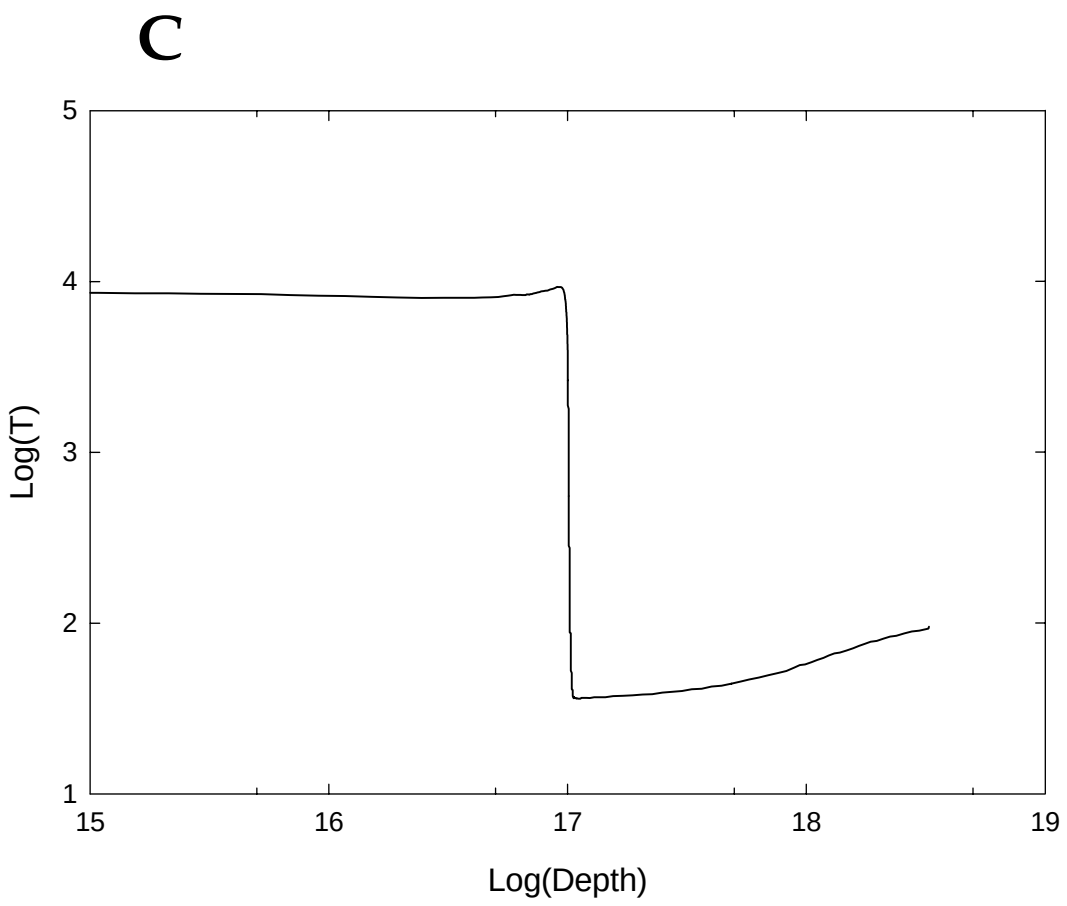

Figure 2.10 The fractional abundances of hydrogen (A) and calcium (B) in various forms as a function of depth (in centimeters) into the Veil for our best model. Also shown is the temperature vs. depth (C) into the Veil, with the temperature in units of Kelvins. The drop in temperature corresponds to the hydrogen ionization front. Also of note is that our calculations predict the majority of calcium to be in the form of Ca^{++}.

Chapter 3: Physical Conditions in Orion's Veil II: A Multi-component Study of the Line of Sight Toward the Trapezium

3.1 Introduction

Star formation is controlled through a balance among gravitational, magnetic, and thermal energies (e.g. review by Heiles & Crutcher 2005). Magnetic fields are the least understood of these processes because of the few available measurements of field strengths.

Orion's Veil is the absorbing layer of gas in front of the Trapezium region (O'Dell 2001, O'Dell & Yusef-Zadeh 2000) and one of the few regions where *maps of magnetic field strengths exist* (Troland et al. 1989). The Veil is also the location of the anomalously high ratio of total to selective extinction that is common in regions containing rich young star clusters (O'Dell 2002). This paper seeks to understand the role of magnetic fields in Orion's Veil, along with the overall physical conditions in the Veil. We discuss the observational data in Section 3.2. In Section 3.3 we describe the measurement of column densities derived from the analysis of UV spectra. We describe the results of our analysis in Section 3.4 and summarize our conclusions in Section 3.5.

3.2 Previous Studies of the Veil

Orion's Veil has a wealth of observational data that makes it suitable for exploring the role of magnetic fields in star-forming regions (see below). Magnetic fields have been measured across the bright central region of M42, but the present study is only concerned with the line of sight towards the Trapezium Cluster, the ionizing stars of M 42.

Our earlier paper, Abel et al. (2004; henceforth A04), analyzed IUE spectra which could not resolve the two main velocity components seen in 21 cm

absorption. A04 presented a series of photoionization simulations of the gas and derived global conditions. The current paper briefly reviews the observational data then uses higher-resolution UV data to resolve the velocity components seen in 21 cm absorption and to derive physical conditions in each.

3.2.1 H I 21 cm Observations

The background ionized blister that forms M42 produces strong free-free radio continuum emission that is absorbed by the Veil. In particular, H I 21 cm absorption has been observed by van der Werf & Goss (1989) and more recently by Troland et al. (in preparation—data given in A04). van der Werf & Goss (1989) identify three H^0 velocity components across the face of the Veil, but only two obvious components are associated with the line of sight towards the Trapezium. The VLA observation shows two clear components (see Figure 3.1). Using the labels of van der Werf & Goss (1989), component A has a V_{LSR} of 1.3 km s^{-1} with a *FWHM* of 3.8 km s^{-1} while for component B these values are 5.3 km s^{-1} and 2.0 km s^{-1} respectively. We report all velocities in the local standard rest (LSR) frame, to convert to heliocentric velocities add 18.1 km s^{-1}. Additionally, we use the Doppler *b*-parameter in our analysis of the STIS UV data ($b = FWHM/1.665$ – see Figure 3.1 & Table 3.1).

The 21 cm optical depth profile is shown in Figure 3.1. This profile, also shown in A04, represents a 25″ region centered on θ^1 Ori C and having a velocity resolution of 0.32 km s^{-1}. The integrated optical depth for each component is proportional to the ratio $N(H^0)/T_{spin}$, where T_{spin} is the excitation temperature for the 21cm transition (see, for instance, Spitzer 1978). If the column density is known through other means, such as Lα absorption, we can estimate T_{spin} in each component. T_{spin} is often, but not always, approximately equal to the kinetic temperature T_{kin} (Liszt 2001). Component A has $N(H^0)/T_{spin} = 1.78\times10^{19}$ cm^{-2} K^{-1} and component B has $N(H^0)/T_{spin} = 2.35\times10^{19}$ cm^{-2} K^{-1} (A04).

In the presence of a magnetic field, Zeeman splitting of the F=1 state allows the line of sight magnetic field strength for each 21 cm component to be determined. For the A and B components B_{los} = -45 ±5 μG and -54±4 μG, respectively, where the negative sign indicates that the magnetic field vectors are pointed toward the observer. Each of these values is a lower limit upon the total field strength B_{tot}. Table 3.1 summarizes the radio observational data for each component.

3.2.2 Optical

O'Dell & Yusef-Zadeh (2000) combined HST Hα and 20 cm radio continuum measurements to measure the extinction across the entire extent of M42 at 1.5" resolution. The Veil is the source of this extinction (O'Dell 2002) and towards the Trapezium has A_V = 1.6 mag.

Optical absorption studies have also yielded information on the chemical composition of the Veil in the directions of the Trapezium and other stars. The most recent and highest resolution study is the one by Price et al. (2001). They observed Ca II, Na I, K I, CH, and CH^+ optical absorption lines at many positions in the Veil. A04 argue that Ca^+ and Na^0 are trace stages of ionization in the Veil owing to the ionizing flux of the Trapezium stars. Hence, the Ca II and Na I lines trace only a small fraction of the mass. We do not consider either line further in our analysis. However, the Price et al. (2001) study did not detect either CH or CH^+ in the Veil, with only upper limits of Log[N(CH)] ≤ 11.8 and Log[N(CH^+)] ≤ 12.0. The near absence of UV H_2 absorption (see below) means the Veil must be nearly devoid of molecules toward the Trapezium stars. This conclusion is consistent with the absence of detectable CH and CH^+ absorption.

3.2.3 UV

The Veil has been observed by three UV missions, Copernicus, the International Ultraviolet Explorer (IUE), and most recently with the Hubble

Space Telescope Imaging Spectrograph (STIS). Most of what we know about the chemical composition of the Veil comes from these UV observations.

3.2.3.1 Copernicus

Copernicus was unable to detect H_2 in the Veil, setting an upper limit of $\mathrm{Log}[N(H_2)] \leq 17.55$ (Savage et al. 1977). In the diffuse ISM, the observed reddening along this line of sight, E(B-V) = 0.32 (Bohlin & Savage, 1981) is usually associated with H_2 column densities 2-3 orders of magnitude higher than observed by Copernicus. A04 found that the lack of H_2 towards the Trapezium is due to two effects, larger grain sizes found in the Orion environment (Cardelli et al. 1989), and the large UV flux incident upon the Veil owing to its close proximity (~1-3 parsecs) from the Trapezium.

Other regions of the Orion complex are known to contain larger abundance of H_2. Recent observations by France and McCandliss (2005) have measured H_2 column densities ~10^{19} cm^{-2} for a sightline towards Orion. The sightline they studied, however, was ~12′ away from Trapezium in the plane of the sky, and not towards the Trapezium itself.

3.2.3.2 IUE

Most of the column densities for atomic and singly ionized species in the Veil come from the archival study of Shuping & Snow (1997). The spectral resolution of IUE is insufficient to determine column densities for each of the H I 21 cm components, so the column densities they report are the sum of components A and B. Combining their column densities with theoretical calculations, A04 calculated a global model that best fit the observed level of ionization.

Column densities in excited states of C I and O I, and the column density ratios C II/CI, Mg II/Mg I, and S II /S I, were decisive in constraining the photoionization simulations of A04. The excited-state column densities represent the population of the $^3P_{0,1,2}$ states and are referred to as C I, C I*, C I** and O I, O I*, and O I**. For each, the total column density is just the sum of the column

densities of the three levels. The relative populations of these states are sensitive to the hydrogen density, n_H, in an H^0 region, since collisions with H^0 will be the primary excitation mechanism for these levels (Keenan 1989; Roueff & Le Bourlot 1990). The column densities of Mg I and II, S I & II, and C I & II tell us about the level of ionization for a given element. By reproducing the observed levels of ionization, the A04 model was able to place the Veil ~1-3 parsecs from the Trapezium.

3.2.3.3 STIS

The most recent and highest resolution UV spectra of the line of sight to θ^1 Ori B are presented in Cartledge et al. (2001; GO 8273) and Sofia et al. (2004; GO 9465). Cartledge et al. used the E140H echelle grating centered at 1271 Å, while Sofia et al. used the E230H grating centered at 2263, 2313 (two spectra), and 2363 Å. These two studies dealt primarily with the abundances of carbon and oxygen along translucent lines of sight, so they only reported the total column density of O I, Kr I, and C II. Cartledge et al. (2001) also derive a total H I column density towards θ^1 Ori B from Lα absorption. Towards this line of sight, $N(H^0)$ = 4.8 (± 1.1) $\times 10^{21}$ cm^{-2}. For comparison, Shuping & Snow (1997) analyzed IUE observations to find $N(H^0)$ = 4.0 (± 1.0) $\times 10^{21}$ cm^{-2} toward θ^1 Ori C.

The STIS velocity resolution of ~2.5 km s^{-1} allows comparison between the 21 cm H I and UV absorption lines. Independent of the 21 cm analysis, Cartledge et al. (2001) found O I absorption lines with V_{LSR} of 0.9 and 5.9 km s^{-1}, which correlate well with the 21 cm data. The *b* values reported in their absorption model, 1.9 (±0.4) and 1.3 (±0.7) km s^{-1}, are similar to the 21 cm *b* values of 2.3 (±0.04) and 1.2 (±0.02) km s^{-1}. These values for *b* were derived from the Kr I line, and they should be entirely due to turbulence because of the large mass of Kr.

The correspondence in *V* and *b* between the UV and radio data makes it extremely likely that both profiles are sampling the same gas components. It should be possible to determine column densities for many species in each

velocity component independently. For comparison, Figure 3.1 shows the O I, C I, and Kr I absorption profiles on the same velocity scale as the 21 cm H I profile.

3.3 Data & Analysis

Five STIS spectra are in the HST archives. This paper focuses on the single short-wavelength E140H spectrum with its many atomic, ionic and molecular lines. The longer wavelength E230H spectra include the C II] 2325Å line analyzed by Sofia et al. (2004) and a wealth of Fe II lines. We do not consider the E230H spectra in this study.

3.3.1 Data reduction

We used two software packages to analyze the STIS data. We began with pipeline processed x1d.fits files and used IRAF[1] (Tody, 1993) tasks to improve the S/N by coadding overlapping spectra from different echelle orders and grating tilts. The resulting average S/N ratio is 30-35, as determined by IRAF. The continuum flattened, normalized spectra were then analyzed with the spectral fitting package VPFIT[2] to derive column densities. VPFIT employs a χ^2 analysis to fit Voigt profiles to one or more velocity components in absorption lines. For each such component, VPFIT accepts an initial guess for the column density (N), heliocentric center velocity (V) and line width (b). VPFIT then determines the best-fit profile to an absorption line and reports estimates for N, V and b. VPFIT also estimates errors in these quantities based upon the IRAF-derived S/N ratio of the data.

---

[1] IRAF is distributed by the National Optical Astronomy Observatories, which are operated by the Association of Universities for Research in Astronomy, Inc., under cooperative agreement with the National Science Foundation

[2] VPFIT is available at http://www.ast.cam.uk/~rfc.vpfit.html

Several atomic and instrumental parameters are needed for this analysis. Rest wavelengths λ_{ij} and oscillator strengths f_{ij} for each transition come from Morton (2003), except for H_2 transitions where we use data from Abgrall et al. (2000) and Wolnievicz et al. (1998). The instrumental response profile, which is convolved with the Voigt profile, is also required. We assume the instrumental profile for the E140H echelle grating is a Gaussian with a FWHM of 1.37 km s^{-1} (STIS Handbook).

We used VPFIT on the STIS spectra to derive column densities N_A, N_B for each of the two Veil velocity components, A and B. In doing so, we fixed the center velocities V_A, V_B of the two components to the values derived very accurately from the 21 cm H I absorption profile (Figure 3.1, Table 3.1). The fitting process involves an estimate of the Doppler width parameter *b* for each component. These parameters cannot be well determined because the instrumental response profile provides only about seven independent spectral channels across an absorption line. However, column densities for the two velocity components are insensitive to *b* for lines of relatively low optical depth. Therefore, we were able to derive accurate column densities for the two velocity components for many species in the Veil. These include C I, C I*, C I**, O I, Cu II, Ni II, Ge II, P II, and Mg II (Table 3.2). In Table 3.1 we list values for the *b* parameters derived by VPFIT for optically thin lines were O I] λ1355.57Å, Cu II λ1358.77Å, and Kr I λ1235.84 Å. As expected, the *b* values have rather large errors. For optically thick (saturated) lines in the STIS spectrum, it is impossible to derive N_A, N_B independently. For these lines, we derived the *total* column density for the species (i.e. both velocity components included). Optically thick lines for which total *N* were derived include for S II, S III, N I, Si II, Si II*, O I*, O I**, P III, and C II. For the highly saturated S III line, arising in ionized gas, we derived total *N* and *V* for the line as a whole. The STIS spectra reveal other absorption lines along this line of sight (Price et al., 2001). However, they have very different

velocities and are not associated with components A or B. Therefore, we do not consider these components in our analysis.

3.3.2 Column Densities

We can estimate $N(H^0)$ for each velocity component from STIS data. The Lα line (Cartledge et al. 2001) yields total $N(H^0)$. From species that are expected to be the dominant ionization stage in H^0 regions, we can apportion $N(H^0)$ between the two velocity components. The H^0 region should be fully filled with O^0 and Kr^0 since these elements have ionization potentials > 13.6 eV. Also, Kr is not depleted in the ISM (Cartledge et al. 2001), so a constant Kr/H ratio is expected for both components. We find that 2/3 of the Kr column density resides in component B, and the same is true for O. Therefore, the same ratio must apply to H^0, and we conclude that $N(H^0) \sim 1.6\times10^{21}$ cm^{-2} for component A and $\sim 3.2\times10^{21}$ cm^{-2} in component B (Table 3.3).

We have measured excited-state column densities for both components A and B. These include level populations for C I ($^3P_0$), C I* ($^3P_1$), and C I** ($^3P_2$). Through the theoretical calculations given in A04, we then determine the volume density in each velocity component. In another useful density diagnostic, O I* and O I**, both lines become somewhat saturated. However, the derived velocity of O I* and O I** absorption (~0 km s^{-1}) makes it likely that both excited states come from component B. Also, as we will show below, the density implied C I* absorption is consistent with O I* and O I** coming from component B.

In addition to the atomic and first ion species, the E140H spectrum shows H_2 in absorption. This is the first reported H_2 column density along the line of sight towards the Trapezium. Table 3.4 summarizes our results. Previous missions failed to detect H_2 owing to a lack of spectral resolution and sensitivity (IUE, Copernicus) or the inability to observe the Trapezium (FUSE). The observed transitions are the L0-4 $P(3)$ 1342.26 Å, L0-3 $P(3)$ 1283.11 Å, L0-3 $R(3)$ 1278.72 Å, and L0-4 $R(1)$ 1333.8 Å, where the usual spectroscopic notation has been used.

The v=3-0 $P(3)$ and v=3-0 $R(3)$ H_2 absorption lines arise from the same lower level; therefore, the four absorption lines can be used to derive column densities for three H_2 levels. A comparison between the H I and H_2 v=3-0 $P(3)$ line profiles is shown in Figure 3.1.

We measured the equivalent width (W_λ) of each transition and each component. We then determined the column density by assuming the absorption is on the linear part of the curve of growth. This assumption should be valid, since the optical depth for all the observed lines was 0.2 or smaller. We find that $N(H_2)$ for component A is at least five times smaller than $N(H_2)$ for component B (Table 3.4).

3.3.3 A Blue-shifted Velocity Component in [N II] 6583 Å

The [N II] 6583 Å emission line data of Doi, O'Dell, & Hartigan (2004) were used to search for velocity components not associated with the primary layer of ionized material that provides most of the light from the Orion Nebula (M42). In Figure 3.2 we show an average spectrum of a region 45.5"x110.7" (long axis oriented north-south) centered 50.7" with a position angle of 132° from θ^1 Ori C. This data set has a FWHM of about 8 km s^{-1}. The asymmetric line profile has been deconvolved with IRAF subtasks into three components, all having a FWHM of 16 km s^{-1}. The strongest component at 0 km s^{-1} has 81% of the total energy. To the red (16 km s^{-1}) is a component with 6% of the total energy, while to the blue (-19 km s^{-1}) is a component with 13% of the total energy. The strongest component arises from the primary layer of emission and the redward component must be the velocity shifted light arising from scattering in the background PDR beyond M42's ionization front (O'Dell, Walter & Dufour 1992, Henney 1998, O'Dell 2001).

Using the method of calibration of the HST WFPC2 emission line filters (O'Dell & Doi 1999) and the images of O'Dell & Wong (1996), one finds that the total [N II] surface brightness is 2.6×10^{-13} erg cm^{-2} s^{-1} $arcsec^{-2}$, with an error of ±

20%. The average extinction at Hβ in the sample region is about $c(H\beta) = 0.6$ (O'Dell & Yusef-Zadeh 2000), so the extinction correction at 6583 Å is a factor of 2.69. The extinction corrected surface brightness is therefore 7.0×10^{-13} erg cm^{-2} s^{-1} arcsec^{-2}. This corresponds to a surface brightness of 9.2×10^{-14} erg cm^{-2} s^{-1} arcsec^{-2} for the blueward component. Although Doi, O'Dell, & Hartigan (2004) show that there are blue-shifted velocity components across the face of M42 due to high velocity shocks, they are too weak to account for the component we see in this large-area sample. As described in Section 3.4, the blueward component is an important constraint to the ionized gas.

3.4 Results

3.4.1 The Density of the Neutral Layers

The populations of levels within ground terms of atoms depend on density and temperature (Jenkins et al. 1998). Their observed column densities are then related to physical conditions. For component A the observed ratio of excited to total carbon is N(C I*)/ N(C I_{tot}) = 0.34 with a range between 0.29 and 0.76 allowed, and N(C I**)/ N(C I_{tot}) = 0.13 with an allowed range of 0.03 to 0.39. For component B N(C I*)/ N(C I_{tot}) = 0.43 with a range of 0.32 to 0.55 and N(C I**)/ N(C I_{tot}) = 0.36 ranging from 0.26 to 0.48 respectively. Such high values are only possible in regions where n_H, T, or some combination of n_H and T, is high (Keenan 1989). Similar ratios can be found in our data set for O I*, O I**, and Si II* column densities, but the lines are saturated so we cannot resolve both components.

These observed ratios and the predicted values presented in Figure 2.4 allow n_H to be determined. The range of the level population ratios quoted above either measures a density or places a lower limit to it. For component A we find $n_H \approx 10^{2.5}$ cm^{-3} with the range $10^{2.1} < n_H < 10^{3.7}$ cm^{-3} allowed, while for component B $n_H \sim 10^{3.4}$ cm^{-3} with $n_H > 10^{2.3}$ cm^{-3}. The Copernicus upper limit to $N(H_2)$, combined with Figure 2.6, requires that $n_H < 10^4$ cm^{-3} in both components. In

Section 3.4.2, we show that the H_2 column density is, to within 1σ, between 10^{14} - 10^{15} cm^{-2}. This H_2 column density further constrains n_H to be between 10^2 and $10^{3.5}$ cm^{-3} for both components.

Our estimates for $N(H^0)$ and n_H for each component can be used to derive the corresponding physical thickness l of each region ~1.7 parsecs for component A and ~0.4 parsecs for component B. The average density of both components is $\overline{n_H} = N(H^0)/l = 10^{2.9}$ cm^{-3}, very close to A04's value of $10^{3.1\pm0.2}$ cm^{-3} derived from IUE observations that did not resolve the lines.

The O I lines are saturated and cannot be deconvolved into two components. The measured total column density ratios are N(O I*)/ $N(O\ I_{tot})$ ~$10^{-3.5}$ and N(O I**)/ $N(O\ I_{tot})$ ~ $10^{-3.8}$. This ratio is an increasing function of density (A04) so almost all O I* and O I** absorption comes from the dense component B. The predicted O I* and O I** are almost an order of magnitude smaller for the lower density of component A.

3.4.2 H_2 Abundances in Both Components

The detection of H_2 further constrains the physical conditions in the Veil. The observed H_2 absorption lines arise from highly excited v=3, 4 and J=1, 3 levels, a signature of rapid photodissociation through excited electronic states (Black & van Dishoeck 1987). To illustrate this effect, we recomputed the best-fitting model, using the values of n_H and $N(H^0)$ given in Table 3.4 and including the H_2 model described in Shaw et al. (2005). Figure 3.3 shows the predicted column densities as functions of v and J.

For this plot, the higher J values at a given v correspond to higher excitation energies. The calculation shows that the level populations peak for the J=1, 3 ortho-H_2 levels, which are also the ones observed in the STIS spectrum. We only detect levels from v = 3 and 4 because of the available wavelength coverage. Lower-v levels have higher population but they produce lines shortward of our STIS spectrum.

The v and J H_2 states we see in absorption do not trace the bulk of H_2. The absorption lines detected are strong lines that lie in unblended regions of the spectrum. Other v and J states with higher H_2 column densities are either weaker or blended. Strong lines are predicted for $\lambda < 1215$ Å but the spectrum has less signal to noise in this region. Other lines are blended with C II 1335 Å, Lα, or other strong lines.

The levels we detect have very high excitation potentials, between $1.7\text{-}2.2\times10^4$ K above the ground state. A04 show that the Veil is predominantly atomic because of the rapid H_2 photodissociation rate. This Solomon process (Abgrall et al. 1992) mainly leads to population of highly excited levels within the ground electronic state, producing the populations we observed. The level populations for H_2 are therefore far from thermodynamic equilibrium because of UV pumping (Black & van Dishoeck 1987).

Even though the observed levels do not trace the majority of H_2, we can estimate the total column density by combining Figure 3.3 with the measured column densities. We made this estimate by multiplying $N[H_2(v,J)]$ derived from each line, by the ratio $N[H_2(\text{total})]/N[H_2(v,J)]$ predicted by our models and given in Table 3.4. The predicted total column density, the last column of Table 3.4, then allows both the errors in the observations and the models to be judged. The observational errors are substantial and we include the same level, measured from two lines, to judge this error. We find the total $N(H_2)$ in both components to be $\approx 10^{14.6}$ cm^{-2} with an error of 0.3 dex.

The H_2 column density in the Veil is close to the point where self-shielding by the Lyman/Werner bands decreases the H_2 destruction rate (Draine & Bertoldi 1996). Because each component moves with a different radial velocity, neither component can shield the other. Additionally, for atomic regions with a high H_2 destruction rate, $N(H_2)$ will scale linearly with both n_H and $N(H)$ (Draine and Bertoldi 1996). The larger n_H and $N(H)$ are larger for component B, which

explains why the H_2 column density is higher in that component. Given the low H_2 abundance in the Veil, it is unlikely that other molecules will be observable for this sightline.

3.4.3 The Temperature of both Components

Several estimates are possible for temperatures in the two velocity components. We can estimate T_{spin} in each component by combining $N(H^0)$ (Table 3.3 and Section 3.2) with the ratio of $N(H^0)/T_{spin}$ derived from the 21 cm data. We find $80 < T_{spin} < 110$ K for component A and $100 < T_{spin} < 165$ K for component B, with most probable values of 90 K and 135 K, respectively. Information about T_{kin} comes from two sources. First, we can place upper limits to T_{kin} by assuming the 21 cm H I line widths are entirely due to thermal motions. These limits are $T_{kin} < 87$ K for component A and $T_{kin} < 320$ K for component B. Second, we can use the density-temperature relationship found by A04. The densities derived in Section 3.4.1 imply $T_{kin} = 50$ K for component A and $T_{kin} = 80$ K for component B.

These estimates suggest $T_{kin} < T_{spin}$ for both components. In many astrophysical environments, $T_{kin} = T_{spin}$. This equality holds as long as the level populations that determine T_{spin} are in thermal equilibrium (Liszt 2001). We plan to discuss reasons why $T_{kin} < T_{spin}$ in a future paper.

3.4.4 The H^+ Region near the Veil

STIS data show that an H^+ region exists somewhere in *front* of the Trapezium, as S III and P III absorption lines must come from an H^+ region. This H^+ region is distinct from the main H^+ region that lies behind the Trapezium stars. The observed S^{2+} column density is within 0.1 dex of the A04 model (Table 2.2), while the P^{2+} differs from A04 by 0.35 to 0.91 dex. Note that A04 used the observed S abundance for the Orion H^+ region while the P abundance has not, to our knowledge, been measured. If P^{2+} is the dominant stage of ionization, then this implies that the P/H ratio in Orion is $\sim 5 \times 10^{-7}$, which is within 25% of the

observed solar abundance (Savage & Sembach 1996). The value of 1.6×10^{-7} used in A04 may, therefore, be ~0.5 dex too small. If S^{2+} is the dominant stage of ionization in the H^+ region, then this implies that $N(H^+)$ for the ionized gas is ~10^{20} cm^{-2}.

In addition to the STIS data, optical studies of the Veil also reveal the presence of an H^+ layer. The major difficulty in deconvolving the contributions from various regions is that the entire range of velocities seen along the line of sight, ~20 km s^{-1}, is not much larger than the thermal line width for 10^4 K gas. The [N II] 6583Å emission (A04) and the He I 3889Å absorption (O'Dell et al. 1993) must come from ionized gas. The observed [N II] surface brightness of 9.2×10^{-14} erg cm^{-2} s^{-1} $arcsec^{-2}$ agrees within 25% of the value predicted byA04 (7.3×10^{-14} erg cm^{-2} s^{-1} $arcsec^{-2}$), and the predicted optical depth of He I 3889Å (0.85), which A04 did not report, is within 15% of the observed value, $\tau(3889) \sim 1$ (O'Dell et al. 1993).

The S III, P III, He I, and [N II] lines formed in the H^+ layer all have roughly the same velocity, indicating these species are located in the same physical region. Figure 3.4 shows the optical depth profiles of S III and P III on the same velocity scale as the 21 cm H I absorption. The lines are quite optically thick, accounting for the noise near the line center. The line center velocities are -13.6 ± 0.9 km s^{-1} for S III and -13.3 ± 3.0 km s^{-1} for P III. The large error is due to line saturation for S III, and because the P III absorption line is partially blended with a C II absorption line. O'Dell et al. (1993), derived a velocity of -17.1 ± 1.0 km s^{-1} for the He I 3889Å absorption line, which is consistent with the velocity of the [N II] 6583Å emission line (-19.0 ± 3.0 km s^{-1}, see Section 3). O'Dell et al. (1993) also reported that the unpublished thesis of Jones (1992) showed an [O II] velocity component at -15 km s^{-1} near the Trapezium.

The velocity of the H^+ layer is surprising if it is the ionized surface of the Veil facing the Trapezium, as suggested by the agreement with predictions of A04.

We know that an H^+ region must lie between the Trapezium and the Veil in order to provide shielding for the atomic layers. If the H^+ region is a photoevaporative flow from the main Veil then the ionized gas is accelerated towards the source of ionization in the rest frame of the Veil. But the H^+ velocities are observed to be approaching the observer at ~-15 km s^{-1} in this rest frame. If the ionized gas lies between the Trapezium and the Veil then it must be a matter-bounded layer which happens to be moving towards the Veil. If the ionized layer is a photoevaporative flow then it must lie on the near side of the Veil. In this case we do not detect the H^+ layer that shields the Veil from the ionizing radiation of the Trapezium. Therefore, we would be forced to conclude that the Veil is considerably further from the Trapezium than was deduced in A04.

The H^+ layer is in one of two possible configurations relative to the Veil; between the Trapezium and Veil or between the Veil and Earth (see A04 for the geometry of this line of sight). If the H^+ layer is on the far side of the Veil, the layer is ionized by the Trapezium, primarily θ^1 Ori C. If the H^+ layer is on the near side of the Veil, then the source of ionization must be ι Ori, an O9 III star 300-600 parsecs from earth (Gualandris, Portegies Zwart, & Eggleton 2004) and 31′ from the Trapezium in the plane of the sky. This was the placement favored by O'Dell et al. (1993). However, the star ι Ori is not luminous enough to account for the ionization. The [N II] surface brightness given in Section 3.3.3 and Figure 2.8 is roughly independent of density when the density is below the line's critical density. In this case, the surface brightness is set by the flux of ionizing photons striking the layer. If θ^1 Ori C ionizes the H^+ layer, then the layer's distance from θ^1 Ori C is ~1.3 parsecs (A04). Since an O9 star has ~10 times fewer ionizing photons than an O6 star (Vacca et al. 1996), ι Ori would have to be ~0.4 parsecs away from the H^+ layer in order to explain the [N II] surface brightness. The angular separation of ι Ori from the line of sight to the Trapezium, the minimum distance ι Ori can be from the H^+ layer, is 4.4 parsecs

and its true distance must be larger. This conclusively places the H^+ layer between the Veil and Trapezium.

Our identification of the H^+ layer resolves a 40-year controversy over the physical model for the Orion Nebula (for a complete description of the controversy, see the review by O'Dell (2001)). The presence and strength of the He I absorption 3889Å line has been known since the work of Adams (1944). Wurm (1961) used the strength and blue-shift of this line (with respect to the He I emission lines) to argue that the Orion Nebula is a thin layer of ionized material lying beyond the Trapezium stars. This is the correct model usually credited to Zuckerman (1972) and Balick, Gammon, & Hjellming (1973). Münch & Wilson (1962) applied a very different interpretation to the same data, arguing that the nebular gas was optically thick to its own dust component (proven incorrect in O'Dell (2002)) and distributed symmetrically about the Trapezium stars. The newly discovered H^+ region reconciles, for the first time, the correct physical model for the nebula, the line strength, and its velocity.

We conclude that the H^+ layer is a distinct matter-bounded layer that lies between the Trapezium and the Veil, and happens to be moving towards the Veil. The fact that an ionized layer is not detected at the Veil velocity suggests that the H^+ layer we detect extinguishes much of the ionizing radiation produced by the Trapezium. Therefore the layer has a significant optical depth in the Lyman continuum. We have computed the radiative acceleration of the gas as part of the evaluation of the radiation – gas interactions (Henney et al. 2005). We find that the H^+ layer has a radiative acceleration $a_{\rm rad}$ equal to 5×10^{-7} cm s^{-2} and is due to Lyman continuum absorption by hydrogen and, to a lesser extent, by dust. The separation between the stars and the Veil is ~2 pc. A layer of gas that is free to move over this distance would be accelerated to a velocity of 25 km s^{-1} in ~1.5×10^5 years.

Dynamical instabilities may provide an explanation for why the H^+ layer absorbs nearly all of the ionizing radiation. Mathews (1982) points out that a radiatively accelerated photoionized cloud becomes Rayleigh-Taylor unstable at the H^+ ionization front and he proposed that this circumstance provides a natural process to truncate a cloud at this point – neutral gas is not efficiently accelerated and ablates off the H^+ zone.

The H^+ layer is an extended layer that covers much of the same region as the Veil. He I absorption is seen towards all Trapezium stars (O'Dell et al. 1993), and also towards θ^2 Ori A, which is ~2′ away from the Trapezium in the plane of the sky. At a distance of 500 parsecs, this shows that the gas has a lateral extent of at least 0.25 pc in the plane of the sky. If the gas has the same density as the Veil ($\sim 10^3$ cm^{-3}) then it has a physical thickness of 0.1 parsecs. Like the layers of the Veil, it appears as a sheet of gas.

We know, however, that the H^+ layer and Veil do not interact and therefore are separated by some distance. The A04 model, which had the H^+ layer as a simple extension of the mostly atomic gas, placed the Veil ~2 parsecs away from the Trapezium. This calculation under-predicts the observed [N II] surface brightness by ~20%. To within the observational error, Figure 8 of A04 places the ionized layer 1.1-1.6 parsecs away from the Trapezium, with a mean value of 1.3 parsecs.

We can estimate the collision time between the H^+ and H^0 layers. A04 found that the 1σ estimate of the H^0 layers from the Trapezium is 1-3 parsecs (A04). We also have a 1σ estimate for the distance of the H^+ layer. The maximum separation distance between the two layers is therefore 1.9 parsecs. Given the H^+ layer's current radiative acceleration and relative velocity (15 km s^{-1}), a collision between the H^+ layer and the Veil will happen in < 85,000 years. If we take the best-fit values for the distance of the H^+ and H^0 layers from the Trapezium, then the collision time is ~40,000 years.

3.4.5 Energetics

Physical parameters in the two Veil layers reveal the relative importance of thermal, turbulent, magnetic and even gravitational energies. These energies can be estimated from the observed linewidths (Δv_{tot}), magnetic field strengths (B_{los}) and column densities $N(H^0)$, together with model values for the gas density (n_H) and T_{kin} (Table 3.1 and 3.3). Moreover, energies in the two Veil layers may be compared with typical values for the galactic cold neutral medium (CNM), an interstellar regime that is also observable in 21 cm H I absorption. We use the best-fit model values for n_H and T_{kin} to compute the most probable energies for each H I velocity component. We also compute each parameter using upper and lower limits upon n_H and T_{kin} as established by the model or by other constraints. For parameters involving the magnetic field, we apply a statistical correction to convert the observed B_{los} into the most probable estimate for the total field strength B_{tot}. These factors are $B_{tot} = 2B_{los}$ and $B^2_{tot} = 3B^2_{los}$, appropriate for parameters dependent upon B and B^2, respectively (Crutcher 1999). Definitions and symbols for physical parameters below (e.g. the turbulent Mach number M_{turb}) are taken from Heiles & Troland (2005). In converting n_H in the mass volume density, we have assumed the usual fractional helium abundance of 0.1.

In Table 3.5 we list the derived parameters for the two Veil components along with median values for these parameters appropriate to the CNM of the galaxy. These latter values come from the 21 cm H I absorption survey of Heiles & Troland (2005 and references therein). For each parameter, we list the most probable value along with a range of values. The ranges are based upon the allowed ranges in T_{kin} and n_H in the two Veil components (Section 3.4.1 and 3.4.3). The turbulent Mach number M_{turb} *squared* is the ratio of turbulent to thermal energy densities. Values of $M_{turb} > 1$ imply supersonic turbulence. Veil component B is very supersonically turbulent, like the CNM. Veil component A appears more quiescent; it may be only mildly supersonic. The parameter β_{th} is

the ratio of thermal to magnetic energy densities. This ratio is always < 1 in the interstellar medium and often << 1 in self-gravitating regions (Crutcher 1999, who uses the symbol β_p). For the Veil components, $\beta_{therm} << 1$. The parameter β_{turb} is the ratio of turbulent to magnetic energy densities. This same ratio is also expressed in terms of the Alfvenic turbulent Mach number, where $M^2_{Alf,turb} = 0.67 \beta_{turb}$. In self-gravitating clouds, existing magnetic field observations suggest $\beta_{turb} \approx 1$, a state of magnetic equipartition (See Crutcher 1999, who provides values for the Alfvenic Mach number m_A, where $m_A^2 = \beta_{turb}$). Also, in the non self-gravitating CNM, $\beta_{turb} \approx 1$, again a state of approximate magnetic equipartition. However, Veil component A has $\beta_{turb} << 1$. Therefore, turbulent energy densities in this component are much less than magnetic energy densities. The energetics of Veil component A appear strongly dominated by the magnetic field, the first such region in the interstellar medium yet to be identified. This conclusion is consistent with the results of A04 who modeled values for n_H and T_{kin} averaged over the two Veil components. Note that A04 characterized β_{turb} in terms of the ratio of the actual gas density n_H to the equipartition density n_{eq}. The latter density is the approximate density required for magnetic equipartition, and $n_H/n_{eq} = 1.9\beta_{turb}$. Veil component B has $\beta_{turb} \approx 1$, consistent with magnetic equipartition as in the CNM and in self-gravitating clouds. In summary, Veil component B is similar to CNM and to most self-gravitating gas in the galaxy in that thermal energy is insignificant compared to turbulent and magnetic energies, and the latter two are comparable (magnetic equipartition). However, Veil component A is quite different. In this component, magnetic energy strongly dominates thermal and turbulent energies, both of which are comparable although relatively small.

Another magnetic parameter of interest is the mass-to-flux ratio, M/Θ. This parameter is a measure of the ratio of gravitational to magnetic energies in a *self-gravitating* cloud. A critical value exists for this ratio such that a self-gravitating

cloud will be supported indefinitely by magnetic pressure if M/Θ for the cloud is less than the critical value and if slippage between charged and neutral particles (ambipolar diffusion) does not occur. (See Crutcher 1999 and references therein.) Of course, the Veil layers of Orion are not likely to be self-gravitating. However, the ratio M/Θ is conserved if ambipolar diffusion is not an important process. Therefore, M/Θ in the Veil today may be representative of M/Θ in Orion gas that once was (or will become) self-gravitating. Crutcher (1999) provides a relationship for λ, the ratio of M/Θ to the critical value. In particular, $\lambda = 0.5 \times 10^{-20}\, n(H^0)/B$, where $n(H^0)$ is in cm^{-3} and B is in μG. Applying this relation and using $B = B_{los}$ for each component (Table 3.1), we find that λ = 0.18 and 0.30 for components A and B, respectively. These values of λ are *upper limits* because $B \geq B_{los}$. We conclude that λ < 1 for both Veil components, so they both are said to be magnetically subcritical. The CNM also appears to also be magnetically subcritical (Table 3.5). However, self-gravitating gas generally appears to be magnetically critical (λ ≈ 1, Crutcher 1999).

3.4.6 Veil properties

Some properties of the Veil resemble the CNM in the galaxy. These include kinetic temperature, existence of supersonic turbulence and a magnetically subcritical state. In other ways, of course, the Veil is quite different, reflecting, no doubt, its association with OMC-1. H^0 column densities in each of the Veil components are an order of magnitude greater than typical CNM column densities of $2\text{-}3 \times 10^{20}$ cm^{-2} (Heiles & Troland 2005). Also, n_H is 1-2 orders of magnitude higher in the Veil than in typical CNM, and the magnetic field strengths are an order of magnitude higher. As a result, total pressures in the Veil components are comparable to each other and about two orders of magnitude higher than in the CNM or in diffuse interstellar material in general. The Veil layers are not likely to be gravitationally stable on their own. They may be confined by the gravitational field of the background molecular cloud OMC-1,

coupled to the cloud via the magnetic field. However, higher spatial resolution extinction observations (O'Dell & Yusef-Zadeh 2000) show that there are small clumps in the Dark Bay region of the Veil.

While distinctly different in many physical properties from the CNM, the two Veil components are also different from each other. Component A appears less supersonically turbulent, somewhat cooler, significantly lower in density, and thicker than component B. In addition, component A is dominated by magnetic field energy. Curiously, magnetic field strengths in both components seem essentially the same despite the factor of eight lower density in component A implied by the best fit model. That is, there is no apparent connection of field strength to gas density in the two Veil components, a property that also applies to diffuse gas in the galaxy (e.g. Heiles and Crutcher 2005). Both the Veil components and the CNM are magnetically subcritical. It is possible, therefore, that interstellar gas in a magnetically subcritical state does not experience an increase in field strength with density. This phenomenon, which bears further theoretical study, may result from motion of gas primarily along field lines or else from decoupling of the neutral gas from the field, that is, ambipolar diffusion.

Which of the two Veil components lies closer to the Trapezium? Van der Werf & Goss (1989) argued that component B arises in dissociated H_2 gas, closer to the stars while component A represents halo gas from the molecular cloud, undisturbed by the Orion H^+ region. However, the H_2 abundance in both components can be explained without considering the Veil-Trapezium distance. Additionally, the H^+ region near the Veil (Section 3.4.4) is decoupled from the Veil gas. We therefore cannot definitively say which component is closer to the Trapezium.

Table 3.1 – Observational Data

Parameter	Component A	Component B
$N(H^0)$ / T_{spin} (cm^{-2} K^{-1})	1.78×10^{19}	2.35×10^{19}
b - H I (km s^{-1})	1.20 ± 0.02	2.30 ± 0.04
V_{LSR} (km s^{-1})	5.30 ± 0.01	1.30 ± 0.03
b - O I] λ1355.57Å (km s^{-1})	1.56 ± 0.43	2.20 ± 0.32
b - Cu II λ1358.77Å (km s^{-1})	1.61 ± 0.35	2.05 ± 0.28
b - Kr I λ1235.84 Å (km s^{-1})	1.72 ± 1.01	2.14 ± 0.76
B_{los} (μG)	-45	-54

Table 3.2 – STIS Derived Column Densities in the Veil

Species	Log[N(X)] (cm^{-2}) Component A	Log[N(X)] (cm^{-2}) Component B	Log[N(X)] (cm^{-2}) Total
O I	17.51 ± 0.06	17.83 ± 0.04	18.00 ± 0.03
C I ($^3P_0$)	12.86 ± 0.13	12.86 ± 0.13	13.16 ± 0.09
C I*	12.67 ± 0.24	13.19 ± 0.10	13.30 ± 0.10
C I**	12.24 ± 0.47	13.12 ± 0.10	13.17 ± 0.10
C I_{tot}	13.14 ± 0.22	13.56 ± 0.10	13.69 ± 0.06
Ni II	13.12 ± 0.03	13.40 ± 0.02	13.58 ± 0.02
Cu II	12.28 ± 0.05	12.52 ± 0.04	12.72 ± 0.03
P II	13.71 ± 0.33	14.32 ± 0.24	14.41 ± 0.20
Kr I	12.08 ± 0.11	12.31 ± 0.08	12.51 ± 0.06
Ge II	11.79 ± 0.05	11.95 ± 0.04	12.17 ± 0.03
Mg II	15.30 ± 0.04	15.58 ± 0.03	15.76 ± 0.02
O I*	N/A	14.31 ± 0.08	14.31 ± 0.08
O I**	N/A	14.06 ± 0.06	14.06 ± 0.06
N I	N/A	N/A	17.74 ± 0.03
Si II	N/A	N/A	16.52 ± 0.02
Si II*	N/A	N/A	15.37 ± 0.06
P III	N/A	N/A	13.59 ± 0.24
C II[1]	N/A	N/A	17.82 (+0.12, -0.19)
S II	N/A	N/A	15.97 ± 0.12
S III	N/A	N/A	14.98 ± 0.06

[1] Column density taken from Sofia et al. (2004)

Table 3.3 – Physical Conditions

Parameter	Component A	Component B
$N(H^0)$ cm^{-2}	$1.6(1.4\text{-}2.0)\times10^{21}$	$3.2(2.4\text{-}3.9)\times10^{21}$
n_H cm^{-3}	$10^{2.5}$ ($10^{2.1}$-$10^{3.5}$)	$10^{3.4}$ ($10^{2.3}$-$10^{3.5}$)
l (parsecs)	1.3	0.5
T_{spin} (K)	90 (80-110)	135 (100-165)
T_{kin} (K)	50 (< 87)	80 (< 80)

Table 3.4 – H_2 Absorption Data

H_2 Absorption Line	W_λ (mÅ)	$N(H_2)_{obs}$ (cm^{-2})	$[H_2(tot)/H_2(v,J)]_{A04}$	$[N(H_2)]_{tot}$ (cm^{-2})	W_λ (mÅ)	$N(H_2)_{obs}$ (cm^{-2})	$[H_2(tot)/H_2(v,J)]_{A04}$	$N(H_2)_{tot}$ (cm^{-2})
	Component A				Component B			
L0-3 *R*(3) 1278.72	1.58 ± 0.60	$10^{12.27\ +0.14\ -0.21}$	63.4	$10^{14.1}$	$2.28\ ^{+1.25}_{-0.81}$	$10^{12.49 \pm 0.19}$	73.8	$10^{14.4}$
L0-3 *P*(3) 1283.11	0.56 ± 0.47	$10^{11.82\ +0.26\ -0.81}$	63.4	$10^{13.6}$	$3.44\ ^{+0.51}_{-0.44}$	$10^{12.77 \pm 0.06}$	73.8	$10^{14.6}$
L0-4 *R*(1) 1333.80	0.51 ± 0.70	$10^{11.78}$ (<12.15)	135.8	$10^{13.9}$	$2.50\ ^{+2.27}_{-1.19}$	$10^{12.28 \pm 0.28}$	158.2	$10^{14.5}$
L0-4 *P*(3) 1342.26	0.39 ± 0.36	$10^{11.67\ +0.28\ -1.03}$	97.8	$10^{13.7}$	$2.82\ ^{+0.49}_{-0.44}$	$10^{12.52 \pm 0.07}$	113.1	$10^{14.6}$
			$\overline{N(H_2)_{tot}}$ =	$10^{13.8}$			$\overline{N(H_2)_{tot}}$ =	$10^{14.5}$

Table 3.5 - Magnetic Parameters for the Veil

Parameter	Component A	Component B	CNM
M_{turb}	1.8 (0 – 2.2)	3.5 (3.4 – 5.0)	3.7
V_A (km s^{-1})[10]	9.4 (3.0 – 14.8)	4.0 (3.6 – 14.2)	1.5
β_{therm}	0.01 (0.003 – 0.17)	0.088 (0.004 – 0.12)	0.29
β_{turb}	0.014 (0.007 – 0.014)	0.50 (0.045 – 0.6)	1.9
λ	0.09 (0.08 – 0.11)	0.15 (0.11 – 0.18)	0.22

[10] V_A is the Alfven velocity

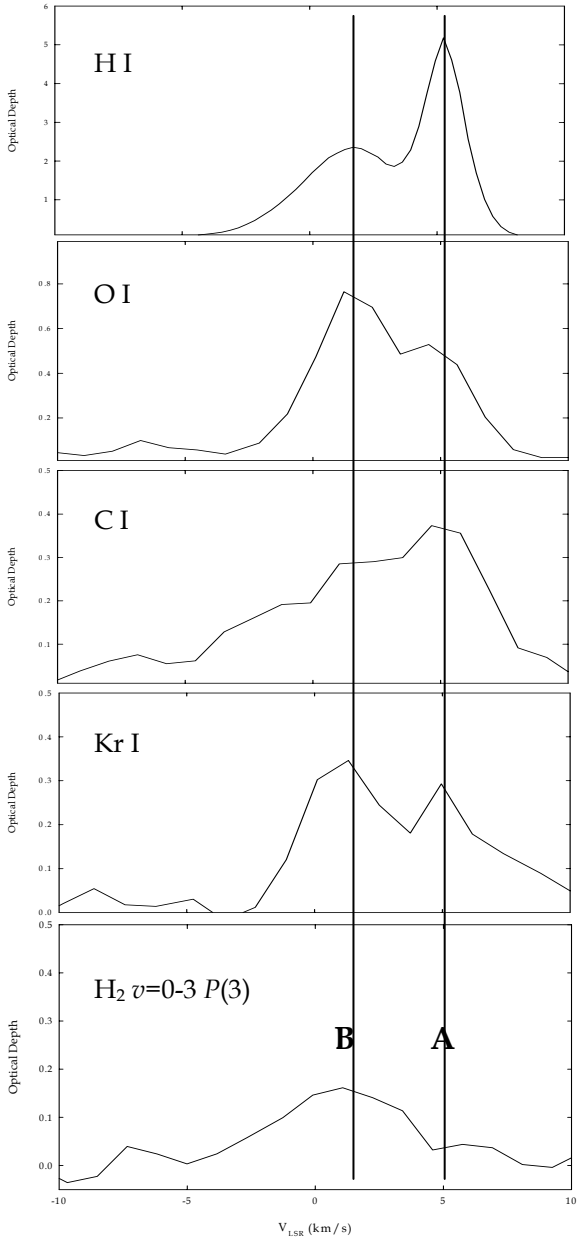

Figure 3.1 Optical depth line profiles toward θ¹ Ori B. The H I 21 cm profile and three STIS UV profiles are shown. The x-axis is given in V_{LSR}, to allow for comparison between the H I and UV absorption lines. The solid vertical lines represent the position of the 21 cm velocity components. A clear correlation is seen between the H I and UV absorption lines.

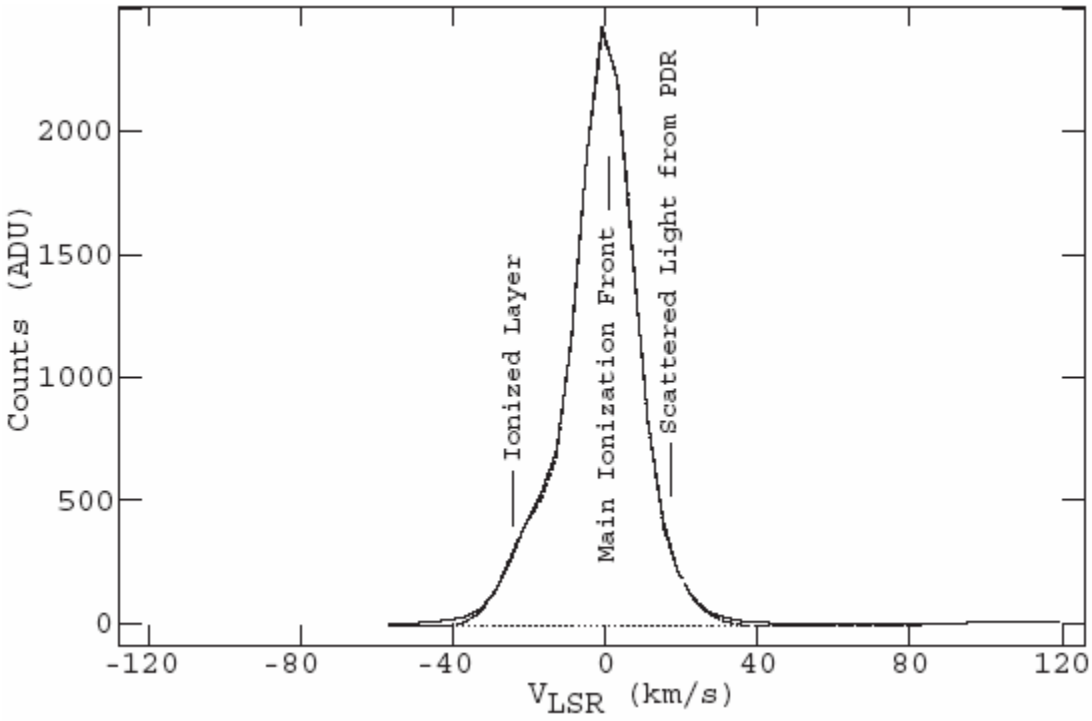

Figure 3.2 The profile of the [N II] emission line of a region to the southeast of the Trapezium from the data described in Doi, O'Dell, & Hartigan (2004) is shown, together with its deconvolution into three major velocity components as described in the text. The featured designated as the "Ionized Layer" corresponds to the newly identified H II layer that produces the newly discovered S III and P III UV absorption lines and the He I 3889Å line that has been observed for half a century but never explained.

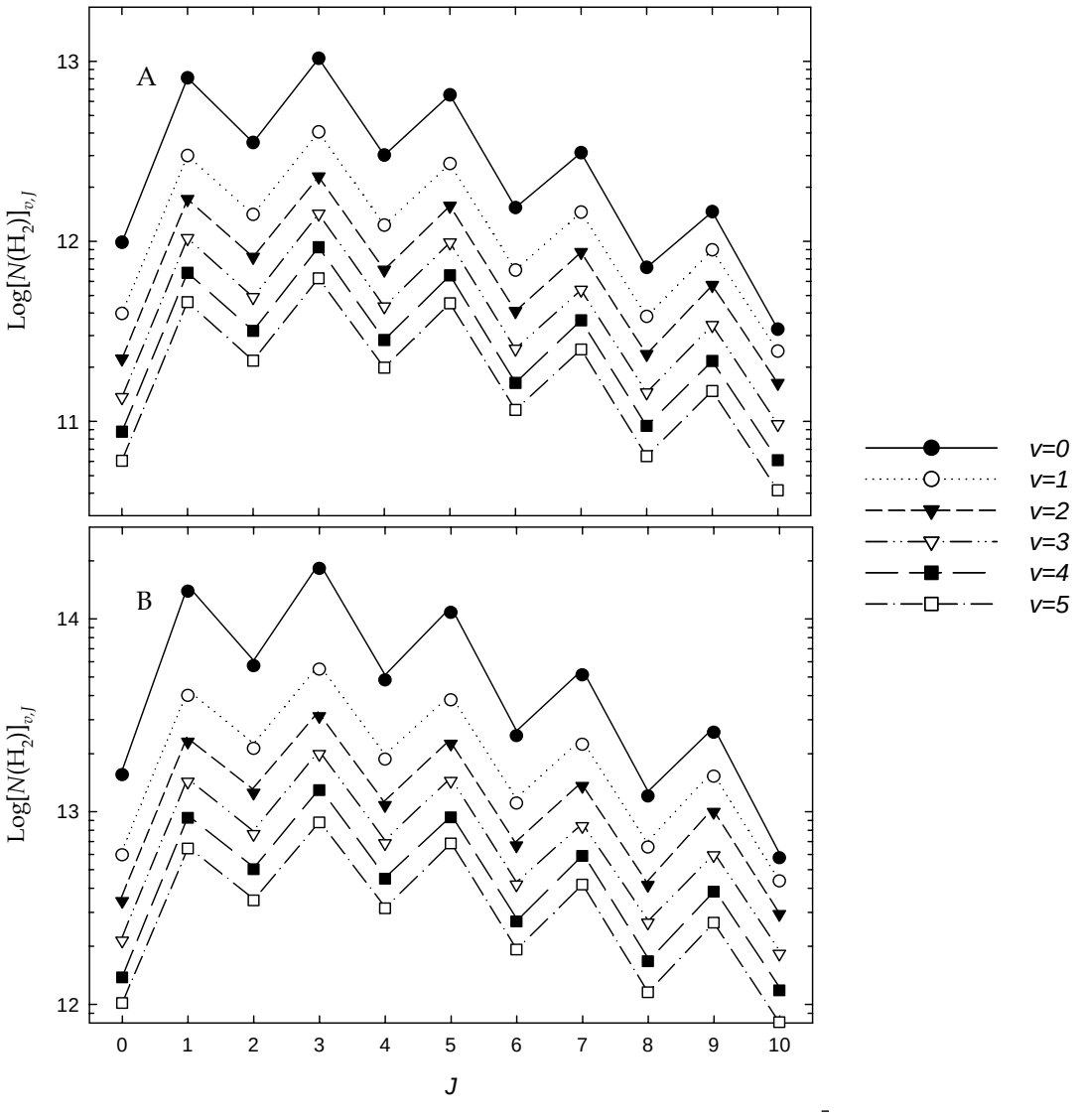

Figure 3.3 Predicted H_2 column densities for each component from the A04 model and n_H derived in this work. Due to the proximity of the Veil to the Trapezium, UV pumping of H_2 forces the level populations out of thermodynamic equilibrium. For a given v the largest column densities are in the J=1 and 3 states, which agrees with observation.

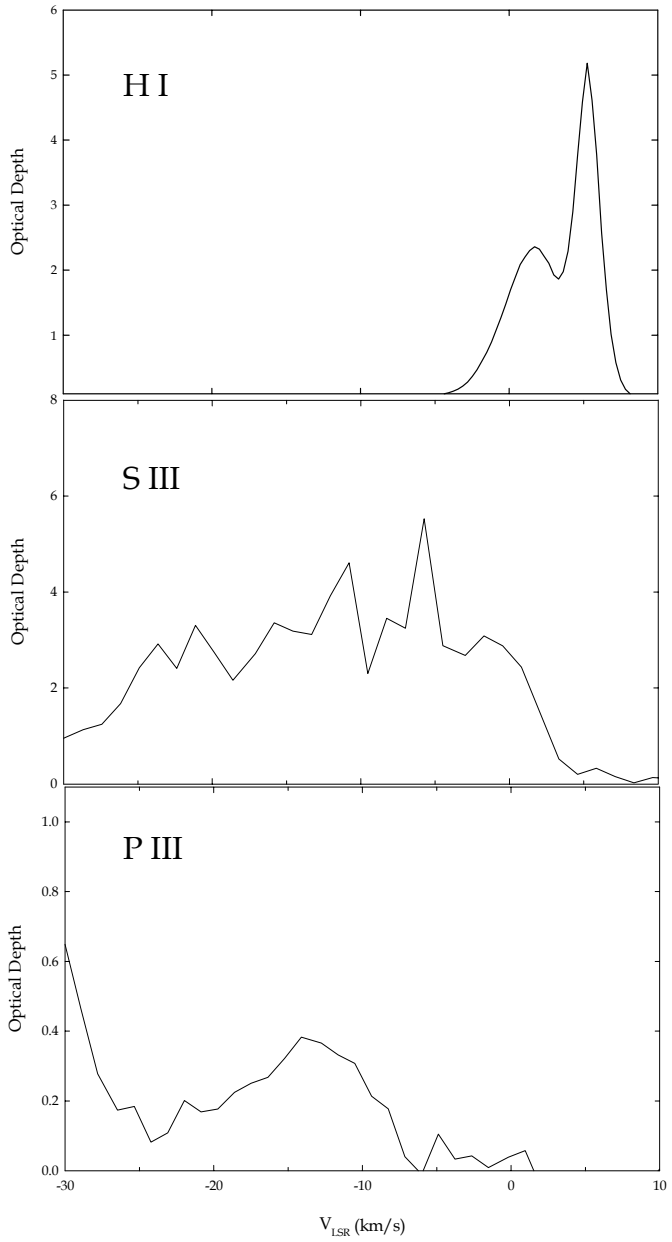

Figure 3.4 Optical depth profiles of ionized species, on same velocity scale as the 21 cm H I absorption. The S III and P III absorption is blue shifted 10-15 km s^{-1} relative to the Veil. Since the ionized gas is located between the Trapezium and Veil, the two layers will eventually collide.

Chapter 4: The H II Region/PDR Connection: Self-Consistent Calculations of Physical Conditions In Star-Forming Regions

4.1 Introduction

A major goal of infrared missions such as Spitzer, SOFIA, Hershel, and JWST is to understand the physical processes in galaxies and local regions of star formation. Such regions include starburst galaxies, Ultraluminous Infrared Galaxies (ULIRGs), embedded O stars in molecular clouds, and blister H II regions. Infrared spectroscopy can reveal conditions in ionized, photodissociated, and molecular gas. Observations combined with theoretical calculations reveal the temperature of the ionizing stars, T_*, electron density n_e, ionization parameter U, total hydrogen density n_H, and UV radiation field G_0. These, in turn, can yield information about the ionized, atomic, and molecular mass, the star formation rate, the chemical and thermal structure, elemental abundances, area and volume filling factors, number of stars required to produce the ionization, and the number of clouds and their radii (Wolfire, Tielens, & Hollenbach, 1990).

Up to now H II regions and PDRs have been treated as separate regions. This paper presents unified H II region / PDR calculations that make interpretation of observations on a self-consistent basis possible.

4.2 Physical Picture

4.2.1 Structure of Clouds with Embedded Ionizing Stars

Evans (1999) outlines the structure of molecular clouds, or star-forming regions. As gravitational collapse of the cloud takes place, O stars hot enough to

ionize H create an H II region. The level of ionization of an H II region can be characterized by U, the dimensionless ratio of the flux of ionizing photons, ϕ_H, to n_H at the illuminated face, given by:

$$U = \frac{\phi_H}{n_H c} \tag{4.1}$$

where c is the speed of light. Typical values for U vary from about 10^{-1} to 10^{-4} (Veilleux & Osterbrock 1987).

These O stars are either embedded deep in the molecular cloud or form on the edge of the molecular cloud and create a blister-type H II Region, similar to the Orion Nebula (O'Dell, 2001). In the case of starbursts, the same physical mechanisms probably occur, only on a much larger scale.

Hydrogen makes the transition from ionized to atomic form when all photons with energies $h\nu >$ 13.6 eV are absorbed. Once hydrogen becomes primarily atomic, the H II region ends and the Photodissociation Region, or PDR, begins (Tielens & Hollenbach, 1985). Hydrogen makes the transition from atomic to molecular across the PDR. Other molecules can form after H_2 since H_2 is a primary catalyst.

PDRs are characterized by n_H and the strength of the Far-Ultraviolet (FUV) field (G_0) between 6 and 13.6 eV relative to the background interstellar radiation field (Habing 1968).

$$G_0 = \frac{\int_{912\text{Å}}^{2067\text{Å}} I_\lambda d\lambda}{1.6x10^{-3}\ (\text{ergs cm}^{-2}\ \text{s}^{-1})} \tag{4.2}$$

The value of G_0 strongly influences the physical conditions in PDRs (Wolfire, Tielens, & Hollenbach, 1990; Kaufman et al., 1999). Hollenbach & Tielens (1997) give a complete description of the physical processes in a PDR.

4.3 Infrared Diagnostics – Theory and Observations

4.3.1 H II Region Diagnostics

T_* and U are determined through observations of lines of more than one ionization stage of the same element. For instance, a common diagnostic used in H II regions is the ratio of [Ne III] 15.56 μm to [Ne II] 12.81 μm (Verma et al., 2003; Giveon et al., 2002). A higher line ratio corresponds to a higher level of ionization, corresponding to a higher T_* and U. Other line ratios that can characterize the radiation field are [S IV] 10.51 μm to [S III] 18.71 μm or 33.48 μm; [N III] 57.21 μm to [N II] 121.7 μm or 205.4 μm line (Rubin et al, 1994); and the ratio of [Ar III] 8.99 μm to [Ar II] 6.99 μm.

The electron density is determined through ratios of lines of the same ion (Osterbrock & Ferland 2005). The average electron energy is much greater than the excitation potential for mid-infrared transitions, eliminating the temperature dependence of the line ratio. However, each line will have a different critical density, which makes the line ratio dependent on n_e. Examples of density diagnostics in the infrared are the [O III] 52 μm line to [O III] 88 μm, [S III] 18.71 μm to [S III] 33.49 μm, and [N II] 121.7 μm to [N II] 205.4 μm (Rubin et al. 1994; Malhorta et al. 2001).

4.3.2 PDR diagnostics

Infrared fine-structure lines can also determine the physical conditions in the PDR and molecular cloud. These lines include [C II] 158 μm, [C I] 370 μm, 609 μm, [O I] 63 μm, 146 μm, the [Si II] 35 μm, and [Fe II] 1.26μm, 1.64μm lines. These are important coolants in PDRs (Hollenbach & Tielens, 1997). Observations of the intensity of these lines combined with theoretical calculations help to determine physical conditions in star forming regions (Tielens & Hollenbach 1985; Wolfire, Tielens, & Hollenbach 1990). Kaufman et al.'s (1999) calculations show how these lines vary over a wide range of n_H and G_0. The basic premise is that, by observing as many lines as possible, theoretical

calculations can be compared to observations to determine n_H and G_0. These then determine such properties of star forming regions as the mass of the cloud, number of clouds, filling factor, chemical composition, and temperature.

4.3.3 H II Region Contributions to PDR Diagnostics

Previous calculations have treated the H II region and PDR separately. PDR calculations typically do not consider hydrogen-ionizing radiation, and define a PDR as starting where H is predominantly atomic. Diagnostic emission lines are assumed to originate in only one of these regions.

Some ions (for example, C^+ or Si^+) are present in both the H II region and PDR, and their lines, in this case [C II] 158 μm and [Si II] 35 μm, can form in both. Even the [O I] 63 μm, 146 μm lines can form in H II regions (Aannestad & Emery, 2003). Calculations that ignore the H II region (essentially all current PDR simulations) will underestimate the line intensity, leading to incorrect value of n_H and G_0. This can lead to erroneous conclusions for the physical conditions.

It is already known that the H II region can contribute to "PDR" lines. Kaufman et al. (1999) note the need to correct observations for any possible H II region emission before using their contour plots. There are several ways to make this correction, both observational and computational. Petuchowski & Bennett (1993) and Heiles (1994) note that the contribution of the H II region intensity to the [C II] 158 μm line should be proportional to [N II] 122 μm. The most common computational approach is to run a separate model of the H II region to estimate its contribution to a PDR diagnostic (Carral et al. 1994). They found that as much as 30% of the [C II] line can come from the H II region, with the greatest contribution coming from low-density H II regions adjacent to PDRs. A study of S125 by Aannestad & Emery (2003) found that ~40% of the [C II] 158 μm and ~20% of the [O I] 63 μm line intensity came from the H II region.

The overall approach of considering the two regions separately has many difficulties. One is that it is nearly impossible to match boundary conditions for

two separate simulations. The density of the PDR, relative to the H II region, is assumed to be the inverse ratio of their temperatures, $\approx 10^2$, as suggested by gas pressure equilibrium. The transition between the H II region and PDR is not included, leading to a lack of continuity.

Dynamical processes link these two regions in nature (see Henney et al. 2005). The physical properties of the PDR are a consequence of the transport of gas and radiation through the H II region, while the H II region is the result of the flow of gas through the PDR. Our approach is to compute self-consistently the temperature, density, and ionization starting with the H II region and progressing through the PDR.

We discuss computational details in Section 4.3 and in Appendices A, B, and C. In Section 4.4 we describe the physical processes for a standard model that begins in the H II region and extends deep into the molecular cloud. Section 4.5 shows how H II region and PDR infrared diagnostic lines vary with U, n_{H^+}, and T_*, under the assumption of constant pressure. We will also determine the H II region contribution to commonly used PDR diagnostic emission lines. We will then show applications to our calculations in Section 4.6, and end with a list of conclusions in Section 4.7.

4.4 Calculations

We use the developmental version of the spectral synthesis code Cloudy, last described by Ferland et al. (1998). Shaw et al. (2005) and Henney et al. (2005) describe recent advances in its treatment of H_2 and dynamics.

We have expanded the molecular reaction network to include ~1000 reactions involving 68 molecules. We describe the molecular network in Appendix E and in Abel et al. (2004). Our chemical equilibrium agrees very well with other PDR codes presented at the Leiden 2004 PDR workshop (http://hera.ph1.uni-koeln.de/~roellig/).

Van Hoof et al. (2004) describe the grain physics. We self-consistently determine the grain temperature and charge as a function of grain size and material, for the local physical conditions and radiation field. This determines the grain photoelectric heating of the gas, an important gas heating process, as well as collisional energy exchange between the gas and dust. The rates at which H_2 forms on grain surfaces is derived using the temperature- and material-dependent rates given in Cazaux & Tielens (2002). We include grain charge transfer as a general ionization – recombination process, as described in Appendix F. We also treat stochastic heating of grains as outlined in Guhathakurtha & Draine (1989), which can affect the dust continuum shape.

Primary and secondary cosmic ray ionization processes are treated as described in Appendix G. We include a rigid-rotor model for the v= 0 rotation levels of CO. This predicts line intensities for the lowest 30 rotational transitions.

Our calculations include all stages of ionization for the lightest 30 elements. We use a complete model of the hydrogen atom in calculating the H I emission-line spectrum and ionization rates (Ferguson & Ferland 1997), as well as a complete model of the helium isoelectronic sequence (Porter et al. 2005). Ionization processes include direct photoionization, charge transfer, the Auger effect, dielectronic, collisional, and cosmic ray ionization. In the H II region, the most important of these processes is photoionization, although charge transfer ionization can be important for some species, in particular oxygen (Kingdon and Ferland 1999).

We cover the range of observed H II regions, with n_{H^+} between 10^1 and 10^4 cm^{-3}, and U between 10^{-4} and 10^{-1}. Both n_{H^+} and U were incremented by 1 dex. All calculations stop at an A_V of 100 magnitudes, ensuring that they extend deep into the molecular cloud.

We use the non-LTE CoStar stellar atmospheres (Schaerer & de Koter, 1997) and vary the T_* from 34,000 to 46,000 K in steps of 4,000 K. This range of T_* covers

stars roughly ranging from spectral type O8 to O5 (Vacca et al. 1996), and spans the calculations performed by Giveon et al. (2002). Combining this range of T_* with the range of n_{H^+} and U, we have a total of 64 calculations.

Our calculations depend sensitively on the stellar continuum. Figure 4.1 shows continua emitted by single stars of temperatures 33,500 K, 35,000 K, 40,000 K, and 48,000 K, roughly corresponding to O8 to O5 stars. We assumed the temperature-luminosity relation given by Vacca et al. (1996). As T_* increases, the total luminosity of the star also increases. However, the Lyman continuum luminosity, which sets the scale of the H II region, increases far more rapidly than the luminosity of the Balmer continuum, which activates the PDR. This means that, for a fixed density, the size of the H II region relative to the PDR increases with increasing T_*. As we discuss in Section 5.3, this has important consequences to the interpretation of PDR emission-line diagnostics.

We use gas-phase abundances based on an average of the abundances in the Orion Nebula, with the complete set of abundances given in Baldwin et al. (1996). For the most important species, the abundances by number are He/H = 0.095, C/H= 3×10^{-4}; O/H= 4×10^{-4}, N/H= 7×10^{-5}, Ne/H= 6×10^{-5}, and Ar/H= 3×10^{-6}. We have assumed S/H= 2×10^{-6} based on observations of starburst galaxies by Verma et al. (2003). The complete set of assumed fractional abundances can be found in Ferland (2002).

We assume a galactic ratio of visual extinction to hydrogen column density, $A_V/N(\mathrm{H})$, of 5×10^{-22} mag cm^2. Grain size distributions for gas adjacent to H II regions, such as Orion (Cardelli et al. 1989) and starburst galaxies (Calzetti et al. 2000) tend to have a larger ratio of total to selective extinction than observed in the ISM. We therefore use a truncated MRN grain size distribution (Mathis et al. 1977) with R = 5.5, which reproduces the Orion extinction curve (Baldwin et al. 1991).

We also include size-resolved PAHs in our calculations, with the same size distribution that is used by Bakes & Tielens (1994). The abundance of carbon atoms in PAHs that we use, $n_C(PAH)/n_H$, is 3×10^{-6}. PAHs are thought to exist mainly in regions where hydrogen is atomic (Giard et al. 1994). We therefore scale the PAH abundance by the ratio of H^0/H_{tot} ($n_C(PAH)/n_H = 3\times10^{-6}\times [n(H^0)/n(H_{tot})]$).

We link the H II region and PDR by assuming constant total pressure. This equation of state includes radiation pressure, both from the stellar continuum and internally generated light, gas pressure, and turbulent, ram, and magnetic pressures when appropriate (Baldwin et al. 1991; Henney et al. 2005). Constant pressure is a first approximation to the actual flow (see Henney et al. 2005) and was assumed by previous authors (Carral et al. 1994).

We will distinguish between the H II region and PDR contributions to an emission line in the following. We define the start of the PDR as the position where $n(H^+)/n(H_{tot})$ falls below 1% (Shields & Kennicutt 1995). Tests show that the relative contributions are not sensitive to smaller values of this threshold, while larger values will diminish the H II region contribution.

4.5 A single cloud

In order to calculate the physical conditions in the ionized, atomic, and molecular gas, we must include all relevant physical processes in each regime. In this section we describe the chemical and thermal structure of a typical cloud. We also describe important physical processes and their treatment. We show in Figures 2-15 the results of our calculations for T_* = 38,000 K, $U = 10^{-2}$, and n_{H^+} of 3,000 cm^{-3}. Other parameters are the same as those given in Section 3.

4.5.1 Incident and Transmitted Continuum

Figure 4.2 shows the incident and transmitted continuum at three different points in our calculation. These points are where the ionized hydrogen fraction

falls to less than 1%, the point where the H_2 fraction reaches 50%, and the shielded face of the cloud.

This plot shows the importance of including emission from the H II region in calculating the conditions in the PDR. The transmitted continuum at an ionization fraction of 1% is the radiation field that is incident upon the PDR, given our definitions of these regions. Photoelectric and dust absorption in the H II region removes the Lyman continuum photons. Additionally, dust re-emits absorbed starlight at infrared wavelengths. This causes a rise in the transmitted continuum for $\lambda > 1$ μm. Deeper in the cloud, molecular dissociation, grain absorption, and photoionization of species with ionization potentials less than 13.6 eV absorb the Balmer continuum. This continuum will depend strongly on the properties of the H II region, and this forms a further link between two regions. All radiation with wavelengths $\lambda < 1$ μm is absorbed at the shielded face of the cloud. This leaves only cosmic rays and the infrared spectrum to heat the gas.

Figures 4.3-4.7 show the ionization structure for H, O, C, Ne, and Si across this cloud. We use A_V as our depth parameter, which is customary for PDR calculations (Tielens & Hollenbach 1985) but not for H II regions. For Figure 4.3, we show the density of H^+, H^0, and H_2 vs A_V, while Figures 4.4 – 4.7 show the ionization fraction, defined as $n(X^{i+})/n(X_{tot})$ vs A_V. Figure 4.3 shows how, under the assumption of constant pressure, n_H increases as T decreases. For reference, the depth into the H II region is given by $R\text{-}R_0 = 6.32\times10^{17} \times A_V$ (cm).

4.5.2 H II Region

The radiation field of the ionizing source produces an H II region at the illuminated face. Most of the heavy elements are doubly ionized due to the high U ($10^{-1.5}$) and T_* (38,000 K). Higher-energy photons are absorbed as we approach the H ionization front. Species with ionization potentials greater than hydrogen become atomic, while species with ionization potentials less than hydrogen

remain either singly (ex. C, Si, S) or doubly (ex. Ca or Sc) ionized beyond the ionization front.

The ionization front occurs at an A_V of ~1. Classical Strömgren sphere theory (Osterbrock and Ferland 2005), predicts that the ionization front should occur at an A_V of 1.5 for this ionization parameter and dust-to-gas ratio. The size of the H II region is smaller due to absorption of a portion the Lyman continuum by dust (Bottorff et al. 1998). Dust also strongly absorbs the Lα line. Rees, Netzer, & Ferland (1989) and Ferland et al. (1998) discuss the solution of the multi-level hydrogen atom and transport of resonance line radiation.

The temperature (Figures 8 and 9) is determined by energy conservation. Figures 10-12 gives the total heating & cooling rates, and identifies important heating and cooling processes. Since energy is conserved, total heating = total cooling. We therefore only show a single rate in Figure 10. The H II region temperature is ~10^4 K and the dominant heating / cooling processes are photoionization of hydrogen balanced by fine-structure excitation of optical and infrared lines of [O II], [O III], and [N II] . The single most important coolant is the [O III] 5007Å line.

4.5.3 PDR

The transmitted radiation from the H II region (Figure 4.2) determines the conditions in the PDR. Hydrogen makes the transition from atomic to molecular and other molecules form, as shown in Figure 4.3.

Grain physics dominates conditions in the PDR. Grain photoelectric heating is the dominant heating mechanism (Figure 4.11), although photoionization of carbon is significant. PAHs have a large abundance in the atomic hydrogen region, and these small grains contribute significantly to the total heating (Bakes & Tielens 1994), although graphite and silicate grains are also significant. As Figure shows, the dust temperature depends on grain type and size (van Hoof et al. 2004). Dust also extinguishes the radiation field across the PDR.

Figure 4.13 shows the cumulative emission in each line integrated from the illuminated face to any depth in the cloud, for [O I] 63 μm, [O I] 146 μm, [C II] 158 μm, and [Si II] 35 μm. These lines are predominantly excited by collisions with H^0. Almost all emission in these four lines comes from the PDR, with a negligible contribution from the H II region. Figure 4.14 shows that these lines are also the dominant coolants in the PDR. In dense PDRs, these lines can heat the gas when radiative excitation followed by collisional de-excitation becomes important (see Figure 4.12; also Tielens & Hollenbach 1985).

Line and dust heating is sensitive to the continuum transmitted through the H II region. Dust absorbs the UV continuum and re-emits it in the infrared (Figure 4.2). This H II region continuum enters the PDR and some is absorbed by lines and dust, eventually heating the gas. The dust continuum emitted by the H II region must be self-consistently treated if we are to correctly treat line and dust heating, and other processes that depend on the IR continuum. Our calculations self-consistently treat these physical processes, since we calculate the dust continuum produced by the H II region and its effects on the PDR.

The dust temperatures influence molecular formation, since they are important in determining the molecular reaction rates, in particular the H_2 formation rate on grain surfaces (we use Cazaux & Tielens 2002). In addition, the FUV radiation field (11.2 eV ≤ hν ≤ 13.6 eV) destroys H_2 by the Solomon process. Our calculations can include a detailed microphysical treatment of H_2 to treat the Solomon process (Shaw et al. 2005), although for this calculation we treat the H_2 assuming the equivalent three-level molecule (Tielens & Hollenbach 1985) and treat dissociation using the self-shielding function of Draine & Bertoldi (1996). H_2 forms quickly once all photons greater than 11.2 eV are extinguished. This occurs at about an A_V of ~4.5.

Other molecules form once H_2 forms (Figure 4.14), since it acts as a catalyst for the formation of other molecules through a series of ion-molecule reactions

(Prasad & Huntress 1980). A complete description of the molecules considered in our reaction network is given in Appendix E. The second-most abundant molecule that forms after H_2 is CO. Shortly after H_2 forms, carbon makes the transformation from C^+ to CO (with a small amount of C) at an A_V of ~8. Figure 4.13 also shows the integrated emission in the lowest three rotational transitions for CO.

4.5.4 Molecular Cloud

The gas is predominantly molecular deep in the cloud. CO forms at the point where its electronic bands are well shielded and other molecules form in deeper regions. The most important are N_2, O_2, H_2O, OH, SO, and CN. All molecules reach their asymptotic abundances by an A_V of ~30.

CO collisional excitation is the primary coolant in the molecular gas (Figure 4.12). Both ^{12}CO and ^{13}CO are included in our calculation, and both contribute to the total cooling.

The gas is heated primarily by grain collisions. Figure 4.15a-b shows the grain opacity and the transmitted continuum in the 1-100 μm range at an A_V of 20. The integral of these two quantities is proportional to the local heating of each grain species. In the 10-40 μm range, the silicate opacity is considerably higher than the graphite opacity. Absorption of the infrared continuum by silicate grains causes the silicates to be hotter than other gas constituents. In the molecular region the gas and graphite grains have $T \approx 45$ K while the silicates are typically 5 K hotter. Collisional energy exchange between these cooler constituents and the warmer silicates then heats the gas. In addition to grain collisions, line de-excitation and cosmic ray ionization makes a small contribution to the total heating.

4.6 Results and Discussion

4.6.1 Density

Here we present the results of our grid of calculations, spanning a wide range of U, T_*, and n_{H^+}. Here n_{H^+} is just the ionized hydrogen density at the illuminated face, which for all calculations is also n_H at the illuminated face.

Our results are presented as a series of contour plots (Figures 4.16 – 4.33). The value of n_{H^+} at the illuminated face (and hence the initial value of n_H) is the x-axis on the contour plots. Figure 4.16 and 4.17 shows the total hydrogen density at two important depths. Figure 4.16 shows n_H at the point where the ionized hydrogen fraction falls to less than 1%. In general, n_H at this point has increased by a factor of ~5-20, corresponding to the decrease in temperature from ~10^4 K in the ionized region to 500-2,000 K at the start of the PDR. Figure 4.17 shows n_H at a deeper point, where the fraction of hydrogen in the form of H_2 exceeds 90%. Most PDR lines will have fully formed by this point, where T ~ 100 K and n_H has increased by about two orders of magnitude. Although not plotted, there is an additional increase in n_H in deeper regions as other molecules, such as CO, form and the gas becomes even colder.

Most PDR calculations assume a constant n_H, so no direct comparison is possible between the density in our calculations and the density used in PDR calculations. The densities shown in Figure 4.16 and 4.17 are close to the lower and upper limits to n_H that would be used in equivalent constant-density PDR calculations. For example, consider a case where T_* = 38,000 K, n_H = 100 cm^{-3} and U = 10^{-2}. This set of parameters yields an n_H at the face of the PDR of ~2×10^3 cm^{-3} and ~2×10^4 cm^{-3} when all hydrogen is in the form of H_2. The average density in the PDR falls somewhere in between.

4.6.2 H II Emission Line Diagnostics

In this section, we discuss our results for infrared emission lines that are produced in the ionized gas. Figure 4.18 to 4.21 show our ratios involving different stages of ionization of the same element. We will use $R(\mathrm{X})^{numer}_{denom}$ as shorthand notation for all line ratios. Here X refers to the element, and *numer*/*denom* refers to the wavelengths of the upper and lower ionization stages. The four line ratios we calculate are $R(\mathrm{Ne})^{15.5\,\mu m}_{12.8\,\mu m}$, $R(\mathrm{S})^{18.7\,\mu m}_{10.5\,\mu m}$, $R(\mathrm{N})^{57\,\mu m}_{122\,\mu m}$, and $R(\mathrm{N})^{57\,\mu m}_{205\,\mu m}$. Observations of these emission-line ratios can determine T_* and U. These two parameters in turn yield information on the total flux of ionizing photons, the number of stars required to produce the observed level of ionization, and the age of the starburst.

Each figure shows several general trends. Each ratio is sensitive to both U and T_*. As T_* increases, the incident continuum produces more high-energy photons, leading to greater production of Ne^{2+}, N^{2+}, and S^{3+}, which leads to stronger emission from these species. The results are very similar for a T_* of 42,000 K and 46,000 K. In the case of the nitrogen lines, the critical density of the [N III] 57 μm line is ~2.7×10^2 cm^{-3}, so collisional de-excitation effects become important for larger densities. This is not the case for the neon and sulphur lines, whose critical densities exceed 10^4 cm^{-3}. Figure 4.18 and 4.19 show that, for the range of n_{H^+} considered here, the Ne and S ratios depend only on T_* and U.

Ratios of lines emitted by the same ion are sensitive to density rather then T_* or U. Figure 4.22 shows three such density diagnostics, $R(\mathrm{S})^{18.7\,\mu m}_{33.5\,\mu m}$, $R(\mathrm{O})^{52\,\mu m}_{88\,\mu m}$, and $R(\mathrm{N})^{122\,\mu m}_{205\,\mu m}$, for T_* = 38,000 K. The contours are nearly vertical, confirming their utility as density diagnostics. Note that n_{H^+} is, to within 10%, n_e in the H II region.

4.6.3 PDR Emission Line Diagnostics

Calculated intensities (in units of erg cm^{-2} s^{-1}) of common PDR diagnostic emission lines are shown in Figure 4.23 – 4.26. Shown are the predicted intensities of the [O I] 63 μm, [O I] 146 μm, [C II] 158 μm, and [Si II] 35 μm lines. Observations of these lines can be combined with theoretical calculations to determine n_H and G_0 (Wolfire et al. 1991; Kaufman et al. 1999). This in turn helps to determine the mass of the molecular and atomic gas, number and radii of clouds, chemical and thermal structure, and the volume-filling factor.

Figure 4.27shows the dependence of G_0 on U and n_H. G_0 scales linearly with both parameters because it is proportional to the flux. Additionally, G_0 does not depend strongly on T_*. Comparing Figures 4.23-4.26 with Figure 4.27 shows that the line intensities closely follow the UV flux, as expected. These figures give line intensities rather than line ratios, and are directly applicable for nearby resolved PDR regions. Line ratios must be used for observations of extragalactic sources, which are not spatially resolved. Figure 4.28 and 4.29 give the ratio of [O I] 63 μm to [O I] 146 μm, and the ratio of [O I] 63 μm to [C II] 158 μm. These include contributions from the ionized gas in addition to the PDR.

4.6.4 Ionized Gas Contributions to PDR Emission

We show in Figure 4.30 -4.33 the percentage contribution of emission from the ionized gas to the PDR diagnostic lines shown in Figure 4.23 – 4.26.

The ratio G_0/n_H and T_* are the two most important factors that determine the contribution from ionized gas to PDR lines. The emission lines shown in Figure 4.23 – 4.26 are generally excited by H^0 collisions in the PDR. The ratio G_0/n_H determines the size of the atomic region. For high values, H_2 is photodissociated to a larger depth and the size of the atomic hydrogen region is large, while H_2 forms quickly for small values. T_* is important because it determines the continuum shape, and hence the ratio of the flux of UV photons to the flux of hydrogen-ionizing photons. For regions with a large H II region but a small

atomic region, a larger fraction of the PDR line will form in the H II region. As a result, the predictions depend on the continuum shape.

By combining Figures 4.1, 4.27 with 4.30 – 4.33, we can understand the contribution from ionized gas to PDR emission lines. As T_* increases, more hydrogen ionizing flux is generated relative to G_0 (see Figure 4.1 and 4.27). This increases the amount of ionized gas relative to the atomic gas. The relative increase in ionized to atomic gas causes more of the total PDR diagnostic line emission to come from the H II region. We find that for $T_* > 42{,}000$ K, combined with $G_0 < 100$, at least 10% of the emission from all four PDR diagnostic lines considered emerges from the ionized gas. For the [O I] lines there is a good correlation between the relative sizes of the H II region and the atomic region and the contribution to the [O I] lines from the ionized gas. The ionization structure of O closely follows that of H since the two are strongly coupled by charge transfer, and their ionization potentials are nearly equal. The contribution of the ionized gas is greater for the 146 μm line. The 63 μm line is always stronger in the PDR due to its lower excitation potential while the lines have similar intensities in the H II region.

The [Si II] 35 μm and [C II] 158 μm emission from the ionized gas is significant over a wider range of U, n_{H^+}, and T_*. The ionization potentials of atomic carbon and silicon are less than 13.6 eV so the first ions are present in both regions. At least 10% of the 35 μm emission and 5% of the 158 μm emission comes from the ionized gas. We still see the general trend that higher T_* combined with a lower UV flux produces more total emission from the ionized gas.

We should note once again that our calculations all assume that the ionized, atomic, and molecular gas are in pressure equilibrium. The equation of state is dominated by gas pressure since turbulent and magnetic pressures are not included. If turbulent or magnetic pressure dominates then the density law will be different. We further assume a static geometry. Currently an effort is

underway to incorporate dynamics into our calculations. This will allow us to treat the dynamical interaction of H II regions with molecular clouds. As explained in Bertoldi & Draine (1996), when advection is included, the ionization and molecular dissociation front can merge. The predicted size of the ionized and atomic regions will change, making the ionized region larger compared to the atomic region. As our calculations above show, this will lead to a larger contribution of the ionized gas to PDR diagnostics. This is an important future area of study to interpret fully the emission line spectra of star-forming regions.

4.7 Applications to Observations

Our calculations have many applications to astrophysical environments. Most importantly, we have outlined a methodology where we self-consistently calculate the emission-line spectrum of the ionized, atomic, and molecular gas along with continuum emission from the dust.

Observations of lines from different ions of the same element determine T_* and U (Figures 4.18 – 4.21), while line ratios from the same ion can determine the gas density (Figure 4.22). For our assumed equation of state (constant pressure), T_*, U, and n_{H^+} also determine the conditions in the PDR**.** Consider an example. For T_* = 38,000 K, U = 0.01, and n_{H^+} = 100 cm^{-3}, we can use Figures 4.16, 4.17, and 4.27 to determine n_H and G_0 for the atomic and molecular gas. Of course, we can also invert this logic. If one makes observations of PDR emission lines, we can determine G_0 and n_H in the PDR. We can then use Figures 4.16, 4.17, and 4.27 to determine what values of U and n_{H^+} reproduce the observations.

We next apply our calculations to some of the early-published results of the Spitzer mission. Below are examples of extragalactic observations where we deduce some physical characteristic of the region of interest by comparing our calculations to the observed spectral features.

4.7.1 NGC 253

NGC 253 is a starburst galaxy with a wealth of infrared observations. Previous works by Carral et al. (1994), Verma et al. (2003), and Devost et al. (2004) have deduced abundances, T_* (34,500 ± 1,000) K, Q(H) ($10^{53.2}$ photons s^{-1}), G_0 (~2×10^4), n_e (430^{+290}_{-225} cm^{-3}) and a density of the atomic gas of 10^4 cm^{-3}. Additionally, Carral et al. (1994) find that the ionized and atomic regions are in gas pressure equilibrium.

Since NGC 253 is in gas pressure equilibrium, we can use our methodology to calculate the conditions in the ionized and atomic gas simultaneously. Comparing Figure 4.22 to the observed ratios $R(\mathrm{S})^{18.7\mu m}_{33.5\mu m}$ of 0.5 (Verma et al., 2003) and $R(\mathrm{O})^{52\mu m}_{88\mu m}$ of ~1-2 (Carral et al. 1994), we find n_{H^+} of ~100-200 cm^{-3}, significantly lower than the previous results. The observed ratio $R(\mathrm{Ne})^{15.5\mu m}_{12.8\mu m}$ of 0.14 – 0.2 (Devost et al. 2004), together with their T_* corresponds to U ~0.01.

Let us now consider the PDR diagnostic lines. We will adopt 0.01 for U, 34,000 K for T_*, and 150 cm^{-3} for n_{H^+}. Figure 4.28 shows that the predicted ratio of [O I] 63 μm to [C II] 158 μm (~1), for the derived U and n_{H^+}, is in excellent agreement with the observed ratio of 0.8-1.1 (Carral et al. 1994). Our calculations suggest that G_0 is ~5×10^3 (Figure 4.27), about four times lower than what Carral et al. (1994) deduce. Had we used n_e = 430 cm^{-3}, as deduced by Carral et al. (1994) rather than the density derived from the [S III] lines, we would have obtained their G_0. However, this would then overestimate the [O I] to [C II] line ratio by a factor of 3. Using Figure 4.16 and 4.17, we estimate an n_{H} in the PDR of 2,000 -20,000 cm^{-3}. The density derived by Carral et al. (1994) of 10^4 cm^{-3}, lies within the range of densities we derive.

We wish to highlight two important points regarding our analysis of NGC 253. First, T_* and two H II-region line ratios determine U and n_{H} in the ionized, atomic, and molecular gas. Calculations with these parameters

reproduce the observed [O I] 63 μm to [C II] 158 μm PDR line ratio. This supports the conclusion by Carral et al. (1994) that NGC 253 is in gas pressure equilibrium. Secondly, for our values of U and n_{H^+}, we find that ~30% of the [C II] 158 μm line and 20% of the [Si II] 35 μm line are produced in the ionized gas. Carral et al. (1994) found a similar estimate of the contribution of the H II region to the [C II] line. Had we ignored the H II region, we would have overestimated the [O I] 63 μm to [C II] 158 μm line ratio by a factor of ~1.4, resulting in a lower G_0 and n_H in the PDR. This would have led to large uncertainties in conditions derived with these two parameters.

4.7.2 NGC 7331

NGC 7331 is a nearby spiral galaxy observed by Spitzer as part of the SINGS survey (Smith et al. 2004). They observed $R(\mathrm{Ne})^{15.5\mu m}_{12.8\mu m}$ and $R(\mathrm{S})^{18.7\mu m}_{33.5\mu m}$, together with the lowest three rotational lines of the ground vibrational state of H_2. They derived densities in the ionized and atomic region of < 200 cm^{-3} and 5000 cm^{-3}, respectively. They found G_0 ~10^2-10^3 based on the H_2 lines and the dust continuum, and conclude that the region is in pressure equilibrium.

Following the same procedure as NGC 253 we compared our calculations with SST observations. According to Figure 4.22, the observed ratio $R(\mathrm{S})^{18.7\mu m}_{33.5\mu m}$ of 0.4-0.67 indicates n_{H^+} < 200 cm^{-3}, in agreement with Smith et al. (2004). We therefore adopt a value of 150 cm^{-3}, which gives $R(\mathrm{S})^{18.7\mu m}_{33.5\mu m}$ =0.55. Unfortunately, we do not have an estimate of T_*. The observed $R(\mathrm{Ne})^{15.5\mu m}_{12.8\mu m}$ of 0.64–0.75 implies, from Figure 4.18, that T_* > 34,000 K. This is because $T_* \leq$ 34,000 K requires that U > 10^{-1}, an unlikely result. Assuming Smith et al.'s (2004) G_0, Figure 4.27 combined with Figure 4.18 implies T_* < 38,000 K. We therefore assume T_* = 36,000 K ± 2,000 K. Assuming this value of T_*, we vary U to reproduce the observed $R(\mathrm{Ne})^{15.5\mu m}_{12.8\mu m}$. Our results were: Log[$U$] = -2.5; $R(\mathrm{Ne})^{15.5\mu m}_{12.8\mu m}$ = 0.68 (0.64–0.75); $R(\mathrm{S})^{18.7\mu m}_{33.5\mu m}$ = 0.55 (0.40-

0.67); $G_0 = 9\times10^2$, n_H (PDR) = 3×10^3 cm^{-3}, and n_H (H_2 fully forms) = 4×10^4 cm^{-3}. The values of U and T_* are new to this work, the other parameters are in agreement with Smith et al. (2004).

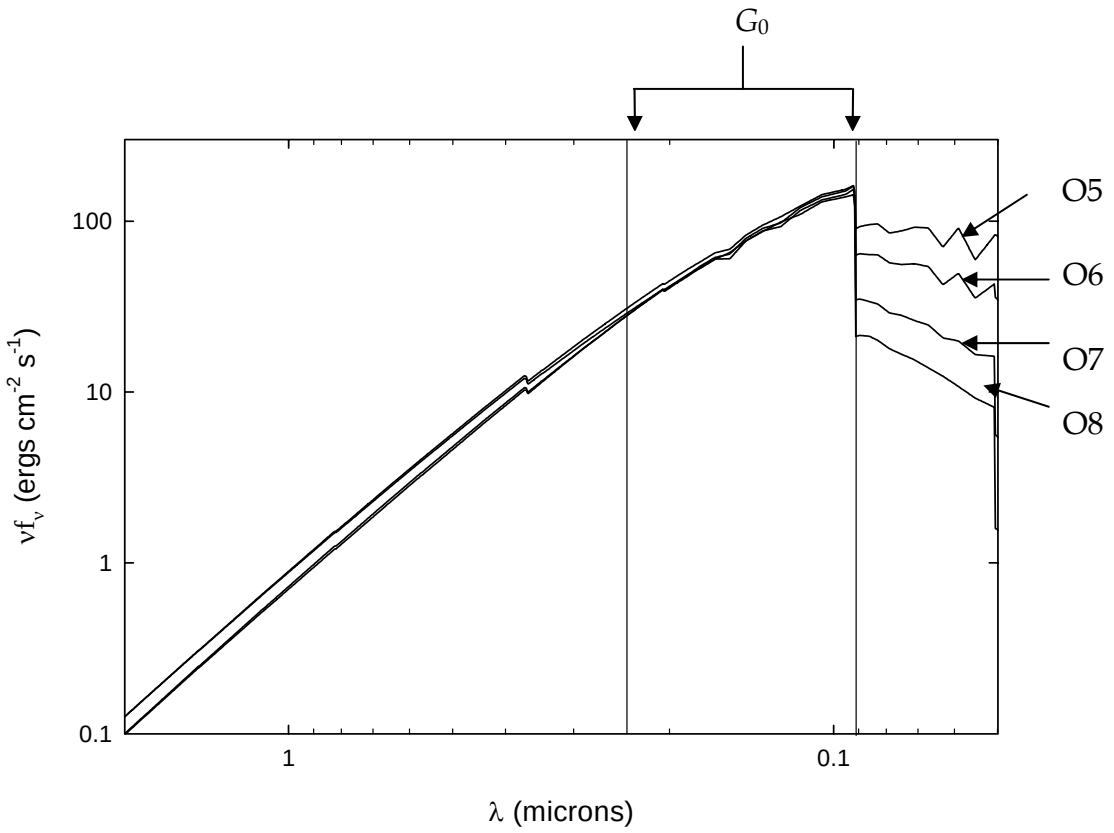

Figure 4.1 Dependence of the continuum shape on the stellar spectral classes considered in our calculations. The area between the vertical lines represents the continuum used to define G_0. The Lyman continuum depends strongly on spectral type, while G_0 is relatively constant. This causes the size of the H II Region relative to the PDR to vary, which affects the contribution of the H II region to PDR emission-line diagnostics.

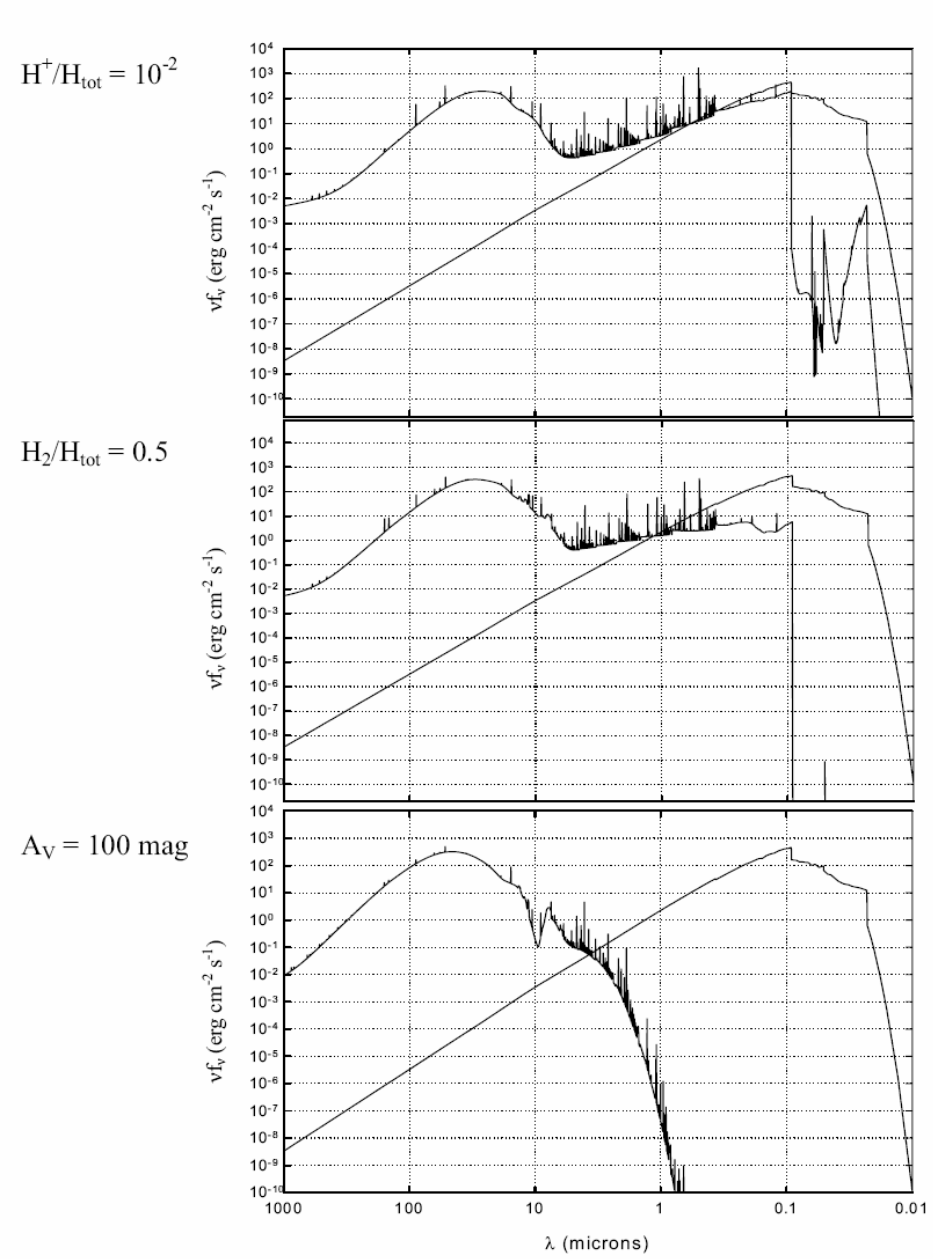

Figure 4.2 Continuum at three positions along a ray into a standard cloud. The incident and net local continuum is shown at three positions; the hydrogen ionization front, the point where half the hydrogen is H_2, and the shielded face. At the hydrogen ionization front the Lyman continuum is strongly absorbed by hydrogen and dust and reemitted in the infrared by dust. PAH emission is present at the half-H_2 point, along with graphite absorption at 2175Å. All radiation with $\lambda < 1\mu m$ is absorbed at the shielded face, the silicate feature is clearly seen in absorption, and a rich IR emission spectrum produced by atoms and molecules is observed.

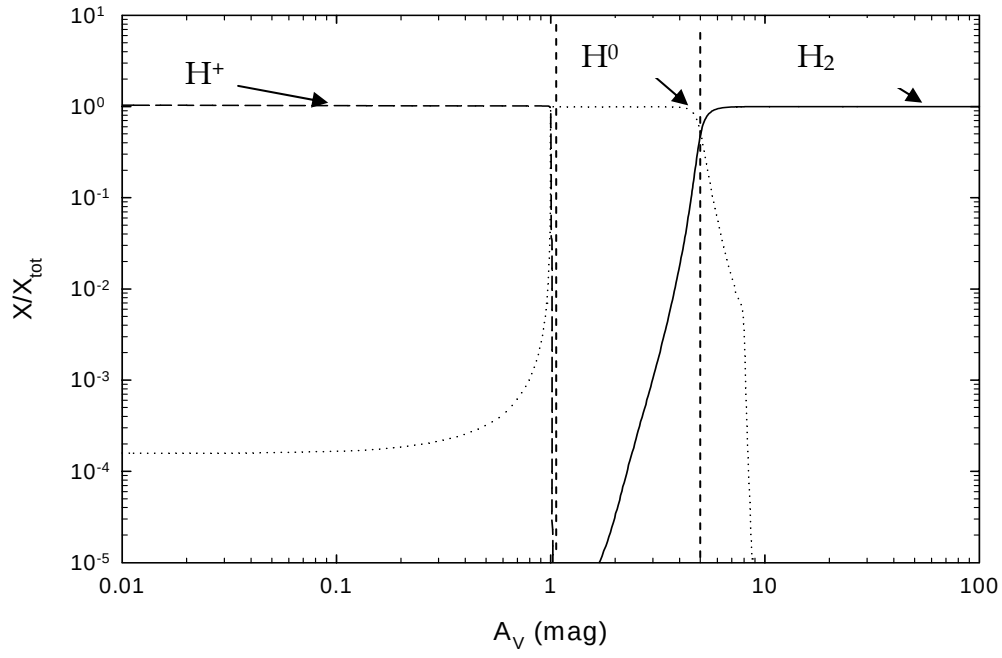

Figure 4.3 The H^+, H^0, and H_2 density structure of the standard cloud. This shows the classic transition from ionized to atomic and finally to molecular gas. From the illuminated face to the shielded face, n_H increases by ~10^3 due to the assumption of constant gas pressure. The two vertical lines represent the hydrogen ionization front and the half-H_2 point.

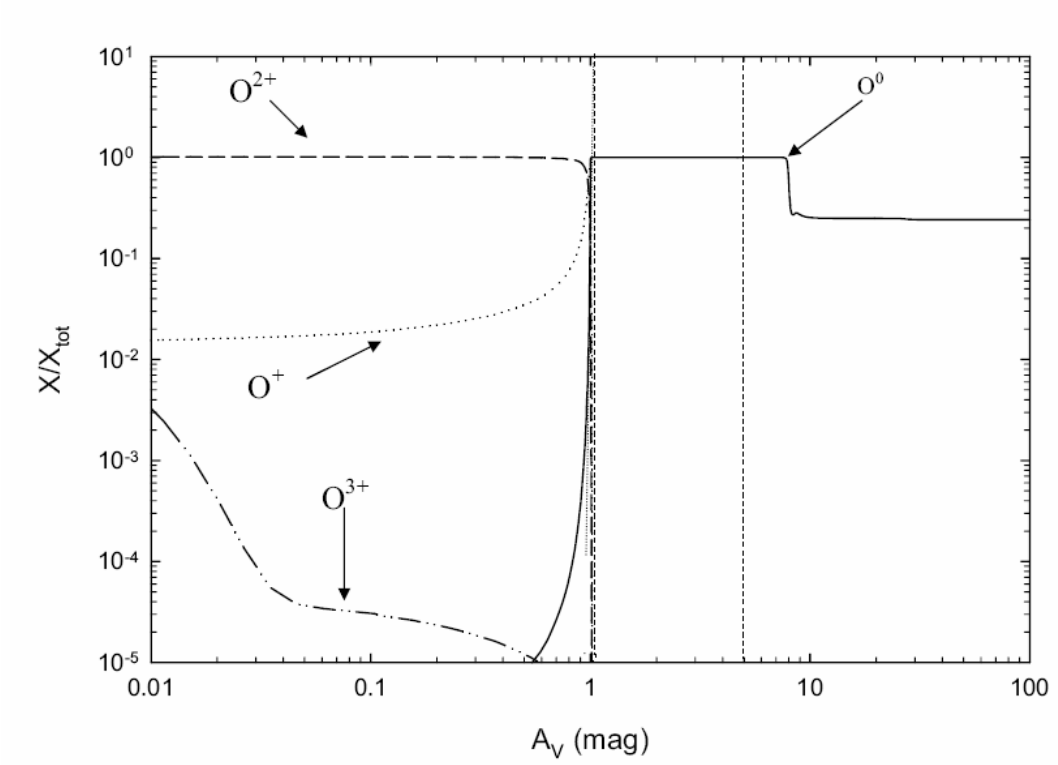

Figure 4.4 The oxygen ionization structure for our standard cloud. At the illuminated face, O is in the form of O^{2+} and O^+. At the hydrogen ionization front, most O is in the form of O^0 due to rapid charge exchanges with H^0. the relative abundance of O^0 decreases deep in the cloud due to the formation of CO.

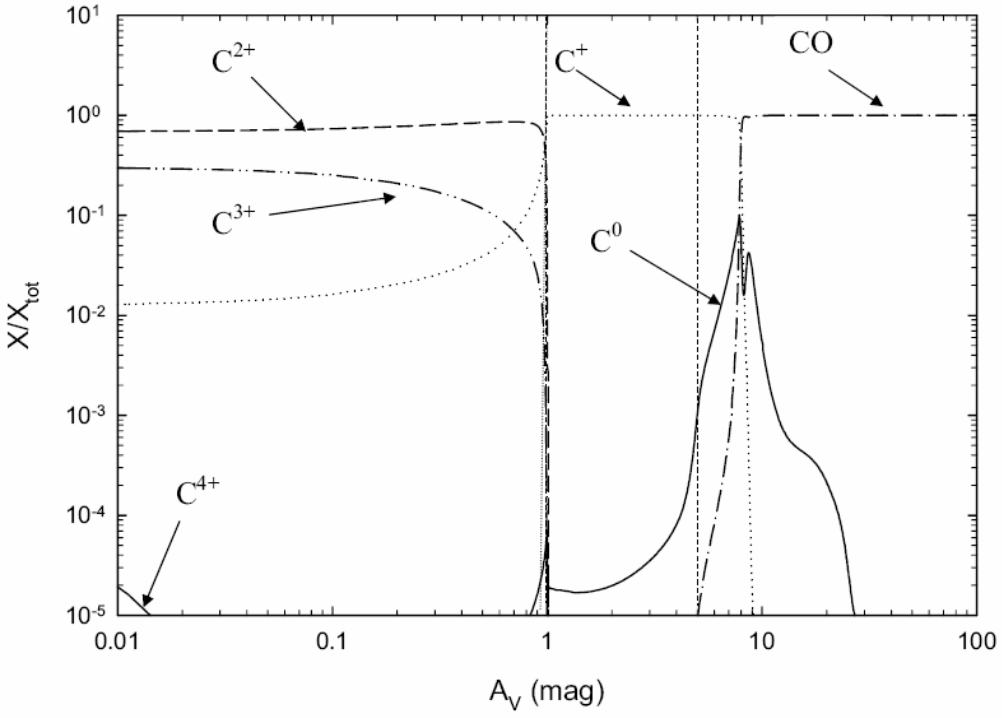

Figure 4.5 The carbon ionization structure for our standard cloud. At the illuminated face, C is predominately in the form of C^{2+} and C^{3+}, with some C^+. Near the hydrogen ionization front carbon becomes predominately C^+. Once H_2 forms, carbon makes the classic PDR transition from C^+ to C^0 and quickly over to CO.

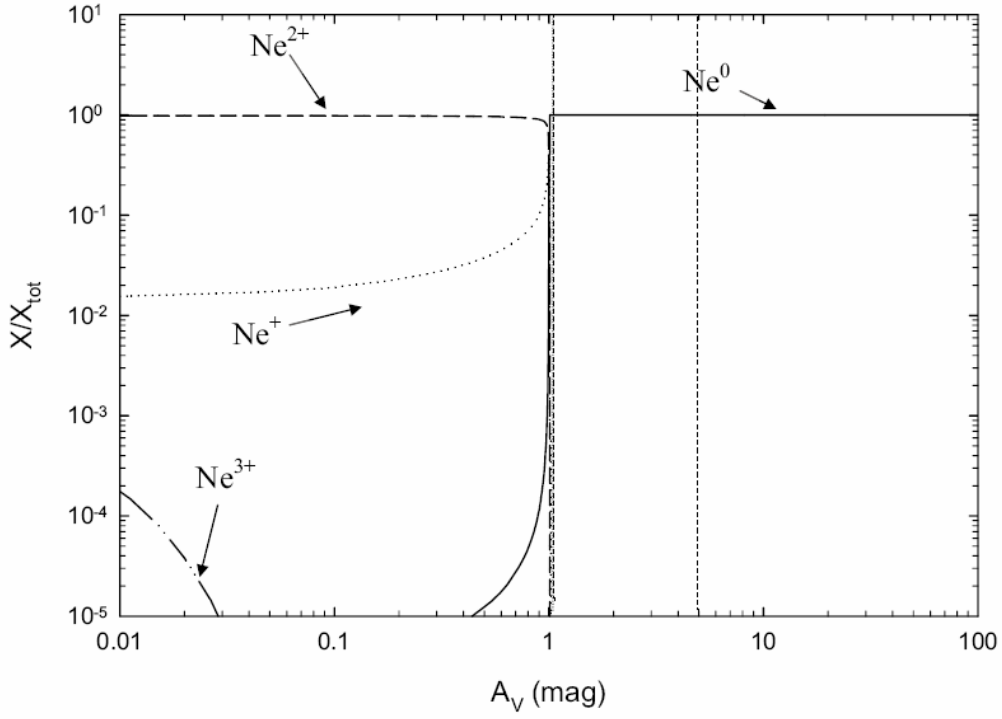

Figure 4.6 The neon ionization structure for our standard cloud. Neon is singly and doubly ionized in the H II region, while it becomes atomic at the hydrogen ionization front. Ne^0 has a closed shell, and therefore is not chemically active in the molecular cloud.

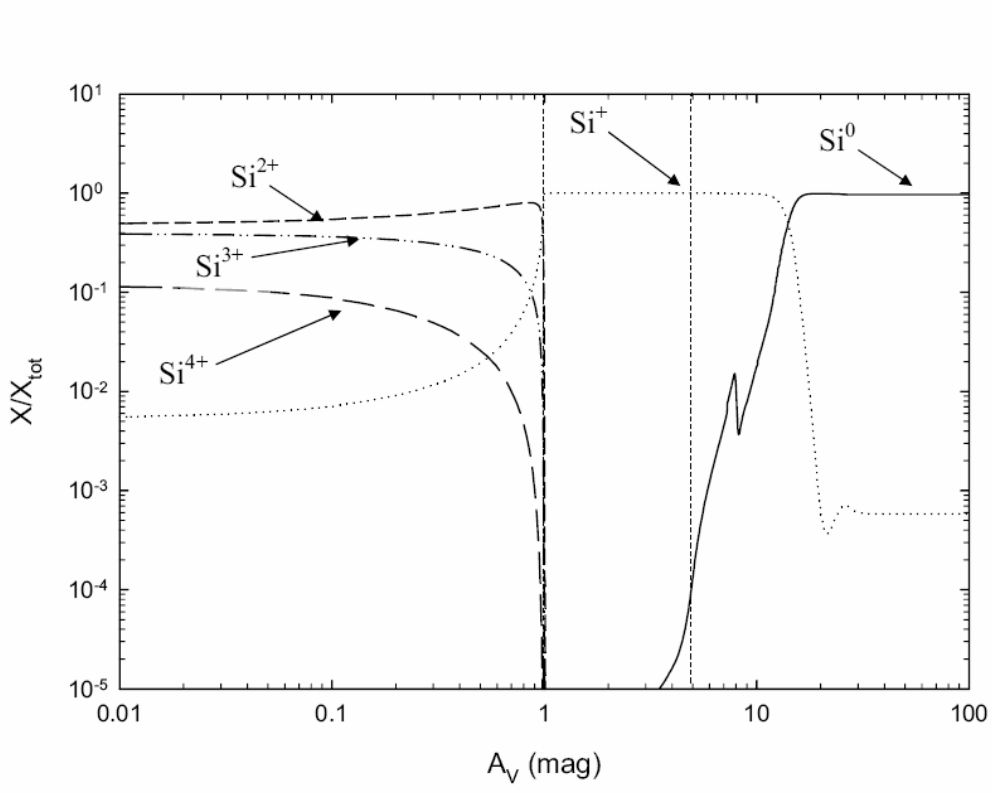

Figure 4.7 The silicon ionization structure for our standard cloud. Silicon is in the form Si^{2+}, Si^{3+}, and Si^{4+} in the H II region As the hydrogen ionization front is approached, Si^+ becomes the dominant stage of ionization. Si^+ remains the dominant ionization stage through the PDR, becoming neutral at an A_V of ~15.

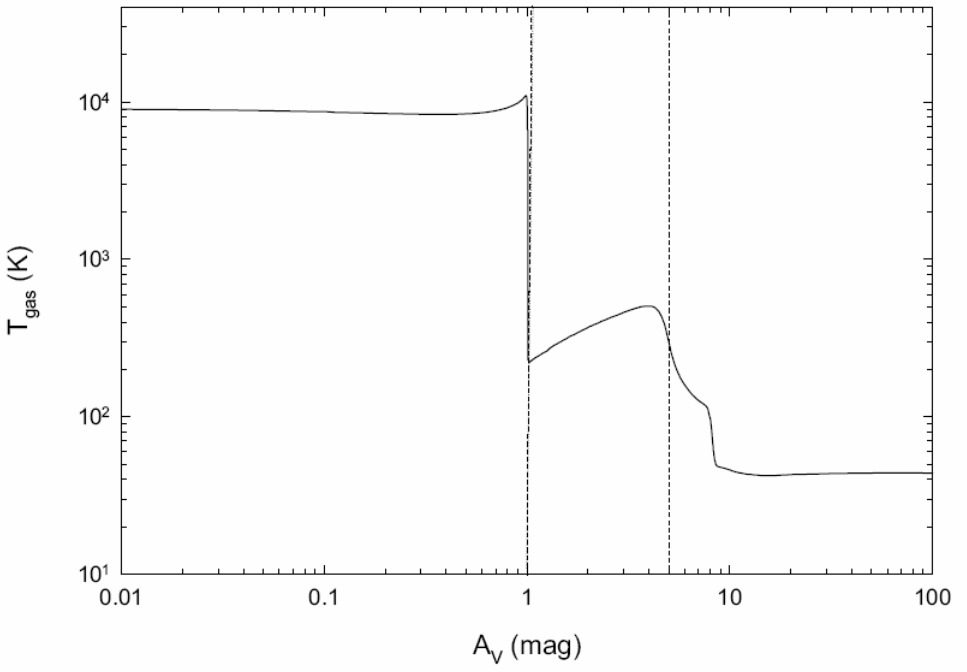

Figure 4.8 Gas temperature for our standard cloud. The temperature is ~10^4 K in the H II region. At the ionization front, H^0 photoionization no longer heats the gas, and the temperature falls to a few hundred Kelvin. The temperature continues to fall as the gas becomes more molecular, eventually reaching a temperature of ~40 K at the shielded face.

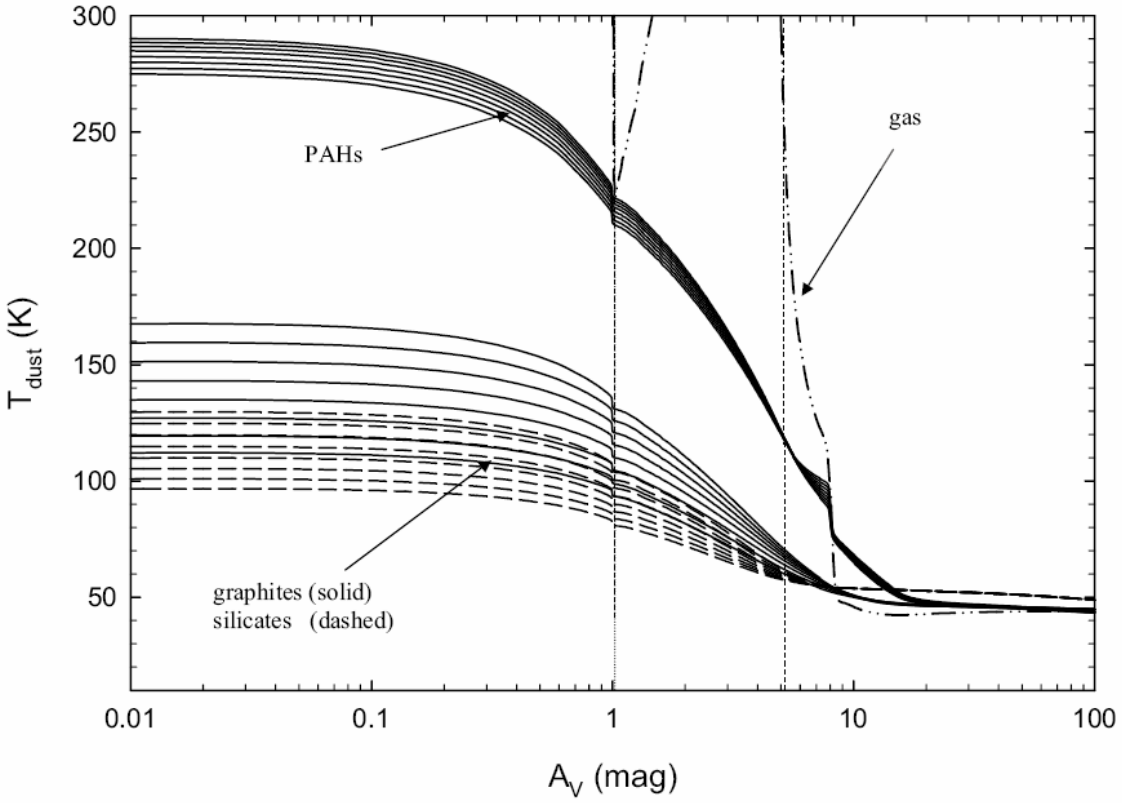

Figure 4.9 Dust temperature for all species and sizes considered in our standard cloud. PAH temperatures are shown. We assume that the PAH abundance is proportional to the atomic hydrogen fraction. PAHs are the hottest grain species in the H II region but their abundance is negligible. Additionally, graphite is somewhat hotter than the silicates in the H II region and PDR due to their optical properties. Deep in the cloud, the gas and dust temperatures equilibrate, with the silicate dust temperature ~5 K higher (see Figure).

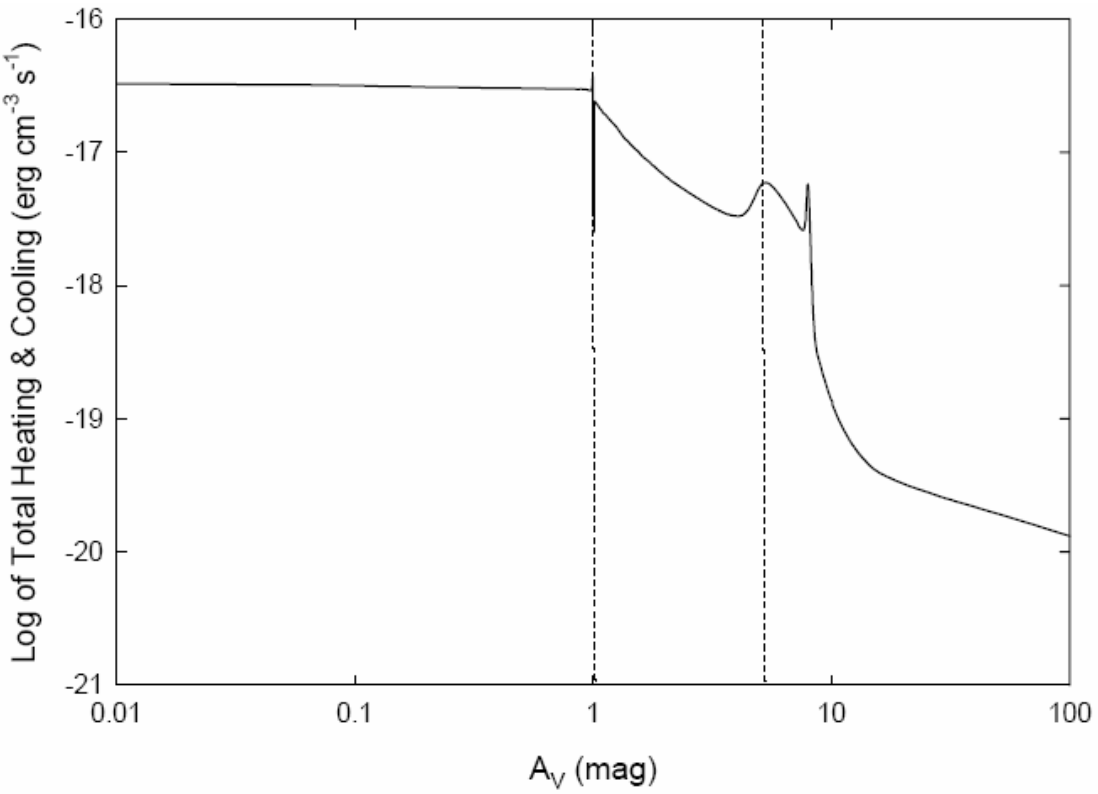

Figure 4.10 Total heating and cooling rate in our standard cloud. We assume energy balance so the two curves overlap. This plot can be compared with Figures 11 and 12 to determine the total heating or cooling rate for a given species.

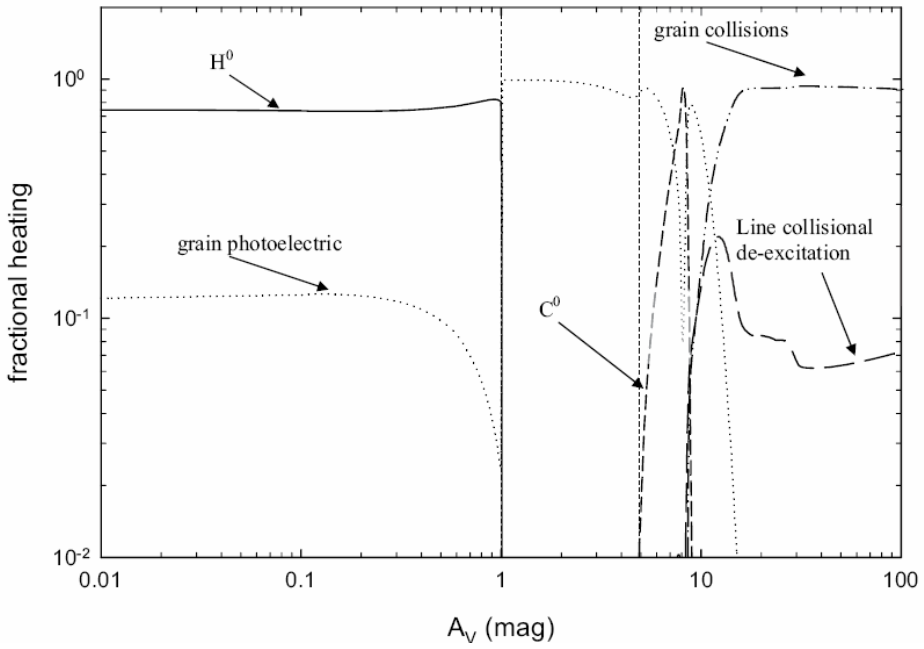

Figure 4.11 Important heating processes in our standard cloud. In the H II region, heating is dominated by photoionization of H^0. In the PDR, grain and carbon photoionization dominates. Eventually, carbon and dust photoionizing photons are extinguished. Deep in the cloud grain collisional heating (see Figure 15) and heating due to line collisional de-excitation are the primary heating agents.

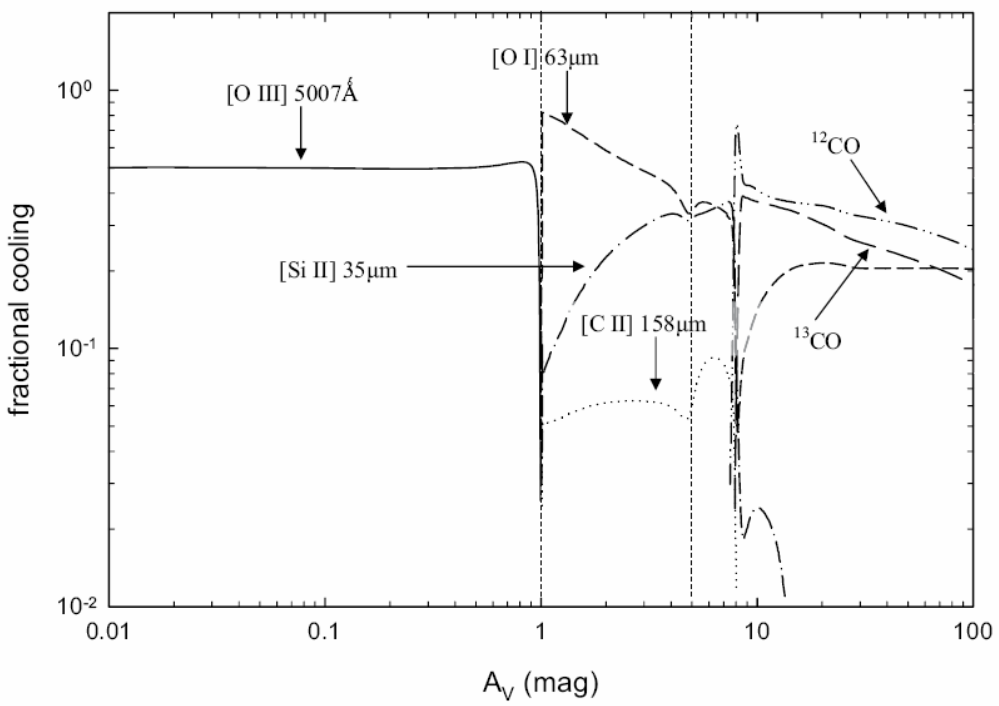

Figure 4.12 Important cooling processes in our standard cloud. Cooling is dominated by fine structure excitation followed by radiative de-excitation. The [Si II] 35 μm and [C II] 158 μm line peaks as hydrogen makes the transition from atomic to molecular. Deep in the calculation, CO is the primary coolant. Carbon monoxide cooling peaks in regions where carbon forms CO, and falls off deep in the cloud where all the CO is in the ground state.

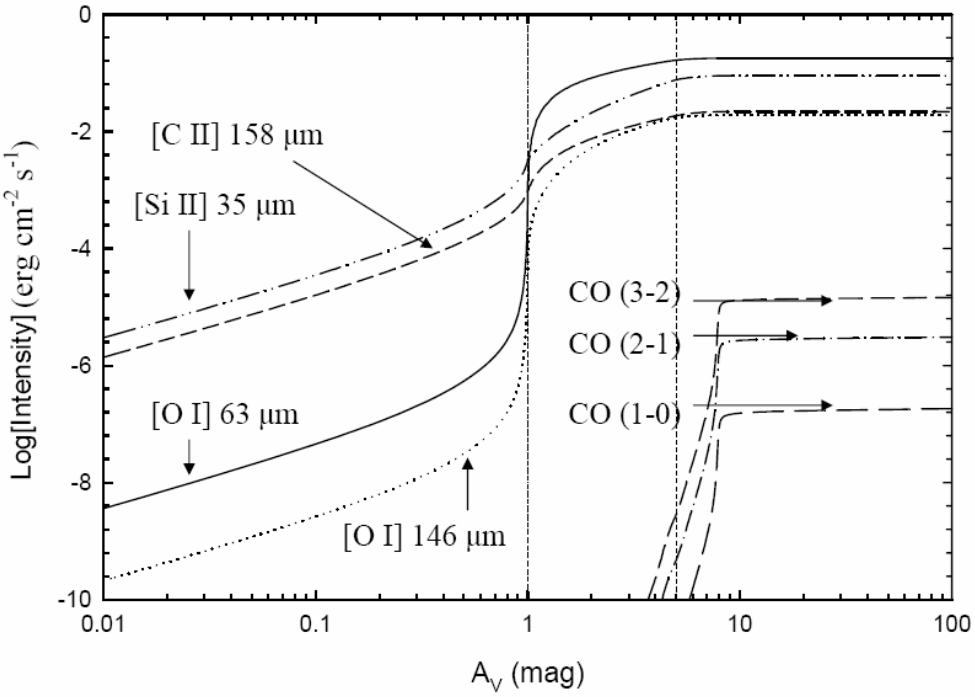

Figure 4.13 Integrated emission of PDR lines in our standard cloud. For our choice of n_H, U, and T^*, the assumption that low-ionization potential lines form in the PDR is valid. In the PDR. C^+, Si^+, and O^0 become the dominant stage of ionization, and collisions with H^0 excite their fine structure levels. CO emission from low J levels occurs at the C^+/C^0/CO transition. Due to the high column densities of the low CO rotational levels, these lines quickly become optically thick

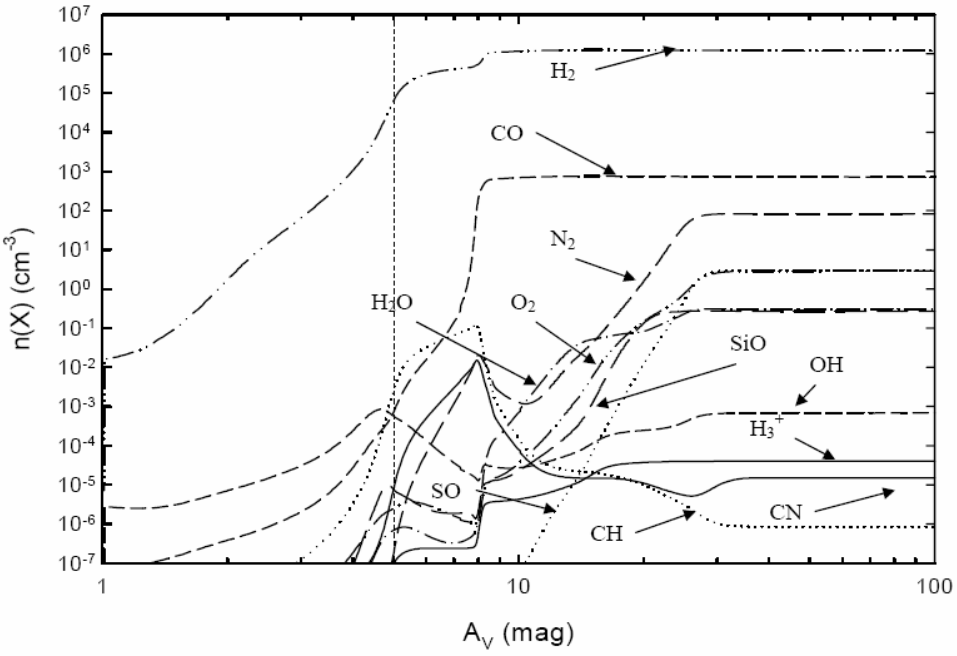

Figure 4.14 Molecular abundances in our standard cloud. The formation of H_2 acts as a catalyst for other molecules, especially CO. Once CO fully forms, other species start to form molecules. At the shielded face, all the hydrogen is tied up in H_2, all carbon is in CO, all nitrogen is in N_2, and a large amount of oxygen is in CO, O_2, and H_2O.

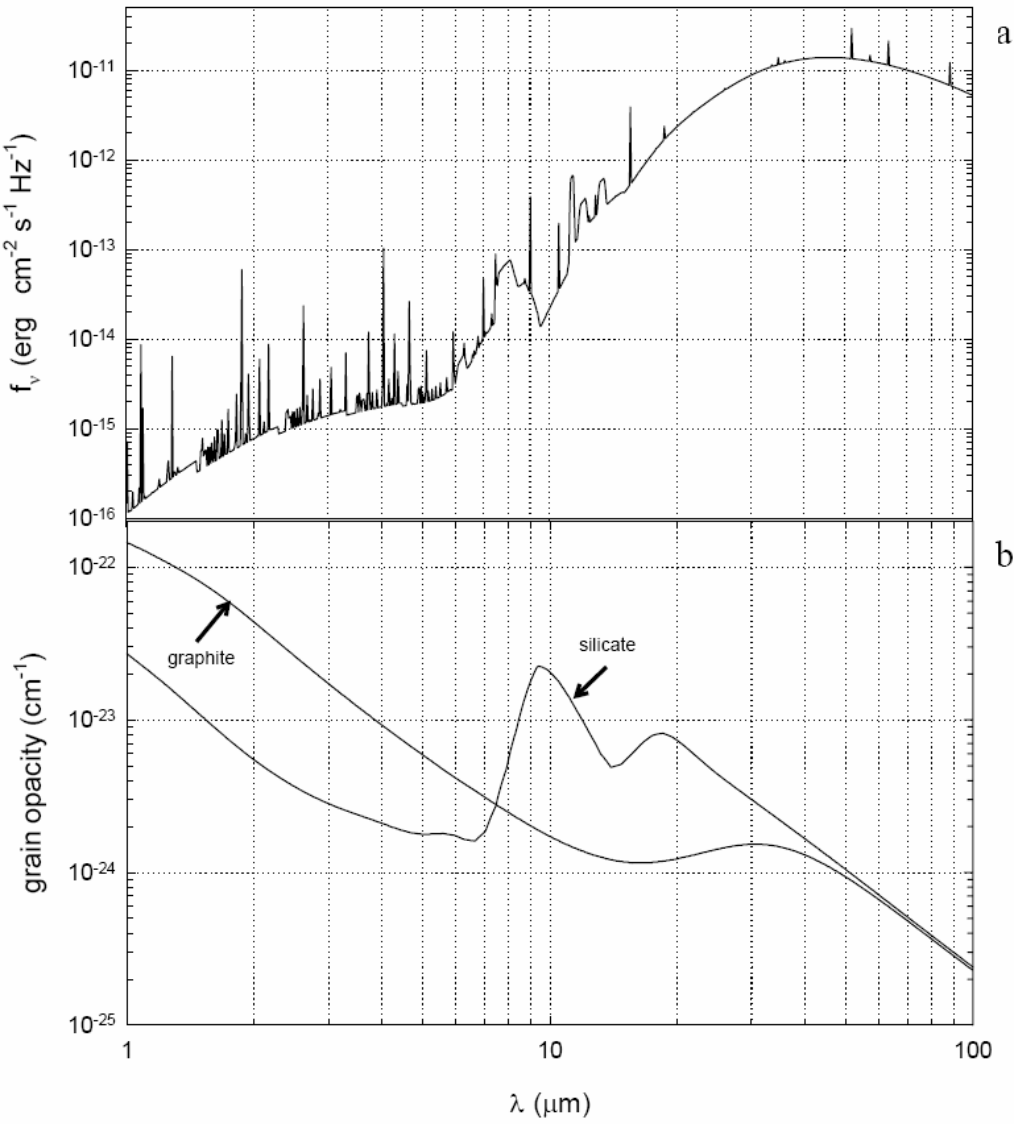

Figure 4.15 Local continuum and grain opacity at A_v =20 in our standard cloud. This plot shows why the silicate dust is hotter than the graphite deep in the molecular cloud. The product of flux and opacity (integrated over frequency) is the heating rate. The large silicate opacity in regions of high infrared flux keeps the silicate grains ~5 K hotter than the gas or graphite deep in our calculation.

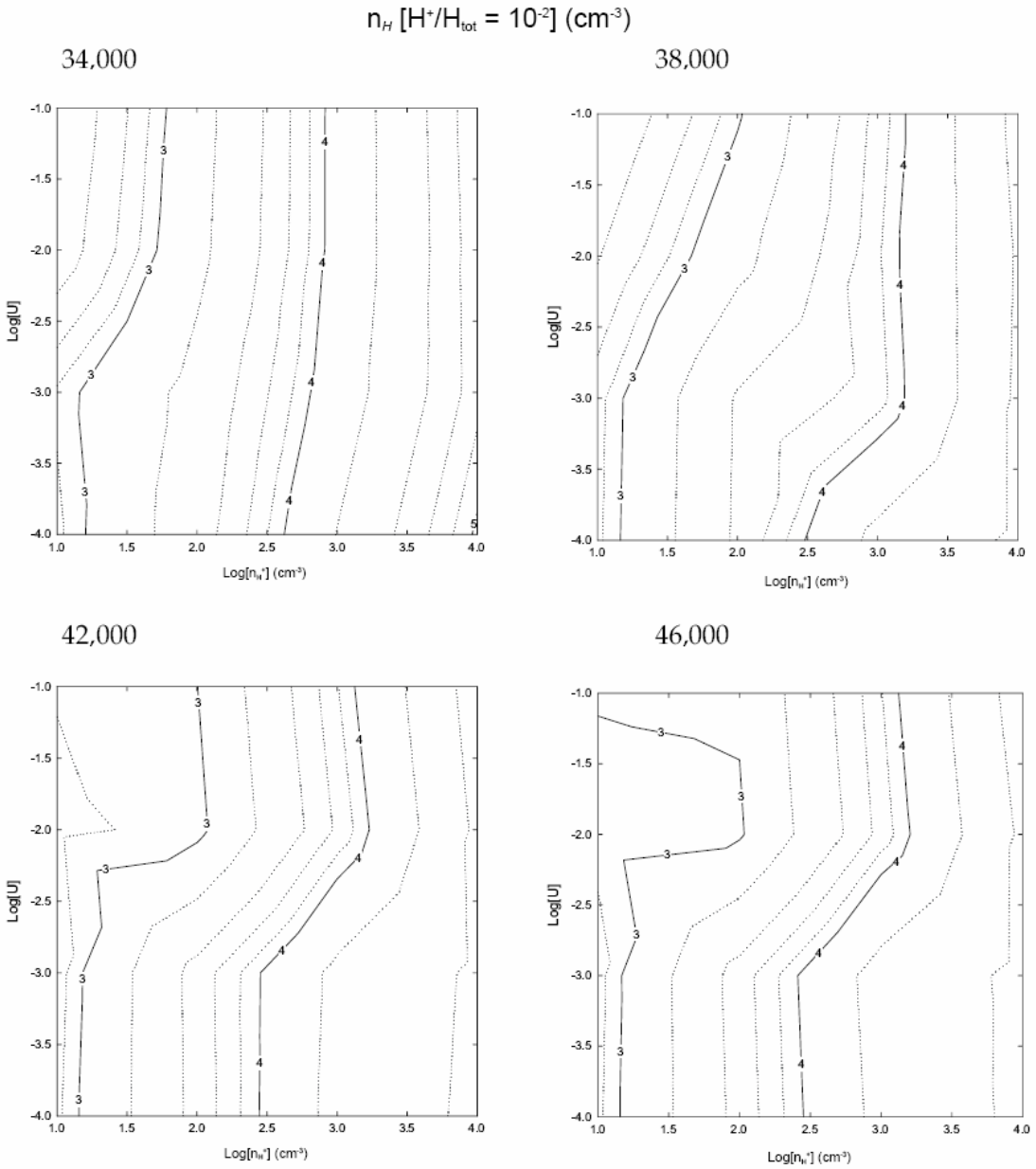

Figure 4.16 Log[n_{H}] at the point in our calculations where the H^+/H_{tot} ratio falls to 1%. This is the hydrogen density at the face of the PDR, for a given U and n_{H^+} ($n_{\mathrm{H}} = n_{H^+}$ at the illuminated face). For a given set of parameters the hydrogen density at the face of the PDR is roughly 1-2 orders of magnitude greater than at the H II region illuminated face. The temperature at the face of the PDR is typically 10^2-10^3 K

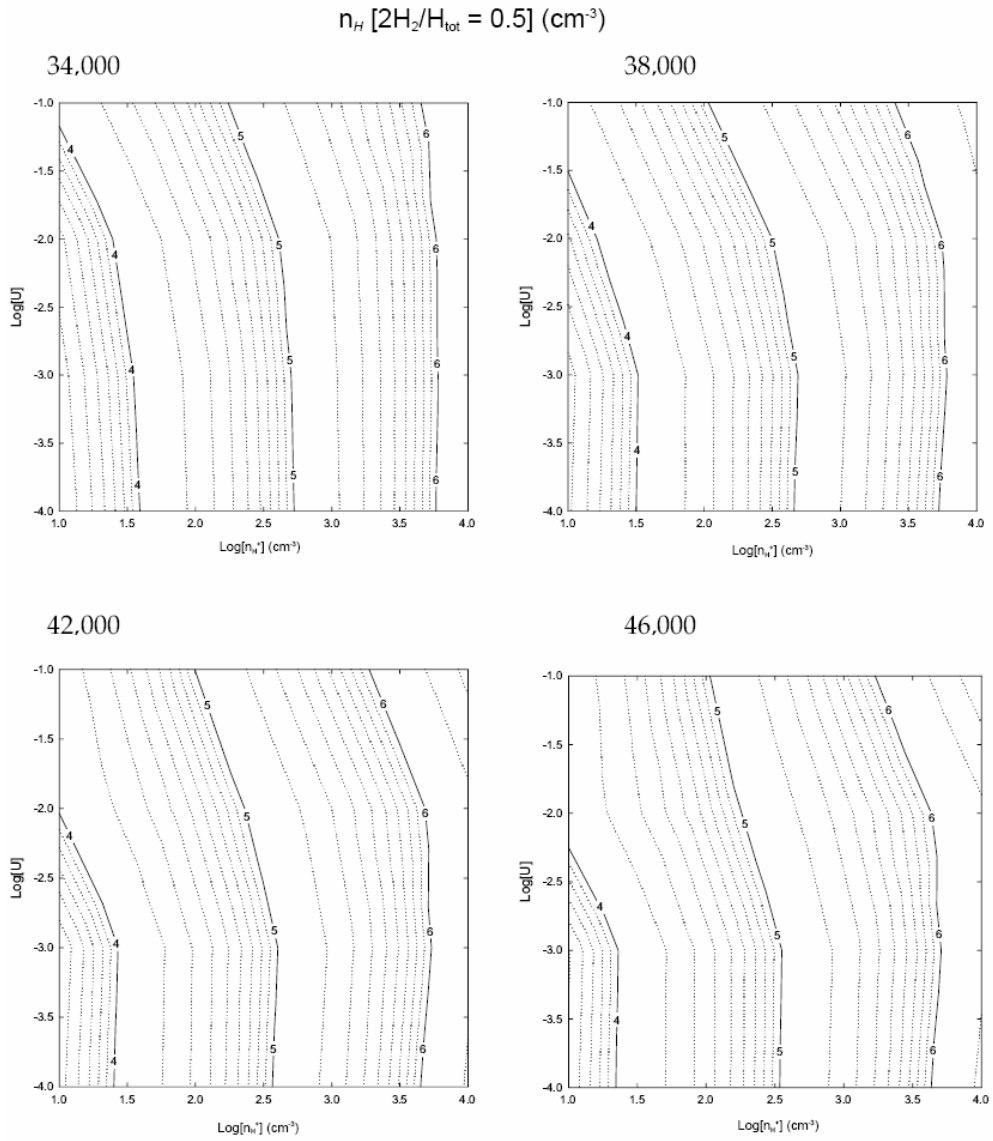

Figure 4.17 Log[n_{H}] at the point when $2H_2/H_{tot}$ reaches 0.9. Our constant-pressure calculations do not produce a single density in the PDR, but a typical PDR density would be an average of the density determined from this plot and Figure 4.16. The density at the $2H_2/H_{tot}$ = 0.9 point is ~2.5 orders of magnitude greater than the density at the illuminated face, and has a temperature of ~40 K.

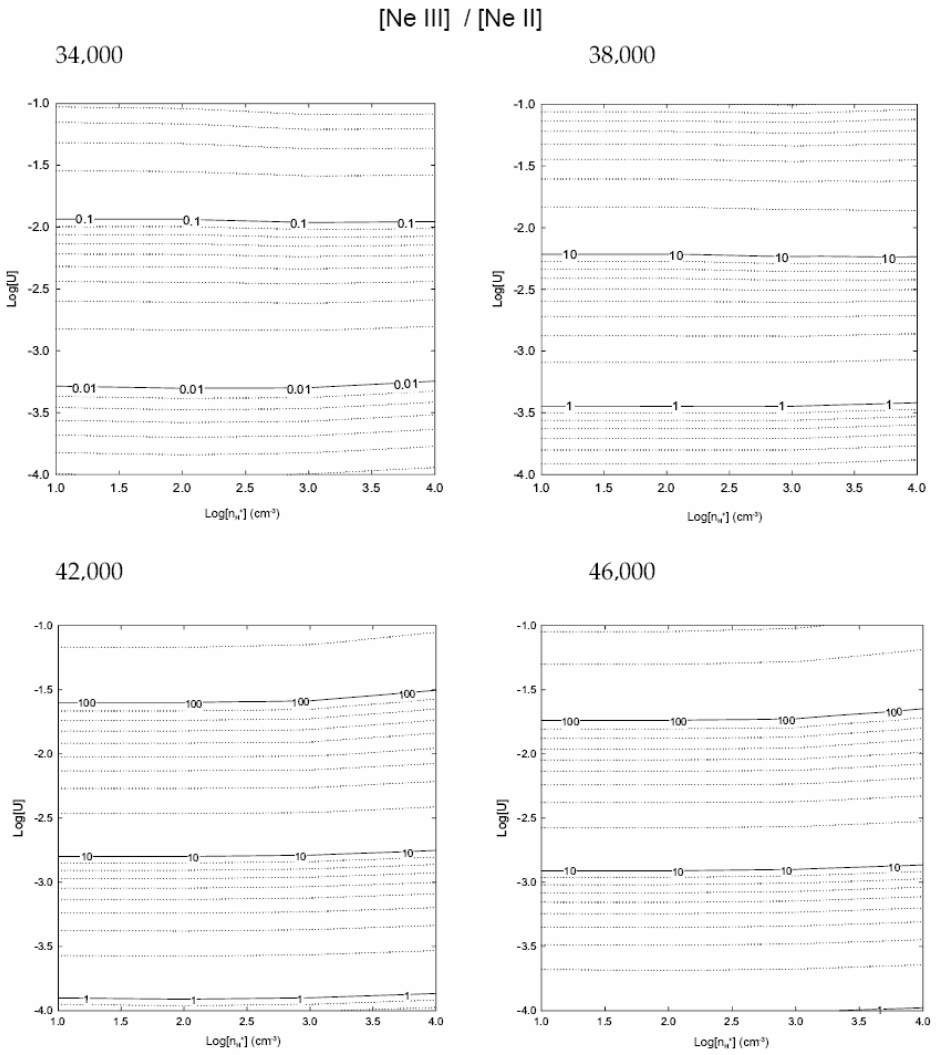

Figure 4.18 Ratio of [Ne II] 15.55 μm to [Ne III] 12.8μm intensity. Because of the large critical densities of these two lines (>10^5 cm^{-3}; Giveon et al 2002), this ratio is sensitive to T^* and U but not n_{H^+} for a range of H II region densities. Both T^* and U can be determined by combining this with Figures 4.19-4.21.

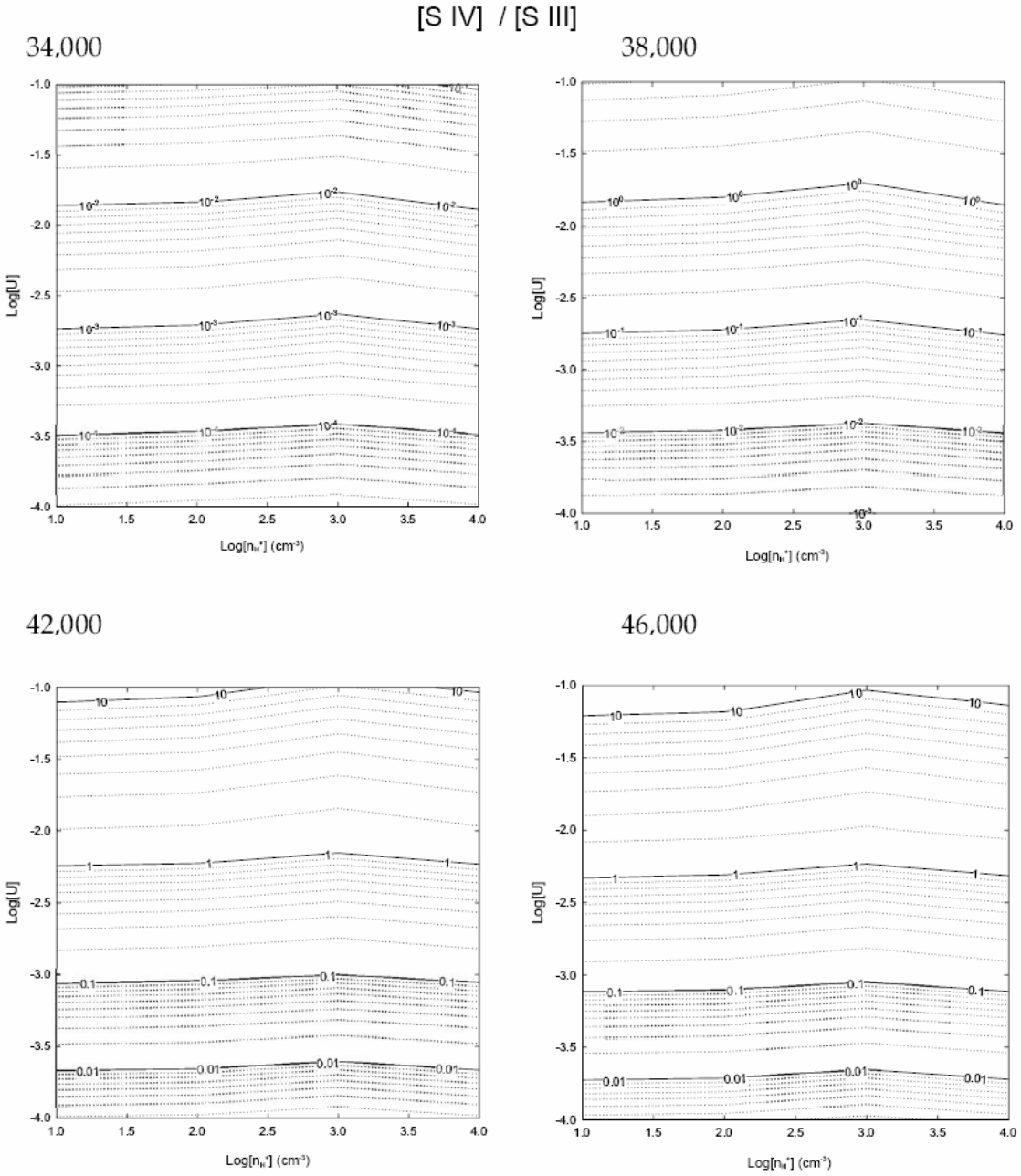

Figure 4.19 Ratio of [S IV] 10.5 μm to [S III] 18.7 μm intensity. The critical density of both of these transitions exceeds 10^4 cm^{-3} (Giveon et al. 2002), making the ratio of these lines insensitive to n_{H^+} in our calculations. The best way to determine T^* and U would be to combine calculations such as those in Figures 4.18 – 4.21 with observations (see Giveon et al. 2002, Morisset 2004).

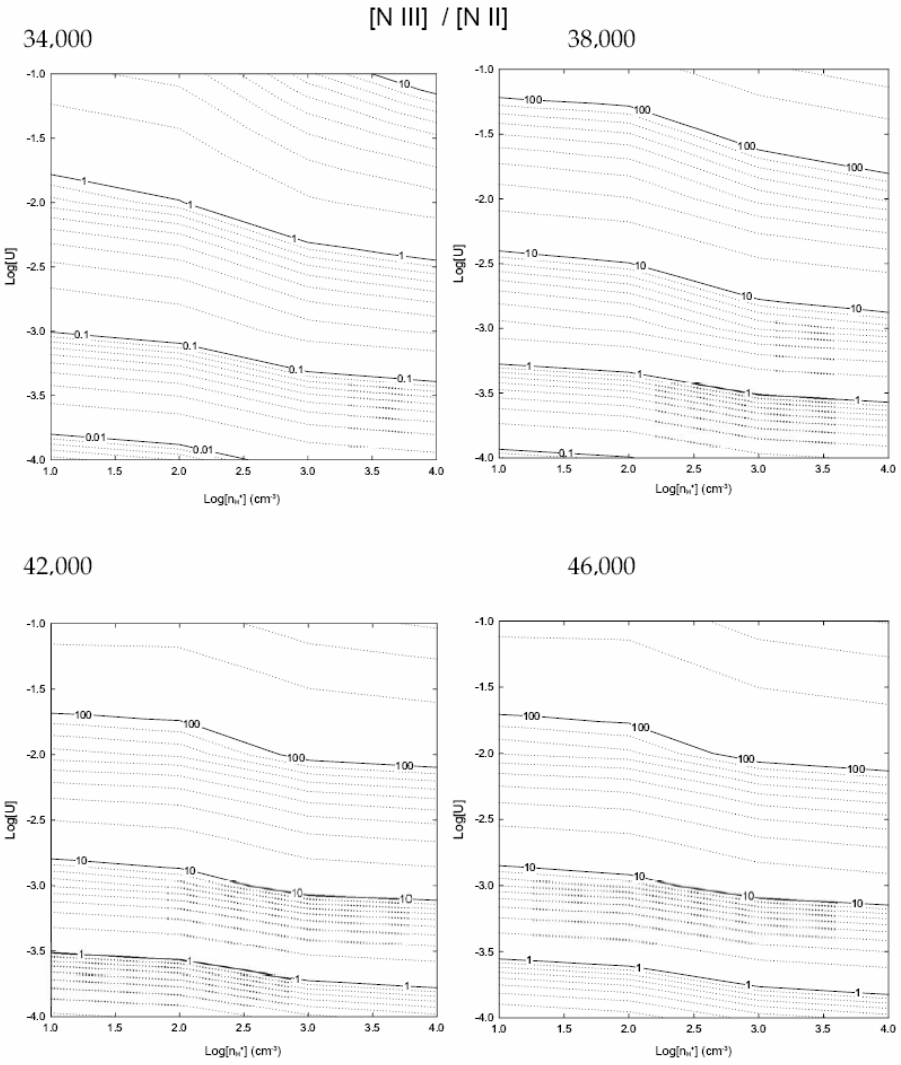

Figure 4.20 Ratio of [N III] 57 μm to [N II] 122 μm intensity. The critical densities for these transitions are less than 10^4 cm^{-3} (Malhorta et al. 2001). This means that, for the range of n_{H^+} considered in our calculations, this ratio can also depend on density in addition to T^* and U .

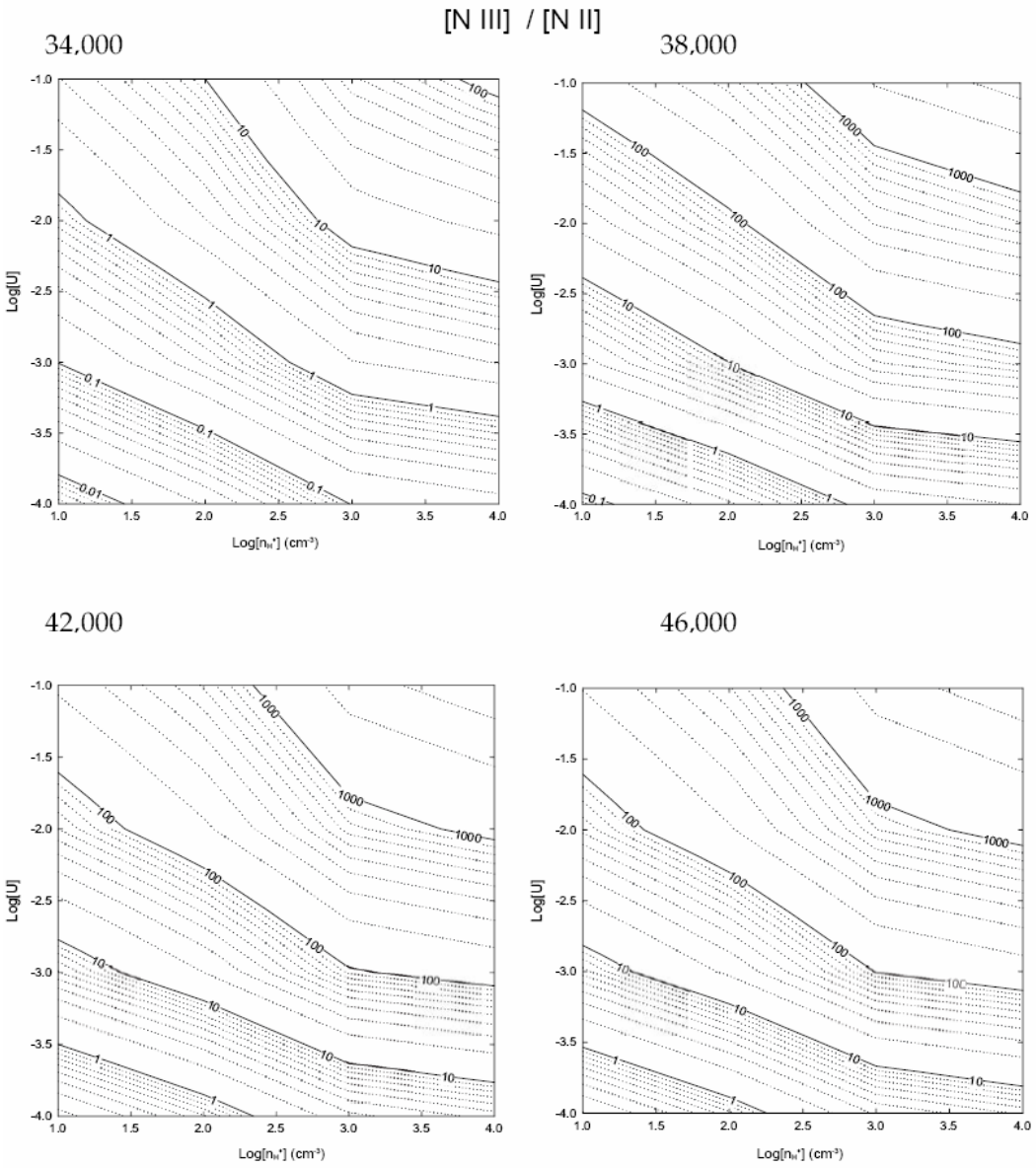

Figure 4.21 Ratio of [N III] 57 μm to [N II] 205 μm intensity. The critical densities for these transitions are less than 10^4 cm^{-3} (Malhorta et al. 2001). This means that, for the range of n_{H^+} considered in our calculations, this ratio can also depend on density in addition to T^* and U .

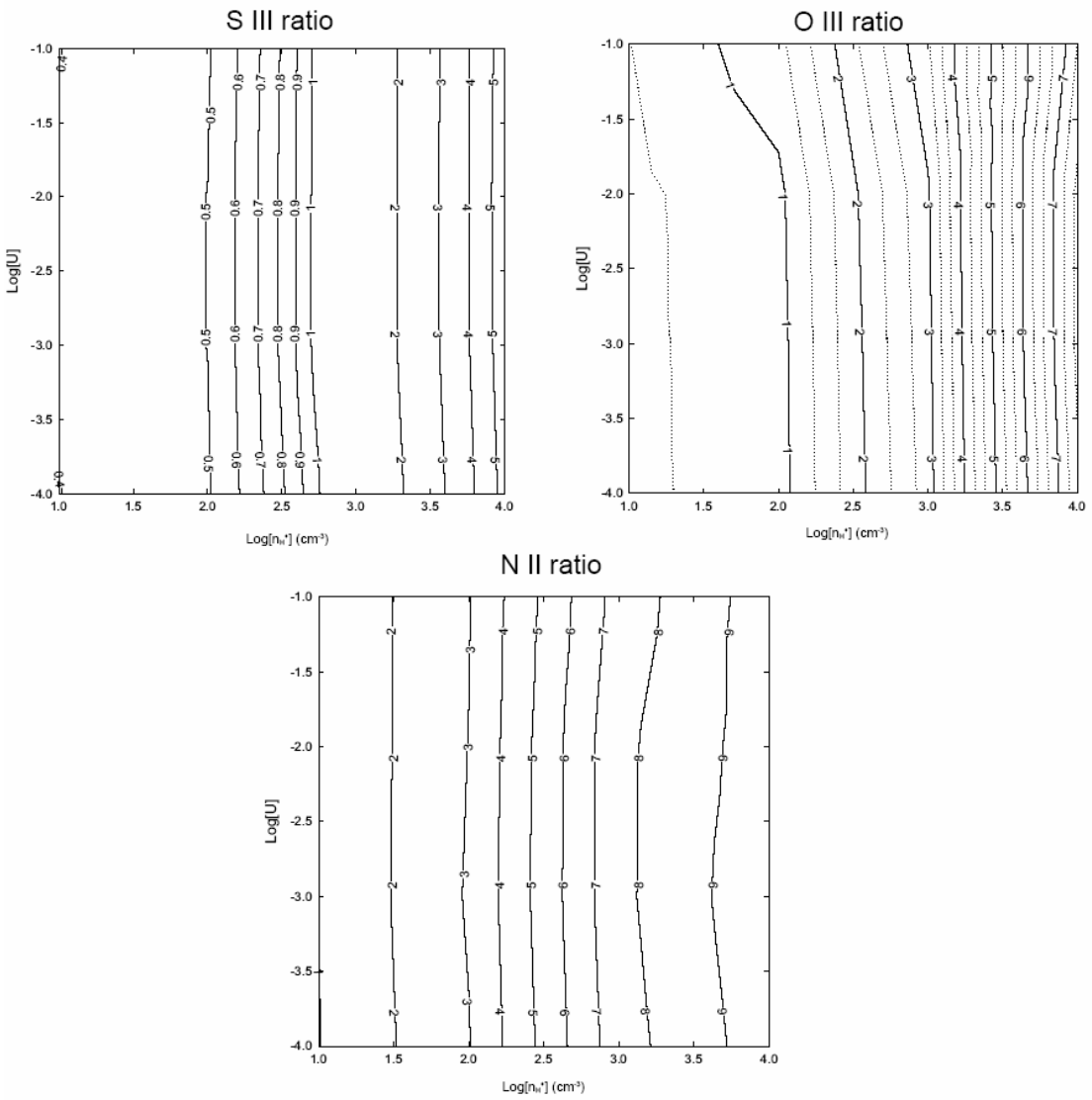

Figure 4.22 Computed H II region density diagnostic line ratios. Plotted is the ratio of the [S III] 18.7 μm line intensity to the [S III] 33.5 μm line, the [O III] 52 μm line intensity to the [O III] 88 μm line, and the [N II] 122 μm line intensity to the [N II] 205 μm line. All line ratios are good density diagnostics in the H II region for $n_{H^+} > 10^2$ cm^{-3}, while the N II ratio continues to be a good diagnostic across the entire range of n_{H^+} considered.

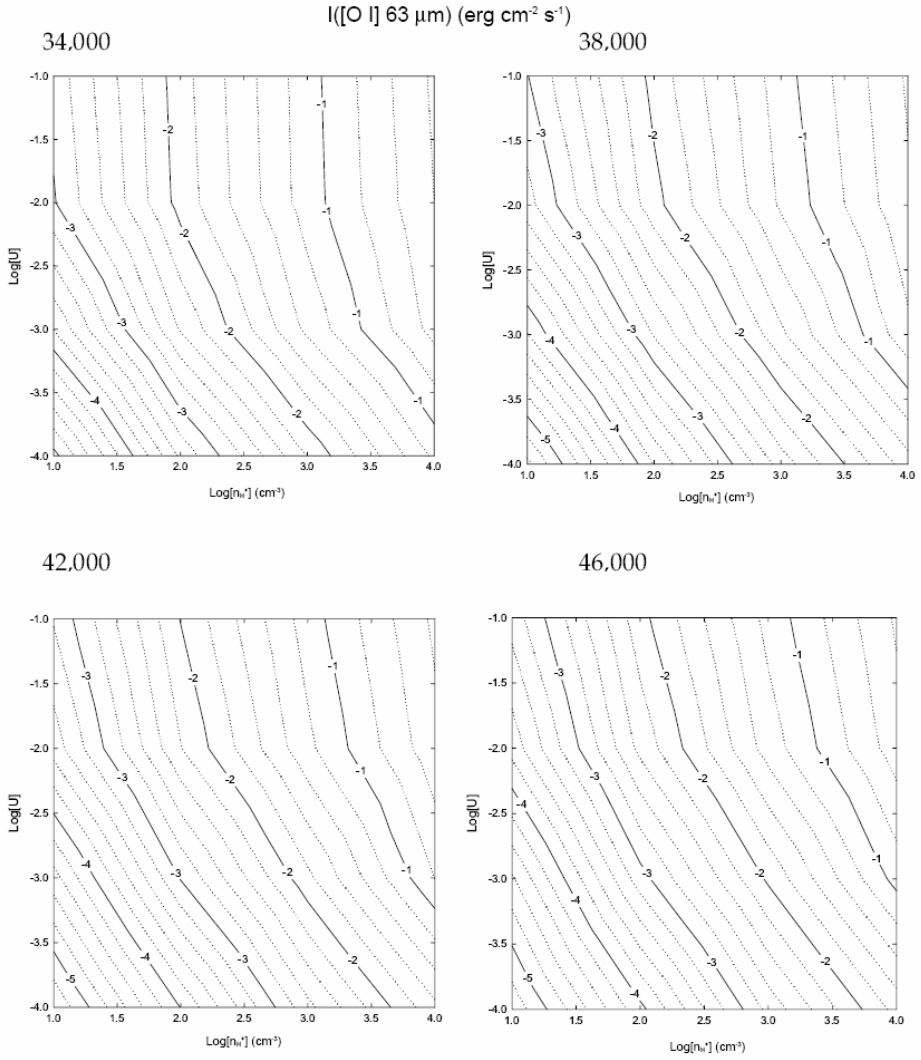

Figure 4.23 The predicted intensity of the [O I] 63 µm line (units erg cm^{-2} s^{-1}). This line and the lines presented in Figures 4.24-4.26 depend on both the hydrogen density in the PDR and G_0.

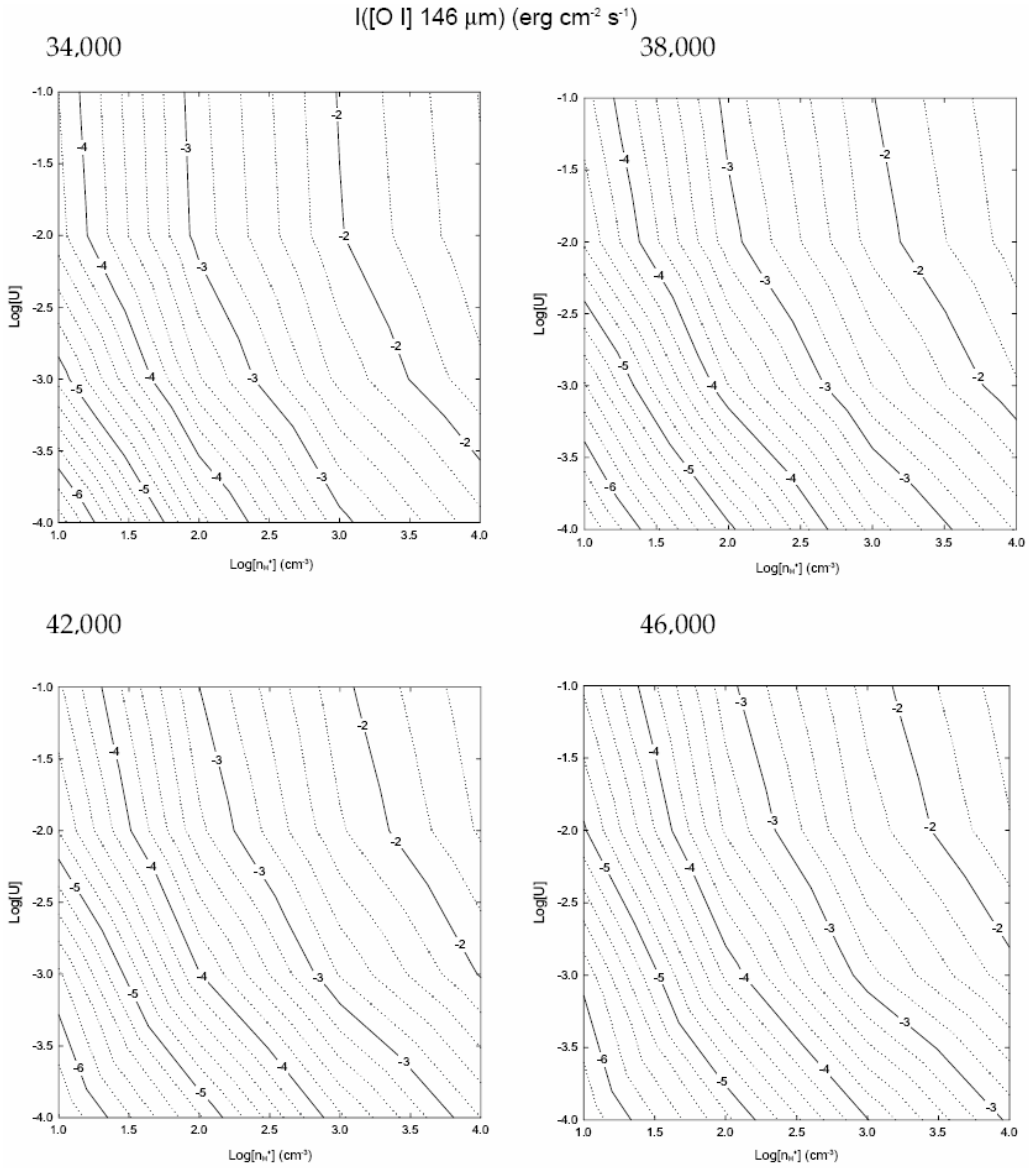

Figure 4.24 The predicted intensity of the [O I] 146 µm line (units of erg cm^{-2} s^{-1}).

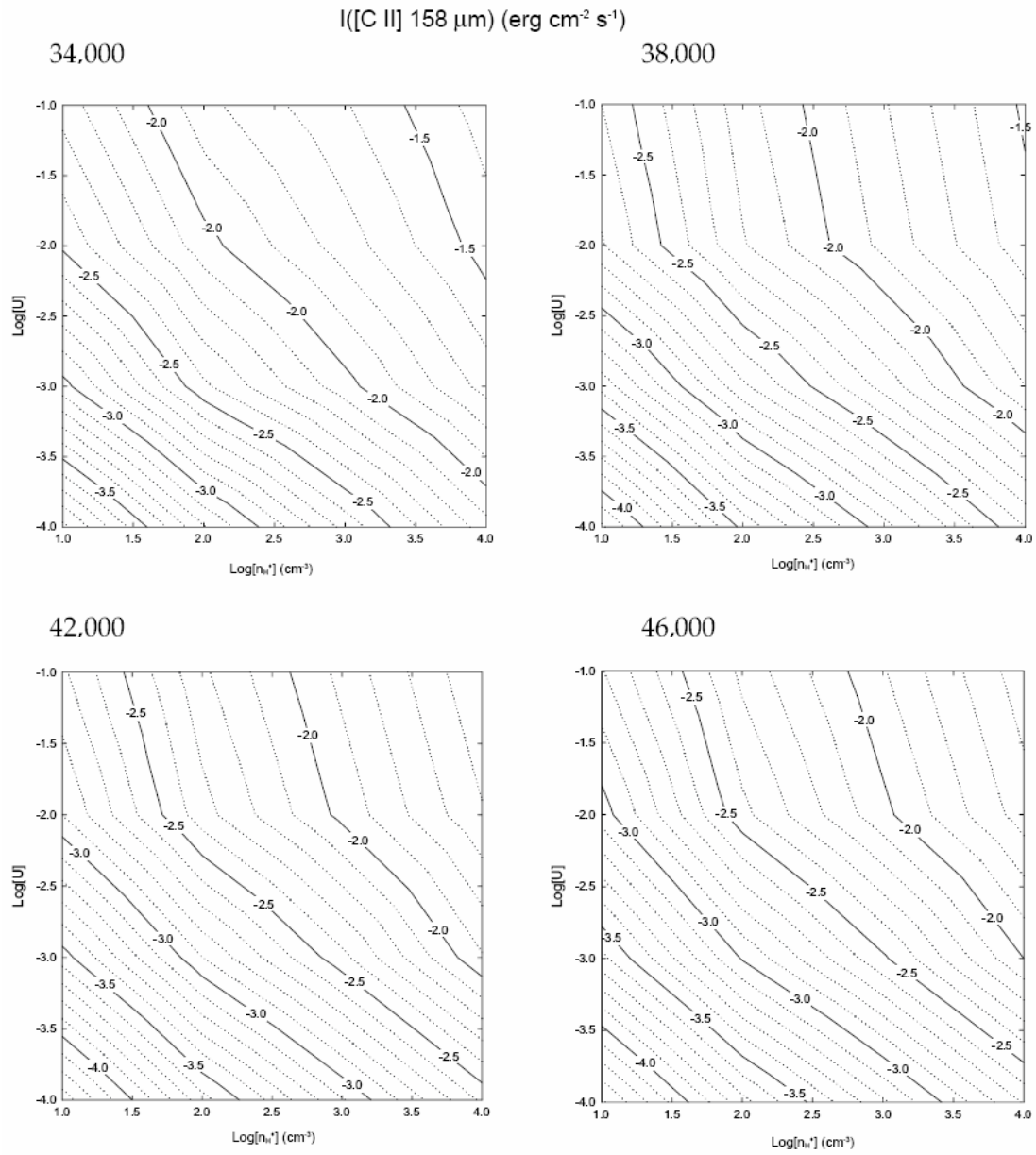

Figure 4.25 The predicted intensity of the [C II] 158 μm line (units of erg cm^{-2} s^{-1}).

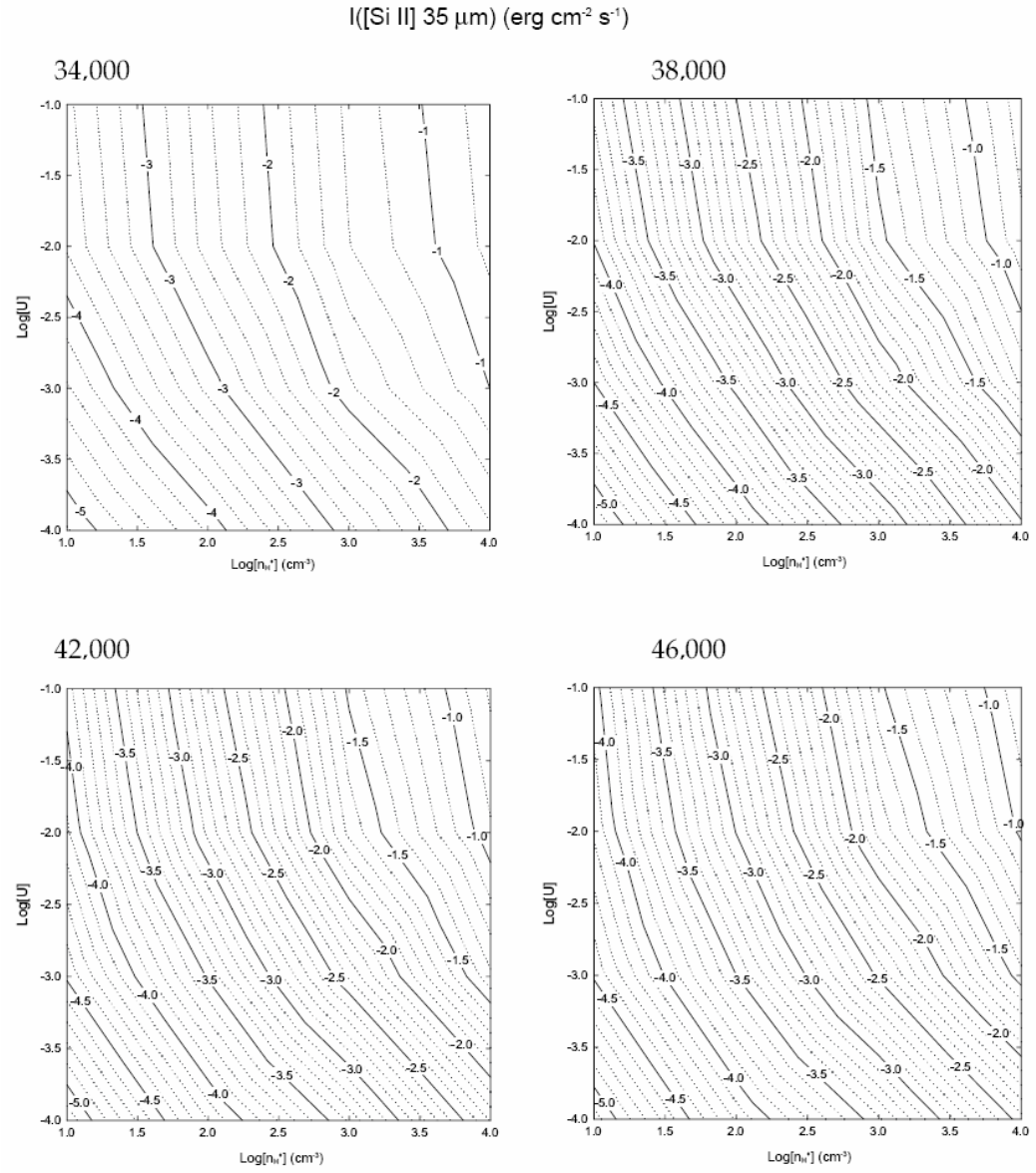

Figure 4.26 The predicted intensity of the [Si II] 35 μm line (units of erg cm^{-2} s^{-1}).

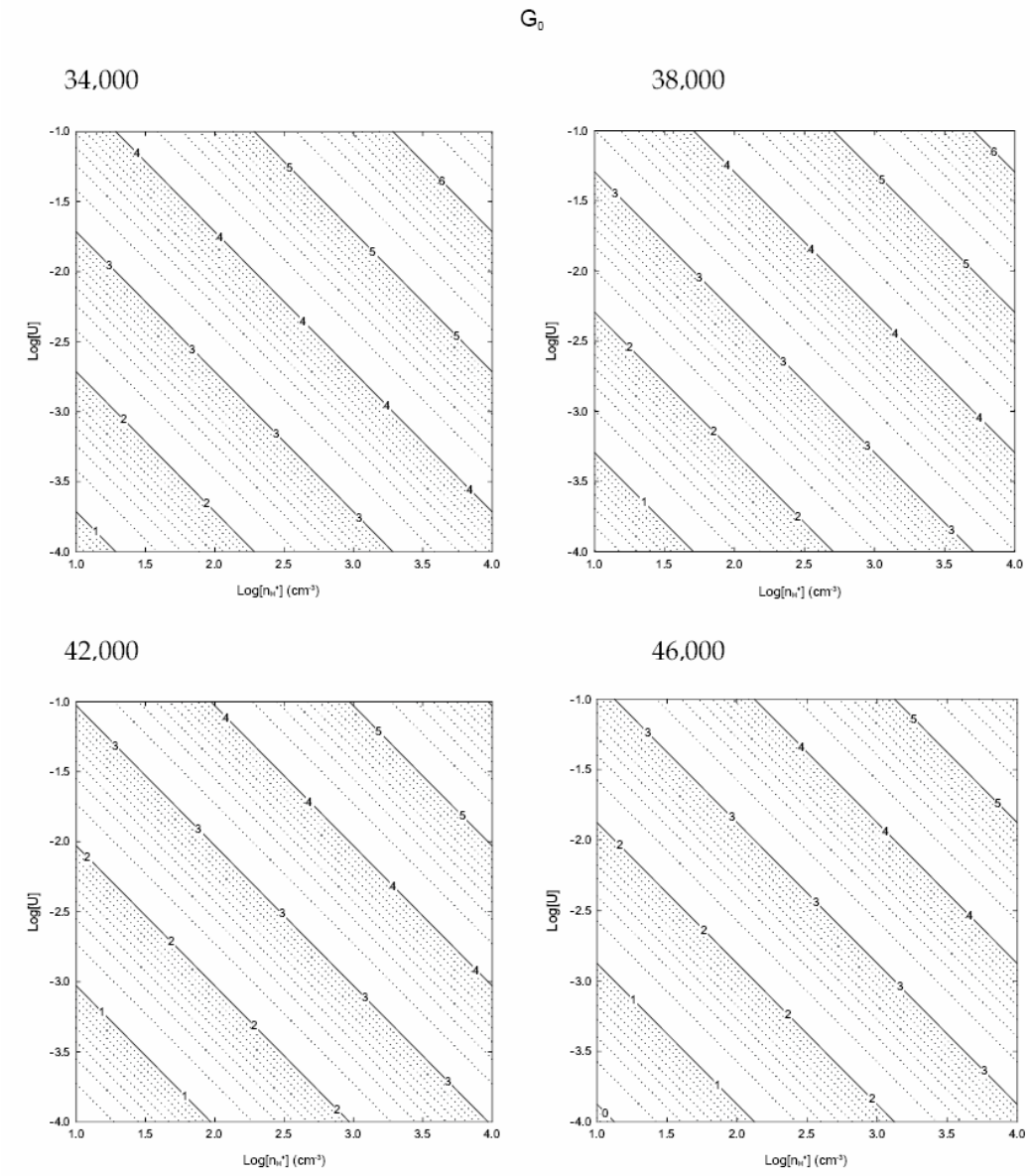

Figure 4.27 Log[G_0] at the illuminated face for our calculations. G_0 depends on T^* and the cloud-star separation and can be posed into the product of U and n_H (see equation 1).

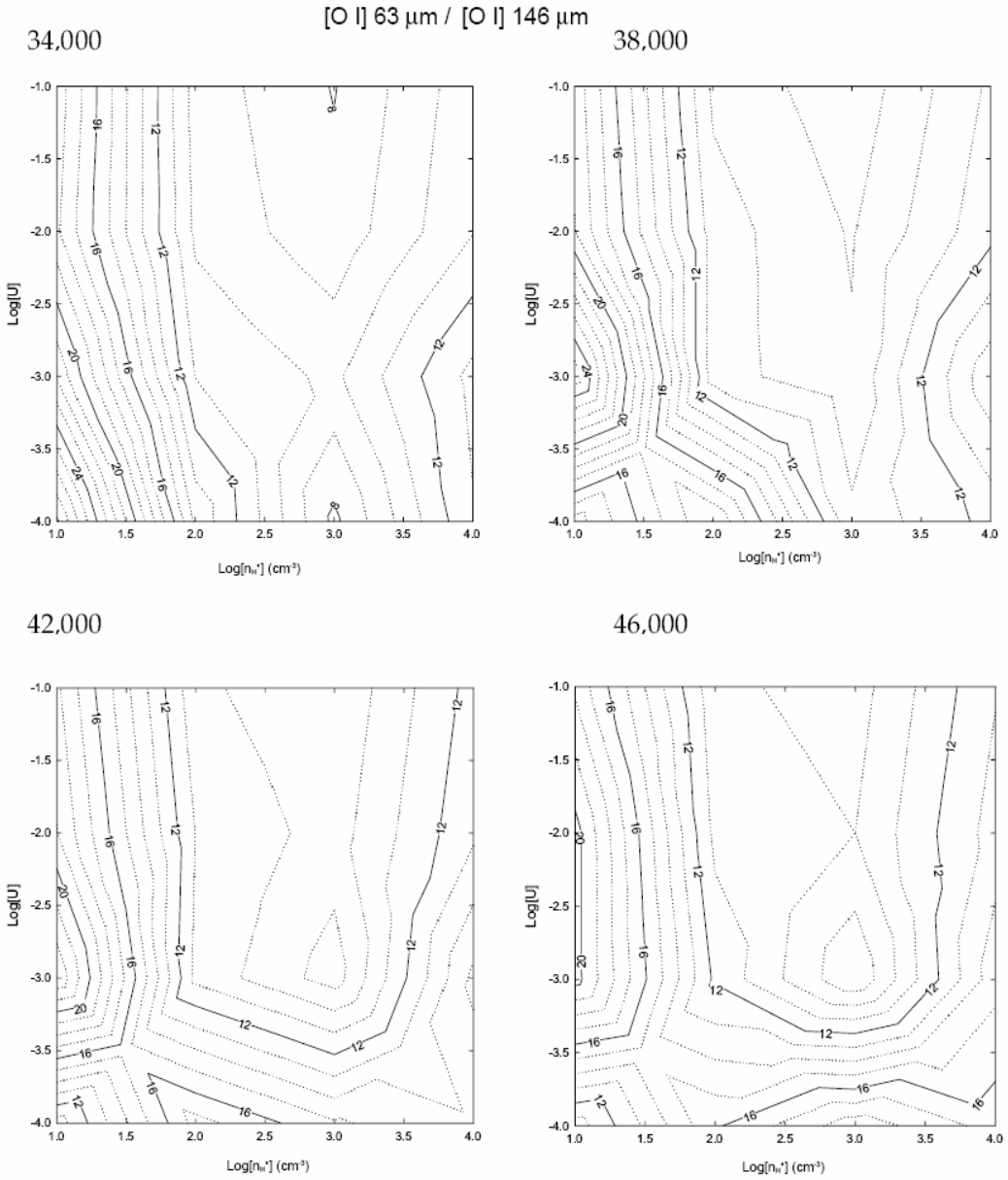

Figure 4.28 The ratio of [O I] 63 µm to [O I] 146 µm line intensities. This ratio is a common diagnostic used to determine physical conditions in PDRs (Kaufman et al. 1999). Over the entire range of parameter space, this ratio varies by only a factor of three.

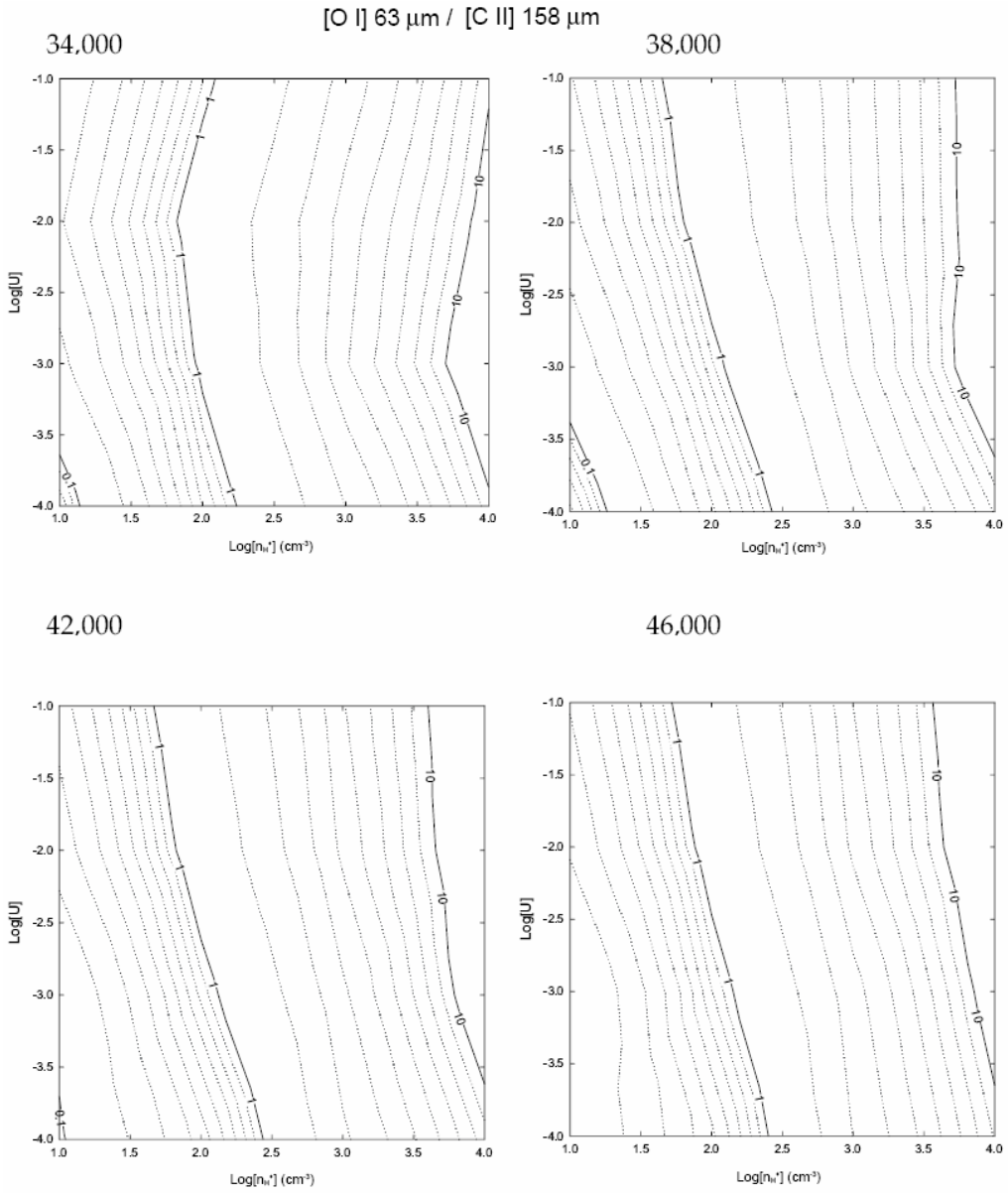

Figure 4.29 The ratio of [O I] 63 µm to [C II] 158 µm line intensities. This is another common PDR diagnostic line ratio (Kaufman et al. 1999). A significant amount of the 158 µm emission can come from the H II region. Without taking the H II region into account (see Figures 30-33), this ratio will be overpredicted, leading to errors in derived physical conditions that use this ratio.

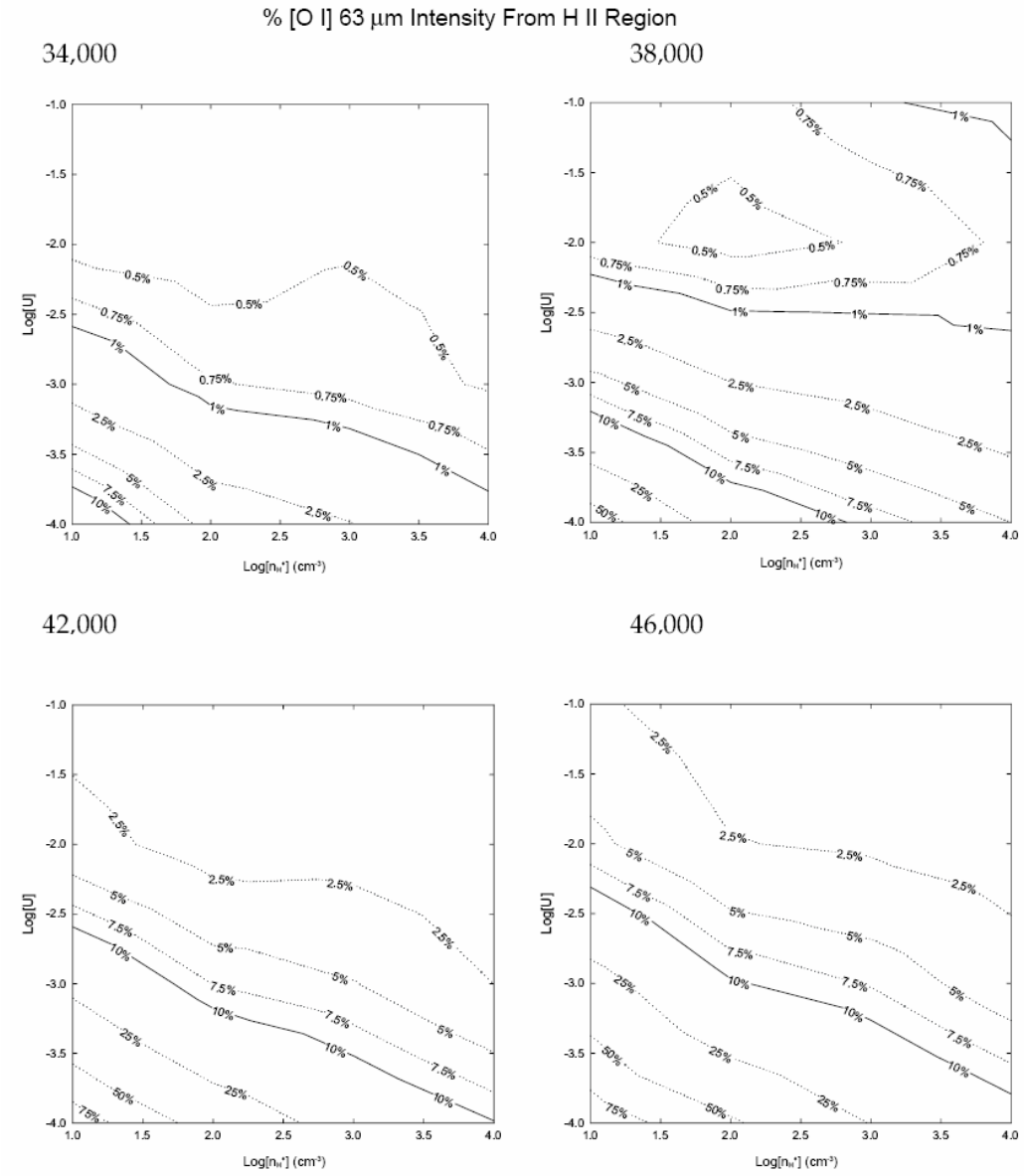

Figure 4.30 The percentage of the [O I] 63 μm line from the H II region for our calculations. The ionization structure of O follows that of H, so some O^0 exists in regions where hydrogen is partially ionized. For low $U \propto G_0/n_{\rm H}$ environments, the size of the atomic region is small. This leads to a larger fraction of the total emission emerging from the H II region.

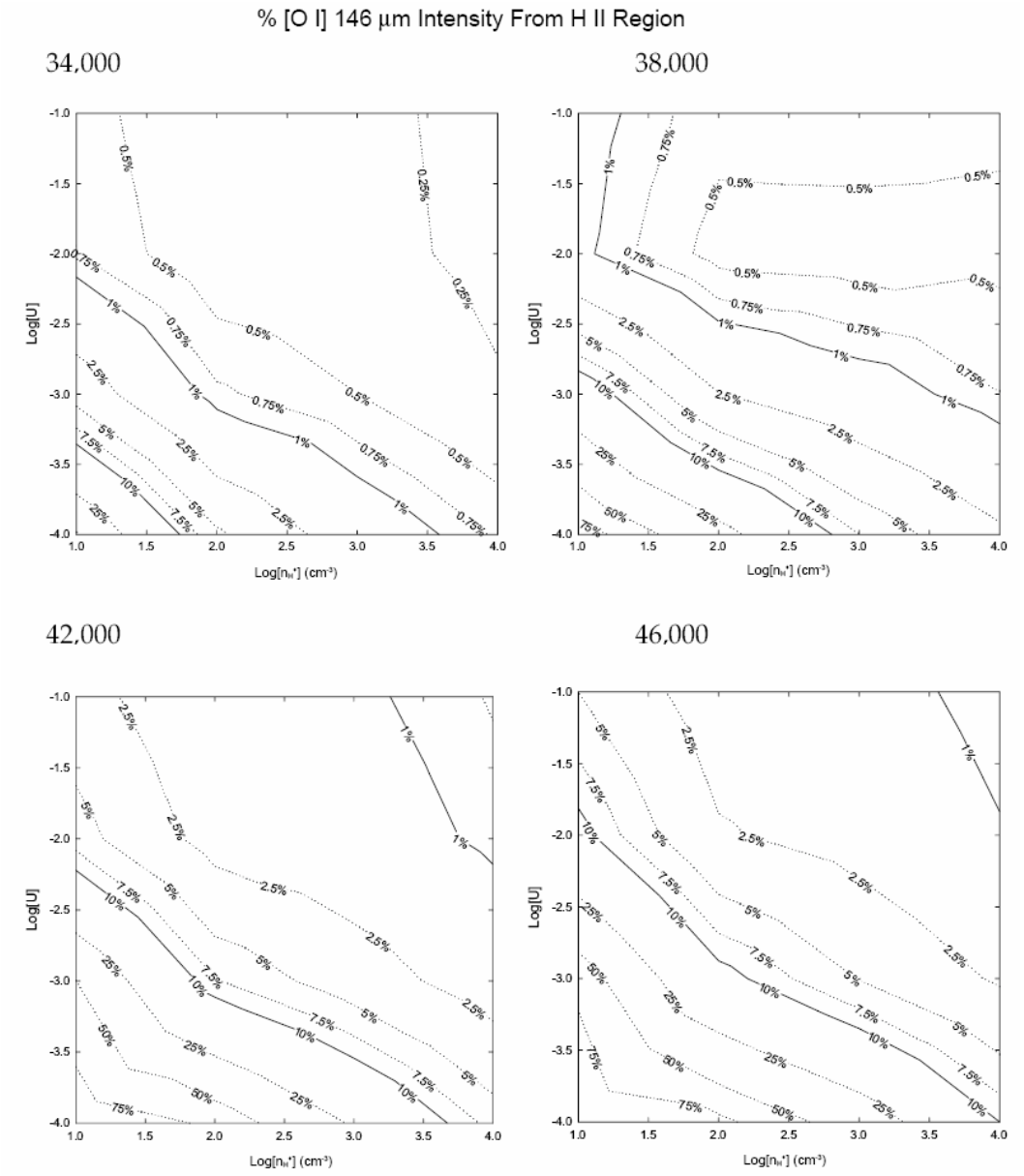

Figure 4.31 The percentage of the [O I] 146 µm line that is produced in the H II region. The logic governing the H II region contribution to [O I] 146 µm emission is exactly the same as [O I] 63 µm.

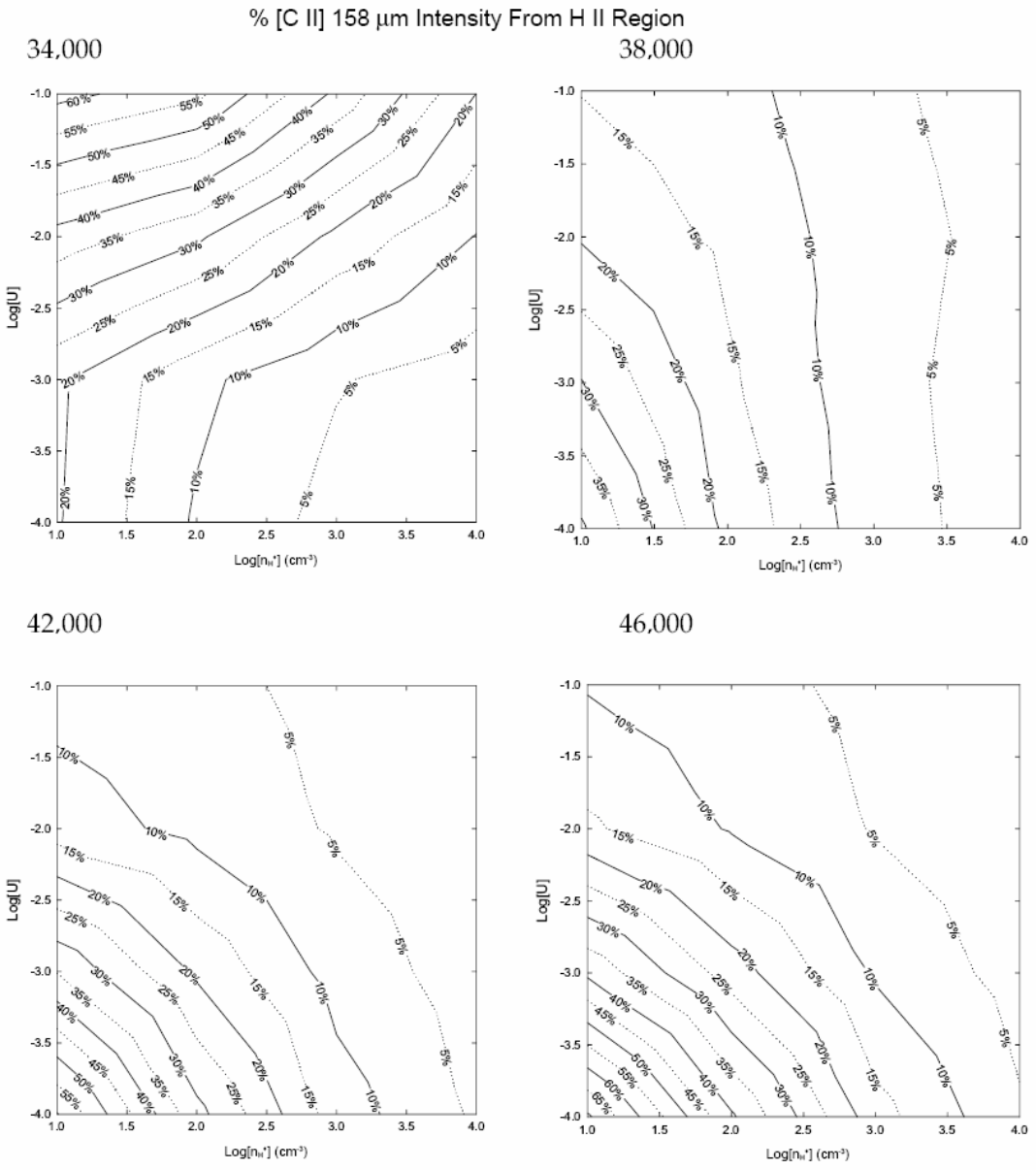

Figure 4.32 The percentage of the [C II] 158 µm line that is produced in the H II region. C^0 has an ionization potential less than 13.6 eV, which means that large amounts of C^+ can exist in ionized gas. For T_* = 34,000 K, C^+ and C^{2+} are the dominant stages of ionization. This leads to a large H II region contribution to the 158 µm line. For higher T^*, more C^{2+} and C^{3+} is found in the H II region and its contribution to the total amount of C II emission is less.

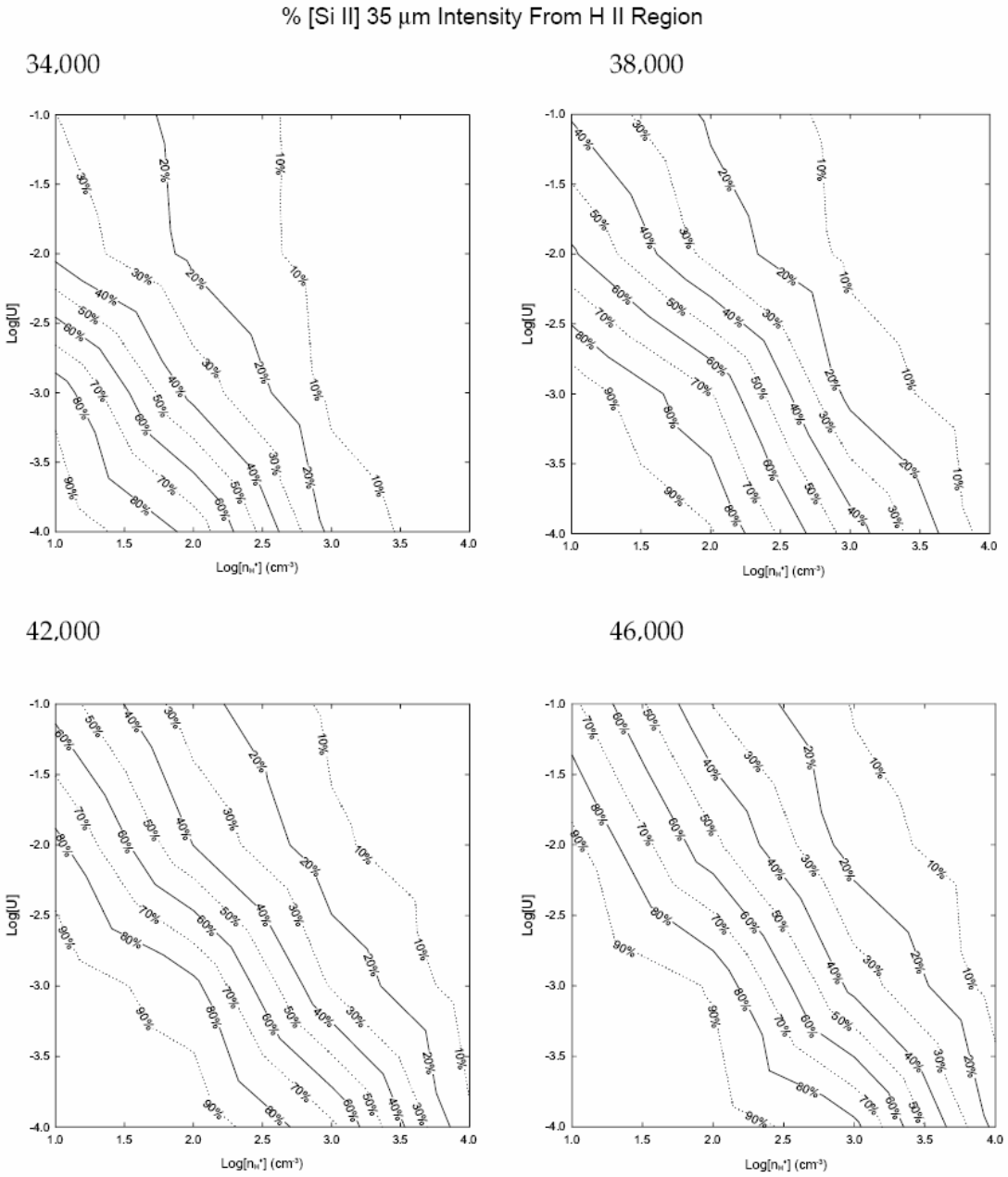

Figure 4.33 The percentage of the [Si II] 35 µm line that is produced in the H II region. Silicon, like Carbon, has a first ionization potential < 13.6eV, which leads to a significant amount of the 35 µm line emission (>10%) coming from the H II region over the entire range of parameter space.

Chapter 5: Determining the Role of Magnetic Fields in Extragalactic Star Forming Regions

5.1 Introduction

Magnetic fields play an important role in the evolution of star forming regions. The magnetic field is coupled to the gas through electromagnetic forces and collisions. Magnetic pressure balances gravitational pressure, decreasing the rate of star formation. Magnetic field measurements, therefore, are vital to understand a star-forming environment.

This paper seeks to determine the importance of magnetic fields in regions where observations of magnetic field strengths are not possible. Such environments include starbursts, ULIRGs, and normal galaxies. In Section 5.2, we analyze the equations governing an H II region and PDR in overall pressure equilibrium and identify infrared spectral diagnostics that can determine the role of magnetic fields in such an environment. In Sections 5.3 & 5.4, we present theoretical calculations of these spectral diagnostics. We end by analyzing previous data on PDRs associated with normal galaxies to determine the role of magnetic fields in these environments.

5.2 Equation of State in Star-Forming Regions

5.2.1 An H II Region and PDR in Pressure Equilibrium

Ionized and molecular gas is often assumed to be in a state of pressure equilibrium (isobaric). This includes many starburst galaxies (Carral et al, 1994; Lord et al 1996) and normal galaxies whose luminosities are dominated by star-formation (Malhorta et al, 2001-henceforth referred to as M01). In addition, a weak-D ionization front (Henney et al. 2005) is also nearly in constant pressure.

Different physical processes dominate the pressure in the H II region and PDR. In the H II region, the dominant pressure is thought to be thermal

pressure, $P^{th}=nkT$, owing to the high temperatures (~10^4 K) in H II regions. In the PDR the magnetic pressure, $P^{mag} = B^2/8\pi$, dominates over P^{th} (Crutcher 1999).

We now consider an H II region in pressure equilibrium with a PDR. The equation of pressure equilibrium can be written as:

$$\sum_i P^i_{\rm HII} = \sum_i P^i_{\rm PDR} \qquad (5.1).$$

If we only consider the effects of P^{mag} and P^{th}, we get:

$$P^{\rm mag}_{\rm HII} + P^{\rm th}_{\rm HII} = P^{\rm th}_{\rm PDR} + P^{\rm mag}_{\rm PDR} \qquad (5.2).$$

The gas is coupled to the magnetic field B though the Lorentz force and collisions. Therefore, B is proportional to some power of density, $B \propto n_{\rm H}{}^{\kappa}$. Observations (Crutcher 1999) and theoretical calculations (Fiedler and Mouschovias 1993) both suggest that $\kappa = 0.5$, where $n_{\rm H}$ is the hydrogen density. For the collapse of a spherical cloud with a magnetic field, magnetic flux conservation implies $\kappa = 0.66$ (see Crutcher 1999). For our calculations, we use the observed relationship $\kappa = 0.5$. The thermal to magnetic pressure, the emphasis of this paper, is insensitive to this detail. Test show that this will be ~5-15 % larger if we assume $\kappa = 0.66$.

Using the $B \propto n_{\rm H}{}^{\kappa}$ proportionality, we find that B in the H II region and PDR are related by:

$$B_{\rm HII} = B_{\rm PDR}\left(\frac{n_{\rm HII}}{n_{\rm PDR}}\right)^{\kappa} \qquad (5.3)$$

where n_{HII}, B_{HII}, n_{PDR}, and B_{PDR} are the hydrogen density and magnetic field strength in the H II region and PDR.

We are now in a position to derive an equation linking B, n, and T in the H II region and PDR. From the definitions of P^{th} and P^{mag}, along with equations 5.2 & 5.3, we have:

$$\left(\frac{B_{PDR}^2}{8\pi}\right)\left(\frac{n_{HII}}{n_{PDR}}\right)^{2\kappa} + n_{HII}kT_{HII} = \frac{B_{PDR}^2}{8\pi} + n_{PDR}kT_{PDR} \tag{5.4}$$

where T_{HII} and T_{PDR} is the temperature in the H II region and PDR. It is often convenient to define P^{th}/P^{mag} in the PDR as β (See, for instance, Heiles & Troland 2005). Inserting this definition into equation 5.4 and solving for β, we get:

$$\beta = \frac{1 - \left(\frac{n_{HII}}{n_{PDR}}\right)^{2\kappa}}{\left(\frac{n_{HII}T_{HII}}{n_{PDR}T_{PDR}}\right) - 1} \tag{5.5}$$

Equation 5.5 yields limits to β and n_{PDR} in constant-pressure environments. When $n_{HII} = n_{PDR}$, $\beta = 0$. The constant-density scenario also has constant pressure when $P^{mag} >> P^{th}$ in the PDR. When $P_{HII}^{th} = P_{PDR}^{th}$, $\beta = \infty$. In this limit, $B = 0$ and thermal pressure dominates. In reality the ratio will lie in between. Typical temperatures are $T_{HII} \approx 10^2 \times T_{PDR}$. Figure 5.1 shows the results of holding the H II region density and ratio of temperatures constant while varying the PDR density. The figure shows the resulting β for $n_{HII} = 10^2$, 10^3, and 10^4 cm^{-3}. If both densities can be measured then β can be determined. Crutcher (1999) found $\beta = 0.04$ for regions of the ISM. If this value of β is representative of the extragalactic ISM,

then $n_{PDR} \approx 5 \times n_{HII}$, rather than the 100:1 ratio found in the constant thermal pressure case.

5.3 Determining β and B through Infrared Spectroscopy

In this Section, we show how infrared observations can determine the density and temperature in each region, which then determines β and B. We identify the combination of infrared H II region and PDR emission-line diagnostics that are needed to determine β and B.

5.3.1 n_{HII}

Observations of emission lines formed in the ground term of the same ion can determine the electron density n_e (Rubin et al. 1994; M01; Abel et al. 2005, henceforth referred to as A05), which is, to within 10%, equal to the hydrogen density. In the infrared, the average electron energy is much greater than the excitation potential, eliminating the dependence of temperature on the line ratio (Osterbrock & Ferland 2005). However, each line will have a different critical density, which makes the line ratio dependent on n_e. Examples of density diagnostics in the infrared are [O III] 51.8 μm / 88.3 μm, [S III] 18.7 μm /33.5 μm, and [N II] 121.7 /205.4 μm.

5.3.2 T_{HII}, T_*, and U

As pointed out by Rubin et al (1994), no direct method exists to determine T_{HII} (which, for H II regions, is more commonly referred to as T_e) using IR diagnostics alone. Dinerstein, Lester, and Werner (1985) showed that the ratio of [O III] infrared to optical emission lines can determine T_{HII}. For a wide range of H II regions with typical abundances, $T_{HII} \approx (0.8\text{-}1) \times 10^4$ K.

For a given chemical composition, knowledge of stellar temperature (T_*), ionization parameter (U, which is the dimensionless ratio of hydrogen ionizing flux to density), and n_{HII} we can also determine, from the use of theoretical calculations, T_{HII} (Shields & Kennicutt 1995). Many elements are observed in

multiple ionization stages in the IR. The ratio of their emission lines is sensitive to the shape and intensity of the radiation field, which is set by T_* and U. Common T_* and U emission-line diagnostic ratios include [Ne III] 15.6μm to [Ne II] 12.8μm, [S IV] 10.8μm to [S III] 18.7μm and [N III] 57.1μm to [N II] 121.7μm. As pointed out by many authors (e.g. Morisset 2004, Giveon et al. 2004) a minimum of two of these emission line ratios are required to independently determine T_* and U for an assumed set of stellar atmospheres.

5.3.3 n_{PDR} & T_{PDR}

Fine-structure line emission from elements with ionization potentials (IP) < 13.6 eV, combined with theoretical calculations, can determine $n_{\rm PDR}$ and $T_{\rm PDR}$ (e.g. Wolfire, Tielens, & Hollenbach 1990; Kaufman et al. 1999). Common lines used for this analysis include [C II] 157.6 μm, [C I] 369.7, 609 μm, [O I] 63.2, 145.5 μm, and [Si II] 34.8 μm. Such an analysis can determine $n_{\rm PDR}$ and the intensity of the UV radiation field relative to the interstellar radiation field, parameterized by G_0 ($1G_0 = 1.6\times10^{-3}$ ergs cm^{-2} s^{-1}; Habing 1968). Knowing $n_{\rm PDR}$ and G_0, theoretical calculations then determine $T_{\rm PDR}$. This approach is similar to determining $T_{\rm HII}$ from $n_{\rm HII}$ and the properties of the hydrogen-ionizing continuum.

PDR calculations assume that the H II region does not contribute to the total fine-structure emission, an assumption which is not always true. In low-density H II regions, or regions where the size of the PDR is small compared to the H II region, a significant portion of [C II], [O I], or [Si II] emission can come from the H II region (Carral et al. 1994; Heiles et al. 1994; A05). In order to use PDR calculations to derive $n_{\rm PDR}$ and $T_{\rm PDR}$, the H II region component to the fine-structure emission must be estimated. Recently, A05 calculated the H II region contribution [C II], [O I], and [Si II] emission for a wide range of stellar temperatures (T_*), ionization parameters (U), and $n_{\rm HII}$ using the spectral synthesis code Cloudy (Ferland et al. 1998). A05 calculated the thermal, chemical, and

ionization balance for an H II region in gas pressure equilibrium with a PDR (P_{th}=constant), but do not include the effects of magnetic fields on the equation of state.

5.3.4 Combining H II and PDR Emission Line Diagnostics

The influence of the magnetic field can be constrained by considering the ratio of an H II region to PDR emission line. We find that the best diagnostic for this purpose is the ratio of [O III] (88.3 or 51.8 μm) to [O I] (63.2 or 145.5 μm). A given n_{HII}, T_*, and U, determines the [O III] emission, since the lines form near the illuminated face of the cloud, where the density is close to the initial density. The resulting [O I] emission depends strongly on the equation of state since these lines form in deeper, well shielded, regions. The effects of the H II region on [O I] emission is < 10% for most combinations of n_{HII}, T_*, and U (A05), so the line is a PDR indicator. For given n_{HII}, T_*, and U, n_{PDR} and T_{PDR} and the resulting [O III]/[O I] ratio only depends on the equation of state. Additionally, by using two oxygen emission lines, the dependence on abundance is eliminated.

5.4 Calculation Details

We use the spectral synthesis code Cloudy (Ferland et al. 1998) to perform our calculations. The physical treatment of PDR physics is discussed in A05.

We varied four parameters, U, T^*, n_{HII}, and the equation of state, in our calculation. The range of parameters are (with increments in parentheses): U =0.03-0.0003 (1 dex), T^* = 30,000–50,000 K (5,000 K), and n_{HII} = 30-3,000 cm^{-3} (1 dex). In all our calculations, the H II region and PDR were connected by assuming either constant density (which would be the case if the magnetic field or turbulence dominates the pressure) or constant thermal pressure (no magnetic field). Our results therefore represent the two possible limiting cases. For simplicity we assume a plane parallel geometry.

We use gas and grain abundances representative of the Orion environment, a typical H II region on the surface of a molecular cloud. The complete set of abundance used is given in Baldwin et al. (1996). A few by number are: He/H = 0.095, C/H= 3×10^{-4}; O/H= 4×10^{-4}, N/H= 7×10^{-5}, Ne/H= 6×10^{-5}, and Ar/H= 3×10^{-6}. We have assumed S/H= 2×10^{-6} based on observations of starburst galaxies by Verma et al. (2003). Grains in the Orion environment are known to have a larger then ISM size distribution (Cardelli et al. 1989), as are those in the starburst galaxies studied by Calzetti et al. (2000). We therefore use a truncated MRN size distribution (Mathis et al. 1977), weighted toward larger grains (Baldwin et al.). PAHs are also included in our calculation with a size distribution given in Bakes & Tielens (1994). PAHs are known to primarily exist in regions of atomic hydrogen (see, for instance, Giard et al. 1994). We assume that the number of carbon atoms in PAHs per hydrogen, $n_C(PAH)/n_H$ is 3×10^{-6}. This abundance is then scaled by the ratio H^0/H_{tot}, to produce low values in ionized and molecular regions (A05).

We consider two sources of ionization, a stellar continuum source and cosmic rays. For the stellar continuum, we used the WMBasic O star atmosphere models of Pauldrach, Hoffman, & Lennon (2001). We use the tabulated supergiant continuum with solar metallicity. Our choice of continua are the same as that used by Morisset (2004) in their determination of T_* and U in our Galaxy. We treat cosmic ray processes as described in Shull & van Steenberg (1985). We include primary ionizations, with an ionization rate $\xi = 5\times10^{-17}$ s^{-1}, and secondary ionizations caused by energetic electrons ejected by cosmic rays. Suchkov et al. (1993) find that the cosmic ray ionization rate in the starburst galaxy M82 is enhanced over Galactic by a factor of 200. Tests show that this level of enhancement has little effect on the [O I] emission from the PDR.

With this set of parameters we determine the ionization and thermal balance. Our calculation begins at the illuminated face of the H II region, continues

through the PDR, and ends deep in the molecular cloud, at a visual extinction (A_V) of 100.

5.5 Results

Figures 5.2 – 5.4 show the results of our calculations. The ratio of the [Ne III] 15.6μm to [Ne II] 12.8μm emission line intensities is the x-axis and the y-axis is the ratio of [O III] 88.3μm to [O I] 63.2μm. As mentioned above, the first ratio is a T_* and U indicator, and the second is primarily sensitive to n_{PDR} and T_{PDR}.

The dependence of the [O I] emission on n_{PDR} and T_{PDR} is clearly seen in Figures 5.2 – 5.4. The [O I] emission is weak relative to [O III] in the constant density, high magnetic field case, since the [O I] emission is proportional to density. In the constant thermal pressure case the PDR density and [O I] emission are considerably higher. This makes the [O III]/[O I] ratio sensitive to the equation of state. For almost all combinations of n_{HII}, T_*, and U, the difference in the [O III]/[O I] ratio for the two equations of state exceeds 1 dex. The only exception is for those for the lowest U, 0.0003, where the H II region makes a significant contribution of the total [O I] emission.

The line ratios presented in Figures 5.2 – 5.4 can determine the equation of state. The neon and sulfur line ratios determine the H II region properties and the [O III]/[O I] ratio determines the continuity between the H II region and PDR. Then, from equation 5.5, we immediately have an estimate for β.

In the next section, we use the extensive dataset of M01 to set limits on β and thermal pressures in star forming regions.

5.6 Deriving β from Current Observational Data

We have shown a methodology by which a complete set of IR observations can determine how the HII region and PDR are connected. Unfortunately this data set does not now exist. The closest is the extensive dataset of M01 (Table C1 & C2). M01 derived values for n_{PDR} and T_{PDR} for 60 galaxies. Unfortunately most

of their galaxies are heavily reddened, so n_{HII} could not be determined from the optical spectrum, and their data set does not include many of the mid-IR lines that are needed for our analysis.

There is sufficient spectral coverage to determine β for NGC 1222. Petrosian & Burenkov (1993) find n_{HII} = 500 cm^{-3} and $T_{HII} \approx$ 9000 K. M01 find $n_{PDR} = 10^{3.5}$ cm^{-3} and T_{PDR} = 325 K. The thermal pressures nT in the PDR and HII region are 1.0x10^6 and 4.5x10^6 cm^{-3} K. Pressure balance requires that the PDR be supported by additional terms, presumably turbulence and magnetic fields. Assuming purely magnetic pressure and equation 5.5 we find β=0.25 in the PDR. This value is about six times greater than the average value found by Crutcher of β=0.04 although he did find some objects with $\beta > 0.25$.

The observational sample of galaxies in M01 largely did not contain infrared H II region emission-line diagnostics. A direct comparison between the thermal pressures in the H II region and PDR was therefore impossible. Both the thermal pressure in the H II region and PDR are required to derive the ratio of thermal to magnetic pressure in the PDR (equation 5.5), so the lack of H II region diagnostics also limits the ability to estimate β.

By making a few simplifying assumptions, we can estimate the thermal pressure in the H II region. The first assumption is that that the galaxies are in pressure equilibrium and that the magnetic field is proportional to density. This allows us to use equation 5.5 in our analysis. The second assumption is that T_{HII} = 10^4 K, which for solar abundances should be accurate to within a factor of two. The third assumption is that $\beta > 0$. The assumption of $\beta > 0$ is obvious (since n, T, and $|B|$ all must be positive). However, if one blindly applied equation 5.5, then one can get the unphysical result $\beta < 0$. Equation 5.5 can yield a negative value if $n_{PDR}T_{PDR} > n_{HII}T_{HII}$, if $n_{HII} > n_{PDR}$, or if $\kappa < 0$. Both $n_{PDR}T_{PDR} > n_{HII}T_{HII}$ and $n_{HII} > n_{PDR}$ are consistent with a region that is not isobaric, making equation 5.5 invalid

in such a region. Additionally, $\kappa < 0$ is not realistic, since one would expect the magnetic field to increase with increasing density.

By making the assumptions above, we used the M01 dataset and equation 5.5 (with $\kappa = 0.5$) to derived a range of H II region densities allowed by observation. Table 5.1 summarizes our results. The lower limit and upper limits to $n_{\rm HII}$ corresponds to the point where the thermal pressures in the H II region and PDR are equal, and where $n_{\rm HII} = n_{\rm PDR}$, respectively. The range of $n_{\rm HII}$ that yields $\beta > 0$ for the measured PDR thermal pressure is typically about 1-1.5 dex.

In addition to the derived range of H II region densities, there is a value of $n_{\rm HII}$ for each galaxy in the M01 dataset that would yield a ratio of thermal to magnetic pressures equal to the ISM value of 0.04. This density is given in the last column of Table 5.1. In general, we find that $\beta = 0.04$ corresponds to $n_{\rm PDR}/n_{\rm HII} \sim 2$.

Figure 5.5 shows how β depends on the value of $n_{\rm HII}$ for three galaxies observed by M01; NGC 278, NGC 1155, and NGC 1266. The β parameter is very sensitive to the derived value of $n_{\rm HII}$, with β varying by 7 orders of magnitude as $n_{\rm HII}$ varies by 1 order of magnitude. This behavior is due to the limits of constant thermal pressure and constant density. If $n_{\rm HII}$ is only slightly less than $n_{\rm PDR}$, equation 5 shows the numerator will become very small while the denominator becomes large. This leads to $\beta << 1$. Conversely, if $n_{\rm PDR}T_{\rm PDR}$ is only slightly less than $n_{\rm HII}T_{\rm HII}$, then the denominator will be small, the numerator large, and $\beta >> 1$. This sensitivity makes an accurate determination of $n_{\rm HII}$ vital in understanding the importance of magnetic fields in the M01 sample.

Future infrared observations of the galaxies observed by M01 can further constrain β. Almost all the galaxies observed by M01 showed [O I] emission, however only a handful also showed [O III] emission. If [Ne III], [Ne II], [S IV], and [S III] emission were measured for the galaxies studied by M01, then the global physical conditions of the ionized and molecular gas would be known

simultaneously. We would then get a better idea of the role of magnetic fields in this large sample of extragalactic star forming regions.

Table 5.1 Thermal and magnetic pressure balance for selected galaxies

Galaxy	$10^{-5}\times P^{th}$ (PDR)[11]	Log[n_{HII}] ($\beta > 0$)[12]	Log[n_{HII}] ($\beta = 0.04$)[13]
NGC 278	1.3	1.2 - 2.7	2.3
NGC 520	26	2.5 - 3.7	3.5
NGC 693	1.2	1.1 - 2.5	2.3
NGC 695	5.4	1.8 - 3.2	2.9
NGC 986	0.6	0.8 - 1.9	1.8
NGC 1022	17	2.3 - 3.5	3.3
NGC 1155	17	2.3 - 3.6	2.7
NGC 1156	1.2	1.1 - 2.6	2.3
NGC 1222	10	2.0 - 3.4	3.1
NGC 1266	140	3.2 - 4.2	4.1
NGC 1317	1.1	1.1 - 2.2	2.1
NGC 1326	1.7	1.3 - 2.6	2.4
NGC 1385	1.6	1.3 - 2.4	2.2
NGC 1482	2.0	1.4 - 2.7	2.5
NGC 1546	2.1	1.4 - 2.6	2.4
NGC 1569	5.2	1.8 - 3.2	2.9
NGC 2388	120	3.1 - 4.2	4.0
NGC 3583	4.4	1.7 - 2.9	2.7
NGC 3620	3.0	1.5 - 2.6	2.5
NGC 3683	1.3	1.4 - 2.6	2.3
NGC 3885	18	2.3 - 3.6	3.3
NGC 3949	3.5	1.6 - 3.0	2.7
NGC 4027	1.6	1.3 - 2.6	2.4
NGC 4102	14	2.2 - 3.1	3.0
NGC 4194	9.3	2.0 - 3.4	3.1
NGC 4490	3.6	1.6 - 2.9	2.6
NGC 4691	5.7	1.8 - 3.1	2.9

[11] Thermal pressure taken from Malhorta et al. (2001)

[12] Calculated from equation 5.5, and assuming $T_{HII} = 10^4$ K

[13] n_{HII} that gives β equal to the value found by Crutcher (1999)

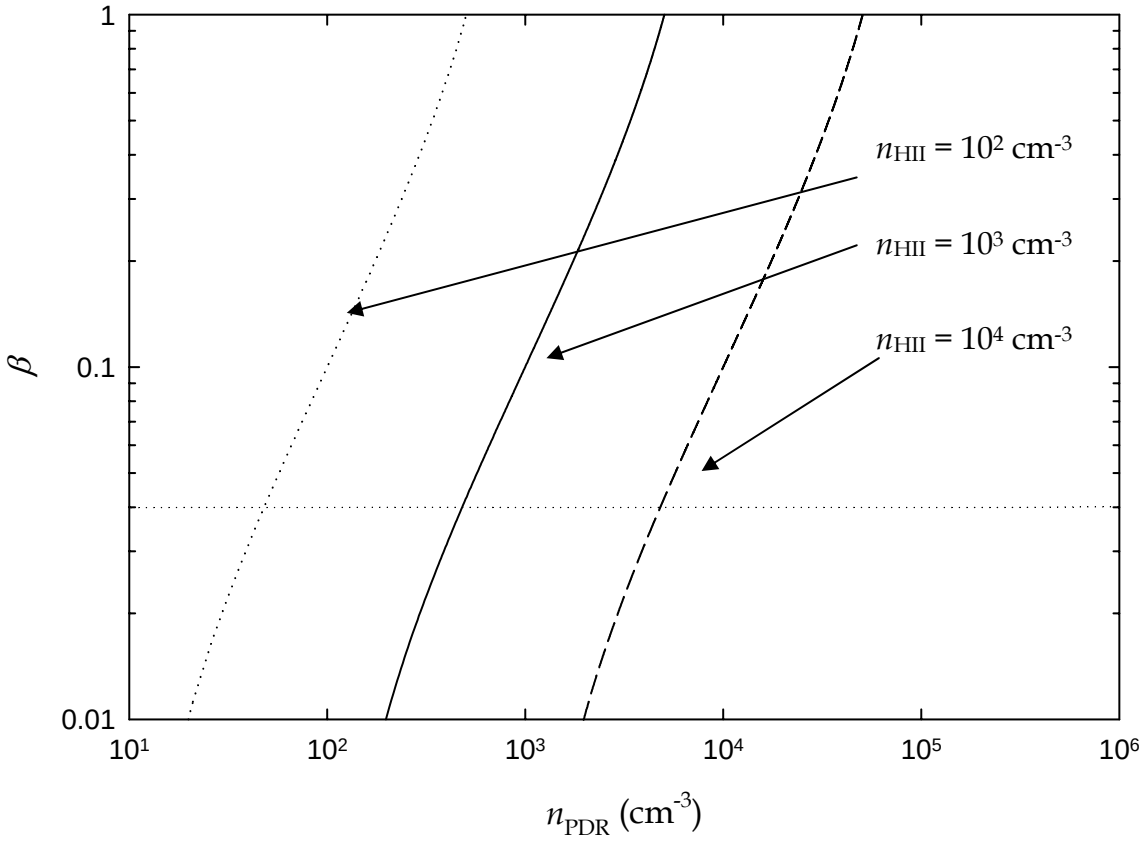

Figure 5.1 Plot showing how β varies with n_{PDR} for three initial values of n_{HII} and T_{HII}/T_{PDR} of 100. When $n_{PDR} \sim n_{HII}$, the magnetic pressure overwhelms the thermal pressure. As n_{PDR} increases relative to n_{HII}, the thermal pressure increases and β becomes larger. The horizontal line at $\beta = 0.04$ corresponds to the ISM value found by Crutcher (1999). For $\beta = 0.04$, $n_{PDR} = 5 \times n_{HII}$.

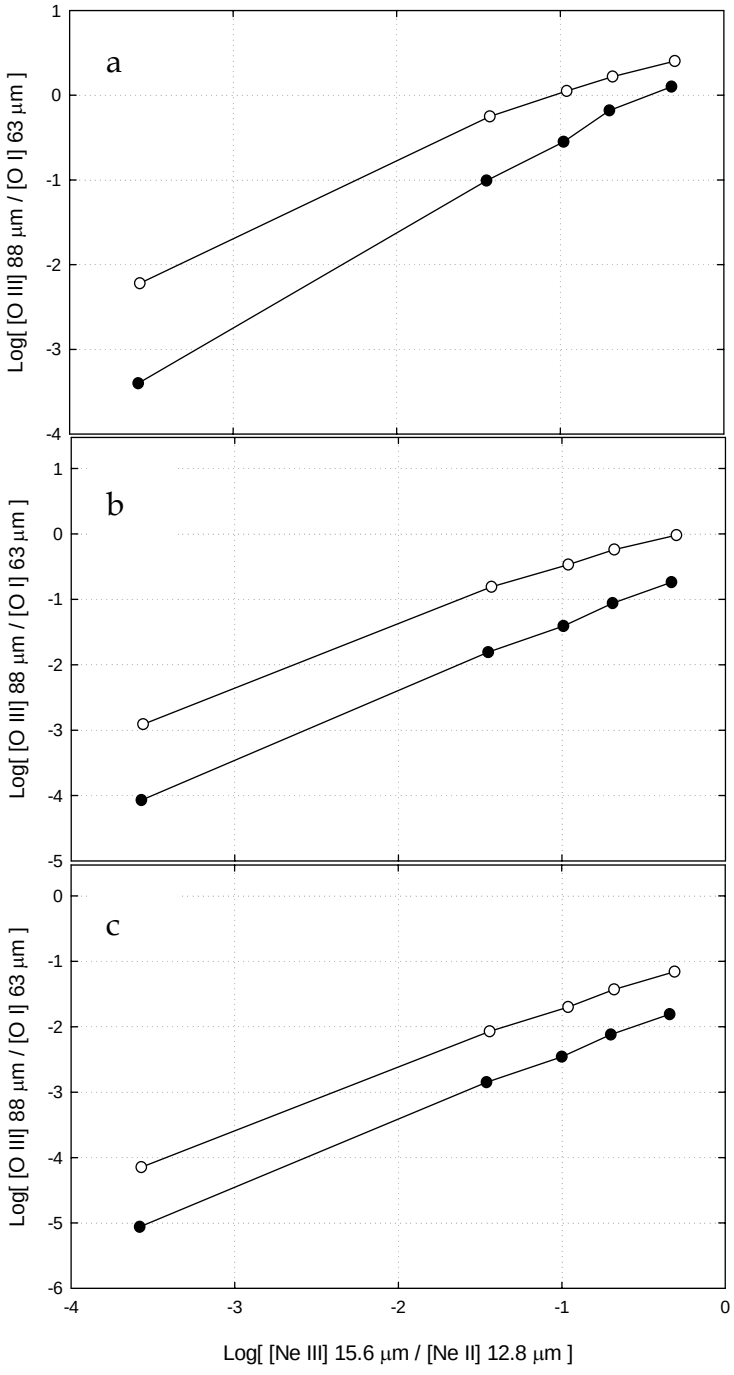

Figure 5.2 Ratio of [Ne III]/[Ne II] vs. [O III]/[O I] for $P^{mag} >> P^{th}$ (open circles), $P^{mag} = 0$ (filled circles), $U = 10^{-3.5}$, and $n_{HII} = 10^{1.5}$, $10^{2.5}$, $10^{3.5}$ cm^{-3} (a, b, and c, respectively). For a given U and n_{HII}, the [O III]/[O I] ratio is sensitive to β. Our calculations, therefore, allow a way to determine β in constant pressure environments.

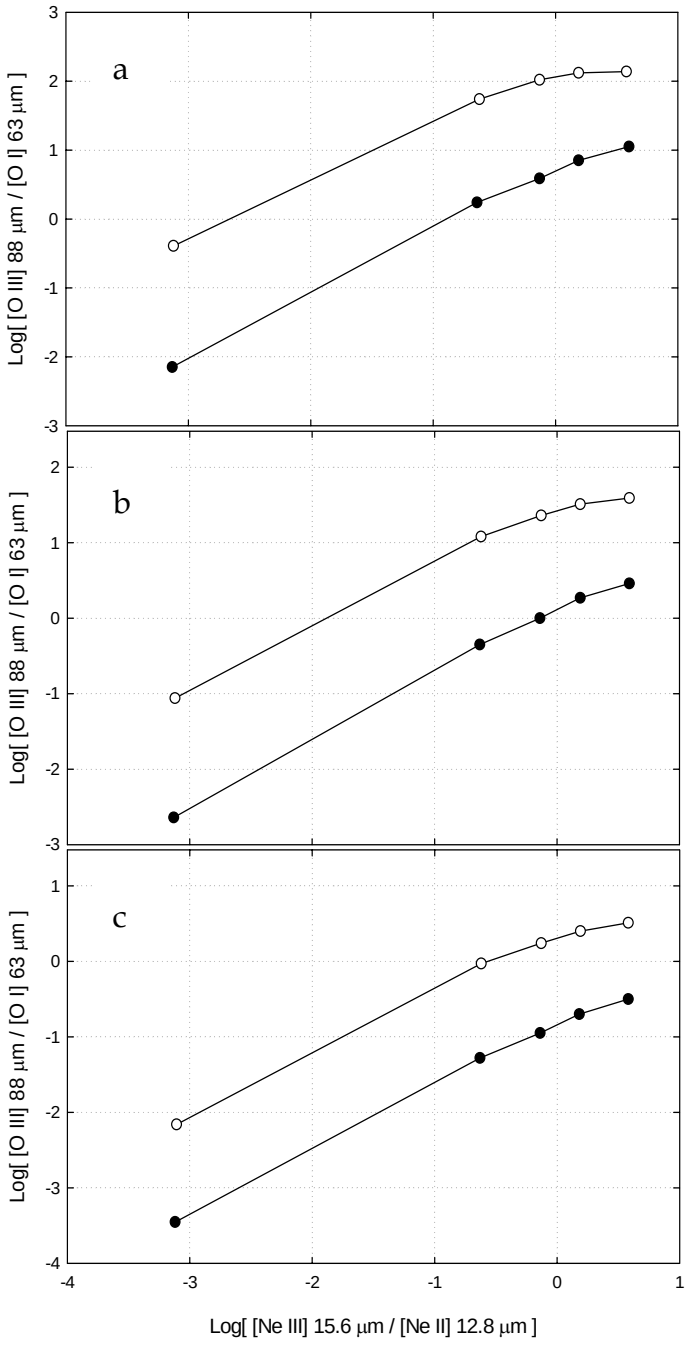

Figure 5.3 Ratio of [Ne III]/[Ne II] vs. [O III]/[O I] for $P^{mag} >> P^{th}$ (open circles), $P^{mag} = 0$ (filled circles), $U = 10^{-2.5}$, and $n_{HII} = 10^{1.5}$, $10^{2.5}$, $10^{3.5}$ cm^{-3} (a, b, and c, respectively). For a given U and n_{HII}, the [O III]/[O I] ratio is sensitive to β. Our calculations, therefore, allow a way to determine β in constant pressure environments.

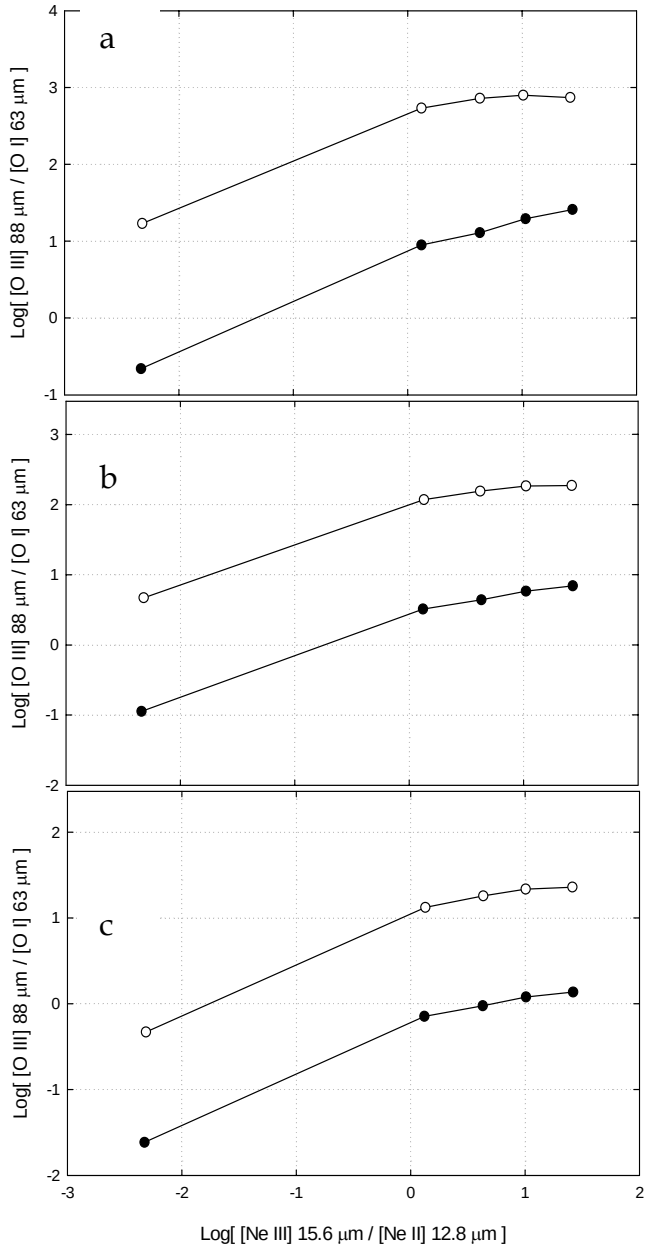

Figure 5.4 Ratio of [Ne III]/[Ne II] vs. [O III]/[O I] for $P^{mag} >> P^{th}$ (open circles), $P^{mag} = 0$ (filled circles), $U = 10^{-1.5}$, and $n_{HII} = 10^{1.5}$, $10^{2.5}$, $10^{3.5}$ cm^{-3} (a, b, and c, respectively). For a given U and n_{HII}, the [O III]/[O I] ratio is sensitive to β. Our calculations, therefore, allow a way to determine β in constant pressure environments.

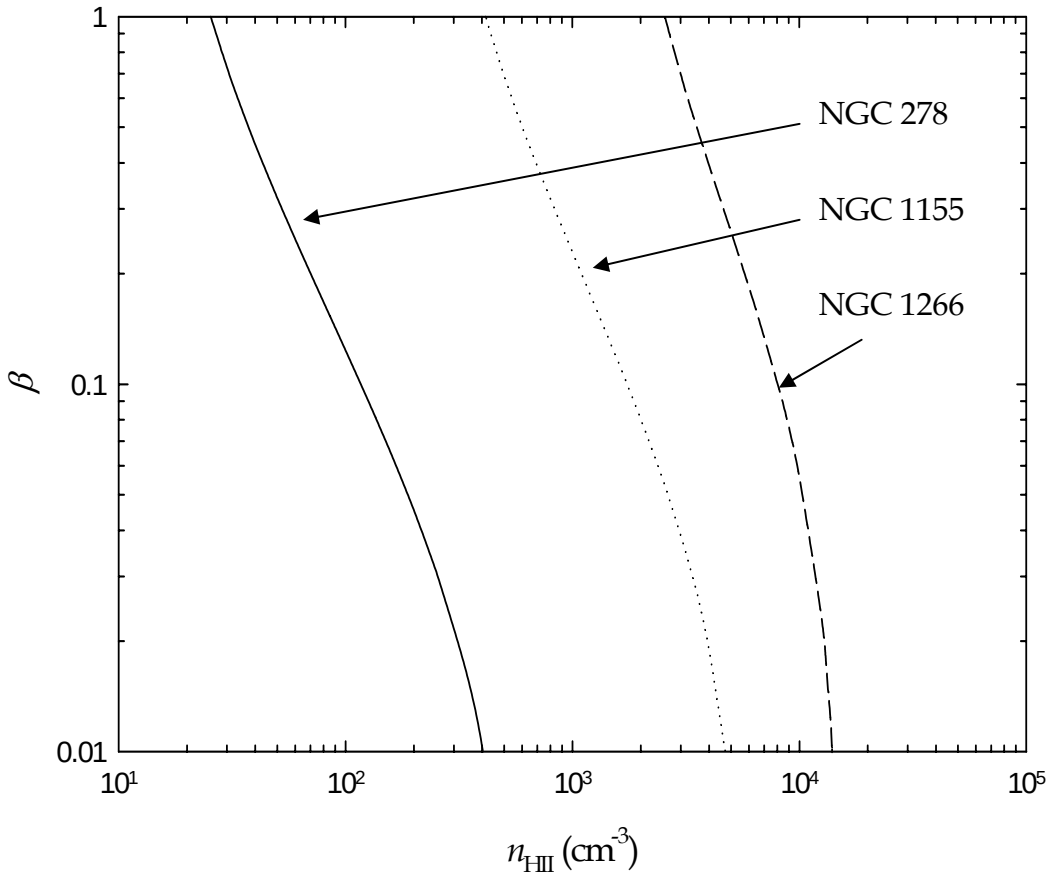

Figure 5.5 Dependence of β on n_{HII} for three galaxies observed by M01. This plot shows that, by knowing n_{HII}, we would be able to estimate β.

Chapter 6: Conclusions

6.1 Summary

We have performed a detailed study of the absorbing screen of material in front of the Orion Nebula, a region known as Orion's Veil. This work combined theoretical calculations with UV, optical, and radio spectroscopy. The combination of observational data and photoionization calculations allowed me and my collaborators to derive many physical characteristics of the Veil. This includes the volume hydrogen density, 21 cm spin temperature, turbulent velocity, and kinetic temperature for each 21 cm component. Calculations constrained the distance of the Veil from the Trapezium stars. The UV observations also detected, for the first time along this sightline, molecular hydrogen. Finally, we determine that the ionized and mostly atomic layers of the Veil are physically distinct regions and will collide in less than 85,000 years.

We have also performed a series of calculations designed to reproduce infrared diagnostics used to determine physical conditions in star forming regions. These calculations self-consistently determined the thermal and chemical structure of an H II region and photodissociation region (PDR) that are in pressure equilibrium. This differs from previous work, which used separate calculations for each gas phase. These calculations spanned a wide range of stellar temperatures, gas densities, and ionization parameters. Such a calculation required expanding the spectral synthesis code Cloudy. These include the addition of a molecular network with ~1000 reactions involving 68 molecular species and improved treatment of the grain physics. Data from the Spitzer First Look Survey, along with other archives, are used to derive important physical characteristics of the H II region and PDR. These include stellar temperatures, electron densities, ionization parameters, UV radiation flux (G_0), and PDR density. The contribution of the H II region to PDR emission line diagnostics

was calculated, which allows for a more accurate determination of physical conditions in PDR. Finally, this dissertation finds that observations of H II diagnostic line ratios combined with a ratio of an H II region emission line to a PDR emission line can determine the ratio of thermal to magnetic pressure, β, with the best diagnostic being the [O III]/[O I] emission line ratio.

6.2 Detailed Conclusions

Below is a list of detailed conclusions from Chapter 2-5:

6.2.1 Primary conclusions from Chapter 2

- Model calculations (Section 2.3) constrain the density in the Veil to $\sim 10^3 \leq n(\mathrm{H}) \leq \sim 10^4$ cm^{-3}. The models also reveal a monotonic connection between density and temperature, higher temperatures are associated with higher densities for $n(\mathrm{H}) \leq 10^4$ cm^{-3}. The best fit model has $n(\mathrm{H}) \sim 10^{3.1}$ cm^{-3} at $T \sim 70$ K.
- Model calculations place the Veil 1-3 parsecs away from the Trapezium, the best fit value is 2 pc. Also, measurements of the surface brightness of [N II] 6583Å require the Veil to be at least 1 parsecs from the Trapezium. These distances are about 2-5 greater than the 0.6 pc value suggested by previous statistical analyses.
- The low column density of H_2 along the line-of-sight through the Veil is not the result of larger-than-normal grains, as previously supposed. Model calculations suggest H_2 is under abundant because of the high UV flux incident upon the Veil. Also, the predicted H_2 abundance is very sensitive to the details describing the dissociation and formation processes. This means that straightforward approximations previously used in calculating the dissociation rate may not accurately predict H_2 abundances in at least some circumstances. In this study, we have used a greatly improved model for the H_2 molecule that incorporates over 10^5 rotational/vibrational levels.

- The models confirm that Ca^+ is only a trace stage of ionization in the Veil. Therefore, studies of Ca II optical absorption profiles may not be representative of the most of the matter in the Veil. However, 21cm H I absorption traces all of the matter in the Veil except the small fraction in the form of H+. Model calculations predict that about 5% of the hydrogen in the Veil is ionized.
- There are two principal velocity components in the 21 cm H I absorption which we designate as the narrow and the wide components. Magnetic field measurements made via the Zeeman effect (Troland et al., private communication) reveal the line-of-sight field strength B_{los} across the Veil. In the direction of the Trapezium stars, $B_{los} \sim -50$ μG for each of these components, with the total field strength statistically expected to be two times larger. We show from model estimates of density in the Veil that the narrow H I component is strongly dominated by the magnetic field. That is, the field energy is much larger than the energy associated with non-thermal motions in the gas. The narrow H I component in the Veil is the only interstellar environment known with this property.
- For the derived density of $10^{3.1}$ cm^{-3} and observed column density of $N(H) \approx 10^{21.6}$ cm^{-2}, the physical thickness of the layer is ≈1 pc. The Veil covers > 1.5 parsecs in the plane of the sky, its aspect ratio is >1:1.5, so is not necessarily a sheet. Were the density high enough to be in energy equipartition, $n \sim 10^4$ cm^{-3}, the Veil would be a thin sheet, with an aspect ratio of 1:15.

6.2.2 Primary conclusions from Chapter 3

- The UV and 21 cm observations have two primary velocity components, a narrower component A and a broader component B.

- n_H is ~$10^{2.5}$ cm^{-3} for component A and ~$10^{3.4}$ cm^{-3} for component B. About 2/3 of the total H^0 column density is associated with the broader of the two observed 21 cm absorption components. $N(H^0)$ is derived from column densities of species that must coexist with H^0, so we can determine T_{spin} for each component. It is likely that $T_{kin} \leq T_{spin}$ in both components. The physical thickness of component A is ~1.3 parsecs and ~0.5 parsecs for component B.
- We observe, for the first time towards the Trapezium, H_2 in absorption. We find that component A has fewer molecules than component B, due to a lower n_H and H^0 column density. The H_2 absorption lines emerge from highly excited states, consistent with the Veil being relatively close to the Trapezium.
- We detect an ionized layer of gas along the line of sight to the Trapezium. The S III, P III, and He I absorption lines all have similar velocities, indicating they are associated with the same region that produces an [N II] emission line component of the nebular spectrum.
- The surface brightness of the newly identified blueshifted [N II] places the ionized gas between the Trapezium and the Veil. The velocity of the ionized gas is blueshifted with respect to the Veil, indicating that it is a distinct layer moving towards the Veil. We find the column density of the H^+ layer is ~10^{20} cm^{-2}, and it is located 1.1-1.6 parsecs away from the Trapezium. Our characterization of this H^+ region resolves a 40-year-old debate on the origin and strength of the He I 3889Å absorption line.
- The ionized layer is probably a radiatively accelerated sheet pushed outward by radiation pressure. At its current distance, the ionized gas will collide with the Veil in < 85,000 years.
- The energy in component A is dominated by the magnetic field, a situation unique in the ISM. In component B, magnetic and turbulent energies are in

approximate equipartition as they appear to be in most regions of the ISM. Both components A and B are magnetically subcritical.

- We cannot determine, given the current data, if component A or B is closer to the Trapezium. Higher resolution H_2 absorption data with better S/N is needed to determine strength of the UV radiation field and place each Veil component along the line of sight.

6.2.3 Primary conclusions from Chapter 4

- We expanded the plasma simulation code Cloudy to include a ~1000 reactions 68 species molecular network, including its effects on the ionization and thermal balance. Our treatment of sized-resolved grains and PAHs are described by van Hoof et al. (2004). These calculations can be applied to starbursts, ULIRGs, and O stars embedded in molecular clouds, as well as blister H II regions.
- We computed the ionization, thermal, and chemical structure of a large number of clouds, assuming constant gas pressure to relate the H II region and PDR. We present grids of results that show how emission lines vary over a wide range of T_*, n_{H^+} and U.
- We predict the contribution of the H II region to PDR emission-line diagnostics. We find that the contribution from the ionized gas is more important for low-density, low-G_0 regions. The H II region contributes a larger percentage of the line emission when T_* is high, since this increases the size of the H II region relative to the PDR.
- We use our calculations to determine the conditions in two star-forming regions: NGC 253 and NGC 7714. Analysis of the full spectrum, including lines from both the H II region and PDR, can self-consistently determine physical conditions.

- It will be possible to use H II region and PDR line ratios to determined densities in each region. When combined with either theoretical or observational measures of the gas temperature, the gas pressure can be obtained in each region. This can then test whether the cloud equation of state is dominated by gas pressure, as seems to be the case in the two objects analyzed here, or whether other pressure terms, perhaps magnetic pressure (Heiles & Crutcher 2005), dominate. The latter is frequently found across the Galaxy.

6.2.4 Primary conclusions from Chapter 5

- We have identified spectral diagnostics that can be used to determine the role of magnetic fields in star forming regions where the H II region and PDR are in pressure equilibrium. Diagnostic ratios that yield U, T_*, and $n_{\rm HII}$, combined with a ratio of an emission line formed in the H II region to an emission line formed in the PDR, the parameter β can be determined. This only requires a single PDR emission line.
- The most promising diagnostic ratio to determine β is the [O III]/[O I] ratio. This is because almost all [O I] emission comes from the H II region, and because the ratio of two oxygen lines makes this ratio relatively insensitive to abundance.
- We have analyzed the data of M01, which derived $n_{\rm PDR}$ and $T_{\rm PDR}$ for a large number of galaxies, and derived ranges of $n_{\rm HII}$ that gives values of β consistent with what is observed in local star forming regions. For NGC 1222, we combine the results of M01 with optical data and find $\beta = 0.25$, six times higher that the value found by Crutcher (1999) in the local ISM.
- Our calculations outline a general methodology to use in determining the equation of state. Currently, the [O III]/[O I] ratio is not commonly observed in star forming regions. With the launch of SOFIA and Hershel anticipated in

2007, the [O III]/[O I] ratio should be observable in many galaxies. When these missions are in operation, the methodology outlines here will be able to derive the contribution of magnetic pressure for a host of galaxies.

6.3 Final Remarks

This work has shown that the best way to analyze such a spectra is through a single self-consistent calculation. Such a calculation would not be possible without the continual improvements made to Cloudy over the last quarter-century. Additionally, the additional physical processes added to Cloudy in this work will provide a powerful theoretical tool for interpreting data obtained by the next generation of telescopes. This dissertation is therefore not all that conceptually different from the work of early astronomers 400 years ago. Kepler relied on Copernicus and Brahe. Newton relied on Galileo, Kepler, and others. Bessel relied on two hundred years of technological advances in the telescope. Whether the technological advances involve a telescope or computational techniques the end result, a better understanding of our universe, remains constant.

Appendices

Appendix A - Sensitivity of N(H_2) to Formation and Destruction Rates

In this section we show the extreme sensitivity that predicted molecular hydrogen column densities have to the formation and destruction rates.

In the interstellar medium, molecular hydrogen forms primarily through catalysis of two hydrogen atoms on grain surfaces. Destruction of H_2 occurs through photoabsorption in the Lyman-Werner bands. Calculating formation and destruction rates for the H_2 molecule can be computationally expensive, since the number of rotational/vibrational levels for H_2 is ~10^5. We will refer to the treatment of all levels of H_2 in calculating formation and destruction rates as using the "complete H_2 molecule", as in Section 2.3.2. The population of each level is determined by balancing processes that correspond to formation into it, destruction from it, and transitions into and out of it into other levels.

Often approximations to the formation and destruction rates are made, with the ultimate goal of increasing calculation speed while at the same time making predictions for H_2 abundances to the same level of accuracy as the complete H_2 molecule. Then the chemistry can be treated as a simple two-component system, and the balance written as

$$n\left(H_2\right)R_d = \frac{1}{2}n(H^0)nR_f \ \text{cm}^{-3}\ \text{s}^{-1} \qquad \text{(A1)}$$

where the photodestruction and grain formation rates are given by R_d and R_f, the stoichiometric factor is ½, and $n(H^0)$ and n are the atomic and neutral hydrogen densities [$n = 2n\left(H_2\right) + n\left(H^0\right)$].

Appendix B - Destruction Rates

Two widely used approximations to the destruction rates of H_2 come from Bertoldi & Draine (1996, henceforth referred to as BD96) and Tielens & Hollenbach (1985, referred to henceforth as TH85). While these approximations increase computational speed, the true dissociation rate may deviate significantly from simple analytical approximations if the UV field excites electrons to many different rotational/vibrational levels.

We tested how variations in these simple approximations to the destruction rates changed the predicted H_2 column density. First, in the case of destruction, we took the destruction rate given in the TH85 paper and scaled it in the following manner:

$$R_d = X \cdot 3.4 \cdot 10^{-11} \beta(\tau) G_0 e^{-2.5 Av} \quad \text{s}^{-1} \qquad \text{(B1)}$$

Here $\beta(\tau)$ is a self-shielding factor that characterizes the amount of the continuum between 6 and 13.6eV that has been absorbed by the Lyman-Werner bands. As H_2 becomes more shielded from these photons, $\beta(\tau)$ will decrease. The parameter G_0 is the flux of UV photons between 6 and 13.6eV relative to the average interstellar value, with the exponential factor accounting for dust absorption of photons in the same range of energy. The scale factor X is a free parameter that we use to test how the predicted H_2 column density varies with changes in the destruction rate. The BD96 destruction rate is very similar with the exception that self-shielding is unity for H_2 column densities less than 10^{14} cm^{-2}, which in terms of equation B1 means that $\beta(\tau)$ varies differently with depth.

As Figure B1 shows, scaling the simple dissociation rate by factors of < 10 can cause the predicted H_2 column density to change by several orders of magnitude. This sensitivity is due to the non-linear effects that changes in H_2 have on the self-shielding. Increasing the H_2 destruction rate will decrease the amount of H_2. Consequently, a decreased H_2 abundance will lead to less absorption of the

Lyman-Werner bands (a higher $\beta(\tau)$), and hence less self shielding. This positive feedback mechanism produces the large changes in H_2 abundance for small changes to the scaling factor seen in Figure B1.

One would not expect either the TH85 or BD96 destruction rate to exactly match the H_2 destruction rate generated by Cloudy. Cloudy self-consistently determines the photodestruction rate for each line including attenuation by absorption, reemission by the gas, and line overlap. This is done for each depth into a cloud. Combining the use of a complete H_2 molecule with a self-consistent treatment of the radiation field gives the most physically realistic treatment of the Solomon process.

We compared the predicted H_2 abundance for three different treatments of the destruction rate, keeping all other parameters fixed. We took our best model and then changed the way we calculated the destruction rate to either that of TH85, BD96, or the complete H_2 molecule in Cloudy. Our results shown in Table B1 clearly demonstrate how approximations to the destruction rate can lead to dramatically different results. For the TH85 rate, the predicted column density was 4 orders of magnitude larger than either BD96 or the complete H_2 molecule. This difference suggests that treating the H_2 molecule as a two level atom causes the calculation to overcompensate for the effects of self-shielding, which lowers the calculated destruction rate. The lower destruction rate then causes an overabundance of H_2 through the same non-linear feedback that is seen in Figure B1. Because the BD96 approximation sets $\beta(\tau)$ equal to one for $N(H_2) < 10^{14}$ cm^{-2}, this approximation will lead to a slightly larger destruction rate and hence less H_2 formation. However, it appears that in general the BD96 dissociation rate approximates the Cloudy dissociation rate fairly well.

Appendix C - Formation Rates

In addition to testing the sensitivity of the predicted H_2 abundance to the destruction rate, we also tested the sensitivity of the H_2 abundance to the formation rate of H_2 by grain catalysis. TH85 use a formation rate given by:

$$R_f = X \cdot 6\times10^{-17}\left(T/300\right)^{0.5} S\left(T\right) \text{ cm}^3\text{ s}^{-1} \qquad \text{(C1)}$$

T is the temperature, and *S(T)* is the sticking coefficient taken from Hollenbach and McKee (1979). Again, we insert a scaling factor *X* to test how the H_2 abundance changes with formation rate.

Figure B1 also shows how scaling the formation rate affects the predicted H_2 abundance. Just like with the destruction rate, the final amount of H_2 is very sensitive to changes in the formation rate. Again, this is due to the non-linear relationship between the rate and the H_2 density. Because the H_2 fraction depends on the grain formation rate and *n* in equation C1, scaling the formation rate will make the H_2 abundance increase/decrease which in turn feeds back into equation C1 through *n*. This feedback quickly leads to large changes in H_2 formation for relatively small changes in X'. Since the formation rate is dependent on the treatment of the grain physics and the observationally determined rate coefficient (Jura, 1974), care must be taken to assure that both of these factors are determined to the highest possible precision.

Appendix D - Grain Size Distribution

We ran one final test, to check how the H_2 column density changed when different grain distributions were considered. We ran a series of models with a density of 10^3 cm^{-3}, approximately corresponding to our best model density. We then varied G_0 from 1 to 10^6 in increments of 0.5 dex. This calculation was

performed for both an Orion grain distribution (absence of small grains) and a standard ISM grain distribution, designed to reproduce the standard interstellar extinction curve (R=3.1). This calculation, unlike the rest of our calculations, neglected hydrogen ionizing radiation. We also stopped this calculation at a total hydrogen column density of 4×10^{21} cm^{-2}, as opposed to just the atomic column density $N(H^0)$ in all other calculations.

As shown in Figure D1, the final H_2 column density can be very sensitive to the grain size distribution. For low values of G_0, both size distributions are effective in absorbing the H_2 dissociating continuum. This low dissociation rate allows all the available hydrogen to combine into H_2. As the value of G_0 is increased, a point is reached where, for a given size distribution and total hydrogen column density, the H_2 dissociating continuum is not effectively absorbed. The value of G_0 where this occurs will be smaller for grain size distributions that are weighted towards large grains. Larger grains provide less extinction per unit mass, which in turn keeps the dissociation rate large over a greater depth into the cloud. Figure D1 shows that the critical value of G_0 where the dissociation rate remains large (i.e. self-shielding no longer occurs) is about $10^{2.5}$ for Orion grains and about 10^4 for ISM grains. Over the range of $10^{2.5} < G_0 < 10^{4.5}$, differences in the predicted H_2 column density approaching 6 orders of magnitude can occur. This range of G_0 includes the value of about 10^4 that we estimate for the Veil. Therefore, the anomalous grain size distribution in the Veil is capable of having a very important effect upon the H_2 abundance. For $G_0 > 10^{4.5}$, the sensitivity of H_2 to grain size is lessened. For these high values of G_0, neither size distribution is effective in absorbing the H_2 dissociation continuum, which keeps the dissociation rate high. The H_2 column density will remain small and, as can be seen in equation C1, scale inversely with the dissociation rate. The grain size distribution still affects the predicted H_2 abundance, because the larger grain sizes in Orion are less effective than the ISM grains in absorbing the UV continuum. The Orion grains also have less surface area per unit mass of

hydrogen, which lowers the H_2 formation rate on grains relative to the ISM grain size distribution. These combined effects cause the predicted H_2 column density to be ~1.5 dex lower for our Orion grain size distribution for $G_0 > 10^{4.5}$.

The importance of using accurate formation and destruction rates is not new, Browning et al. (2003) also demonstrate this principal in a different context. However, it is not widely know that small deviations from the true formation and destruction rates can cause H_2 abundance predictions to vary by large amounts, at least for conditions similar to the Veil. One must be sure that any assumptions or approximations to the formation and destruction rates do not significantly affect the final predictions. The best way to do this is to check the approximation versus the more refined, computationally expensive calculation. In the case of this paper, the TH85 destruction rates often led to results that differed significantly from observation. Our "best model" would not be allowed by observation if we had used the TH85 destruction rate. It was not until we calculated a destruction rate determined by using the "complete H_2 molecule" that we obtained results that were consistent with observational data.

Appendix E - Chemical Network in Cloudy—Reactions and Rate Coefficients

As shown in Figure 4.14, our calculations can extend to the point where the vast majority of elements are in molecular form. One of the major improvements to the spectral synthesis code Cloudy is upgrading the molecular network in Cloudy. This network consists of ~1000 reactions, which predict abundances for the following 68 molecules:

H_2, H_2^*, H_2^+, H_3^+, HeH^+, CH, CH^+, OH, OH^+, O_2, CO, CO^+, H_2O, H_2O^+,O_2^+, H_3O^+,CH_2^+,CH_2,HCO^+,CH_3^+, SiH_2^+, SiH, $HOSi^+$, SiO, SiO^+, CH_3, CH_4, CH_4^+, CH_5^+,N_2, N_2^+, NO, NO^+, S_2, S_2^+, OCN, OCN^+, NH, NH^+, NH_2, NH_2^+, NH_3, NH_3^+,

NH_4^+, CN, CN^+, HCN, HCN^+, HNO, HNO^+, HS, HS^+, CS, CS^+, NO_2, NO_2^+, NS, NS^+, SO, SO^+, SiN, SiN^+, N_2O, HCS^+, OCS, OCS^+, C_2, and C_2^+.

We solve a system of linear, time steady equations for the molecular abundances (Atkins 1998). Consider a reaction of the form:

$$aA + bB \rightarrow cC + dD \tag{E1}$$

Here A, B, C, and D can be a molecule, atom, electron, or a photon and the lowercase letters are the stoichiometric coefficients. This reaction has the rate:

$$-kn(A)n(B) = \frac{1}{a}\frac{dn(A)}{dt} = \frac{1}{b}\frac{dn(B)}{dt} = -\frac{1}{c}\frac{dn(C)}{dt} = -\frac{1}{d}\frac{dn(D)}{dt} \quad (\text{cm}^{-3}\ \text{s}^{-1}) \tag{E2}$$

Many reactions will create or destroy a given species, and so the total rate of change of each species will be a sum over many reaction rates.

When the reaction rate contains the product of two densities, both of which are unknown, the equations are *non-linear*. We can linearize the rate by making the difference between the old and new solution small. We assure this by choosing the zone thickness δr so that the conditions in adjacent zones never change by more than a set tolerance.

Using as an example the reaction rate from above, $-kn(A)n(B)$, we can define the difference between the old and new solution as:

$$\Delta_{A,B} = n(A,B)_{new} - n(A,B)_{old} \qquad (\text{cm}^{-3}) \tag{E3}$$

The subscripts *new* and *old* refer to the current (unknown) solution and the previous (known) solution, respectively. In this notation, $n(A,B)_{new}$ is the density that goes into the reaction rate. Using E3, the reaction rate becomes:

$$-kn(A)n(B) = -k\left[\left(\Delta_A + n(A)\right)\left(\Delta_B + n(B)\right)\right] =$$
$$-k\left[\Delta_A\Delta_B + \Delta_A n(B)_{old} + \Delta_B n(A)_{old} + n(A)_{old}\, n(B)_{old}\right] = \quad (\mathrm{cm^3\ s^{-1}}) \qquad \text{(E4).}$$
$$-k\left[n(A)_{new}\, n(B)_{old} + n(A)_{old}\, n(B)_{new} - n(A)_{old}\, n(B)_{old}\right]$$

The last term was derived by ignoring terms to second order in delta. This expression for the rate coefficient now is linear, and allows for a solution through standard matrix inversion methods.

The chemical network is sensitive to details. We have included a complete treatment of the H_2 molecule in Cloudy (Shaw et al., 2005). This determines populations of 1893 levels producing 524,387 emission-lines, along with a detailed treatment of the self-shielding of H_2 electronic transitions. We also use other self-shielding functions. The calculations presented in this paper use the self-shielding function of Draine & Bertoldi (1996). Like H_2, CO is destroyed by absorption in electronic transitions, which we treat by using the dissociation rate given by Hollenbach, Takahashi, & Tielens (1991) with a rate coefficient derived by van Dishoeck and Black (1988). We determine the abundance of excited H_2 (H_2^*) following Tielens & Hollenbach (1985). In this approach, reactions form both H_2 and H_2^*, with the temperature barrier removed for reactions with H_2^*. Excited H_2 is very reactive, and, at shallow depths where the Solomon process produces a large population in H_2^*, its inclusion changes chemical equilibrium. In deeper regions, where H_2 is well shielded, nearly all H_2 is in the ground state.

We can include the effects of CO depletion on grain surfaces, using the treatment given in Hasegawa & Herbst (1993), but did not treat this process in our calculations.

We use the UMIST database (Le Teuff, Millar, & Markwick, 2000) for the vast majority of our rates. There are exceptions, however. For instance, an important reaction that forms CO involves C^+ and OH

$$C^+ + OH \rightarrow CO^+ + H \qquad \text{(E5)}$$

$$C^+ + OH \rightarrow CO + H^+ \qquad \text{(E6).}$$

In UMIST, these reactions have a rate, $k = 7.7\times10^{-10}$ cm^{-3} s^{-1}, which does not depend on T. Table 1 of Dubernet et al. (1992) shows that, over their range of study, $T < 100$ K, the rate does depend strongly on T. We have derived a power law fit to the Dubernet et al. (1992) data, which fits their data for $T < 100$ K. Written in the same format as the UMIST, our derived rate is:

$$k = 2.7\times10^{-9}\left(\frac{T}{300}\right)^{-0.3508} \quad [\text{cm}^3\ \text{s}^{-1}] \qquad \text{(E7)}$$

For the important charge transfer reactions between O and H, we use rates based on Stancil et al. (1999) that extends to $T = 10^7$ K. For $H^+ + O \rightarrow H + O^+$, the UMIST rate diverges from the rate derived by Stancil et al. for $T > 10{,}000$ K, while the reaction $H + O^+ \rightarrow H^+ + O$ diverges for $T > 41{,}000$ K. Cloudy is widely used to calculate conditions in hot plasmas, so it is necessary to have rates that extend over all physical regimes.

We compute photo-interaction rates by integrating the local continuum over the photo cross section, as

$$k = \int \frac{4\pi J_\nu}{h\nu}\,\sigma_\nu\,d\nu \qquad [\text{s}^{-1}] \qquad \text{(E8)}$$

Here the integral is over the relevant photon energies, σ_ν is the photo-cross section, and J_ν is the local radiation field (Figure 4.2). This radiation field includes the attenuated incident continuum and diffuse emission produced within the H II region and PDR. This allows such processes as photo-interactions with Lα or the IR continuum produced by hot grains in the H II region to be self-consistently included.

Two important rates, H radiative recombination and He charge transfer recombination with H, are significantly different from the UMIST database. The UMIST rate of reaction R^H for $H^+ + e \rightarrow H + h\nu$ is:

$$R^H_{rad-rec} = 3.50\times10^{-12}\left(\frac{T}{300}\right)^{-0.75} \quad 10 < T < 20{,}000 \quad [\mathrm{cm^3\ s^{-1}}] \qquad \text{(E9)}$$

This differs from the exact rates computed by Ferland et al. (1992) by ~30% for $T < 100$ K. This is important because, even though H^+ is only a trace species in a PDR, its absolute abundance is large. It can be a significant electron donor, and this affects molecular reaction rates and therefore molecular formation. An approximation to the radiative recombination rate, over the UMIST T range, is:

$$R^H_{rad-rec} = 3.50\times10^{-12}\left(\frac{T}{300}\right)^{-0.75} - 3.0\times10^{-12}\left(\frac{T^{1.05}}{40}\right)^{-1.3} \quad [\mathrm{cm^3\ s^{-1}}] \qquad \text{(E10)}$$

The first term is just the UMIST rate, while the second term is a correction factor that allows for better agreement at low T. Figure E1 shows how the Cloudy recombination rate, UMIST rate, and the best fit to the Cloudy recombination rate vary over the range 10-20,000 K. The rate becomes negative for $T < 2$ K. The lower bound of T for most UMIST rates is 10 K, so our rate is stable over the range covered by UMIST.

The UMIST rate for the charge transfer process $He^+ + H \rightarrow H^+ + He$ is a factor of 4 too large. This rate in UMIST should be:

$$R^{He}_{ch-tr} = 1.21\times10^{-15}\left(\frac{T}{300}\right)^{0.18} \quad 10 < T < 1000 \quad [\mathrm{cm^3\ s^{-1}}] \qquad \text{(E11).}$$

The original rate was derived by Zygelman et al. (1989), while Stancil et al. (1998) give the correct rate. Charge transfer recombination of He with H is the main formation process for He^0 at the illuminated face of a PDR. The large rate leads to a factor of four decrease in the density of He^+, affecting the abundances of

other molecules due to reactions of He^+. This primarily affects molecular abundances for low A_V, or translucent clouds. For high A_V, the abundance of H^0 is significantly less. This makes this rate less important at high A_V.

Appendix F - Charge and Energy Exchange of Gas and Dust

When an atom or ion collides with a grain particle, there is a possibility that an exchange of electrons occurs. We will assume that the atom or ion has charge Z before it hits the grain, and that after the charge exchange it leaves the grain with charge Z_0. The value of Z_0 is determined by assuming that electrons always move into the deepest potential well (i.e., the exchange is always exothermic). This implies that electrons can move in either direction, although in most cases they will move from the grain into the ion. The exchange of electrons will continue until the next exchange would have been endothermic. The ion charge where this condition is reached is by definition Z_0. This definition is deceptively simple as the depth of the potential well of the grain and the ion must be reevaluated each time an electron is exchanged. Expressions for the grain potential were taken from Weingartner & Drain (2001) and will be discussed in more detail in a forthcoming paper. In most cases $Z_0 = 0$, but for third and fourth row elements with low ionization potentials there may be exceptions. Note that Z_0 depends on A and Z, as well as the change of grain Z_i. The rate (per unit projected grain surface area) for this process is given by

$$\alpha_p\left(A, Z \rightarrow Z_0\right) = N_{A,Z}\overline{\nu_A}S_p\sum_{i=1}^{n} f_i\eta_Z, \text{ with } Z \geq 0, \text{ [cm}^{-2}\text{ s}^{-1}\text{]} \qquad \text{(F1)}$$

where f_i is the fraction of the grains that have charge Z_i (see van Hoof et al. 2004 for a detailed discussion of the way the grain charge distribution is derived). $N_{A,Z}$ is the number density of the incoming ion, A^{Z+}, $\overline{\nu_A}$ is the average velocity of that ion, and S_p is the sticking probability for atoms and ions (assumed to be 1 when

$Z \neq Z_0$). When an ion approaches a charged grain, there will be either attraction or repulsion depending on the sign of the charges. This Coulomb interaction will either magnify or diminish the collisional cross section, an effect which is described by the factor $\eta_Z \equiv \tilde{J}(\tau, \nu)$. We use the expressions given in Draine & Sutin (1987), which include polarization effects in the grain induced by the approaching particle. This theory needs two scaling parameters τ and ν which are simply the ratio of the two charges (ν) and of the kinetic energy of the approaching particle and the potential energy of the grain (τ). These parameters are given by

$$\tau = \frac{4\pi\varepsilon_0 akT_e}{(Ze)^2} \tag{F2}$$

$$\nu = \frac{Z_i}{Z} \tag{F3}$$

where *a* is the radius of the grains, and the rest of the symbols have their usual meaning.

Charge exchange between grains and negatively charged ions as well as charged molecules is currently not implemented. These will be added at a later date.

The Cloudy treatment of collisional heating or cooling of the gas due to collisions with the grains was first described in Baldwin et al. (1991). The formulation given in that paper has been largely retained, with the following two exceptions. It is now assumed that the outgoing particle has charge Z_0 instead of always being neutral, as was outlined above. Secondly, the Coulomb interaction between the ion and the grain is treated using expressions from Draine & Sutin (1987). The factor η_Z needed in that formulation has already been discussed, the factor ξ_Z has been replaced by $\tilde{\Lambda}(\tau, \nu)/2$. Since the heating rates of the gas depend on the grain charge, all changes to the charging

physics will affect the heating rates as well. These changes have been partially discussed by van Hoof et al. (2004) and largely follow Weingartner & Draine (2001).

The most important changes with respect to Baldwin et al. (1991) are the introduction of the hybrid grain charge model (which includes a minimum charge for all grains and introduces a bandgap between the valence and conduction band for silicates), the reduction of the work function of graphite, an upgrade of the treatment of the photoelectric effect, and an altered prescription for the sticking efficiency of electrons. A comprehensive discussion of the grain treatment currently included in Cloudy will be presented in a forthcoming paper.

Appendix G - Cosmic Ray Heating

Cosmic rays are the primary source of heating and ionization deep in molecular clouds. Cosmic rays of primary energy E_0 ionize atoms and molecules, primarily hydrogen and helium. The ejected secondary electrons can produce further ionization. The heating and ionization rates depend on the primary ionization rate, electron fraction, and energy of the secondary electron.

Calculations by Shull & van Steenberg (1985, Fig. 3) describe the number of secondary ionizations per primary ionization and the heating efficiency due to cosmic rays. Wolfire et al. (1995) use an equation from Binette, Dopita & Tuohy (1985) that is based on this work, but modified to extend to lower E_0. We also use these results, with the primary cosmic ray energy E_0=35 eV as in Wolfire et al (1995). The form of their equation for the heating efficiency, $\varepsilon(E,x)$, is:

$$\varepsilon(E,x) = \beta_1(x) + \left[\frac{g(E)}{\alpha_1(x)} + \frac{1}{1-\beta_1(x)} \right]^{-1} \qquad \text{(G1)}$$

where E is the primary cosmic ray energy, x is the electron fraction, and $\beta_1(x)$, $\alpha_1(x)$, and $g(E)$ are coefficients that depend upon E and x.

We used Figure 3 of Shull & van Steenberg and derived a best-fit formula for $\varepsilon(E,x)$ as a function of x.

$$\varepsilon(35eV,x) = -8.189 - 18.394x - 6.608x^2 ln(x) + 8.322e^x + 4.961\sqrt{x} \qquad \text{(G2)}$$

which is valid for electron fractions of $1 > x > 10^{-4}$.

Figure Figure G1 compares equation G2 to the expression given by equation A3 of Wolfire et al. (1995). They agree to within 10%.

Cosmic rays effect physical conditions in ways that cannot be treated by only using the UMIST database. We include multi-level atoms of H (Ferguson et al. 1997) and He (Porter et al. 2005), including collisional radiative transfer processes. Cosmic rays excite resonance lines of both H^0 and He^0, and these are degraded into Lα after multiple scatterings. The code computes the mean intensity in all lines, and this is included in the calculation of the radiation field in equation A5. This contributes to grain heating and to photoionization of H^0 and He^0, from the metastable 2*s* and $2\,^3S$ levels respectively. This increases the electron fraction.

Table B1

Variation of H_2 column density with destruction rate treatment

Destruction Rate Treatment	N(H_2) cm^{-2}
TH85	$1.5x10^{19}$
BD96	$5.0x10^{14}$
Cloudy 96 (Complete H_2 molecule)	$1.6x10^{15}$

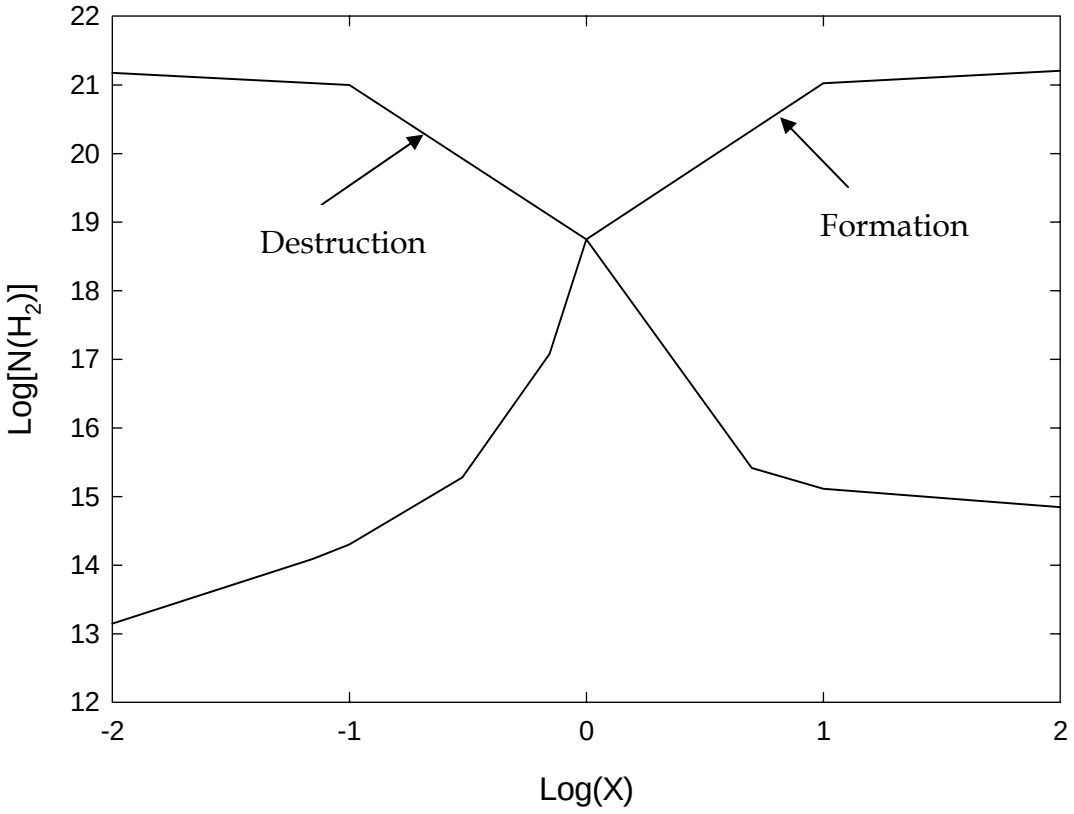

Figure A1 H_2 column density (cm^{-2}) as a function of scaling factor X. This plot clearly illustrates the sensitivity of the H_2 column density to the various rates. Changes in either rate of an order of magnitude can cause changes to the H_2 column density of up to six orders of magnitude. In order to have confidence in predicting the H_2 column density, one must model the H_2 formation and destruction processes as accurately as possible, without resorting to approximations.

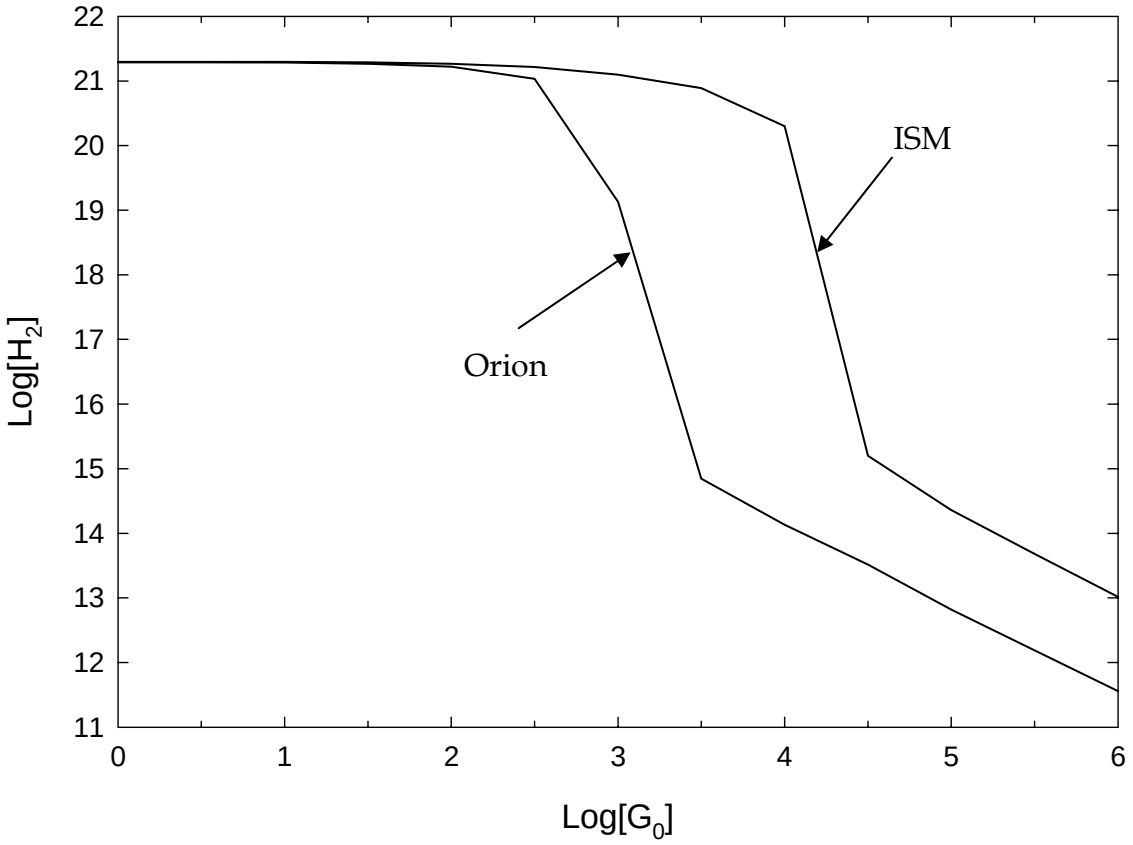

Figure D1 $N[H_2]$ (cm^{-2}) for different grain size distributions over a range of G_0. For $Log[G_0] < 2.5$, H_2 fully forms for both ISM and Orion grains. For larger values the lack of small grains in the Orion distribution is less effective than ISM grains in shielding the H_2 dissociating continuum, and the dissociation rate becomes larger relative to the dissociation rate calculated using ISM grains. This process causes the two size distributions to differ by up to six orders of magnitude for some values of G_0.

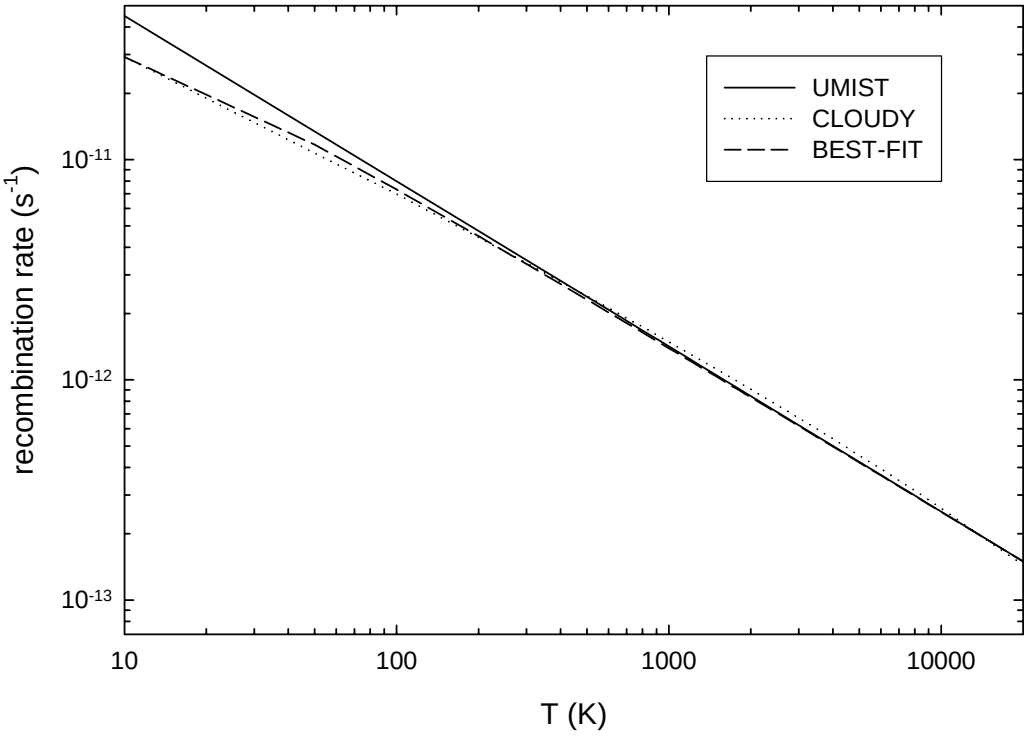

Figure E1 The hydrogen radiative recombination rate used in UMIST (solid line) and in Cloudy (dotted line) versus temperature. Also shown is the best-fit equation to the recombination rate (Ferland et al. 1992, dashed line).

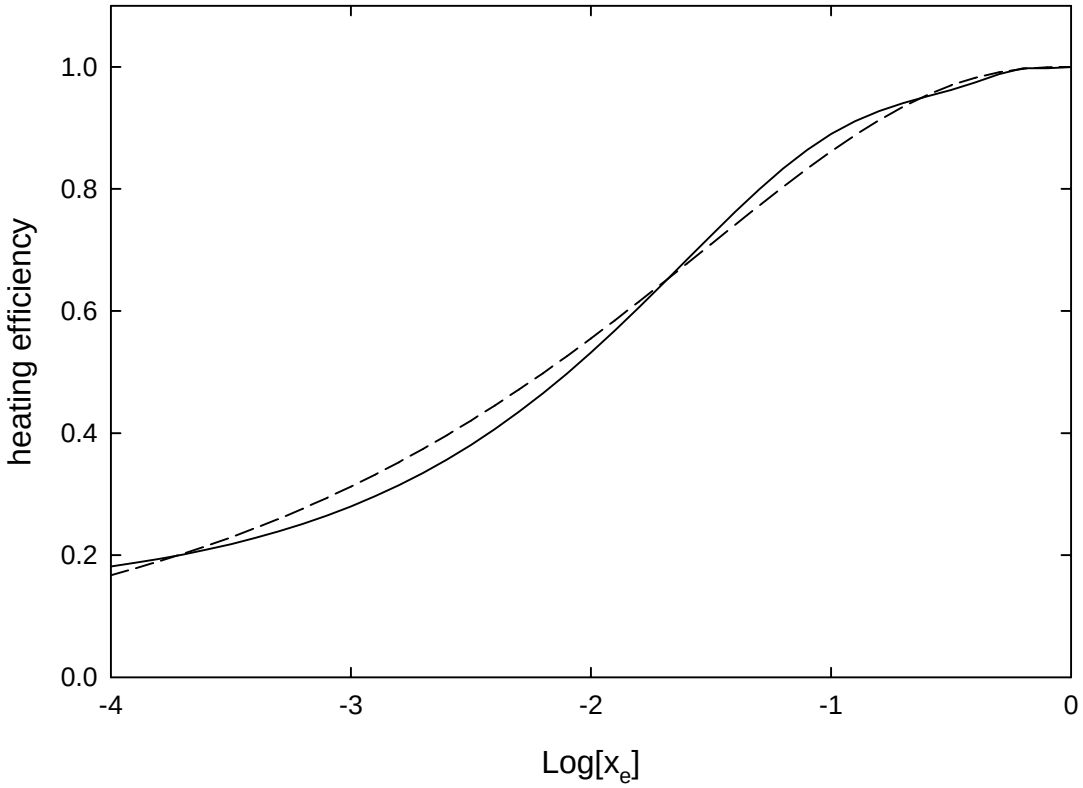

Figure G1 The cosmic ray heating efficiency variation with electron fraction. The solid line is the heating efficiency given by equation 2 of Appendix C, while the dashed line is equation A3 of Wolfire et al. (1995).

References

Aannestad, P. A. & Emery, R. J. 2003, A & A, 406, 155

Abel, N. P, Brogan, C. L, Ferland, G. J., O'Dell, C. R., Shaw, G., & Troland, T. H. 2004, ApJ, 609, 247

Abgrall, H., Le Bourlot, J. Pineau Des Forets, G., Roueff, E., Flower, D. R., & Heck, L. 1992, A&A, 253, 525

Abgrall, H., Roueff, E., & Drira, I. 2000, A&AS, 141, 297

Adams, W. S. 1944, PASP, 56, 119

Allison, A.C. & Dalgarno, A., 1969, Atomic Data, 1, 91

Armour, M., Ballantyne, D., Ferland, G., Karr, J., & Martin, P. G. 1999, PASP, 111, 1251

Atkins, Peter 1998, Physical Chemistry, 6th edition, (Oxford; Oxford University Press)

Bakes, E. L. O. & Tielens, A. G. G. M. 1994, ApJ, 427, 822

Baldwin, J. A. et al. 1996, ApJ, 468, L115

Baldwin, J. A., Ferland, G. J., Martin, P. G., Corbin, M. R., Cota, S. A., Peterson, S. A., Bradley, & M., Slettebak, A. 1991, ApJ, 374, 580

Balick, B., Gammon, R. H., & Hjellming, R. M. 1974, PASP, 86, 616

Bally, J., O'Dell, C. R., & McCaughrean, M. J. 2000, AJ, 119, 2919

Bertoldi, F., & Draine, B.T. 1996, ApJ, 468, 269

Binette, L., Dopita, M. A., & Tuohy, I. R. 1985, ApJ, 297, 476

Black, J, H., & van Dishoeck, E. F. 1987, ApJ, 322, 412

Bohlin, R. C., Savage, B. D. 1981, ApJ, 249, 109

Bottorff, M., Lamothe, J., Momjian, E., Verner, E., Vinkovic, D., & Ferland, G. 1998, PASP, 110, 1040

Browning, M. K., Tumlinson, J., Shull, J. M. 2003, ApJ, 582, 810

Calzetti, D., Armus, L., Bohlin, R. C., Kinney, A. L., Koornneef, J., & Storchi-Bergmann, T. 2000, ApJ, 533, 682

Cardelli, J. A., Clayton, G. C., & Mathis, J. S. 1989, ApJ, 345, 245

Carral, P., Hollenbach, D. J., Lord, S. D., Colgan, S. W. J., Haas, M. R., Rubin, R. H., & Erickson, E. F. 1994, ApJ, 423, 223

Cartledge, S. I. B., Meyer, D. M., & Lauroesch, J. T. 2001, ApJ, 562, 394

Cazaux, S., & Tielens, A.G.G.M., 2002, ApJ, 575, L29-L32

Chandrasekhar, S., & Fermi, E. 1953, ApJ, 118, 113

Crutcher, R. 1999, ApJ, 520, 706

Crutcher, R. M., Troland, T.H., Lazareff, B., Paubert, G., & Kazes, I. 1999, ApJ, 514, L121

Crutcher, R. M.; Troland, T. H.; Goodman, A. A.; Heiles, C.; Kazes, I.; Myers, P. C. 1993, ApJ, 407, 175

Devost, D., et al. 2004, ApJS, 154, 242

Doi, T., O'Dell, C. R., and Hartigan, P. 2004, Aj, 127, 3456

Draine, B. T. & Sutin, B. 1987, ApJ, 320, 803

Draine, B. T., & Bertoldi, F. 1996, ApJ, 458, 269

Dubernet, M. L., Gargaud, M., & McCarroll, R. 1992, A&A, 259, 373

Evans, N. 1999, ARA&A, 37, 311

Ferguson, J. W. & Ferland, G. J. 1997, ApJ, 479, 363

Ferland, G. J. & Elitzur, M. 1984, ApJ, 285, 11

Ferland, G. J. 2002, Hazy, a Brief Introduction to Cloudy (Univ. Kentucky Dept. Phys. Astron. Int. Rep.)

Ferland, G. J., Korista, K. T., Verner, D. A., Ferguson, J. W., Kingdon, J. B., & Verner, E. M. 1998, PASP, 110, 76

Ferland, G. J., Peterson, B. M., Horne, K., Welsh, W. F., & Nahar, S. N. 1992, ApJ, 387, 95

France, K., & McCandliss, S. R. 2005, accepted for publication in ApJL, astro-ph/0507377

Giard, M. Bernard, J. P., Lacombe, F., Normand, P., & Rouan, D. 1994, A&A 291, 239

Giveon, U., Sternberg, A., Lutz, D., Feuchtgruber, H., & Pauldrach, A. W. A. 2002, ApJ, 566, 880

Goudis, C. 1982, *The Orion Complex: A Case Study of Interstellar Matter,* pg. 38 (D. Reidel; Holland)

Gualandris, A., Portegies Zwart, S., & Eggleton, P. P. 2004, MNRAS, 350, 615

Guhathakurtha & Draine, B. T. 1989, ApJ, 345, 230

Habing, H. J. 1968, Bull. of the Astron. Inst. of the Neth., 19, 421

Hasegawa, T. I. & Herbst, E. 1993, MNRAS, 261, 83

Heiles, C. & Crutcher, R. 2005, chapter in *Cosmic Magnetic Fields*, astro-ph/0501550

Heiles, C. & Troland, T. H. 2003, ApJ, 568, 1067

Heiles, C. 1994, ApJ, 436, 720

Heiles, C. 1997, ApJS, 111, 245

Henney, W. J. 1998, ApJ, 503, 760

Henney, W. J., Arthur, S. J., Williams, R. J. R., & Ferland, G. J. 2005, ApJ, 621, 328

Hillenbrand, L. A., Hartmann, L.W. 1998, ApJ, 492, 540

Hollenbach, D. J., & Tielens, A. G. G. M. 1997, 35, 179

Hollenbach, D. J., Takahashi, & T., Tielens, A. G. G. M. 1991, ApJ, 377, 192

Jenkins, E. B. et al. 1998, ApJ, 492, L147

Jones, M. R. 1992, Ph.D. thesis, Rice University

Jura M. 1974, ApJ, 191, 375

Kaufman, M. J., Wolfire, M. G., Hollenbach, D. J., & Luhman, M. L. 1999, ApJ, 527, 795

Keenan, F. P. 1989, ApJ, 339, 591

Kingdon, J. B., & Ferland, G. J. 1999, ApJ, 516, 107

Launay, J.R., Le Dourneuf, M., & Zeippen, C.J., 1991, A&A, 252, 842-852

Le Teuff, Y. H., Millar, T. J., & Markwick, A. J. 2000, A&AS, 146, 157

Liszt, H. S. 2001, A&A, 371, 698

Malhorta, S., Kaufman, M. J., Hollenbach, D., Helou, G., Rubin, R. H., Brauher, J., Dale, D., Lu, N. Y., Lord, S., Stacey, G., Contursi, A., Hunter, D. A., & Dinerstein, H. 2001, ApJ, 561, 766

Mathews, W. G. 1982, ApJ 252, 39

Mathis, J. S., Rumpl, W., & Nordsieck, K. H. 1977, ApJ, 217, 425

McKee, C. F. 1999, osps.conf, 29M

Morisset, C. 2004, ApJ, 601, 858

Morton, D. C. 2003, ApJS, 149, 205

Münch, G., and Wilson, O. C. 1962, ZA, 56, 127

Myers, P. C., Goodman, A. A. 1988, AJ, 326, 27

O'Dell, C. R. 2001, ARA&A, 39, 99

O'Dell, C. R. 2002, RMxAA, 12, 12-15

O'Dell, C. R., Peimbert, M., & Peimbert, A. 2003, AJ, 125, 2590

O'Dell, C. R., Valk, J.H., Wen, Z., & Meyer, D.M. 1993, ApJ, 403, 678

O'Dell, C. R., Yusef-Zadeh, F. 2000, AJ, 120, 382

O'Dell, C. R., & Doi, T. 1999, PASP, 111, 1316

O'Dell, C. R., & Wong, S.-K. 1996, AJ, 111, 846

O'Dell, C. R., Walter, D. K., & Dufour, R. J. 1992, ApJ, 399, L67

Osterbrock, D. E. 1989, *Astrophysics of Gaseous Nebulae and Active Galactic Nuclei*, Mill Valley, CA, Univ. Sci. Press

Osterbrock, D., Tran, H., & Veilleux, S. 1992, ApJ, 389, 305

Osterbrock, D.E., & Ferland, G.J. 2005, *Astrophysics of Gaseous Nebulae and Active Galactic Nuclei* (Mill Valley: University Science Books)

Petuchowski, S. J. & Bennett, C. L. 1993, ApJ, 405, 591

Porter, R.G., Bauman, R.P., Ferland, G.J., & MacAdam, K.B.2005, ApJ, 622, L73

Prasad, S. S. & Huntress, W. T., Jr. 1980, ApJS, 43, 1

Price, R. J., Crawford, I. A., Barlow, M. J., & Howarth, I. D. 2001, MNRAS, 328, 555

Rees, M. J., Netzer, H., & Ferland, G. J. 1989, ApJ, 347, 640

Roueff, E., & Le Bourlot, J. 1990, A&A, 236, 515

Rubin, R. H., Simpson, J. P., Lord, S. D., Colgan, S. W. J., Erickson, E. F., & Haas, M. R. 1994, ApJ, 420, 722

Rubin, R., Simpson, J., Haas, M., & Erickson, E. 1991, ApJ, 374, 564

Savage, B. D., & Sembach, K. R. 1996, ARA&A, 34, 279

Savage, B. D., Bohlin, R. C., Drake, J. F., & Budich, W. 1977, ApJ, 216, 291

Savage, B., D., & Jenkins, E. B. 1972, ApJ, 172, 491

Schaerer, D., & de Koter, A. 1997, A & A, 322, 598

Shaw, G., Ferland, G. J., Abel, N. P., Stancil, P. C., & van Hoof, P. A. M. 2005, ApJ, 624, 794

Shull, J. M., & van Steenberg, M. E. 1985, ApJ, 298, 268

Shuping, R. Y. & Snow, T. P. 1997, ApJ, 480, 272

Smith, J. D. T., et al. 2004, ApJS, 154, 199

Sofia, U. J., Lauroesch, J. T., Meyer, D. M., & Cartledge, S. I. B. 2004, ApJ, 605, 272

Spitzer, L. 1978, *Physical Processes in the Interstellar Medium* (New York; Wiley)

Stancil, P, 2002, private communication

Stancil, P. C., Lepp, S., & Dalgarno, A. 1998, ApJ, 509, 1

Stancil, P. C., Schultz, D. R., Kimura, M., Gu, J. –P., Hirsch, G., & Buenker, R. J. 1999, A & AS, 140, 225

Takahashi, Junko, & Uehara, H., 2001, ApJ, 561, 843-857

Tielens, A. G. G. M. & Hollenbach, D. 1985, ApJ, 291, 722

Tody, D. 1993, "IRAF in the Nineties" in Astronomical Data Analysis Software and Systems II, A.S.P. Conference Ser., Vol 52, eds. R.J. Hanisch, R.J.V. Brissenden, & J. Barnes, 173.

Troland, T. H., and Heiles, C. 2003, accepted by ApJ of November 2002

Troland, T. H., Brogan, C. E., Crutcher, R.M., Goss, W.M. & Roberts, D.A. 2004, ApJ in preparation

Troland, T. H., Heiles, C., & Goss, W.M. 1989, ApJ, 337, 342

Troland, T. H.; Crutcher, R. M.; Goodman, A. A.; Heiles, C.; Kazes, I.; Myers, P. C. 1996, ApJ, 471, 302

Vacca, W.D., Garmany, C.D., & Shull, J.M. 1996, ApJ, 460, 914

van der Werf, P., & Goss, W.M. 1989 A&A 224, 209 (VG)

van Dishoeck & E. F., Black, J. 1988, ApJ, 334, 771

van Hoof, P. A. M., Weingartner, J. C., Martin, P. G., Volk, K., & Ferland, G. J., 2004, MNRAS, 350, 1330

van Hoof, P.A.M., Weingartner, J.C., Martin, P.G., Volk, K., & Ferland, G.J., 2001, in *Challenges of Photoionized Plasmas*, (G Ferland & D. Savin, eds) ASP Conf Ser 247, (astro-ph/0107183)

van der Werf, Paul P., Goss, W. M., Heiles, Carl, Crutcher, R. M., Troland, T. H. 1993, ApJ, 411, 247

Veilleux, S. & Osterbrock, D. E. 1987, ApJS, 63, 295

Verma, A., Lutz, D., Sturm, E., Sternberg, A., Genzel, R., & Vacca, W. 2003, A&A, 403, 829

Walborn N.R., Panek R.J. 1984, ApJ, 286, 718

Watson, W. D., Wiebe, D. S., & Crutcher, R. M. 2001, ApJ, 549, 377

Weingartner, J. C. & Draine, B. T. 2001, ApJS, 134, 263

Wolfire, M. G., Hollenbach, D., McKee, C. F., Tielens, A. G. G. M., & Bakes, E. L. O. 1995, ApJ, 443, 152

Wolfire, M. G., Tielens, A. G. G. M., & Hollenbach, D. 1990, ApJ, 358, 116

Wolniewicz, L., Simbotin, I., & Dalgarno, A. 1998, ApJS, 115, 293

Wurm, K. 1961, ZA ,Ap, 52, 149

Zuckerman, B. 1973, ApJ, 183, 863

Zweibel, E. G. & McKee, C. F. 1995, ApJ, 439, 739

Zygelman, B., Dalgarno, A., Kimura, M., & Lane, N. F. 1989, Phys. Rev. A, 40, 2340

VITA OF NICHOLAS ABEL

Contact Information

- DOB: December 28th, 1976
- Birthplace: New Albany, IN

Degrees Awarded

- B. A. Franklin College of Indiana (08/95 – 05/99)
- M. S. Miami University of Ohio (08/99 - 07/01)

Memberships

- American Astronomical Society (AAS)

Awards & Fellowships

- Catherine and Raymond Cowan Endowed Scholarship in Physics, Franklin College (1997-98)
- Outstanding Teaching Award, Miami of Ohio (2001)
- Outstanding Research Award, Miami of Ohio (2001)
- Kentucky Opportunity Fellowship, University of Kentucky (2001-2003)
- Cochran Fellowship, University of Kentucky (2001-2003)
- Center for Computational Sciences (CCS) Fellowship, University of Kentucky (2004)
- Kentucky Space Grant Consortium Fellowship (KSGC), University of Kentucky (2004)
- CCS Fellowship, University of Kentucky (2005)

Externally Funded Proposals

Ferland, G. J., Abel, N. P. O'Dell, C. R., Troland, T. H., *Physical Processes in Orion's Veil: A High Resolution UV Absorption Study of the Line of Sight towards the Trapezium,* Hubble Space Telescope GO proposal ID #10124. (2004).

Abel, N. P., Ferland, G. J., O'Dell, C. R., Troland, T. H., *Physical Processes in Orion's Veil: A High Resolution UV Absorption Study of the Line of Sight Towards the Trapezium,* Hubble Space Telescope (HST) AR proposal ID #10636. (2005).

Ferland, G. J., O'Dell, C. R., Abel, N. P., *Dynamical flows in PNe: interpreting HST images on a physical basis,* HST theory proposal ID #10653. (2005).

Sarma, A. P., Abel, N. P., Mayo, E., Ferland, G., Troland, T. H. *High Resolution IRS Mapping of the Star Forming Region NGC 6334 A,* Spitzer Space Telescope GO proposal #20220 (2005).

LIST OF PUBLICATIONS

1. Abel, N. P. *A Study on the Evolution of the Uranus/Neptune System and the Rotational Dynamics of the Solar System*, Master's Thesis at Miami University of Ohio (2001)
2. Abel N., Bryant A., Dhakal P., et al. *Observational Consequences of Fine-Structure Line Optical Depths on Infrared Spectral Diagnostics,* PASP 115, 188 (2003)
3. Abel, N. P., Brogan, C. L., Ferland, G. J., O'Dell, C. R., Shaw, G., Troland, T. H. *Physical Conditions in Orion's Veil*, ApJ 609, 247-260 (2004)
4. Ferland, G. J., Abel, N. P., Davidson, K., Smith, N., *Physical Conditions in the Homunculus*, *The Fate of the Most Massive Stars*, ASPC, 332, 298F (2005) astro-ph/0501485
5. Shaw G., Ferland G. J., Abel N. P., Stancil P. C., and van Hoof P. A. M., *Molecular Hydrogen in Star Forming Regions: Implementation of its Micro-physics in Cloudy*, ApJ, 624, 794S (2005)
6. Abel, N. P., Ferland, G. J., van Hoof, P. A. M., & Shaw, G., *Self-Consistent Calculations of Physical Conditions in Star-Forming Regions*, accepted for publication in ApJ (anticipated publication date – 11/2005). astro-ph/0506514
7. Shaw G., Ferland G. J., Srianand, R., Stancil P. C., & Abel, N. P. *Physical Conditions in the ISM Towards HD185418*, submitted to ApJ in May (2005)
8. Abel, N. P., Ferland, G. J., O'Dell, C. R., Shaw, G., Troland, T. H. *Physical Conditions in Orion's Veil II: a Multi-component Study of the Line of Sight toward the Trapezium*, submitted to ApJ in August (2005).
9. Abel, N. P. & Ferland, G. J. *Determining the Role of Magnetic Fields in Extragalactic Star Forming Regions.* In preparation.
10. Ferland, G. J., et al. *Inner Shell Transitions, Their Spectral Signitures, and Effects on Ionization*. In preparation.
11. Mayo, E., Abel, N. P., Troland, T. H., Sarma, A. P., & Lockett, P. B. *VLA OH Zeeman Observations of the NGC 6334 Complex Source A*. In preparation.
12. M. Rollig, et al. *A PDR-Code Comparison Study*. In preparation.

Nicholas Paul Abel